

FUNCTIONALIZED RAFT POLYMERS FOR THE SYNTHETIC INDUCTION OF *Escherichia coli* BIOFILMS

By

José Luis Brioso Jiménez



UNIVERSITY OF
BIRMINGHAM

A thesis submitted to the University of Birmingham for the degree of
DOCTOR OF PHILOSOPHY

School of Chemical Engineering
College of Engineering and Physical Sciences
University of Birmingham
October 2021

UNIVERSITY OF
BIRMINGHAM

University of Birmingham Research Archive

e-theses repository

This unpublished thesis/dissertation is copyright of the author and/or third parties. The intellectual property rights of the author or third parties in respect of this work are as defined by The Copyright Designs and Patents Act 1988 or as modified by any successor legislation.

Any use made of information contained in this thesis/dissertation must be in accordance with that legislation and must be properly acknowledged. Further distribution or reproduction in any format is prohibited without the permission of the copyright holder.

Abstract of the thesis

Functionalized RAFT polymers for the synthetic induction of *Escherichia coli* biofilms

Bacterial biofilms are clusters of microorganisms, embedded in a protective extracellular polymeric matrix, that attach to and colonize biotic and abiotic surfaces. Biofilms are extremely resilient and are responsible for recalcitrant infections and biofouling of industrial material, but there are also multiple industrial uses for biofilm communities in bioreactors, bioremediation, and wastewater treatment. There have been advances within the research community to design materials that are able to modulate bacterial behaviour to induce aggregation and synthetic biofilm formation to sequester bacteria and prevent them from colonizing surfaces, or to induce the formation of synthetic biofilm communities with biotechnological purposes in the industrial sector.

The main topic of this PhD thesis was to investigate the effects of some RAFT linear polymers over the biofilm formation behaviour of *Escherichia coli* aiming to design and test polymeric materials able to aggregate *E. coli* and induce synthetic biofilm formation.

The main polymer used during this research was poly(acryloyl hydrazide) (PAH), a linear polymer scaffold which hydrazide side chains can be easily modified via post-polymerization functionalization in aqueous conditions without the need of further purification steps to test different functional groups to target *E. coli* aggregation and biofilm formation. The results findings obtained during this research suggest that positively charged PAH without further functionalization was able to aggregate and induce biofilm formation in *E. coli* due to electrostatic nonspecific interactions. PAH functionalized with carbohydrates moieties were able to also aggregate and induce the formation of thicker biofilms in *E. coli*. Part of this research was devoted to study the chemical stability of the functionalized PAH's over time, and the co-functionalization of PAH with two different functional groups at the same time was pursued with successful results.

In this manuscript I report for the first time the synthesis, characterization, and loading stability of the novel poly(acryloylglycine hydrazide), a linear scaffold that can be easily functionalized under aqueous conditions without the need of further purification steps. This polymer has a similar structure to PAH, and was designed with the aim to improve on the functionalization loading efficiencies with diverse model functional groups.

Plagiarism disclaimer

I hereby declare that this dissertation is my own original work and has not been submitted before to any institution for assessment purposes. Further, I have acknowledged all sources used and have cited these in the reference section.

Acknowledgements

A PhD is a voyage filled with challenges, a personal journey that could not have been accomplished without the help and support of mentors, colleagues, friends, and family.

I would like to express my gratitude to my supervisors Tim Overton and Francisco Fernandez-Trillo (Paco) for the opportunity given, the support and the mentorship without which this project would not exist.

I would like to thanks the previous and current members of Tim's lab: Maria Charalampous, John Rolley, Ana de Magalhaes, Hong Li, Ikhlās Kasili, Wendy Allen and Stacey Golub, and from Paco's Lab: Daniel Crisan, Ignacio Isua, Oliver creese, Adam Kolodziej, Nicolás Perez-Soto, Adrian Pérez, Andrew Wilkinson, Krystian Ubych, Charlotte Farrow, Carlos Guillen Posteguillo, Tom Leigh, Manal Alanzi, Dr. Andrey Romanyuk , Dr. Sameh Al Sayed, and Pavan Adoni. I hold fond memories shared with them working in the lab and taking some refreshments at the Staff house on Friday nights. I really have to take a moment to reflect and to acknowledge the impact that Daniel Crisan, Ignacio Insua, Adam Kolodziej, Oliver Creese, and Adrian Pérez had on me, they were not only great and supportive colleagues that showed me the intricacies of organic chemistry, they are also magnificent human beings which friendship I hold dear.

I could have not delivered this manuscript if it wasn't for the arduous work of the technicians Allen Bowden (GPC), Cécile Le Duff (NMR), Elaine Mitchell and Ronnie Baglin (Biochemical engineering).

There have been moments I thought I would not make it through the PhD and I found myself surrounded by amazing friends that held my back and pushed my forward, to: Manolo, María, Adrian, Xavi, Sara, Cristina, Giusy, William, Despoina, Paolo, Angela, Anna, Annica, Daniel, Sema, López, Valentín and Curro.

And finally, thanks to my family for the continuous support I received by my sister Ana María, my mother María del Carmen, and my grandmother Ana.

Table of contents

List of figures, schemes, tables and equations	VI
1. Introduction	1
1.1 Bacterial biofilm communities and its importance	1
1.2 Biofilm lifecycle	3
1.2.1 Initial reversible attachment	3
1.2.2 Irreversible attachment	4
1.2.3 Biofilm growth and maturation	5
1.2.4 Dispersion	6
1.3 The importance of surface properties for bacterial colonization and biofilm formation	7
1.3.1 Surface charge	8
1.3.2 Surface wettability	9
1.3.3 Surface roughness	10
1.3.4 Surface topography	11
1.4 Synthetic polymers mediating bacterial aggregation and biofilm formation	13
1.4.1 Bacterial sequestration by cationic polymers	14
1.4.2 Functionalized polymers with biological motifs	15
1.5 Biotechnological applications of biofilm	17
1.5.1 Bioremediation uses of biofilm	17
1.5.2 Biofilm bioreactors	17
1.6 Project objectives	19
2. RAFT polymers for biological applications	20
2.1 Background	20
2.1.1 RAFT polymerization mechanism	21
2.1.2 RAFT polymerization kinetics	22
2.1.3 RAFT agent selection	24
2.1.4 Post-polymerization functionalization as a tool for biological screening	25
2.1.5 Poly(acryloyl hydrazide)	27
2.2 Objectives	29
2.2.1 Co-functionalization and stability of poly(acryloyl hydrazide)	29
2.2.2 Synthesis, characterization, and functionalization of poly(acryloylglycine hydrazide)	29
2.3 Results and discussion	31

2.3.1	Loading stability of poly(acryloyl hydrazide)	31
2.3.2	Poly(acryloyl hydrazide) co-functionalization	36
2.3.3	Synthesis, characterization, and functionalization of poly(acryloylglycine hydrazide)	48
2.4	Summary	79
2.5	Future work	80
2.6	Experimental	81
3.	<i>Escherichia coli</i> aggregation and biofilm formation induced by RAFT polymers	88
3.1	Background	88
3.2	Objectives	90
3.3	Results and discussion	92
3.3.1	PAH as a platform for microbiological applications	92
3.3.2	PAGH as a platform for microbiological applications	122
3.4	Summary	124
3.5	Future work	125
3.6	Experimental	126
4.	References	129

List of figures, schemes, tables and equations

Figure 1.1: Typical stage development of bacterial biofilm.....	3
Figure 1.2: Scheme that highlights surface fimbrial organelles that are involved in bacterial surface attachment.	5
Figure 1.3: Interactions between substrate and bacteria that define the success of initial colonization of a surface.	7
Figure 1.4: Proposed aggregation methods by the action of synthetic polymers.	13
Figure 1.5: <i>V. cholerae</i> life cycle.	14
Figure 1.6: (Bottom) <i>E. coli</i> normal initial colonization of host's epithelia. (Top) <i>E. coli</i> colonization inhibition proposed by Yan et al. ¹²⁶	15
Figure 1.7: Molecular/macromolecular FimH antagonists designed and tested by Yan et al. ¹²⁶	16
Figure 2.1: Different behaviours expected over time on RAFT polymerization depending on changes of [Pn].	23
Figure 2.2: Post-polymerization functionalization	26
Figure 2.3: Post-polymerization functionalization with aldehydes via amino-carbonyl condensation reaction.	27
Figure 2.4: Representative ¹ H-NMR spectra of the functionalization of PAH ₄₀ with 1 equivalent of 4-imidazolecarboxaldehyde in 5% acetic acid buffer in D ₂ O.	32
Figure 2.5: ¹ H NMR spectra of the reaction of PAH ₄₀ with 1 equivalent of 4-imidazolecarboxaldehyde analysed at different intervals for 48 h.	32
Figure 2.6: Change of integral value for the signal corresponding to the aldehyde at 9.63 ppm over 48 h.....	33
Figure 2.7: ¹ H NMR spectra of the reaction of PAH ₄₀ with 0.6 equivalent of 4-imidazolecarboxaldehyde analysed at different intervals for 48 h.	33
Figure 2.8: ¹ H NMR spectra of the reaction of PAH ₄₀ with 0.6 equivalents of 4-imidazolecarboxaldehyde analysed at different intervals for 48 h.	34
Figure 2.9: (Left) ¹ H NMR spectra of the reaction of PAH ₄₀ with 0.6 equivalent of 4-imidazolecarboxaldehyde analysed at different intervals for 48 h. (Right) ¹ H NMR spectra of the reaction of PAH ₄₀ with 1 equivalent of 4-imidazolecarboxaldehyde analysed at different intervals for 48 h.	34
Figure 2.10: PAH functionalization with D-glucose after 24h.	37
Figure 2.11: Stacked ¹ H NMR spectra of PAH functionalization with D-glucose.....	38
Figure 2.12: PAH functionalization with D-mannose after 24 h.....	39
Figure 2.13: Stacked ¹ H NMR spectra of PAH functionalization with D-mannose.	40
Figure 2.14: PAH functionalization with 4-imidazolecarboxaldehyde after 24 h.	41
Figure 2.15: PAH functionalization with 2-amino-3-formylpyridine after 24 h.....	42
Figure 2.16: ¹ H NMR in D ₂ O of PAH co-functionalization with D-glucose and 4-imidazolecarboxaldehyde.....	44
Figure 2.17: ¹ H NMR in D ₂ O of PAH co-functionalization with D-glucose and 2-amino-3-formylpyridine.	45
Figure 2.18: ¹ H NMR in D ₂ O of PAH co-functionalization with D-mannose and 4-imidazolecarboxaldehyde.	46
Figure 2.19: ¹ H NMR in D ₂ O of PAH co-functionalization with D-mannose and 2-amino-3-formylpyridine.....	47
Figure 2.20: ¹ H NMR of acryloylglycine in DMSO- <i>d</i> ₆	48
Figure 2.21: ¹ H NMR of BOC-acryloylglycine hydrazide in DMSO- <i>d</i> ₆	50
Figure 2.22: Comparison of BOC-acryloylglycine hydrazide high temperature ¹ H NMR in DMSO- <i>d</i> ₆ spectra at 25 °C versus 80 °C.....	51
Figure 2.23: ¹³ C NMR in DMSO- <i>d</i> ₆ spectra of BOC-acryloylglycine hydrazide.....	52
Figure 2.24: ESI MS spectrum showing the molecular peak of BOC-acryloylglycine hydrazide plus sodium at m/z=266.12.	53
Figure 2.25: IR spectroscopy of BOC-acryloylglycine.	53
Figure 2.26: ¹ H NMR of samples taken at t ₀ (left) and t ₆₀ (right) from a polymerization of BOC-acryloylglycine hydrazide with CTA in DMSO- <i>d</i> ₆ at 70 °C using ACVA as radical initiator.....	55

Figure 2.27: Graphical representation of BOC-acryloylglycine hydrazide kinetic studies (left column) and fractional concentration of monomer represented by $\ln(M_0/M_t)$ versus time (right column).	58
Figure 2.28: Graphic representation of M_n , $M_{n,th}$ and \bar{D} versus conversion of polymers of different projected DP.	60
Figure 2.29: GPC chromatograms of BOC- P_x of different DPs.	61
Figure 2.30: 1H NMR spectrum of the purified BOC- P_{38} in DMSO- d_6	63
Figure 2.31: UV-Vis spectra of the protected versus de-protected poly(acryloylglycine hydrazide).	63
Figure 2.32: 1H NMR spectroscopy of PAGH DP $_{38}$ in D $_2$ O.	64
Figure 2.33: 1H NMR spectra of P_{38} before (top, in DMSO- d_6) and after (down, in D $_2$ O) de-protection with TFA.	65
Figure 2.34: GPC analysis of PAGH polymers before and after de-protection with TFA.	66
Figure 2.35: 1H NMR spectroscopy in D $_2$ O of the functionalization of PAGH of DP 38/45/72/97 with one equivalent of 4-imidazolecarboxaldehyde in aqueous 5% AcOH pH 2.9, 2/24/48 h after the end of the coupling reaction.	70
Figure 2.36: 1H NMR spectroscopy in D $_2$ O of the functionalization of P_{38} with 0.3/0.6/0.9/1.0 equivalents of 4-imidazolecarboxaldehyde in aqueous 5% AcOH pH 2.9.	70
Figure 2.37: 1H NMR spectrum of the 1:1 functionalization of P_{38} with 4-imidazolecarboxaldehyde (P_{38} -Ald1) in 5% AcOH in D $_2$ O and 95% of DMSO- d_6	71
Figure 2.38: 1H NMR spectrum of 1:1 functionalization of P_{38} with glyoxylic acid (P_{38} -Ald2).	72
Figure 2.39: 1H NMR spectra of the 1:1 functionalization of P_{38} with DL-glyceraldehyde (P_{38} -Ald3).	73
Figure 2.40: 1H NMR spectrum of 1:1 functionalization of P_{38} with Pyridoxal Phosphate (P_{38} -Ald4)	74
Figure 2.41: 1H NMR spectrum of 1:1 functionalization of P_{38} with Formyl Uracil (P_{38} -Ald5)	74
Figure 2.42: 1H NMR spectrum of 1:1 functionalization of PAH $_{37}$ with Glyoxylic acid (PAH $_{37}$ -Ald2).	76
Figure 2.43: 1H NMR spectrum of 1:1 functionalization of PAH $_{37}$ with Pyridoxal Phosphate (PAH $_{37}$ -Ald4).....	77
Figure 2.44: 1H NMR spectrum of 1:1 functionalization of PAH $_{37}$ with formyl uracil (PAH $_{37}$ -Ald4)	77
Figure 2.45: 1H NMR spectrum of 1:1 functionalization of P_{38} with sugars	78
Figure 3.1: Library of functionalized PAH and PAGH polymers to be tested against <i>E. coli</i>	90
Figure 3.2: Proposed method for screening polymer induced bacterial aggregation.	93
Figure 3.3: Spectrophotometry measurements of optic density (λ =600 nm) taken over 24 h after the incubation of 953 μ L of <i>E. coli</i> PHL644 and <i>E. coli</i> PHL628.....	93
Figure 3.4: Spectrophotometry measurements of optic density (λ =600 nm) taken over 24 h after the incubation of 953 μ L of <i>E. coli</i> PHL644 and <i>E. coli</i> PHL628.	94
Figure 3.5: Spectrophotometry measurements of optic density (λ =600 nm) taken over 24 h after the incubation of 953 μ L of <i>E. coli</i> PHL644 and <i>E. coli</i> PHL628.....	95
Figure 3.6: Spectrophotometry measurements of optic density (λ =600 nm) taken over 24 h after the incubation of 953 μ L of <i>E. coli</i> PHL644 and <i>E. coli</i> PHL628.....	96
Figure 3.7: Spectrophotometry measurements of optic density (λ =600 nm) taken over 24 h after the incubation of 953 μ L of <i>E. coli</i> PHL644 and <i>E. coli</i> PHL628.....	96
Figure 3.8: Spectrophotometry measurements of optic density (λ =600 nm) taken over 24 h after the incubation of 953 μ L of <i>E. coli</i> PHL644 and <i>E. coli</i> PHL628.....	97
Figure 3.9: Light microscopy pictures taken at 1000X magnification of <i>E. coli</i> PHL644 26H after initial incubation. (AcOH) bacteria incubated with 47 μ L of 5% AcOH in D $_2$ O buffer.	99
Figure 3.10: Light microscopy pictures taken at 1000X magnification of <i>E. coli</i> PHL644 26H after initial incubation.	100
Figure 3.11: Light microscopy pictures taken at 1000X magnification of <i>E. coli</i> PHL628 26H after initial incubation.	101
Figure 3.12: Light microscopy pictures taken at 1000X magnification of <i>E. coli</i> PHL628 26H after initial incubation.	102
Figure 3.13: Pictures of <i>E. coli</i> PHL644 incubated 2 h (from left to right) with P1, P4 and P5.....	103
Figure 3.14: Spectrophotometry measurements of optic density (λ =600 nm) taken over 24 h of <i>E. coli</i> PHL644.....	105
Figure 3.15: Spectrophotometry measurements of optic density (λ =600 nm) taken over 24 h of <i>E. coli</i> PHL628.....	106
Figure 3.16: Fluorescence microscopy (1000X) pictures of SYTO9/PI stained <i>E. coli</i> PHL644 24 h after being incubated with P1 in 5% AcOH in D $_2$ O buffer.	107
Figure 3.17: Fluorescence microscopy (1000X) pictures of SYTO9/PI stained <i>E. coli</i> PHL644 24 h after being incubated with P4 in 5% AcOH in D $_2$ O buffer.	107

Figure 3.18: Fluorescence microscopy (1000X) pictures of SYTO9/PI stained <i>E. coli</i> PHL644 24 h after being incubated with P5 in 5% AcOH in D ₂ O buffer.	108
Figure 3.19: Fluorescence microscopy (1000X) pictures of SYTO9/PI stained <i>E. coli</i> PHL628 24 h after being incubated with P1 in 5% AcOH in D ₂ O buffer.	108
Figure 3.20: : Fluorescence microscopy (1000X) pictures of SYTO9/PI stained <i>E. coli</i> PHL628 24 h after being incubated with P4 in 5% AcOH in D ₂ O buffer.	109
Figure 3.21: : Fluorescence microscopy (1000X) pictures of SYTO9/PI stained <i>E. coli</i> PHL628 24 h after being incubated with P5 in 5% AcOH in D ₂ O buffer.	109
Figure 3.22: CFU count of CFU at a dilution factor of 10 ⁶ on plate after 24 h of incubation with polymers and controls.	111
Figure 3.23: Absorbance (λ=550) results from crystal violet staining of PHL644 attached to abiotic surfaces.	112
Figure 3.24: 3D model obtained by confocal laser microscopy of PHL644 24h after being incubated with P1 dissolved in 5% AcOH in D ₂ O (pH 2.9).	115
Figure 3.25: 3D model obtained by confocal laser microscopy of PHL644 24h after being incubated with P4 dissolved in 5% AcOH in D ₂ O (pH 2.9).	116
Figure 3.26: : 3D model obtained by confocal laser microscopy of PHL644 24h after being incubated with P5 dissolved in 5% AcOH in D ₂ O (pH 2.9).	117
Figure 3.27: Proposed P1 aggregation mechanism by electrostatic charge compatibility between the positively charged backbone and the negatively charged surface bacteria. Polymers versus bacteria not to scale.	119
Figure 3.28: Spectrophotometry measurements of optic density (λ =600 nm) taken over 24 h when <i>E. coli</i> PHL644 was incubated with 6.17 mM of P10, P11, P12 and their respective controls.	122
Figure 3.29: Cuvettes used for the PAGH aggregation experiment 24 hours after the beginning of the assay.	123
Scheme 1.1: Primary and tertiary cationic methacrylamide polymers used by Perez-Soto et al ¹²⁴	15
Scheme 2.1: Comparison between traditional uncontrolled and RAFT polymerization.	20
Scheme 2.2: Mechanism for addition fragmentation chain transfer.	21
Scheme 2.3: Mechanism of degenerative chain transfer reversible activation.	21
Scheme 2.4: RAFT polymerization mechanism.	22
Scheme 2.5: Example of termination event by combination between growing polymer chains.	23
Scheme 2.6: Guidelines for the selection of R and Z groups of RAFT agents for the polymerization of vinyl monomers.	25
Scheme 2.7: Poly(acryloyl hydrazide) chemical structure.	27
Scheme 2.8: Poly(acryloyl hydrazide) synthesis route developed by Crisan et al. ¹⁶¹	28
Scheme 2.9: PAH hydrazide side chains coupling with aldehydes and sugars.	29
Scheme 2.10: The novel synthesis of poly(acryloylglycine hydrazide) from the monomer BOC-acryloylglycine hydrazide via RAFT polymerization.	30
Scheme 2.11: Test the loading efficiency of PAGH with aldehydes, and sugars to achieve functionalized polymers.	30
Scheme 2.12: Standard aqueous functionalization reaction of PAH with the model of hydrophilic aldehyde 4-imidazolecarboxaldehyde in 5% acetic acid buffer pH 2.9.	31
Scheme 2.13: PAH functionalization with D-glucose.	36
Scheme 2.14: PAH functionalization with D-mannose.	38
Scheme 2.15: PAH functionalization with 4-imidazolecarboxaldehyde.	41
Scheme 2.16: PAH functionalization with 2-amino-3-formylpyridine.	42
Scheme 2.17: PAH co-functionalization reaction with D-glucose and 4-imidazolecarboxaldehyde.	43
Scheme 2.18: PAH co-functionalization reaction with D-glucose and 2-amino-3-formylpyridine.	44
Scheme 2.19: PAH co-functionalization reaction with D-mannose and 4-imidazolecarboxaldehyde.	45
Scheme 2.20: PAH co-functionalization reaction with D-mannose and 2-amino-3-formylpyridine.	46
Scheme 2.21: BOC-acryloylglycine hydrazide synthetic route.	48
Scheme 2.22: Synthesis route of 2-(ethylthiocarbonothioylthio)-2-methylpropanoic acid, the CTA chosen to perform RAFT polymerization of BOC-acryloylglycinehydrazide.	54

Scheme 2.23: Proposed polymerization conditions of BOC-acryloylglycine hydrazide in DMSO.	54
Scheme 2.24: Adaptation to PAGH of the proposed CTA degradation by Creese et al. ¹⁷¹ that leads to the termination events observed during the polymerization of the acryloylglycine hydrazide monomer.	61
Scheme 2.25: De-protection and neutralization of BOC-poly(acryloylglycine hydrazide) to obtain poly(acryloylglycine hydrazide).....	64
Scheme 2.26: PAGH functionalization.....	68
Table 2.1: BOC-PAGH described in the kinetics studies.	62
Table 2.2: PAGH batches used to measure the loading capacity with aldehydes and carbohydrates.	66
Table 2.3: Percentage of PAGH subunits functionalized by one equivalent of 4-imidazolecarboxaldehyde 2/24/48 h after the functionalization reaction in 5% AcOH in D ₂ O	68
Table 2.4: Loading efficiency of P ₃₈ when functionalized with 1 equivalent of different model aldehydes under acidic, basic, and organic loading conditions	75
Table 2.5: Loading efficiency of PAH ₃₇ when functionalized with 1 equivalent of different model aldehydes under acidic, basic, and organic loading conditions.	76
Table 2.6: Percentage of maximum loading efficiency of P ₃₈ with 1 equivalent of carbohydrates under 5% AcOH in D ₂ O pH 2.9.....	78
Table 3.1: Library of functionalized PAH and PAGH polymers to be tested on <i>E. coli</i>	91
Equation 1.1: Extended DLVO theory.	8
Equation 2.1: RAFT polymerization first order kinetics.....	22
Equation 2.2: Projected degree of polymerization (DP) of a RAFT polymer.....	23
Equation 2.3: Theoretical molecular weight (M _n _{th}).....	24
Equation 2.4: M _n is the polymer average molecular weight of a polymer formula.	55
Equation 2.5: M _w is the weight average molecular weight of a polymer formula.	56
Equation 2.6: Dispersity (Đ) index of a polymer sample	56

1. Introduction

1.1 Bacterial biofilm communities and its importance

Most of the world's bacteria populations are found forming part of a biofilm at various stages of growth¹. Biofilms enable unicellular organisms to establish temporary supracellular consortia that facilitate survival against environmental hazards. These communities are attached to biotic or abiotic surfaces and embedded in a self-produced three-dimensional matrix composed of extracellular polymeric substance (EPS)² that enhances the ability of the biofilm community to adapt to environmental, physical, and chemical hazards, increasing the resilience of the bacteria forming part of a biofilm community compared with their planktonic counterparts³.

The main property of a biofilm community is their three-dimensional scaffold that provides structure to the community and is made of a heterogeneous matrix of polymeric substances composed of mostly water (up to 97%), polysaccharides, proteins and extra cellular DNA (eDNA)⁴, that are secreted by the biofilm community. This matrix possess a network of channels that facilitate the diffusion of nutrients and other molecules between cells acting like a rudimentary circulatory system for the biofilm⁵, enabling the emergence of physical and social interaction between microorganisms that elicit a synergistic microconsortium that behaves like a supracellular community⁴. This external matrix contributes to most of the biofilm's mass⁴ (up to ~90%), and it is the one that confers the community with special properties⁶ that planktonic individuals lack.

The formation of the EPS matrix is a dynamic process that is modulated by environmental stress, nutrient availability, and competition by other microorganisms, these factors will contribute to the overall EPS composition and shape. The EPS matrix act as a fortress protecting the biofilm community providing structural and functional properties to the community that individuals lack, like increased hydration and water retention, increased resource capture and digestive capacity, and protection from hazards, in addition the three-dimensional structure of the matrix facilitates cell to cell interactions that can enhance the metabolic capacity of cells in the community and resistance to hazards like antimicrobials⁷.

Biofilm communities confer survival advantages over free planktonic individuals, like protection from sanitizers⁸, antibiotics⁹, and environmental conditions¹⁰.

Studies have shown the presence of subgroups of metabolically inactive bacteria within the biofilm, suspected to be persistent cells that are resistant to a wide range of antibiotics despite sharing the same genetic makeup than the rest of the colony^{11, 12}. These traits make biofilm communities highly resilient and recalcitrant and are the cause of most medical devices associated infections¹³ like catheters, prosthetics, dentistry¹⁴, and contact lenses¹⁵. Biofilms are responsible for important economical losses due to biofouling in many different industrial areas like water systems¹⁶, paper industry¹⁷, hospitals¹⁸, food¹⁹, dairy²⁰, oil²¹. Most foodborne gastrointestinal diseases originate from biofilm forming pathogenic bacteria that live on the domestic environment^{22,23}. There are many beneficial uses for biofilm communities in industry, like wastewater treatment²⁴, biofuel production²⁵, bio-remediation²⁶, bio-catalysis²⁷, and bioreactors²⁸.

A better understanding of biofilm behaviour is necessary to decrease infections associated with medical devices and prosthetics²⁹, biofouling of industrial complexes, spoilage of edibles in the dairy and food industry, and also to improve industrial bioprocesses that use biofilm communities as bio factories. If we achieve to understand biofilm formation, we can design new materials that decrease or nullify biofilm formation, and materials attractive for biofilm formation, that allow us to enhance, modulate, and control its behaviour to improve bio-product processes.

1.2 Biofilm lifecycle

The typical biofilm development and maturation cycle comprises various stages (Figure 1.1): (I) initial reversible attachment of planktonic cells; (II) early irreversible attachment and development of biofilm structure; (III) maturation of biofilm; and (IV) dispersion of cells from the biofilm into planktonic state.

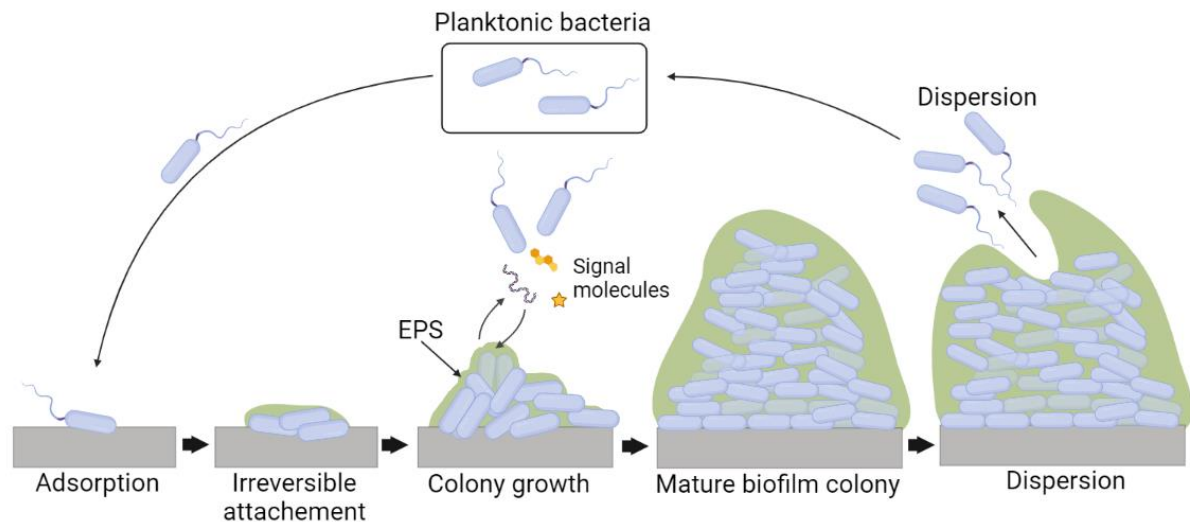


Figure 1.1: Typical stage development of bacterial biofilm. Adapted from Sauer et al.³⁰.

1.2.1 Initial reversible attachment

The first step involves the interaction of the bacteria with the surface to colonize, this process is mainly driven by gravitational forces and Brownian motion³¹.

Bacteria interacting with a surface encounter attractive or repelling forces dependent on pH, temperature, nutrient levels, ionic strength³². Flagellated microorganisms possess a competitive advantage when it comes to overcome these hydrodynamic and repulsive forces, this was demonstrated by Pratt and Kolter³³ using *Escherichia coli* as a model organism for biofilm study, when they described an array of biofilm deficient mutants that carried insertion mutations that perturbed flagellar synthesis, these authors showed that motility provided by flagella was a main driving force necessary for biofilm formation and that it also might be involved into contributing to surface anchoring. This study was corroborated by others authors like Genevaux et al³⁴, and Wood et al³⁵ in two individual studies where they described how the biofilm formation capabilities of *E. coli* was hindered in flagella affected mutants with reduced or impaired mobility. The correlation between flagella, mobility and biofilm formation has been also widely reported in other biofilm model organisms like *Pseudomonas aeruginosa*³⁶⁻³⁸, *Vibrio cholerae*³⁹, and *Listeria monocytogenes*⁴⁰.

Although these studies demonstrated the importance of mobility for the successful colonization of biofilm forming species other studies have demonstrated that flagella are not completely necessary, and that non motile strains of motile bacteria can develop biofilms with the right phenotypes. For example, Prigent-Combaret et al⁴¹ showed that flagella were not necessary to the biofilm development in *E. coli* strains that overproduced curli, suggesting that these structures were compensating the lack of flagella in the initial adhesion stages of biofilm formation. Other authors work^{31, 42, 43} contributed towards this discussion showing that the lack of flagella in *E. coli* did not block

biofilm formation for strains that expressed strong adhesion factors that contributed to anchoring the bacteria to the surface, thus contributing to the initial colonization.

Some studies support that, in some species, the initial stages of surface recognition and attachment are also driven by chemotaxis, the phenomenon by which cell movement is directed in response to an extracellular chemical gradient. Mutations in the gene that encodes for the CheR1 methyltransferase involved in the chemosensory system of *P. aeruginosa* has shown to impair the bacteria's ability to colonize surfaces and develop mature biofilms⁴⁴. In a similar fashion recent studies on *E. coli* have shown that the disruptive mutations on the protein Tar involved in chemotaxis regulation produced strains that generated defective biofilms in uropathogenic *E. coli* (UPEC) strains.

Once a bacterium locates the target surface to colonize and is able to overcome the myriad of unfavourable forces that prevent it from establishing contact, initial adherence is mediated by adhesive extracellular appendages and secreted adhesins³², although this initial attachment is dynamic and not permanent if the conditions are not favourable for the start of a biofilm community. During the early stages of colonization bacteria can detach and revert to a planktonic lifestyle if the conditions are not favourable, a bacterium can be removed by strong hydrodynamic forces, or detach in response of nutrient availability^{45, 46}, or be repelled from the surface by not being able to overcome repulsive forces⁴⁷.

1.2.2 Irreversible attachment

Irreversible attachment is attained by bacteria that are able to withstand electrostatic repulsive forces and hydrodynamic shearing forces that would detach individuals from their initial colonization efforts. Once the bacterium has a strong grip onto the surface a diverse number of extracellular adhesive organelles contribute to permanent anchoring the cell establishing cell-surface interactions and enabling the transition from a planktonic to a sessile lifestyle. Several studies have reported that the main contributors to the permanent anchoring of bacteria promoting a permanent attachment are extracellular organelles (**Figure 1.2**) of the fimbrial family: fimbriae type 1 (also known as pili), curli, and conjugative pili.

E. coli rely heavily in fimbriae type 1 to establish a permanent surface attachment^{33, 48, 49}. Fimbriae type 1 are a filamentous tubular adhesin proteins that can be found in groups of 100-500 on the surface of commensal and pathogenic *E. coli* strains³⁰; these structures are composed of several subunits that are assembled by the chaperone usher pathway (CUP)⁵⁰, the importance of this structure is shown in *E. coli* UPEC^{51, 52} and gut⁵³ colonizers strains, that harbours numerous CUP fimbriae type 1 assembly systems, which play a part in the pili biogenesis and contribute to the initial colonization of the host epithelia in a specific cell-substrate interaction. The adherent properties of the type 1 pili are conferred by the FimH adhesin found at the end tip of the tubular structure of the pili; this adhesin has been shown to recognize mannosylated moieties from the glycocalyx of the eukaryotic host's epithelia in a specific binding interaction⁵⁴ demonstrating its critical role in epithelia colonization and UPEC pathogenesis⁵⁵. Fimbriae type 1 is also involved in the colonization of abiotic surfaces as reported by several authors^{33, 53, 56, 57}. *E. coli* mutants with a loss of function in the sequences encoding for type 1 pili subunits have been reported to show reduced attachment to PVC (widely used in medical devices, pipes, and industrial materials) and other abiotic surfaces^{33, 58}. These studies suggest that fimbriae type

1 have both specific binding activity with eukaryotic substrates mediating the colonization of the host's epithelia, and also a nonspecific binding activity that contributes to the colonization of abiotic surfaces.

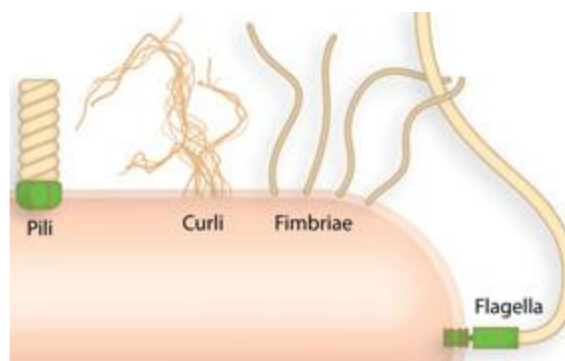


Figure 1.2: Scheme that highlights surface fimbrial organelles that are involved in bacterial surface attachment. From left to right fimbrial organelles: pili, curli fibres, fimbriae, and flagella. Reproduced from Renner and Weibel⁵⁹.

Curli fimbriae are filamentous proteins found on the surface of bacteria in pockets of 6-12 nm diameter, these structures were first reported in *E. coli* but they have also been found in other bacterial genera like *Shigella*, *Citrobacter*, and *Enterobacter*⁶⁰. Studies have shown that curli are a main contributor to bacterial colonization of eukaryotic hosts as they are able to attach to proteins of the extracellular matrix including laminin, fibronectin, and plasminogen⁶¹⁻⁶³. But curli have also been reported to be a strong contributor of abiotic surface colonization promoting cell-to-surface and cell-to-cell interactions⁶¹⁻⁶³.

Conjugative pili, a tubular proteinaceous fimbriae involved in the transfer of conjugative plasmids between bacteria, have been found to contribute to biofilm formation. Various authors^{64, 65} have reported that poor biofilm former *E. coli* K-12 strains were able switch to thick biofilms formation phenotypes after having been transformed by a conjugative plasmid that enables the formation of conjugative pili; they found that the conjugative pili were able to contribute to the colonization of abiotic surfaces through nonspecific interactions with the surface, and also helped stabilize the structure of the biofilm through cell to cell contacts.

1.2.3 Biofilm growth and maturation

Once the bacterium has established permanent residency on a surface contact a series of physiological changes are triggered in responses to the cell to surface attachment, changes in the genetic expression of the organism will up-regulate genes that promote a sessile phenotype³². The main characteristic of biofilm maturation is the three-dimensional growth of the community by the secretion of an extracellular matrix composed of EPS, and the establishment of cell-to-cell interactions promoted by adhesins and fimbrial organelles. This maturation process leads to a distinct environment that favours the display of traits in the bacterial community which their planktonic counterparts lack. As the biofilm community develops it will increase its numbers through bacterial cell division upwards and outwards at the same time it generates more extra cellular matrix to support its growth. EPS is the main contributor to the extra cellular matrix, a viscous hydrated layer whose composition will vary between different biofilm forming bacterial species, but they all have in common that they will be composed of exopolysaccharide polymers, proteins, eDNA, nucleic acids, lipids, and other metabolites that contribute to the generation of a three-dimensional scaffold that embeds the bacterial community.

When it comes to *E. coli* biofilms there have been reports of the important contribution that exopolysaccharides have towards the formation of the EPS matrix that envelop the bacterial community that forms the biofilm, mainly cellulose, PGA, and colanic acid. Cellulose was one of the first components of *E. coli* EPS to be identified in pellicle biofilms, then other authors reported that cellulose synthesis was tied to the development of curli in *E. coli* UPEC and gastrointestinal strains^{66, 67}. Multiple authors have reported⁶⁸⁻⁷¹ that PGA and colanic acid are important contributors to *E. coli* extra cellular matrix architecture.

Extensive research has been done to investigate the extracellular matrix composition in *P. aeruginosa*, which overall composition has been reported to be able to modulate depending on the environmental conditions⁷². Reports attribute to Pel and Psl, two exopolysaccharides, as the primary contributors to the EPS in *P. aeruginosa*⁷³⁻⁷⁵. Both polysaccharides have been reported to increase the persistence of *P. aeruginosa* in the respiratory system. Psl has been shown to increase bacterial attachment to the host's epithelial airway⁷⁵, while upregulated expression of Pel has been associated with persistent lung infections of *P. aeruginosa* in cystic fibrosis patients⁷⁶. Alginate is another polysaccharide that has been reported to be a component of the EPS matrix in *P. aeruginosa* and it has been associated with enhanced antibiotic resistance in recalcitrant infections⁷⁷.

These cooperative efforts to consolidate a three-dimensional scaffold and a transition to a biofilm forming phenotype are coordinated by cell-to-cell communication. Gene expression within the biofilm is regulated in response to the population density in a phenomenon called quorum sensing (QS)⁷⁸; bacteria produce small molecules called autoinducers that will accumulate in the matrix of their surrounding vicinity. As cell density increases the accumulation of these autoinducers does so until a threshold stimulatory concentration is achieved. When this happens bacterial quorum sensing pathways activate, generating a cascade of shifts in the expression of diverse genetic pathways, triggering the change of phenotype from a planktonic lifestyle to sessile biofilm forming one⁷⁹. One of these small molecules with an important role regulating biofilm formation is cyclic di-GMP, this molecule is an intracellular small molecule recognized by the bacteria to coordinate the lifestyle transition between planktonic and sessile lifestyle⁸⁰ as it has been reported that high concentrations of cyclic di-GMP has been associated with biofilm formation, while a low concentration of this small molecule is involved in increased motility and dispersion in *Escherichia coli*, *P. aeruginosa*, and *S. enterica*⁸¹.

1.2.4 Dispersion

Mature biofilms tend to be thriving environments for the bacterial community where they are protected from external harm, but dispersion strategies are present in these communities in response to changes in their surroundings. Although involuntary dispersal through shear and other physical forces is possible, bacteria have developed ways to sense environmental changes and decide if it is still beneficial to maintain a sessile lifestyle or if it is time to revert to a planktonic one. Dispersal strategies can be triggered by changes like a decrease in nutrient availability, oxygen concentration fluctuations, or the increase in chemical hazards like biocides or toxic metabolites⁸². Once bacteria revert to a motile lifestyle, they can remain on it or find new environments with better conditions to colonize and generate a new biofilm community. It is this ability to adapt to the environmental conditions what makes biofilm forming bacteria excellent survivalists.

1.3 The importance of surface properties for bacterial colonization and biofilm formation

As explained previously, biofilm formation is composed of several sequential stages that are regulated by complex mechanisms and that are necessary to achieve the development of the biofilm community. Of all these stages the initial surface recognition and permanent attachment is considered one of the most important, as is the one gatekeeping the maturation and development of a complex biofilm. Failure to accomplish these stages results in a reversion to a planktonic lifestyle and the inability to colonize the surface.

Part of the research community have devoted efforts to better understand the influence that surface physicochemical properties (**Figure 1.3**) have over the initial stages of surface colonization and biofilm formation. This way we can design materials with tailor-made surface compositions to modulate bacterial attachment either preventing it and subsequent biofouling, or enhancing it to use bacterial communities for biotechnological applications.

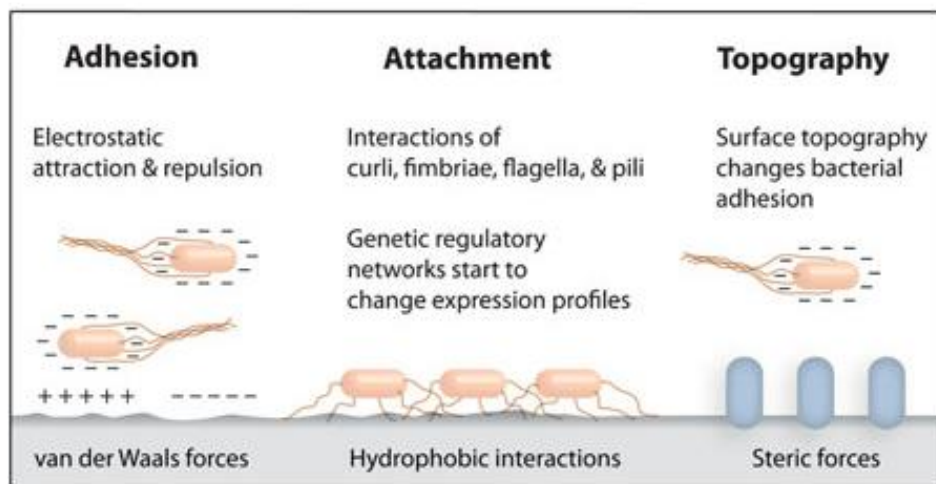


Figure 1.3: Interactions between substrate and bacteria that define the success of initial colonization of a surface. Reproduced from Renner and Weibel⁵⁹.

Thermodynamic approaches have been developed to create a model that explains the main driving forces responsible for the early bacterium-surface interaction from an energy standpoint, such as the XDLVO model, that is an extended version of a thermodynamic model for the study of colloids interaction known as DLVO model (Derjaguin-Landau-Verwey-Overbeek). The XDLVO model is based on the pairwise interactions free energies (AG) between bacteria, surface, and fluid to explain initial bacterial adhesion^{83, 84}. This theory considers bacteria as colloids due to their size (0.5–2 μm) being within the range of colloidal particles⁸⁵. The total adhesion energy (AG_{total}) can be estimated as the sum of Lifshitz-van der Waals interactions, the electrostatic interactions between cell and substrate, and the acid base interactions (**Equation 1.1**). Each of these forces can be either attractive or repulsive depending on the physicochemical composition of the bacterium outer layer and the surface to colonize. Following this model, a negative total free energy will favour adhesion while positive free energy might inhibit initial cell-surface adhesion.

$$AG_{Total} = AG_{LW} + AG_{EL} + AG_{AB}$$

Equation 1.1: Extended DLVO theory. The total interaction energy between the bacterium and a substrate (AG_{Total}) is the sum of the Lifshitz-van der Waals interactions (AG_{LW}), electrostatic double layer interactions (AG_{EL}), and acid-base interactions (AG_{AB}).

Having established a model to explain bacteria to surface interactions we are going to discuss in detail surface properties that are defining the success of initial colonization, and can be used to design materials targeted to interact and modulate the behaviour of biofilm forming bacterium.

1.3.1 Surface charge

Surface charge density is one of the determinant factors that contribute to the success or failure of the initial colonization of a surface by bacteria. Van der Waals forces and electrostatic interactions between bacteria and surface have been reported to be the major contributing forces to the surface charge density⁵⁹. To understand how surface charge density affects initial colonization we, have to first have an insight about the overall electrostatic charges found on bacterial surfaces. Bacteria are usually found to have net negative charges in their surfaces due to the chemical composition of their outer surface, where structures like carboxylic, amino, and phosphate groups contribute to the overall negative charge⁸⁶. This net negative charge on bacteria could explain the success of strategies based on charged surfaces as a way to modulate bacterial colonization and subsequent biofilm formation.

Gottenbos et al.⁸⁷ reported in 1999 an increased adhesion and growth of *P. aeruginosa* on positively charged poly(methacrylates) compared to negatively charged ones. This early research was followed by other groups reporting similar success following a similar strategy based on enhancing initial adhesion by designing positively charged surfaces, like Zhu et al.⁸⁸ who demonstrated how positively charged surfaces made of poly(acrylic acid), and poly(diallyl dimethyl ammonium chloride) enhanced initial adhesion on *Staphylococcus aureus*, *E. coli*, and *P. aeruginosa*. In a similar fashion Kovacevic et al.⁸⁹ reported enhanced initial colonization by *P. aeruginosa* on positively charged multilayers of poly(allylamine hydrochloride) compared to a negatively multilayer made of poly(styrene sulfate). Other researchers also reported how negatively charged surfaces decreased surface adhesion, Guo et al.⁹⁰ showed that negatively charged polyelectrolyte multilayers partially prevented initial colonization of the surface by *E. coli* and *S. aureus* due to electrostatic charge repulsion. Although many researchers have proved that negatively charged surfaces diminish bacterial colonization there have also been reports where some bacterial species are able to conquer electrostatic repulsion thanks to their extracellular fimbrial organelles⁹¹, implying that bacteria have developed strategies to colonize even surfaces with a net positive free energy. There is also the consideration that increased initial adhesion due to charge compatibility might not equate to increased biofilm development, Terada et al.⁹² used polyethylene sheets with electrostatic modifications as experimental surface and reported that *E. coli* presented an increased initial colonization of positively charged polyethylene surfaces but that same charge density decreased cell viability that translated in a slower biofilm development. They also reported significant changes in biofilm shape and structure depending on the charge density of the colonized surface. *E. coli* biofilm formed on negatively charged polyethylene surfaces was heterogeneous and mushroom shaped, presenting a diminished hydrodynamic resistance compared to the biofilms developed on positively charged surfaces counterparts that had a more homogeneous and dense structure presenting a higher resistance to the same stresses.

These scientific reports suggest that the surface charge of a surface is an important factor in the outcome of the initial bacterial adhesion, and that can modulate the phenotype of biofilm communities. Further research is needed to better understand how this physicochemical property affects the biofilm cycle so we can develop better strategies to modulate its behaviour.

1.3.2 Surface wettability

Surface wettability is an important property of materials that define its interactions with water. It can be quantified by the contact angle of the interface between the material and water, that will classify the material as hydrophobic or hydrophilic. The wettability of a surface is a quality that depends mostly on its surface energy (due to the chemistry of the material) and also to its roughness⁹³ (that is the height variation on a surface). The importance of this property is incorporated in the XDLVO theory as the free energy of the acid base interactions (AG_{AB})⁹⁴.

But how does this property affect initial adhesion and colonization? In general, bacteria with a surface composed of mostly hydrophobic motifs favour the colonization of apolar hydrophobic surfaces, while hydrophilic bacteria prefer to adhere to hydrophilic materials⁸⁵. But there is an intrinsic problem to how the wettability of a material is defined, as contact angle measurements are considered on flat even surfaces on the macroscopic scale, something far from the practical bacteria-surface interface that happens on the microscopic scale, where uneven surface topography plays an important role for the contact angle of a material and hence its wettability, making it possible that the measured contact angle of a material presents different values and wettability properties depending on the macro and the microscale its measured even when they present identical chemical composition. For example, a hydrophobic material with a rough surface can present small protrusions filled with air bubbles instead of liquid due to the properties of the material. Although this material is theoretically favoured by hydrophobic bacteria, these pockets of air make it a difficult interface for many bacteria to colonize it. This points at how the theoretical models are helpful but flawed as they do not consider the importance of surface topography and should not be used to draw adamant conclusions over the proclivity of a material to be colonized by bacteria based just on theoretical models.

Advances have been made using the wettability of engineered materials as a main driving force to control bacterial adhesion. Lorenzetti et al.⁹⁵ reported a reduced *E. coli* adhesion on hydrophilic titanium substrates with a TiO₂-anatase nanostructured coating. Other efforts were directed towards the use of polystyrene surfaces, like Yuan et al.⁹⁶ who reported how moderately hydrophobic polystyrene surfaces induced higher *E. coli* adhesion compared to their super hydrophilic counterparts that limited bacterial binding. Verhorst et al.⁹⁷ focused their efforts on the design of anti-biofouling materials for pelvic floor implants. They reported that hydrophilic surfaces made of poly-4-hydroxybutyrate showed reduced *S. aureus* and *E. coli* colonization compared to hydrophobic polypropylene surfaces, a common material used in pelvic floor implants that is prone to biofouling and associated infections. These advances in surface engineering show a correlation between hydrophobicity of a material and increased colonization, and hydrophilicity with reduced initial adhesion, but this trend does not seem to be an immutable rule as there have been reports of extreme surface modifications on materials that achieved super hydrophilicity or super hydrophobicity that impaired surface adhesion. Ozkan et al.⁹⁸ reported that super hydrophobic polyurethane surfaces modified with zinc oxide and copper nanoparticles had anti biofouling properties as they showed

greatly reduced *S. aureus* adhesion. In a similar fashion against the trend previously mentioned Yoon et al.⁹⁹ reported that the design of super hydrophobic stainless steel surfaces coated with TiO₂ presented anti-biofouling properties as *E. coli* presented greatly reduced adhesion.

Overall, there have been interesting advances in the design of engineered wettable surfaces that have reported promising results modulating bacterial adhesion, but a better understanding of the main driving properties of the success of these materials is necessary to better understand the mechanisms governing biofilm lifecycle and further improve material design to enhance or block bacterial colonization.

1.3.3 Surface roughness

Roughness has been reported as an important surface property that can affect initial bacterial adhesion and has been described as an important parameter in the biofouling literature^{100, 101}. It is a physical property that describes height variations on the surface of a material, and does not report anything about the geometrical configuration of a material in the three dimensional space as topography does. Surface roughness can be described by different quantitative measurements: R_a (the average height), R_q (the root mean square of the height values), and R_z (the difference in height between the average of five highest peaks and five lowest valleys)⁹⁴. This makes difficult to compare advances reported by research groups depending on the roughness parameter they used for their surface characterization.

Scientific studies reports have been conflicting when it comes to the influence of roughness in the initial bacterial colonization of a surface. Some have found a direct correlation between increased roughness and increased colonization of materials: Bollen et al.¹⁰⁰ reported an increase of 25 fold in oral bacterial colonization on rougher titanium surfaces; Medilanski et al.¹⁰¹ studied the biofouling of stainless steel surfaces and reported increased colonization on rougher surfaces by *P. aeruginosa*, *P. putida*, *Desulfovibrio desulfuricans*, *Rhodococcus spp*; Arnold and Bailey¹⁰² reported higher attachment and biofouling of rougher stainless steel surfaces by indigenous bacteria of poultry rinse. While similar research studies¹⁰³⁻¹⁰⁵ performed on stainless steel biofouling have reported no significant differences between the colonization of surfaces with different roughness.

The problem is that roughness as a physical descriptor only cares about height variations on a surface without considering the three dimensional structure or disposition of these peaks and valleys of the surface, a property that is defined by the topography of a material (another surface property). Two materials with the same roughness could have a completely different topography that could affect other physicochemical surface properties like wettability, affecting differently the colonization efforts of microorganisms and consequent bacterial attachment. Another problem of this descriptor is the lack of discrimination between bacterial adhesion and surface retention in many of these scientific reports, as is not always clear if the bacteria that remained on a surface did it as a successful attachment or because the valleys of the material provided protection from detachment due to shear forces but did not promoted further colonization¹⁰⁶.

Overall, scientific reports point out that roughness is important for surface adhesion, but this descriptor alone cannot explain for the contradicting reports due to the lack of topography characterization in these studies. It is clear that important topographical information is missed when

roughness is the only descriptor used. This has led part of the biofilm community into research how roughness and a defined topography affects bacterial colonization of surfaces.

1.3.4 Surface topography

Topography is defined as the three-dimensional geometrical disposition of the vertical difference (defined as roughness) on a material surface. There have been efforts dedicated to the development of materials with microbiological applications thanks to the use of lithographic technology to design topographic surfaces with defined patterned structures in the nano and micrometric scales¹⁰⁷.

There have been reports of many mechanisms involved in how topography conditions the success of bacterial colonization over a surface and this is dependent on the topographical scale.

There are mechanisms that are enabled in the nanometric scale with patterns smaller than the size of the bacterial cell such as: lithographic patterns that disrupt bacterial attachment due to leaving gaps in the surface-bacteria interface changing the overall physicochemical forces at play, leading to a change in the attractiveness of a material from an electrostatic standpoint; nanopillars able to induce cell membrane deformation and disruption; and changes of the chemical gradient between a surface and a bacterium due to the entrapment of molecules involved in chemotaxis by patterns in the nanometric scale. Then there are other mechanisms induced by topography at the micrometric scale, that are in the range of the size of a bacterial cell such as: those that affect bacterial attachment by patterns that induce anti-attachment properties like changes in the material hydrodynamics that prevent bacteria from contacting the surface by increasing shear hydrodynamic forces; patterns that induce air entrapment thus preventing bacterial colonization; patterns that affect bacterial organization by segregating and ordering bacteria in ways that prevent them to stockpile into each other inhibiting cooperative efforts; and the use of complicated attachment trends to modify the topography and chemistry of a surface.

Promising research towards the use of topographic materials with nanoscale motifs has been reported.

For example Feng et al.¹⁰⁸ designed nanoporous aluminium oxide surfaces with patterned surface with pores sizes of 15 and 25 nm, they reported a decrease in attachment by *E. coli*, *Listeria* spp., *S. aureus*, and *Staphylococcus epidermidis*, these pores in the material acted decreasing the available surface that the bacteria could interact with reducing the amount of attractive electrostatic forces available to support their initial attachment and increasing the total energy barrier that the bacteria had to overcome. Other antibiofouling approaches have been taken by some authors that have designed materials with nanopillars topographic patterns, like a bed of nails, that disrupt and break bacterial membranes. Such approach was taken by Dickson et al.¹⁰⁹, who successfully imprinted nanopillared topography onto poly(methyl methacrylate) films. They found that the modified surface reduced bacterial adhesion compared to flat controls, and also reported an increased mortality of the cells that adhered due to membrane disruption induced by the bactericidal effect of these nanopillars. A third approach in the nanoscale range has been done aiming to disrupt the conditioning film present in some surfaces, a layer of adsorbed molecules (mostly proteins) frequent in solid surfaces immersed in a liquid. These macromolecules adhered to the surface can modify its electrostatic and topographic properties. There have been contradictory findings whether a conditioned surface has an inhibitory effect¹¹⁰⁻¹¹² over colonization, or if it enhances it¹¹³⁻¹¹⁵. One approach that has been done regarding this

surface property is to design surface topographies that disrupt the kinetics of protein adsorption, like the study made by Lazzara et al.¹¹⁶ who reported that anodic aluminium oxide materials with highly dense nanoporous surfaces were able to act as highly efficient sinks for proteins in the liquid phase, modifying how bacteria sense the surface. Tuson and Weibel¹¹⁷ agree that a nanoporous topography might conceal chemotaxis molecules used by bacteria to direct their movement towards surfaces to colonize.

There have also been reports in the use of topographies in the micro scale to elicit antibiofouling mechanisms. Micro topographic patterns have been found to affect the hydrodynamic forces involved in surface microfluidics¹¹⁸. Lee et al.¹¹⁹ used computational fluid dynamics simulations reporting the formation of vortices on surfaces with micro wells that could have an impact in surface colonization. Other authors have focused on similar approaches, but this is still an ongoing effort with mostly theoretical results. Other anti-biofouling approaches have been made regarding the use of micro topographies able to stabilize air-liquid interfaces capable of trapping air bubbles larger than the typical bacteria cell, thus preventing them from contacting the material surface, most of the efforts made in this regard has been theoretical. Marmur¹²⁰ proved that air entrapment between micrometric surfaces is theoretically possible and thermodynamically stable. Some authors considered the possibility of using topographies that were able to achieve liquid-liquid interfaces to prevent surface adhesion, using surface topography to entrap a lubricant into the micropores that prevented bacterial contact with the surface in a similar fashion as the air-liquid interface. Following this method Epstein et al.¹²¹ reported the design of surfaces with anti-biofouling based on lubricant-liquid interfaces that can prevent bacteria from reaching the surface due to the high interface tension. Other approaches in the design of anti-biofouling surfaces have been made designing patterns in the micro scale big enough to align bacterial cells and preventing them to reach others to achieve cooperative efforts. Lai¹²² reported that the use of grafted silicon surfaces were able to decrease *P. aeruginosa* colonization by a 20% compared to flat controls, showing that the ordering of early colonizers could interfere with biofilm colonization due to them being unable to form clusters thanks to a pattern that generates space constraints.

1.4 Synthetic polymers mediating bacterial aggregation and biofilm formation

So far, the principles of biofilm formation and the forces that drive the colonization and maturation of biofilm communities on surfaces have been discussed as part of the introduction of this study to have a better understanding of the biological background of this thesis. There has also been an emphasis into highlighting efforts in the biofilm research community towards the design of surface materials able to modulate biofilm formation by either enhancing initial attachment or preventing biofouling. Many of these strategies have the disadvantage that these surfaces can be masked by the deposition of molecules in suspension and bacterial debris, masking their chemical composition and thus preventing the attractive/repulsive layer to interact with the bacteria.

The principal research objective of this study was to design and test synthetic linear polymers that aim to interact with bacteria and elicit biofilm formation, so a discussion about advances in polymer chemistry towards the modulation of bacterial behaviour and biofilm formation is necessary.

The two main proposed mechanisms for the aggregation of bacteria due to the effect of synthetic polymers are by bridging¹²³, based on the use of cationic polymers that are able to interact with bacteria by charge compatibility, adsorbing into multiple bacteria creating polymer bridges between each other; or by depletion aggregation¹²³, where non adsorbing polymers generate an entropically driven force that leads to self-organization of the bacteria into small clusters of laterally aligned cells (**Figure 1.4**).

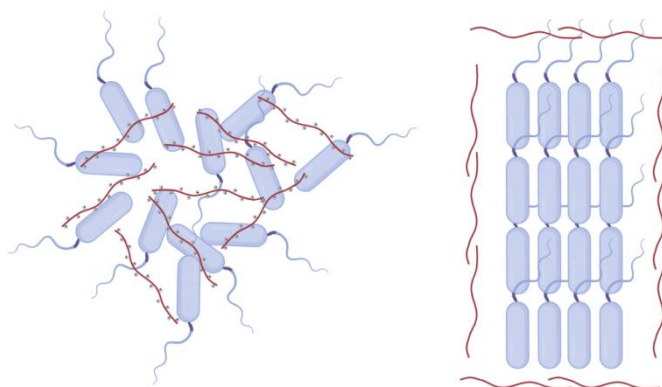


Figure 1.4: Proposed aggregation methods by the action of synthetic polymers. Left: aggregation by bridging. Right: aggregation by depletion. Polymer and bacteria size not to scale.

Both aggregation mechanisms result in clumps of aggregated bacteria that can develop into synthetic biofilm communities. The outcome of these aggregations depends on the polymer and bacteria surface composition and the strength of their interaction, they can result into strong aggregations that develop into mature communities, or they can be easily disrupted if the interaction is weak.

In the next part of this section different approaches that have been reported by the polymer community targeting bacterial aggregation will be described, this discussion is necessary to have a better insight about the advances of the polymer community towards biofilm control.

1.4.1 Bacterial sequestration by cationic polymers

Bacterial resistance to antibiotics has been a growing preoccupation from the scientific community and efforts have been directed towards the research of inhibitory strategies to tackle pathogenic microorganisms that do not rely on antibiotics.

One of such approaches was developed by previous members of our group, Perez-Soto et al.¹²⁴ who designed cationic linear polymers in liquid suspension to aggregate *Vibrio cholerae* and prevent them from colonizing the host epithelia. *V. cholerae* is a gut pathogen whose life cycle (**A, Figure 1.5**) comprises of planktonic bacteria that recognize and colonizes the gut host epithelia, developing a resilient biofilm community that generates more planktonic bacteria that would be released and would be able to colonize other hosts. While in planktonic stage *V. cholerae* has upregulated the genes expression responsible of the virulence and colonization factors, but when it is in the sessile aggregated part of its life cycle those genetic routes are downregulated and the bacteria are unable to colonize the host. Perez-Soto et al.'s¹²⁴ strategy (**B, Figure 1.5**) was to design linear cationic polymers that could interact with *V. cholerae* in planktonic stage sequestering them and inducing aggregation by bridging due to the charge compatibility between the positively charged polymers and the negatively charged bacterial surface. They designed two primary and tertiary cationic methacrylamide polymers (**Scheme 1.1**) that proved successful at sequestering *V. cholerae*, and when tested in vitro with human epithelial intestinal Caco-2 cells proved to decrease *V. cholerae* ability to adhere and colonize the epithelial cells, showing that the use of cationic polymers with therapeutic applications as an antibiotic alternative is a possibility and a growing field of research.

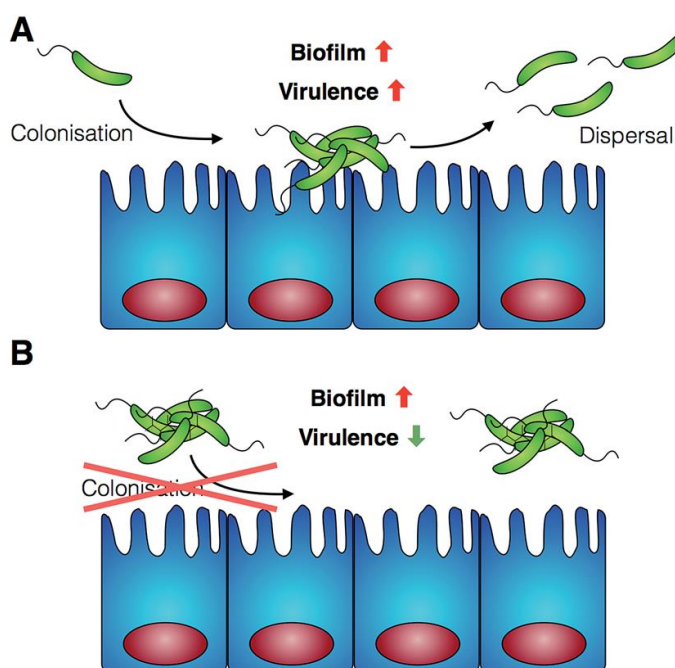
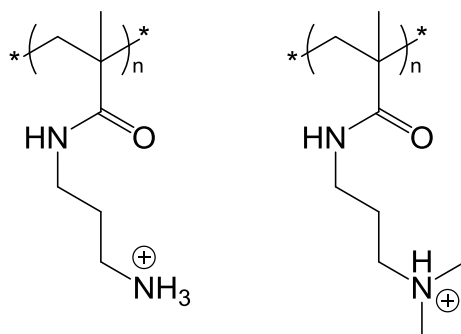


Figure 1.5: *V. cholerae* life cycle. A) *V. cholerae* planktonic life cycle. B) Disrupted *V. cholerae* colonization of the gut epithelia due to synthetic aggregation induced by polymers. Reproduced from Perez-Soto et al.¹²⁴.



Scheme 1.1: Primary and tertiary cationic methacrylamide polymers used by Perez-Soto et al.¹²⁴.

1.4.2 Functionalized polymers with biological motifs

Another strategy to target infectious bacteria without the use of antibiotics is the design and synthesis of polymers with biological motifs that target specific bacterial receptors.

E. coli pathogenic strains are responsible for most urinary tract and bowel infections¹²⁵. Fimbriae type 1 present a FimH adhesin on their tip that is responsible for the initial colonization efforts of *E. coli* strains as it recognizes and attaches to the oligomannosides residues of the urothelial cell's glycocalyx. This is a mandatory prerequisite for the colonization and further biofilm formation; if disrupted it might lead to the inhibition of bacterial colonization. Yan et al.¹²⁶ reported the use of such strategy (**Figure 1.6**). They used n-Heptyl α -D-mannose (HM) (**Figure 1.7**), a nanomolar antagonist of the FimH adhesin, as the building blocks of linear and star shaped HM-glycopolymers (**Figure 1.7**) with the aim to induce bacterial aggregation.

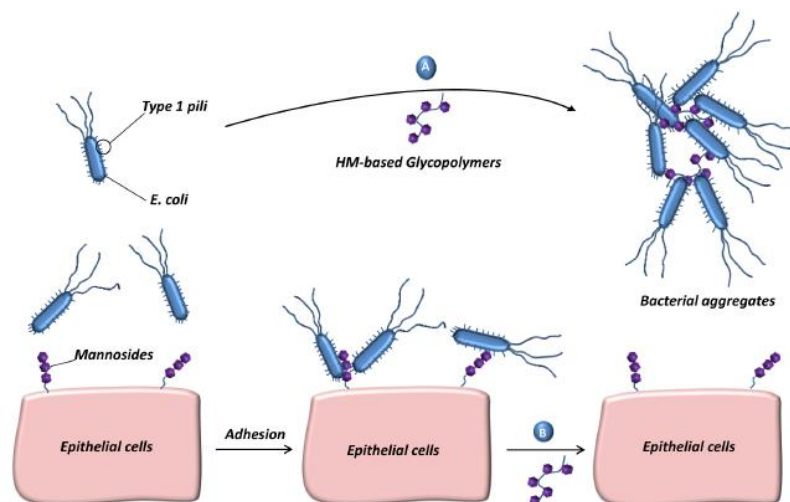


Figure 1.6: (Bottom) *E. coli* normal initial colonization of host's epithelia. (Top) *E. coli* colonization inhibition proposed by Yan et al.¹²⁶. Reproduced from Yan et al.¹²⁶.

Yan et al.¹²⁶ reported that their experiments in vitro showed that their HM-glycopolymers were able to inhibit bacterial adhesion and disrupt initial colonization of T84 cells at very low polymer concentrations compared to their control molecular FimH antagonists. This study showed the potential of therapeutic polymers based on specific targeted interactions.

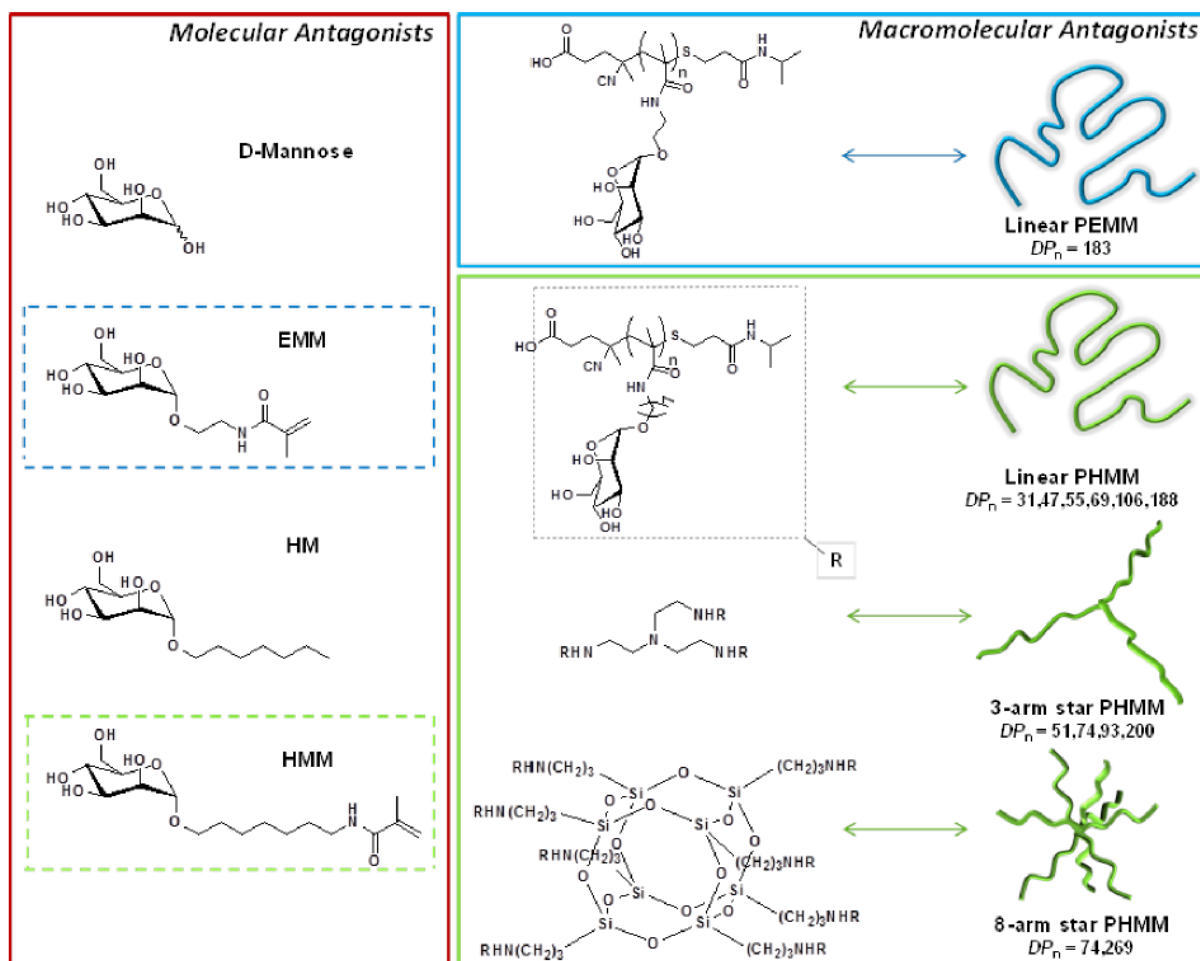


Figure 1.7: Molecular/macromolecular FimH antagonists designed and tested by Yan et al.¹²⁶, reproduced from Yan et al.¹²⁶. Molecular antagonists acronyms: D-mannose; EMM (N-[2-(α -D-mannopyranosyloxy)ethyl] methacrylamide); HM (*n*-Heptyl α -D-mannose); HMM (N-[7-(α -D mannopyranosyloxy)heptyl]methacrylamide)]. Macromolecular antagonists acronyms: PEMM (poly EMM); PHMM (poly HMM).

1.5 Biotechnological applications of biofilm

Strategies to disrupt biofilm formation have been discussed due to their impact in health and industry. But there are also potential applications of materials able to induce bacterial aggregation and further biofilm formation, as there are many uses in different industries that make use of biofilm communities due to their recalcitrant properties that make them highly resilient.

Biofilm communities have been used in industrial processes being part of bioreactors where biofilm communities can convert nutrients into products of interest like proteins, and as part of bioremediation efforts to detoxify soils and wastewater. Many of the conditions of these processes might be harsh for planktonic bacteria but biofilm resistance to hazards make them more suitable for these industrial bioprocesses.

1.5.1 Bioremediation uses of biofilm

Industrial processes all around the world have generated waste that has contaminated soil and water resources. Many approaches have been taken to treat many of these contaminated sediments, like translocating and storing them where they cannot harm wildlife and natural aquifers, but that is a temporary band aid that does not solve permanently the problem. There is an incentive to find better and more suitable and efficient approaches to detoxify the environment.

Indigenous soil bacterial communities have shown they are able of sequestering persistent heavy metals and metabolizing organic pollutants^{127, 128}. These biofilm communities provide a structure and an increased resistance to environmental hazards, like chemical and shear stress. Planktonic bacteria of the same species can metabolize the same pollutants but have a decreased survivability compared to their biofilm counterparts. In addition, biofilm communities can be composed of multiple species that direct collaborative metabolic efforts complementing each other in their bioremediation properties¹²⁹.

Interesting examples of the use of biofilm communities able to detoxify contaminants with bioremediation applications have been reported by the scientific community. *Dehalococcoides spp.* and *Dehalobium chlorocoercia*, from the phylum *Chloroflexi*, for instance are capable of metabolizing halogenated hydrocarbons via organohalide respiration. These species have shown potential to decontaminate chlorinated organic solvents¹³⁰. Arsenic sequestration from industrial mining has been demonstrated by a number of biofilm forming species like *Desulfosporosinus auripigmentum*, *Herminiimonas arsenicoxydans* and *Thiomonas spp*¹³¹ showing potential for the bioremediation of heavy metal in mining operations.

There have been approaches for the design of biofilm carriers that exploit the bioremediation capabilities of some microorganisms for wastewater treatment with the aim to decontaminate organic pollutants and heavy metals¹³².

1.5.2 Biofilm bioreactors

Biofilm bioreactors are vessels that use the metabolism of immobilized biofilms to transform nutrient into valuable compounds, or to be able to process contaminated liquids from industrial processes. Microorganisms are forming biofilm communities on substrates that increase their surface area to have a better access to the liquid column of the reactor. Biofilms allow for bioreactors that can be

under continuous and repeated batch processes, instead of the traditional planktonic reactors that rely on one-batch cycles.

There have been reports of biofilm bioreactors for wastewater treatment¹³³, gas and odor treatment¹³⁴, sulfide removal and sulfur production¹³⁵, bioethanol production¹³⁶, biobutanol production¹³⁷, lactic acid production¹³⁸, recombinant protein expression¹³⁹, and hydrogen generation¹⁴⁰.

1.6 Project objectives

This project focused on the design of linear polymer scaffolds that could be easily modified post polymerization without the introduction of further purification steps with the aim of testing chemical functional groups that aggregate *E. coli* and induce synthetic biofilm communities.

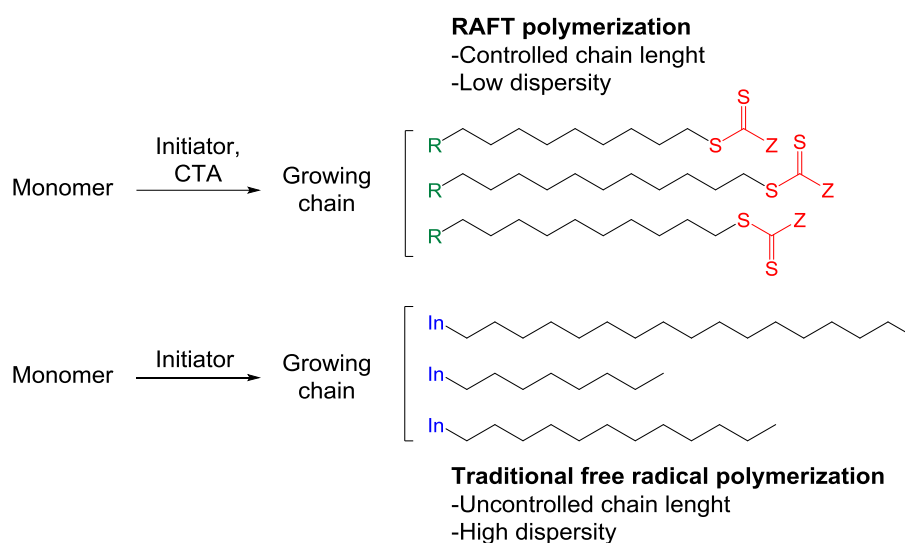
Chapter 2 is dedicated to polymer chemistry. It focuses on the polymer scaffold poly(acryloyl hydrazide) and studies on its stability and co-functionalization with a small library of functional groups; as well as the synthesis and characterization of the novel polymer scaffold poly(acryloylglycine hydrazide), followed by studies on its stability and functionalization.

Chapter 3 was dedicated to the testing of functionalized polymers with the aim to elicit biofilm formation of *E. coli*. The effects generated for the microorganisms were tested and characterized with an array of different experiments to prove that our polymers were able to aggregate *E. coli* without compromising its integrity.

2. RAFT polymers for biological applications

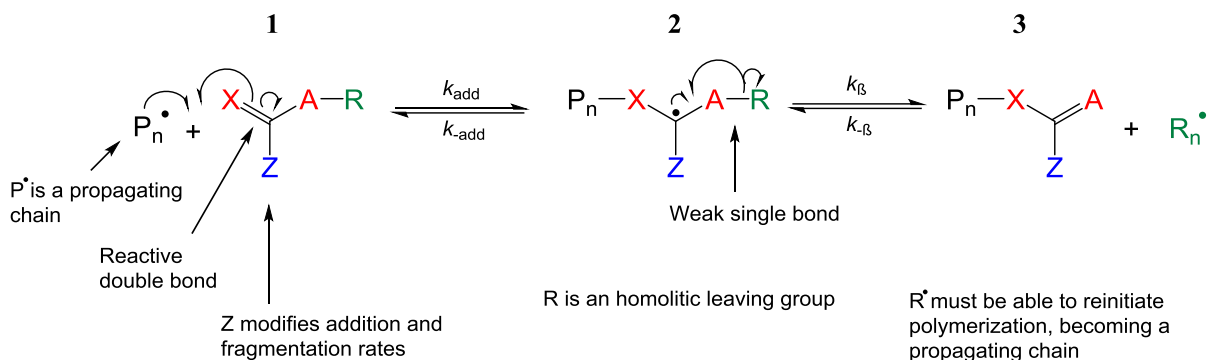
2.1 Background

Reversible addition fragmentation chain transfer (RAFT) is one of the most versatile and powerful controlled free radical polymerization techniques; it relies upon a kinetic strategy for the controlled synthesis of polymeric architectures in contrast with traditional uncontrolled free radical polymerization (**Scheme 2.1**). Since its first report in 1998¹⁴¹ the RAFT technology has been recognized as a useful tool for the development of complex polymeric structures: block¹⁴², star¹⁴³, crosslinked¹⁴⁴, stimuli responsive¹⁴⁵, nanoparticles¹⁴⁶, and polymers with biological applications¹⁴⁷.



Scheme 2.1: Comparison between traditional uncontrolled and RAFT polymerization.

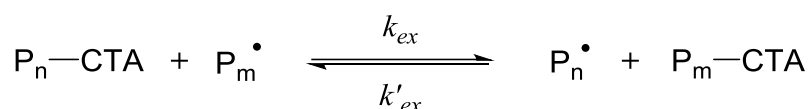
The RAFT reaction uses chain transfer agents (**CTAs**) for a controlled radical polymerization¹⁴⁸, allowing the synthesis of complex polymeric architectures with a projected molecular weight, low molar mass dispersity (**Đ**), and continuous chain growth. These transfers agents mediate a two addition fragmentation mechanism during polymerization (**Scheme 2.2**), and are unsaturated compounds of general structure **1**, where C=X is a reactive double bond towards radical addition. X is usually CH₂ or S, and Z must be a chemical group able to confer the transfer agent reactivity so is able to propagate radicals, and at the same time give a stable intermediate (**2**). R (**3**) is a homolytic leaving group, that must be able to reinitiate the polymerization with a similar reactivity as the initial transfer agent. A can be CH₂, O, or S, and is generally the same as X.



Scheme 2.2: Mechanism for addition fragmentation chain transfer.

2.1.1 RAFT polymerization mechanism

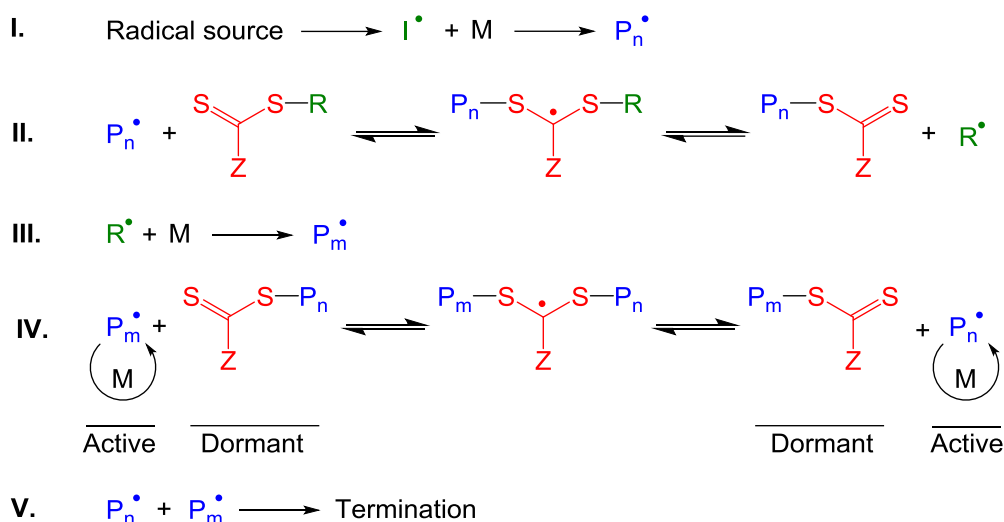
RAFT polymerization is based on an equilibrium between active and dormant chains achieved by degenerative chain transfer¹⁴⁹ (**Scheme 2.3**). In this mechanism, P_n -CTA is attacked by the propagating radical P_m^\bullet to form the active species P_n^\bullet and the dormant species P_m -CTA. This equilibrium is an exchange reaction where there is no change in the total number of radicals during the activation/deactivation mechanism.



Scheme 2.3: Mechanism of degenerative chain transfer reversible activation. (CTA) chain Transfer Agent.

The steps of RAFT polymerization (**Scheme 2.4**) are:

- **Step I. Initiation:** a free radical initiator is activated, starting the polymerization (P_n) of a monomer (M).
- **Step II. Reversible chain transfer:** the propagating radical (P_n^\bullet) attacks the double bond of the RAFT chain transfer agent (CTA) releasing a new radical initiator (R^\bullet).
- **Step III. Reinitiation:** the reaction of the new radical initiator R^\bullet with a monomer (M) forms a new propagating radical (P_m^\bullet).
- **Step IV. Chain equilibrium:** equilibrium between active propagating chains (P_n^\bullet and P_m^\bullet) and a dormant CTA is achieved, this provides equal probabilities to all propagating chains to grow and results in the production of polymers with lower \bar{D} .
- **Step V. Termination:** propagating chains react producing a dead polymer that cannot be reinitiated.



Scheme 2.4: RAFT polymerization mechanism.

2.1.2 RAFT polymerization kinetics

RAFT polymerizations feature first order kinetics (Equation 2.1), where the rate of polymerization (R_p) is a linear function over time with respect of the logarithm of the monomer concentration $[M]$.

$$R_p = - \frac{d[M]}{dt} = k_p [P_n^\bullet][M]$$

$$\ln \frac{[M_0]}{[M]} = k_p [P_n^\bullet]t$$

Equation 2.1: RAFT polymerization first order kinetics.

This linear tendency in the rate of polymerization (Figure 2.1) is true if the contribution of non-reversible terminations is negligible and the growing chains concentration $[P_n^\bullet]$ remains constant through the polymerization. A downward curvature (Figure 2.1) on the kinetic plot means that there is a decrease in $[P_n^\bullet]$ that might be caused by the increase in termination reactions, undesirable side reactions, or the destruction of radicals by redox processes. A slow upwards curvature (Figure 2.1) on the kinetics reflects a retardation in the polymerization due to a slow initiation, this behaviour can be explained due to a delay caused by a pre-equilibrium stage where the inactive RAFT CTAs are converted to the polymeric RAFT establishing a chain equilibrium stage, certain CTAs with strong stabilizing groups Z like aromatics are known to cause retardation in polymerization initiation.

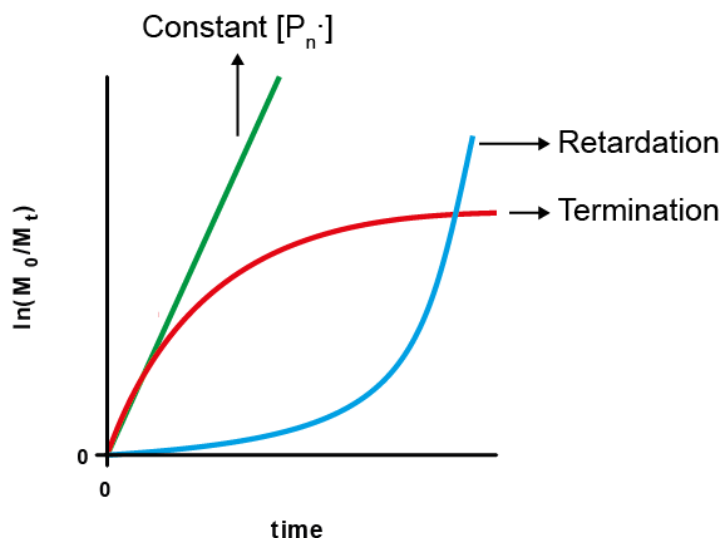


Figure 2.1: Different behaviours expected over time on RAFT polymerization depending on changes of $[P_n\cdot]$.

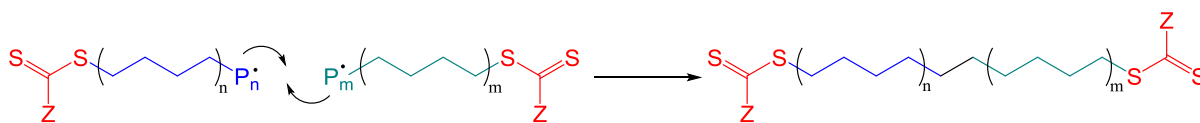
In an ideal RAFT polymerization we can control and predict the final degree of polymerization (**DP**) (**Equation 2.2**) of a reaction tweaking the molar ratio between monomer and the CTA, and the rate of monomer conversion (ρ), the difference between the monomer concentration at the beginning (t_0) and end (t_{final}) of the polymerization ($\rho = (1 - [M]_{t_0}/[M]_{t_{\text{final}}})$).

$$DP = \frac{[M]}{[CTA]} \rho$$

Equation 2.2: Projected degree of polymerization (DP) of a RAFT polymer.

For example, if we have a molar ratio $[M]:[CTA]=100:2$ and we let the monomer react until $\rho=0.8$ (80% conversion) our final polymer will have a projected DP of 40 subunits ($100/2 \times 0.8=40$).

It is important to not carry the polymerization reaction until full monomer conversion, that is because the higher the DP the longer the time the growing polymer chains spends as propagating radical increasing the probability of terminations like radical-radical combination events between growing chains (**Scheme 2.5**), or other side reactions leading to the destruction of the radical chain end or the CTA^{149, 150}. These undesirable events generate early terminations in growing chains that create a discrepancy between the theoretical molecular weight ($M_{n_{\text{th}}}$) (Equation 2.3) and the one obtained through the experimental polymerization reaction, leading to an increase of the final \bar{D} and overall less control over the qualities of the final product.



Scheme 2.5: Example of termination event by combination between growing polymer chains.

$$Mn_{th} = \frac{[M]\rho M_M}{[CTA]} + M_{CTA}$$

Equation 2.3: Theoretical molecular weight (Mn_{th}). M_M and M_{CTA} are the molecular weight of the monomer and the CTA, respectively.

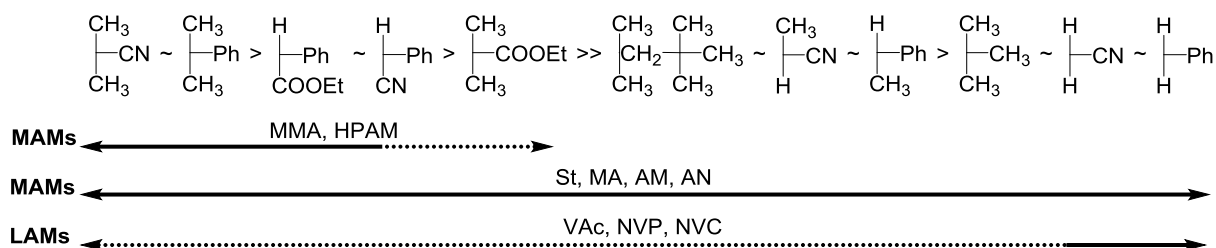
Chain termination is an inevitable phenomenon in radical polymerization because of the high reactivity of free radicals, to decrease the chances of undesirable terminations it is recommended to stop RAFT polymerization reactions between 80-90% of their monomer conversion.

2.1.3 RAFT agent selection

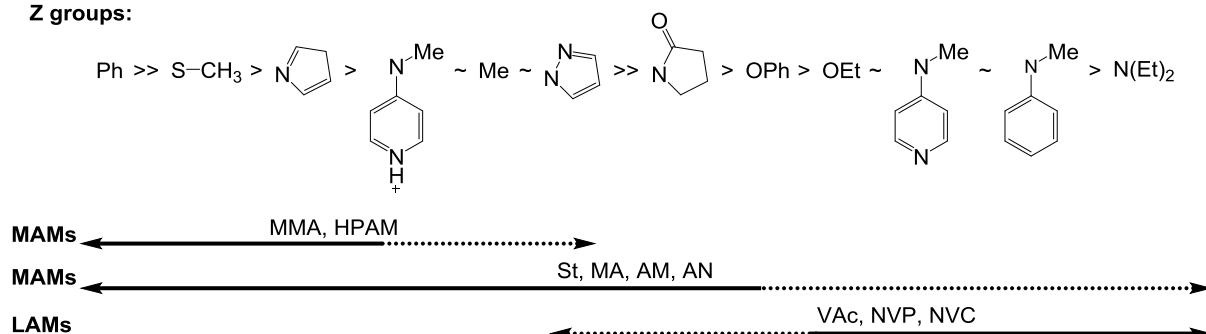
RAFT enables controlled polymerization over a varied range of monomers available for free radical polymerization. The controlled addition-fragmentation reaction will depend on the composition of the leaving group R and the stabilizing group Z, these groups have to be chosen (**Scheme 2.2**) accordingly depending of the monomer to polymerize to increase the control over the kinetics and dispersity of the reaction. Most vinyl monomers ($CH_2=CH-R$) can be classified in two families depending on their reactivity: “more activated monomers” (MAMs) and “less activated monomers” (LAMs). MAMs have their vinyl group conjugated to a double bond (butadiene, isoprene), an aromatic ring (styrene, vinylpyridine), a carbonyl group ((meth)acrylates and (meth)acrylamides, maleic anhydride, maleimide), or a nitrile (acrylonitrile). LAMs have a double bond next to oxygen, nitrogen, halogen, sulfur lone pairs, or saturated carbons (vinyl acetate, N-vinylpyrrolidone, vinyl chloride, 1-alkenes)¹⁵¹.

RAFT agents can be classified depending on their stabilizing Z group into: dithioesters, trithiocarbonates, xanthates, and dithiocarbamates. Dithioesters have very high transfer constants and are considered among the most effective CTAs for the polymerization of MAMs, but are prone to hydrolysis. Some MMAs experience retardation during the polymerization, dithioesters are bad choices for LAMs as they inhibit most polymerizations. Trithiocarbonates are less reactive but more stable than dithioesters. They can be synthesized by simple methods, and enable controlled polymerizations of most MMAs. They are very popular CTAs for the polymerizations of (meth)acrylic monomers. Xanthates and dithiocarbamates are the CTAs of choice for controlled polymerization of LAMs; they are versatile as they can also be used in the polymerization of some MAMs as acrylates, acrylamides and styrenes, but with less controlled \bar{M}_n than dithioesters and trithiocarbonates. This makes them useful for the RAFT polymerization of block copolymers of MAMs and LAMs.

R groups:



Z groups:



Scheme 2.6: Guidelines for the selection of R and Z groups of RAFT agents for the polymerization of vinyl monomers, adapted from reference¹⁵² with permission of the author. Transfer and fragmentation rates decrease from left to right. Dashed lines indicate partial control over polymerization, like control over molecular weight but poor control over dispersity, or retardation in some LAMs. Monomer abbreviations: MMA = methyl methacrylate, HPAM = *N*-(2-hydroxypropyl)methacrylamide, ST = styrene, MA = methyl acrylate, AM = acrylamide, AN = acrylonitrile, VAc = Vinyl acetate, NVP = *N*-vinylpyrrolidone, and NVC = *N*-vinylcarbazole.

2.1.4 Post-polymerization functionalization as a tool for biological screening

Functional polymers are macromolecules that have unique properties conferred by the presence of chemical functional groups¹⁵³ that are different to the ones of the backbone chains and that can modulate the chemical, physical, biological, and pharmacological properties of the polymer.

Functional polymers may be prepared by directly polymerizing monomers with functional groups, but there is still a wide range of chemicals that cannot be directly polymerized, these groups may prevent polymerization or might generate side reactions that contribute to the loss of control over the polymerization¹⁵⁴.

Post-polymerization functionalization is based in the polymerization of monomers that carry highly chemoselective handles, a chemical group that can be modified with a wide range of functional groups in further reactions steps (**Figure 2.2**). This is a highly attractive approach for testing libraries of chemical groups with biological applications, as a single polymer precursor can be modified to generate many functional polymers with different properties that will share identical chain length, tacticity, molecular weight, and \bar{D}^{155} . These are highly desirable properties from the point of view of making reproducible materials with uniform bioactivity¹⁵⁶.

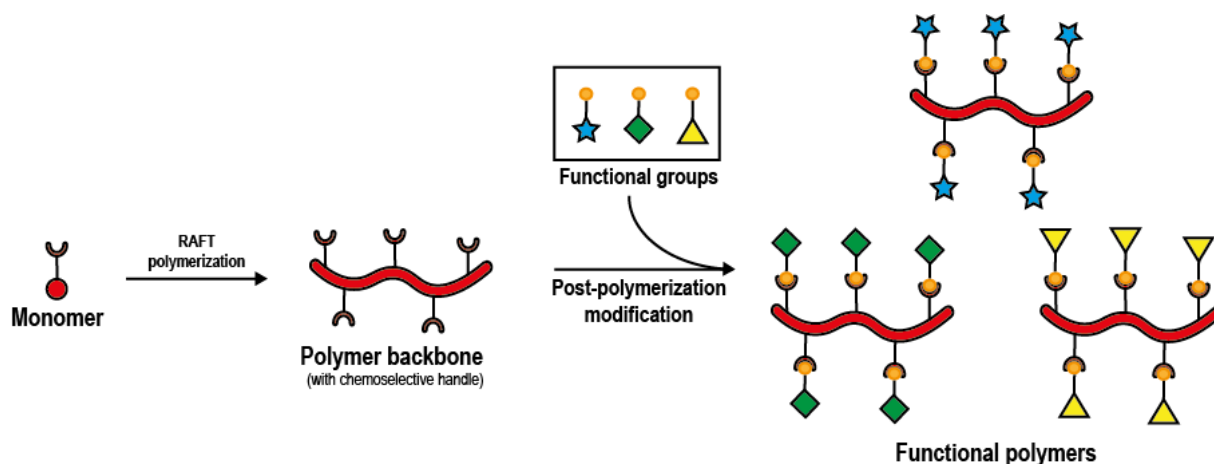


Figure 2.2: Post-polymerization functionalization

There are some considerations to take when designing a polymer scaffold aimed to be modified with functional groups towards biological applications:

- The chemoselective handle must not prevent the monomer from being polymerized, this might require the use of protecting groups that are inert towards the polymerization step that need to be removed prior to the post-polymerization functionalization step.
- The chemistry used for the conjugation reaction of the functional group ligand with the monomer handle should be simple, efficient, and reproducible, and the bond between the handle and the ligand should be stable at physiological pH. Conjugation reactions that require further purification steps should be avoided.
- The functional group ligands used for biological applications should be commercially available to ease the organic synthesis workload.
- The functionalized polymer product should be soluble in aqueous conditions at physiological pH so it can be used towards modulating *in situ* the physiology of the targeted biological organism.

We want a conjugation chemistry reaction that does not require further purification steps, is efficient, reproducible, uses biocompatible solvents (ideally water), and that creates a bond stable at physiological pH. These requirements would allow for the direct use on biological samples after the post-polymerization functionalization coupling step.

Amine-carbonyl condensation chemistry (**Figure 2.3**) is a prime candidate for the post-polymerization functionalization of scaffolds. It is a coupling reaction between amines, hydroxylamine, hydrazines or hydrazides with the carbonyl group of a ketone or an aldehyde generating water as the only side product of the reaction.

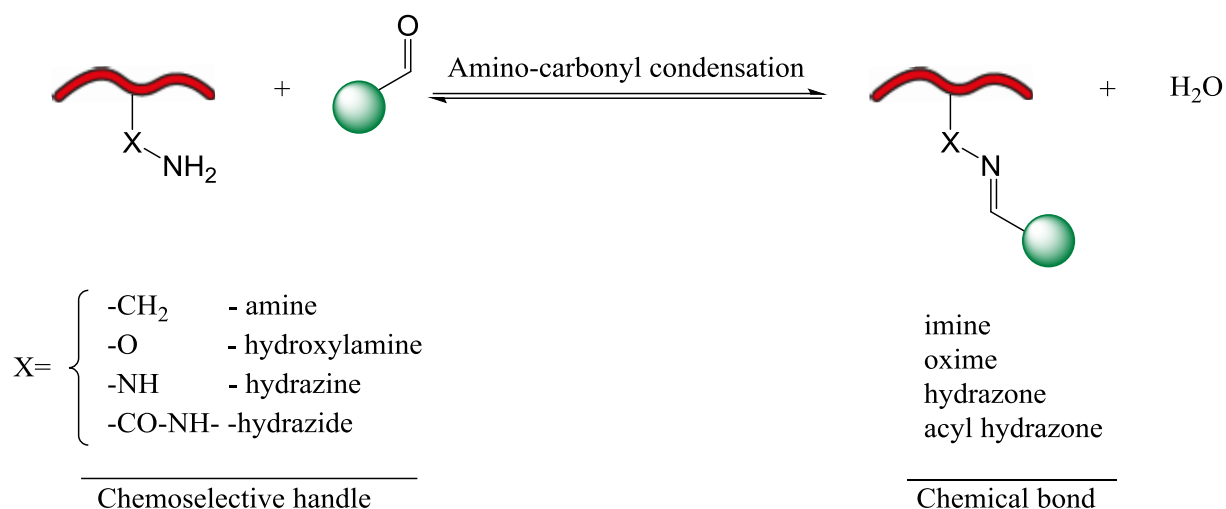
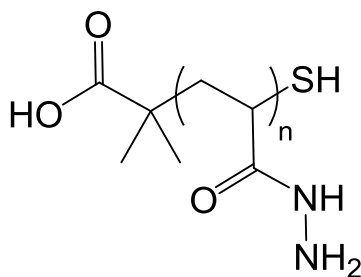


Figure 2.3: Post-polymerization functionalization with aldehydes via amino-carbonyl condensation reaction. Adapted from Dr Oliver Creese PhD thesis¹⁵⁷.

This functionalization reaction is ideal for post polymerization modification as it can be performed on water, and there is a wide range of commercially available aldehydes carrying functional groups of biological interest that can be used to functionalize polymers. Hydrazides are the most attractive of all the available chemoselective handles because they generate an acyl hydrazone bond when coupled with an aldehyde or ketone that is stable at physiological pH^{154, 158, 159}. This reaction fulfils all the desired requirements, as they can be used to functionalize polymers in aqueous conditions at physiological pH without the need of further purification so it can be used on biologicals samples right after functionalization.

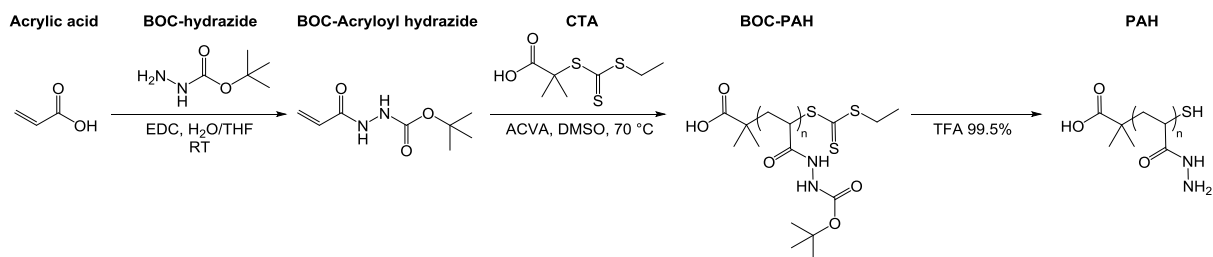
2.1.5 Poly(acryloyl hydrazide)

Poly(acryloyl hydrazide) (**PAH**) (**Scheme 2.1**) is a polymer scaffold first reported by Carolyn R. Bertozzi¹⁶⁰ synthesized by activated ester post-polymerization functionalization of acetoxime acrylate with the addition of excess hydrazine. **PAH** is an acrylic polymer with a hydrazide side chain able to anchor aldehydes and sugars through amine carbonyl condensation chemistry. This polymer was successfully functionalized¹⁶⁰ with a wide range of reducing sugars resulting in high loading efficiencies and stability at physiological pH. It proved to be a good candidate for biological testing of functional groups but the use of excess hydrazine during the synthesis process was undesired as it is highly toxic and would pose a problem to use with living organisms.



Scheme 2.7: Poly(acryloyl hydrazide) chemical structure.

Daniel Crisan, a member of our laboratory, worked in an alternative synthetic route ¹⁶¹ that avoided the use of toxic hydrazine. This route (**Scheme 2.8**) reported the preparation of PAH by polymerization of boc-hydrazide, and a subsequent de-protection in acid. This new route allowed for direct use of functionalized PAH on biological samples without the risk of including toxic impurities.



Scheme 2.8: Poly(acryloyl hydrazide) synthesis route developed by Crisan et al.¹⁶¹.

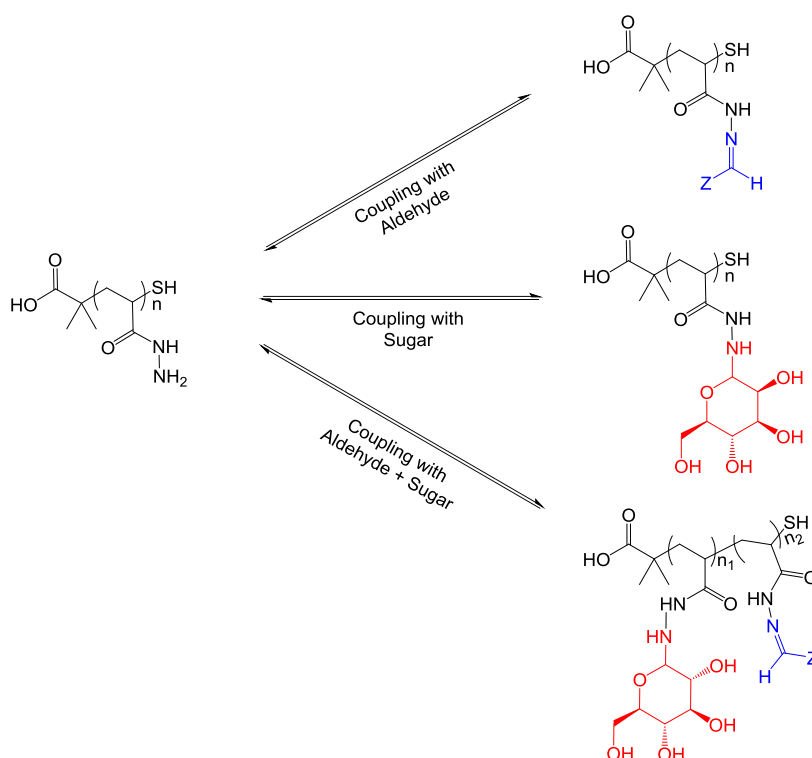
Crisan et al.¹⁶¹ extensively tested the post polymerization loading efficiency of **PAH** with aldehydes in a variety of solvent and pH conditions that proved that it was a desirable platform for testing of functional groups with biological applications.

2.2 Objectives

2.2.1 Co-functionalization and stability of poly(acryloyl hydrazide)

Dr Daniel Crisan developed a novel **PAH** synthesis route and tested its post-polymerization loading efficiency as part of his PhD thesis¹⁶², but there was still the need to analyse the loading stability of the acyl hydrazones formed after the functionalization of the polymer side chains with aldehydes. The first objective of this section will be testing the hydrazone bond stability generated after the functionalization of **PAH** with aldehydes.

Although Daniel Crisan et al.¹⁶¹ studied the loading efficiency of **PAH** with aldehydes in great detail they never tried to load sugars or co-functionalize the backbone with both aldehydes and sugars. The second objective will therefore be to test the co-functionalization efficiency of **PAH** with sugars and aldehydes (**Scheme 2.9**).



Scheme 2.9: PAH hydrazide side chains coupling with aldehydes and sugars. One of the objectives of this research is to test PAH capability to be co-functionalized with both sugars and aldehydes.

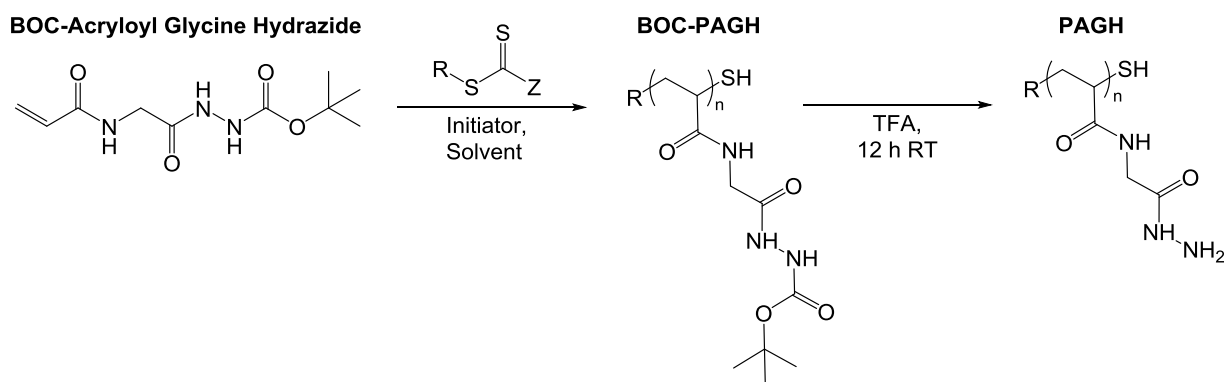
2.2.2 Synthesis, characterization, and functionalization of poly(acryloylglycine hydrazide)

When **PAH** was tested for loading efficiency Crisan et al.¹⁶¹ did it in a 1:1 side chain to aldehyde ratio. This is important as using an excess of aldehydes would require additional purification steps that would be against the direct use after post-polymerization functionalization. Although Crisan et al.¹⁶¹ got success with their loading experiments in a variety of conditions¹⁶¹ these results were never close to full loading efficiency of one equivalent of aldehyde per equivalent of side chain. This might have been due to lack of enough aldehyde equivalents to push the reaction towards full side chain

functionalization, or due to steric hindrance between side chains that prevented some of them to be accessible to be functionalized.

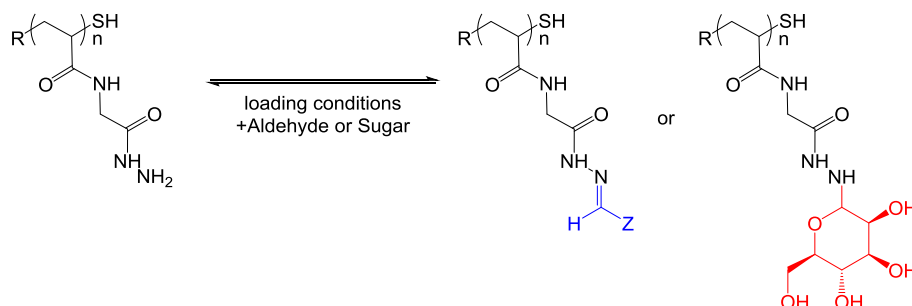
There are two approaches to this problem. First, a change in the ratio of aldehydes in excess to push the reaction equilibrium towards full functionalization of side chains, but this approach adds more undesired purification steps and prevents in-situ testing after post-polymerization functionalization; the other approach would be to design a similar polymer with a longer side chain that could prevent steric hindrance between the polymer sidechain.

The first objective of this section is the development of a new synthetic route via RAFT polymerization of poly(acryloylglycine hydrazide) (**PAGH**) (**Scheme 2.10**). This scaffold is an acrylic polymer with a hydrazide side chain able to anchor aldehydes and sugars through amine-carbonyl condensation chemistry.



Scheme 2.10: The novel synthesis of poly(acryloylglycine hydrazide) from the monomer BOC-acryloylglycine hydrazide via RAFT polymerization.

First, the development of the synthetic route and purification steps of the monomer BOC-acryloylglycine hydrazide was targeted. Once a reliable monomer synthesis route was achieved the next step was focusing on the design and testing of the polymerization conditions and the characterization of **PAGHs** of different molecular weights and dispersities, followed by the testing of the loading efficiency of the polymer hydrazide side chains with different aldehydes and sugars by amine-carbonyl condensation (**Scheme 2.11**).



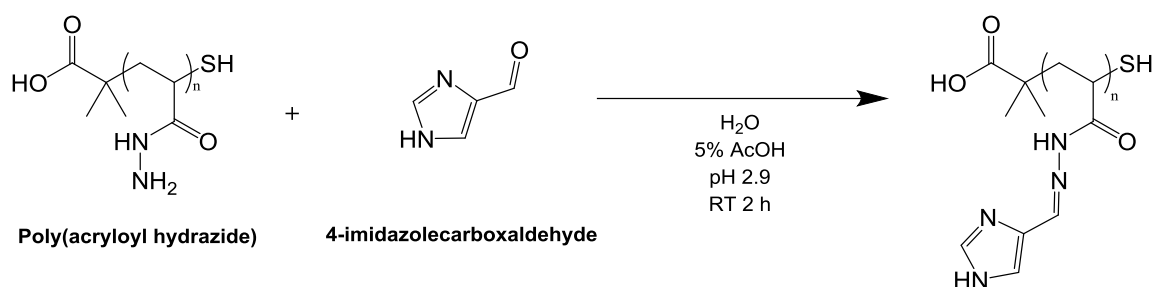
Scheme 2.11: Test the loading efficiency of PAGH with aldehydes, and sugars to achieve functionalized polymers.

2.3 Results and discussion

2.3.1 Loading stability of poly(acryloyl hydrazide)

Dr Daniel Crisan performed extensive work as part of his PhD thesis¹⁶² testing the functionalization capabilities of **PAH** with a wide array of aldehydes under different solvent conditions. Although his work was successful there were still some questions to answer regarding the stability over time of the acyl hydrazone bond created during the functionalization of hydrazides with aldehydes via the amino-carbonyl condensation reaction.

During his research, Dr Daniel Crisan¹⁶² used 4-imidazolecarboxaldehyde as the model of hydrophilic aldehyde for the research of **PAH** functionalization; the standard reaction for the coupling in aqueous conditions was done in a 5% acetic acid (AcOH) buffer in D₂O pH 2.9 with one equivalent of a **PAH** of 40 repetitive subunits and one equivalent of 4-imidazolecarboxaldehyde (**Scheme 2.12**) with an incubation time of 2 h at RT. To proceed with this section, a new **PAH** of 40 subunits (**PAH₄₀**) was synthesized following Dr Daniel Crisan specifications¹⁶², and used as the model polymer of the loading stability studies.



Scheme 2.12: Standard aqueous functionalization reaction of PAH with the model of hydrophilic aldehyde 4-imidazolecarboxaldehyde in 5% acetic acid buffer pH 2.9.

¹H NMR spectroscopy was used to monitor the efficiency of the loading reaction. This method allows for the visualization and quantification of the proton environments of a sample. The functionalization efficiency of the reaction was calculated by measuring the depletion of the integral corresponding with the free aldehyde signal at 9.63 ppm (**Figure 2.4**), a signal of 1 proton would mean that 100% of the aldehyde was free in solution, while any decrease from that value would mean the incorporation of said aldehyde into the polymer subunits that could be observed as a broad signal from 6.25-8.75 ppm, hence the decrease in the free aldehyde signal's value at 9.63 ppm. In this example the value of the free aldehyde signal after the completion of the reaction was of 0.17 protons, meaning that the remaining 0.83 had been functionalized into 83% of the **PAH₄₀** subunits.

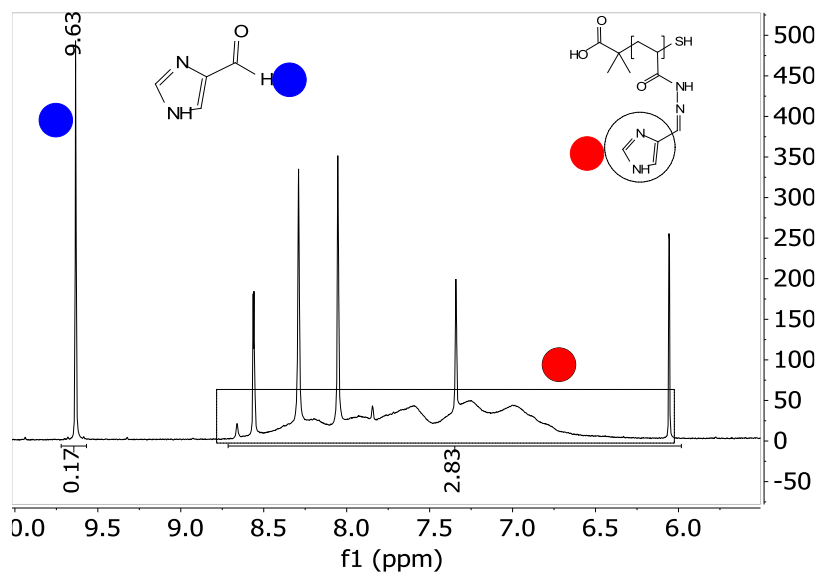


Figure 2.4: Representative ^1H -NMR spectra of the functionalization of PAH_{40} with 1 equivalent of 4-imidazolecarboxaldehyde in 5% acetic acid buffer in D_2O .

The loading stability of **PAH₄₀** was tested over time reacting it with one equivalent of 4-imidazolecarboxaldehyde on 5% of acetic acid buffer in D_2O pH 2.9 for 2 h at RT then monitoring the spectrum generated via ^1H NMR over a period of 48 h (**Figure 2.5**).

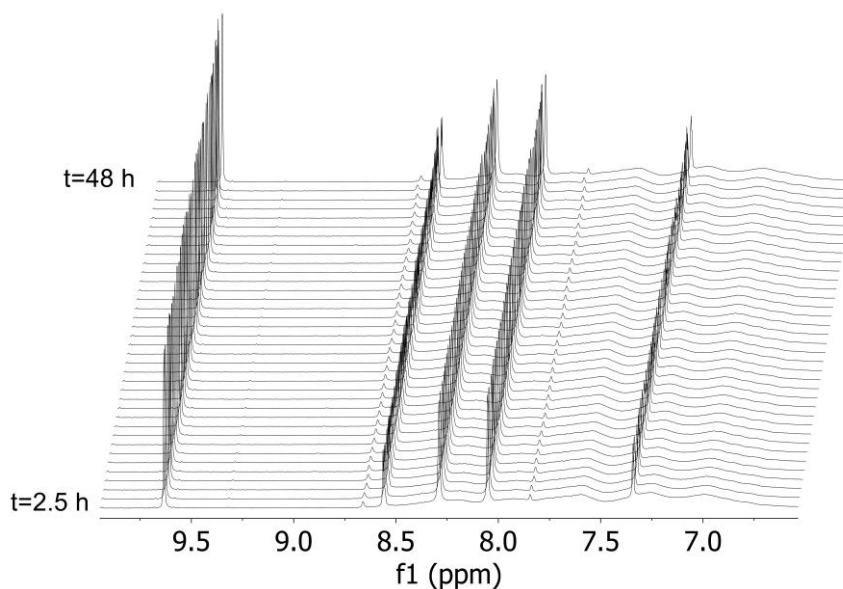


Figure 2.5: ^1H NMR spectra of the reaction of PAH_{40} with 1 equivalent of 4-imidazolecarboxaldehyde analysed at different intervals for 48 h.

An analysis of the integral value corresponding to the free aldehyde peak at 9.63 ppm (**Figure 2.6**) showed that the degree of functionalization of **PAH₄₀** remained constant over a period of 48 h, and that no regeneration of the free aldehyde could be observed.

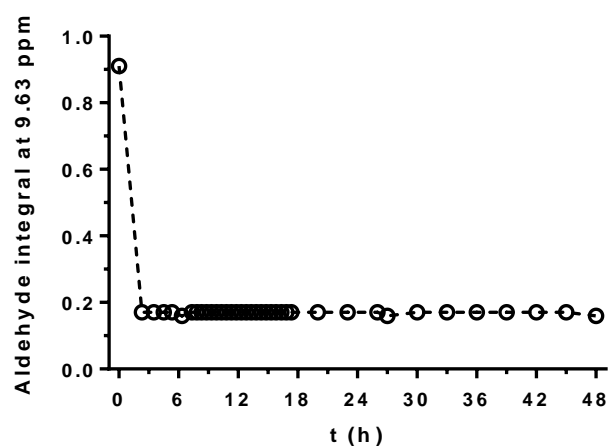


Figure 2.6: Change of integral value for the signal corresponding to the aldehyde at 9.63 ppm over 48 h.

To continue studying the stability of the loaded **PAH₄₀** a new functionalization stability experiment was performed (**Figure 2.7**), this time reacting **PAH₄₀** with 0.6 equivalents of 4-imidazolecarboxaldehyde, enough to achieve full conversion of the free aldehyde into the polymer backbone, so in case that there is aldehyde dissociation from the backbone it could be observed via ^1H NMR; the reaction was performed following the same conditions than the previous stability experiment.

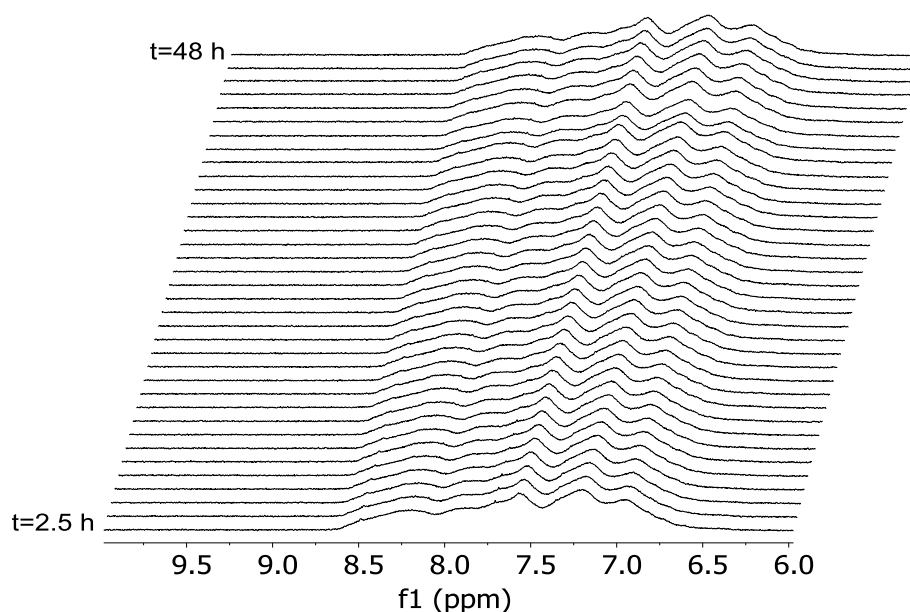


Figure 2.7: ^1H NMR spectra of the reaction of PaH_{40} with 0.6 equivalent of 4-imidazolecarboxaldehyde analysed at different intervals for 48 h.

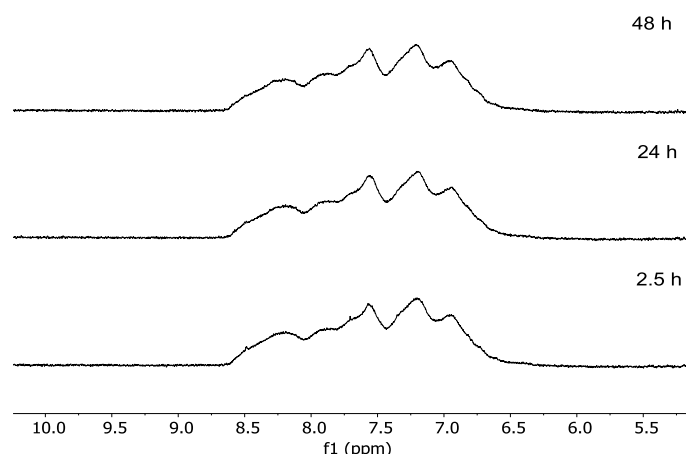


Figure 2.8: ^1H NMR spectra of the reaction of PAH_{40} with 0.6 equivalents of 4-imidazolecarboxaldehyde analysed at different intervals for 48 h.

An analysis of the spectra obtained during the experiment (**Figure 2.7**, **Figure 2.8**) confirmed that full conversion of the 0.6 equivalents of aldehyde into the polymer backbone was achieved and that it remained constant during the length of the 48 h experiment, as no signal corresponding to the free aldehyde expected to appear around 9.63 ppm could be observed. This result was in agreement with the previous experiment when PAH_{40} was coupled with 1 equivalent of 4-imidazolecarboxaldehyde and the level of functionalization remained constant.

The outcome of the loading stability experiments suggest that the functionalization reaction reached thermodynamic equilibrium and that any dissociation of a functionalized aldehyde that could happen would be compensated by the reformation of the hydrazone bond.

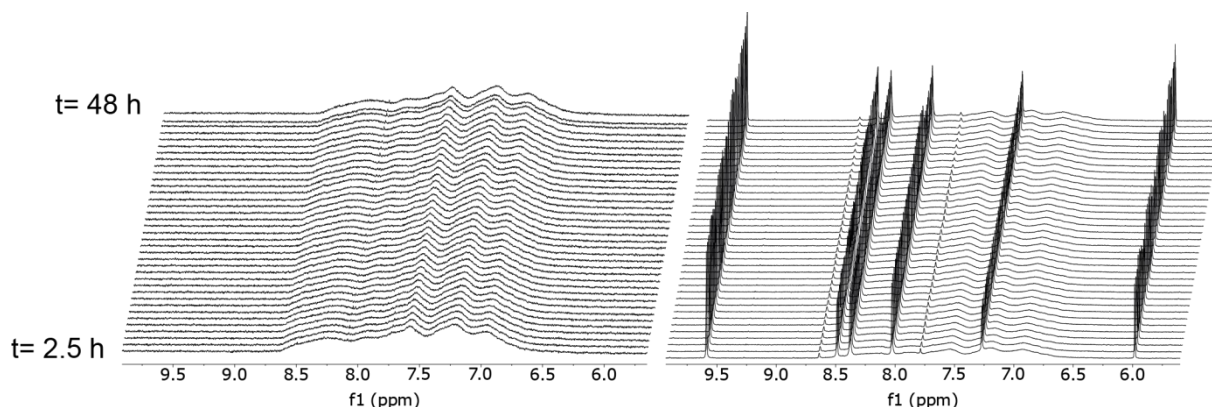


Figure 2.9: (Left) ^1H NMR spectra of the reaction of PAH_{40} with 0.6 equivalent of 4-imidazolecarboxaldehyde analysed at different intervals for 48 h. (Right) ^1H NMR spectra of the reaction of PAH_{40} with 1 equivalent of 4-imidazolecarboxaldehyde analysed at different intervals for 48 h. Both samples reacted for 2 h at RT, and were diluted twofold prior to the NMR analysis.

Both experiments were repeated by reacting PAH_{40} with 0.6 and 1 equivalent of 4-imidazolecarboxaldehyde in two separate experiments, incubating for 2 h at RT using 5% acetic acid buffer as solvent, but this time twofold diluting the samples taken from the reactions before proceeding with the monitoring of the functionalization loading via ^1H NMR over the course of 48 h (**Figure 2.9**). These conditions were used to test if a change of the concentration of the sample would

result in a significant change in the thermodynamic equilibrium of the system. When analysing the results it was observed that the loading functionalization remained constant during the whole duration of the monitoring meaning that a dilution of the sample did not affect the loading efficiency and that there was no discernible dissociation of functionalized aldehyde from the polymer.

Overall, these experiments confirmed the stability over time of the hydrazone bond created by amine-carbonyl condensation during the functionalization of **PAH** with aldehydes. The data obtained from these experiments contributed to the publication of a scientific paper by Daniel Crisan et al¹⁶¹.

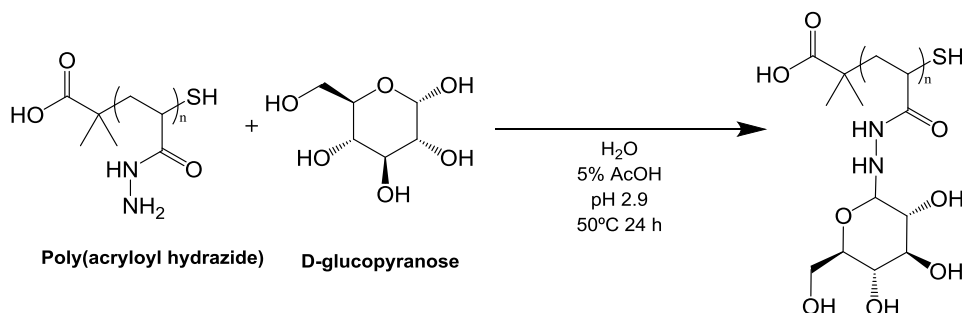
2.3.2 Poly(acryloyl hydrazide) co-functionalization

Crisan et al.¹⁶¹ had success with the individual functionalization of **PAH** with aldehydes but never tested the loading efficiency of aldehydes combined with other functional groups like carbohydrates. We are interested in this combination as sugars are common biological motifs recognized by receptors of living organisms. For example gut bacteria like *E. coli* fimbriae type 1 FimH would recognize and attach to the epithelial walls of a host when recognizing a repetitive pattern of D-mannose¹⁶³. A scaffold could be modified with sugars that allowed the polymer to get attached to the biological target, and then other aldehyde functional groups with other biological applications could get access to other surface receptors for a targeted biological application. A 40 subunit **PAH** (**PAH₄₀**) was used as the model polymer for all the functionalization reactions in this section.

D-glucose functionalization

A modified version of the protocol created by Crisan et al.¹⁶¹ was used to perform the co-functionalization experiments. Two 500 mM stocks of the hexose and the polymer **PAH₄₀** were prepared, then dissolved in 5% AcOH in D₂O. The reaction was performed mixing 1:1 equivalent volume solutions until a final concentration of 250 mM.

Then it was let react at 50°C for 24 h while stirring. The length of this reaction was higher than when functionalizing with aldehydes because hexoses tend to stay in cyclic form most of the time and the polymer handle can only be functionalized by the sugars when they change to its linear aldehyde form.



Scheme 2.13: PAH functionalization with D-glucose.

The reaction was characterized by ¹H NMR in D₂O using DMAP (4-Dimethylaminopyridine) as an integration standard to compare between the functionalized sample and the sugar control, this standard was added in the same quantity in both controls and reaction sample and was used as a common standard to integrate their signal peak values so the intensity of the signal between samples could be compared. This characterization technique was used as it allow to observe the changes in the proton environment between the control and reaction sample.

The NMR spectra from a successful functionalization experiment would show the decrease of the intensity of the signals corresponding to the free sugar and the creation of new signals corresponding of the incorporation of D-glucose into the polymer handles.

The proton environments of the reaction and control samples were analysed by monitoring their NMR spectra (**Figure 2.10**). The broad proton signals corresponding to **PAH's** backbone could be found from

0.25-2.30 ppm. Polymer signals tend to coalesce and appear as broad peaks due to their poor molecular rotation and repeating units being situated in marginally different chemical environments. From 2.75-3.80 ppm the peaks corresponding to the alcohol groups of the free sugar could be observed. At 3.85-4.1 ppm appeared a new broad signal that did not exist in the control sample and corresponded with the amine-carbonyl condensation of α -D-glucose with the hydrazide handle of **PAH**. This new signal showed that the functionalization reaction was successful, and that the polymer was loaded with the sugar. The spectra also showed signals corresponding to the β proton at 4.50 and α proton at 5.10, these two signals corresponded to the anomeric carbon of the free sugar that can adopt α or β dispositions.

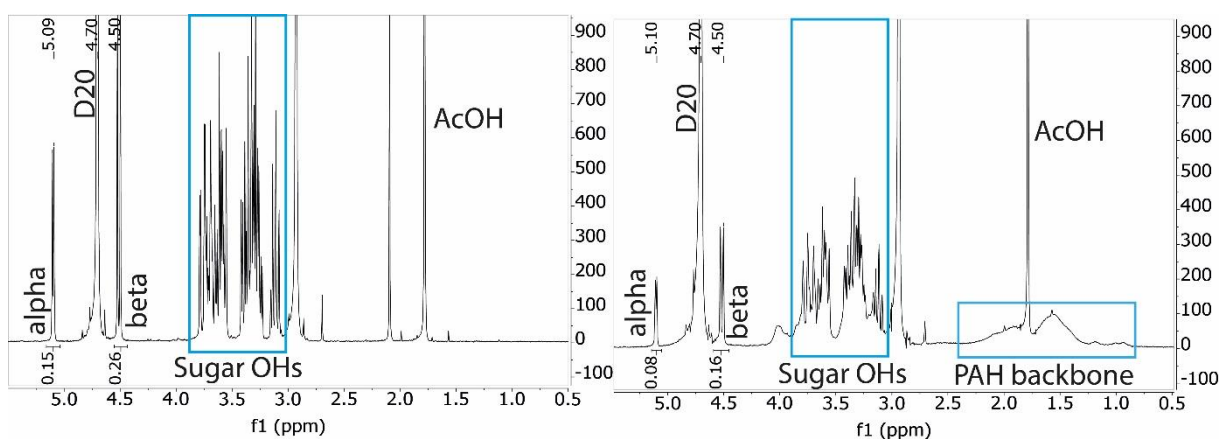


Figure 2.10: PAH functionalization with D-glucose after 24h. (Left) ^1H NMR in D_2O corresponding to the D-glucose control of the reaction. (Right) ^1H NMR in D_2O corresponding to the reaction of PAH with D-glucose.

Comparing in detail the differences between the control and reaction NMR spectra (**Figure 2.11**) showed that there was a noticeable decrease of intensity of the peaks corresponding to D-glucose α and β protons signals in the reaction sample compared to its control, this depletion in the integral signal was due to the decrease of free sugars in solution that had reacted with **PAH** hydrazide's handle. We could observe a new broad signal appearing from 3.85-4.1 that correspond with the α signals of the sugars integrated in the polymer.

These results confirmed that the functionalization reaction was successful. To calculate its efficiency the combined intensity of the peaks corresponding to α and β protons in the functionalization reaction was divided by the integral value of the same peaks on the control reaction to obtain the percentage of free sugar after the reaction takes place. The result was of 58% ($0.24/0.41 \times 100$) of the initial equivalent, meaning that the remaining 42% had been successfully loaded onto the **PAH** handles by amino-carbonyl condensation.

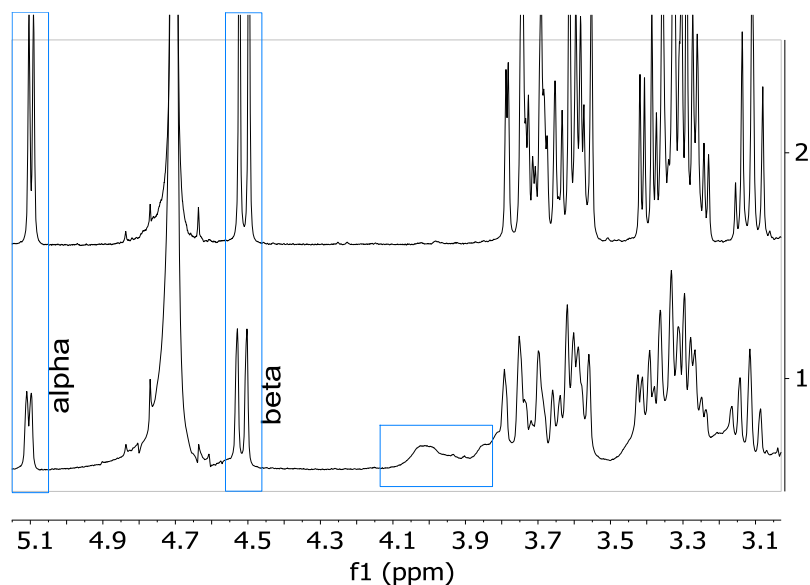
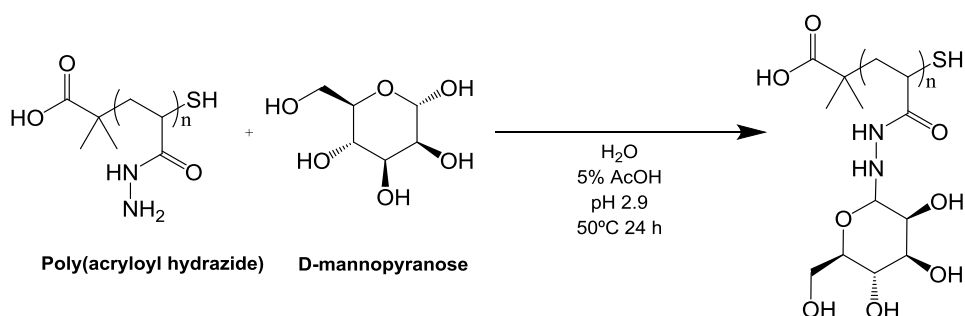


Figure 2.11: Stacked ^1H NMR spectra of PAH functionalization with D-glucose. (Top) spectra corresponds to the D-glucose control sample. (Bottom) corresponds to the reaction sample of PAH with D-glucose spectra.

D-mannose functionalization



Scheme 2.14: PAH functionalization with D-mannose.

The same protocol was followed for the functionalization of **PAH** with D-glucose (**Scheme 2.14**), then the reaction was characterized by ^1H NMR using DMAP as integration standard in both samples. When analysing the spectra (**Figure 2.12**) a similar proton environment than with the functionalization reaction with D-glucose was encountered, α appeared at 5.12 ppm, but in this case the β proton signal could be found at 4.85 ppm, too close to the solvent signal of the D_2O . This meant that the integration intensity values of $\alpha+\beta$ protons could not be used to calculate the loading efficiency of this functionalization reaction.

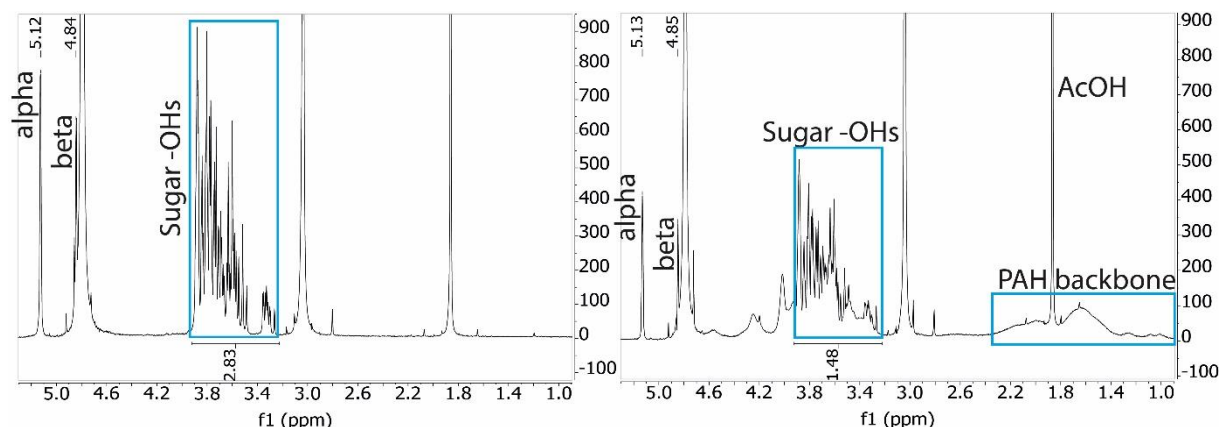


Figure 2.12: PAH functionalization with D-mannose after 24 h. (Left) ^1H NMR in D_2O corresponding to the D-glucose control of the reaction. (Right) ^1H NMR in D_2O corresponding to the reaction of PAH with D-glucose.

When the control and reaction spectra were compared in detail (**Figure 2.13**) it could be observed that new broad signals appeared on the reaction NMR spectra from 3.9-4.65 ppm that corresponded to the α and β protons of the D-mannose functionalized into **PAH**, as it showed the typical broad signals corresponding to the coalescence present in polymers.

Due to the impossibility of calculating the integral value of the β protons a different approach was taken to calculate the loading efficiency of this reaction. The decrease in the signal intensity of the peaks that corresponded to the alcohol groups (-OH) of the free sugar found from 3.25-3.90 were used as an alternative way of calculating the loading efficiency of this reaction. It could be observed that there was a correlation between the depletion of the free sugars in solution with the functionalization efficiency of the reaction, the more sugars that got loaded into the polymer the less intensity of the signal corresponding to the alcohols groups of the free sugar that could be monitored via NMR (**Figure 2.12**) from 3.25-3.90 ppm. The peak intensity of the alcohol groups on the reaction sample (**Figure 2.12**) was calculated then divided by the intensity registered on the control NMR achieving a 52% ($1.48/2.83 \times 100$) of free sugars after the 24 h reaction, meaning that 48% of the initial one equivalent of D-mannose had reacted with the hydrazide handles successfully functionalizing **PAH**.

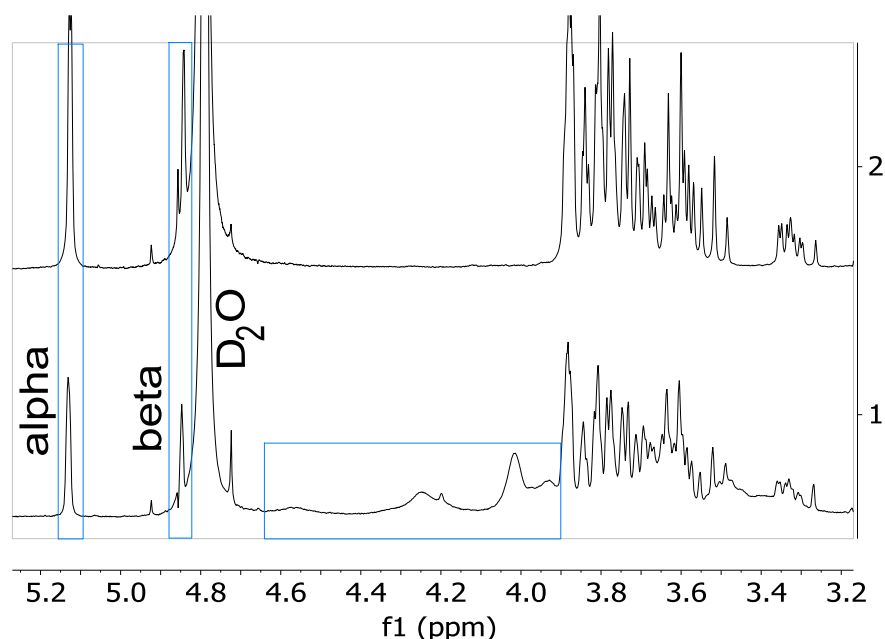


Figure 2.13: Stacked ^1H NMR spectra of PAH functionalization with D-mannose. (Top) spectra corresponds to the D-mannose control sample. (Bottom) corresponds to the reaction sample of PAH with D-mannose spectra.

The results obtained by the functionalization of **PAH** with both sugars were lower than expected. Bertozzi¹⁶⁰ reported a loading efficiency of D-glucose and D-mannose of 83 and 78% respectively when functionalizing **PAH** with 1.1 equivalents of carbohydrates. Efforts trying to replicate such high level loading efficiencies were unsuccessful when functionalizing with 1.0 equivalent of carbohydrates, obtaining 42 and 48% of loading efficiency with D-glucose and D-mannose, respectively.

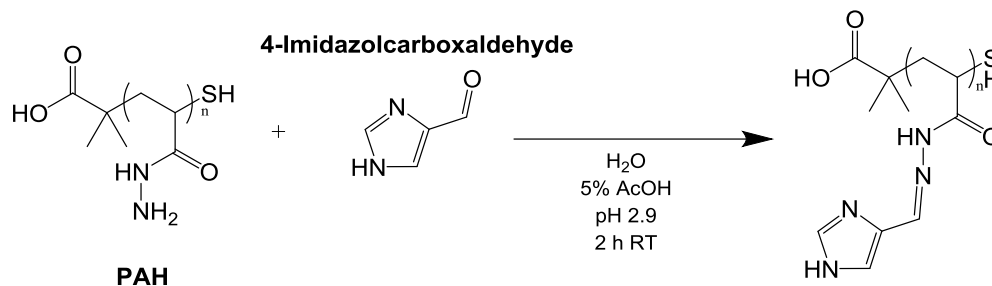
Although a high level of functionalization could not be achieved the results were deemed positive as the loading process with carbohydrates left over 50% of **PAH** handles free to be co-functionalized by aldehydes, which was the main objective of this section.

The next step of this section was to test the loading efficiency of **PAH** with 1 equivalent of 4-imidazolecarboxaldehyde, and 2-amino-3-formylpyridine; these two aldehydes were chosen as they are soluble in aqueous acidic conditions and would be suitable to continue with the co-functionalization of **PAH** functionalized with carbohydrates without changing solvent conditions.

It was decided to test the loading efficiency of **PAH** individually with these model aldehydes before continuing with the co-functionalization efforts.

4-Imidazolecarboxaldehyde functionalization

A modified version (**Scheme 2.15**) of the functionalization reaction used by Crisan et al.¹⁶¹ was used for this reaction. Mixing one 1:1 equivalents of aldehyde and **PAH** to a final concentration of 250 mM dissolved in 5% of AcOH in D_2O , and was let to react for 2 h at room temperature while stirring. The reaction was characterized by ^1H NMR when finished.



Scheme 2.15: PAH functionalization with 4-imidazolecarboxaldehyde.

The proton environment (**Figure 2.14**) shown for 4-imidazolecarboxaldehyde was composed of a single peak at 9.57 ppm corresponding with the free aldehyde group, and two -CH protons whose signals are spread from 6.0-8.5 ppm because 4-imidazolecarboxaldehyde is able to tautomerize. -NH protons are not visible on ^1H NMRs when D_2O is used as a solvent because they exchange their protons with the solvent's deuterium making them invisible in the spectra.

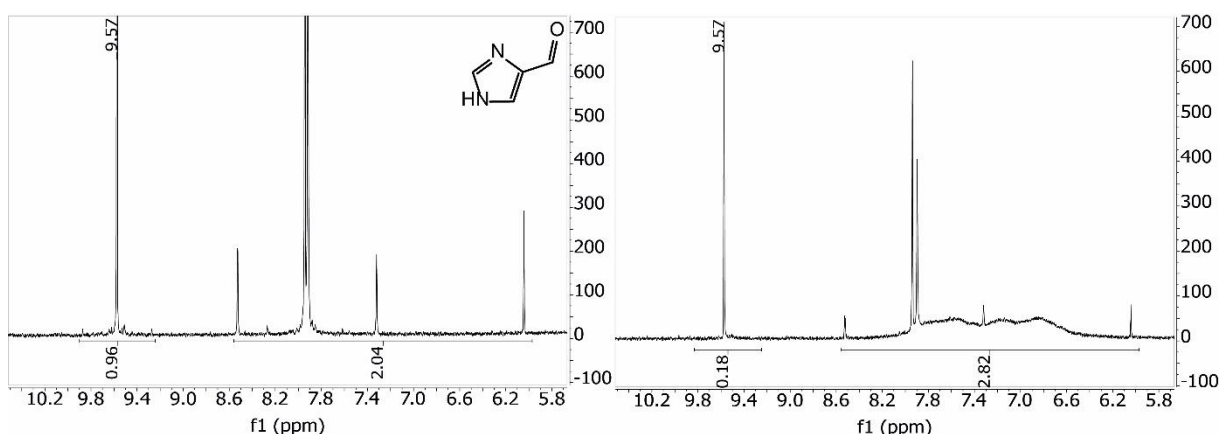


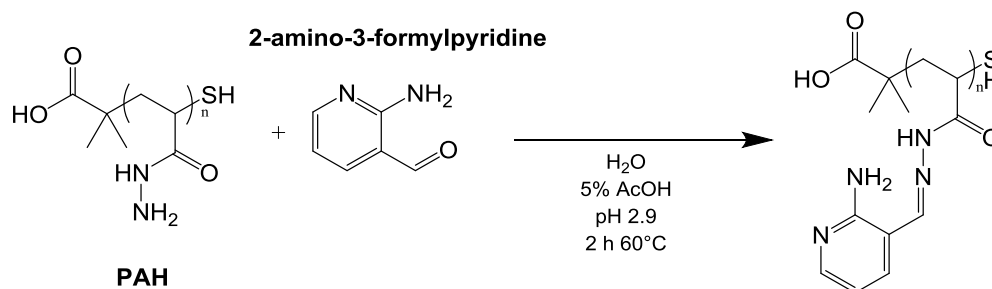
Figure 2.14: PAH functionalization with 4-imidazolecarboxaldehyde after 24 h. (Left) ^1H NMR in D_2O corresponding to 4-imidazolecarboxaldehyde control of the reaction. (Right) ^1H NMR in D_2O corresponding to the reaction of PAH with 4-imidazolecarboxaldehyde.

The generation of a new group of broad signals from 6.6-8.0 ppm could be observed on the reaction spectra (**Figure 2.14**) that was accompanied with a decrease on the integral intensity of the peak corresponding to the free aldehyde at 9.57 ppm when compared to the control reaction, these changes in the spectra were in agreement with the results reported by Crisan et al.¹⁶¹ and therefore confirmed the successful functionalization of **PAH** with 4-imidazolecarboxaldehyde. To calculate the efficiency of this reaction a total of 3 protons were assigned to the integrated regions corresponding to the aldehyde peak at 9.57 ppm and the regions corresponding to the two -CH protons from 6.0-8.5 ppm.

The aldehyde peak is representative of how much unreacted free aldehyde is in the sample with **PAH**, so it could be used calculate that the 82% $([1-0.18]*100)$ of the equivalent used in the reaction had been successfully loaded into the polymer.

2-amino-3-formylpyridine functionalization

For this reaction (**Scheme 2.16**) one equivalent of 2-amino-3-formylpyridine was mixed with one of **PAH** at a final concentration of 250 mM for 2 h at 60°C using H₂O with 5% of AcOH in D₂O as the reaction solvent. A higher temperature during the functionalization process was necessary as 250 mM of this aldehyde was insoluble at RT on these reaction conditions.



Scheme 2.16: PAH functionalization with 2-amino-3-formylpyridine.

The ¹H NMR spectra (**Figure 2.15**) corresponding to 2-amino-3-formylpyridine were composed of the signals corresponding to the proton of the aldehyde peak found at 9.74 ppm followed by three peaks from 6.9-8.2 ppm corresponding to the protons of the -CH groups of the molecule. When comparing between the control and the reaction spectra it could be observed a decrease in the intensity of the free aldehyde peak observed at 9.75 ppm, and the creation of a group of new broad signals at 5.8-8.8 ppm, these changes in the reaction spectra are in agreement with the previous functionalization experiments and therefore indicated that the functionalization reaction with the aldehyde had been successful.

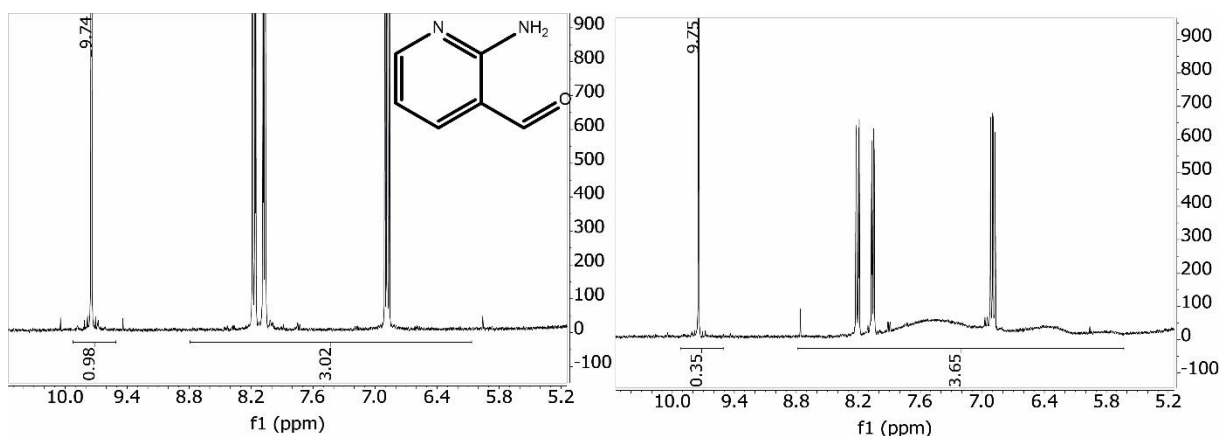


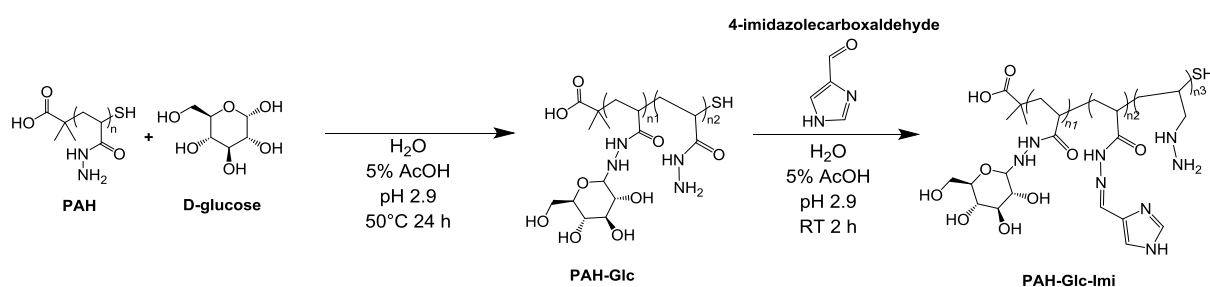
Figure 2.15: PAH functionalization with 2-amino-3-formylpyridine after 24 h. (Left) ¹H NMR in D₂O corresponding to 2-amino-3-formylpyridine control of the reaction. (Right) ¹H NMR in D₂O corresponding to the reaction of PAH with 2-amino-3-formylpyridine.

To calculate the loading efficiency of the reaction a total of four protons were assigned to all the integrated peaks; the free aldehyde peak signal at 9.75 must have a value of 1 proton and any decrease in the signal means that there had been a functionalization of **PAH** equal to the difference, by that account a 65% of the initial free aldehyde equivalent used in the reaction was functionalized onto **PAH**.

These experiments successfully showed that a high level of functionalization was possible when loading **PAH** with one equivalent of aldehyde under aqueous acidic conditions. Having demonstrated the loading efficiency of **PAH** when functionalized individually with aldehydes and carbohydrates it was decided to continue testing the loading efficiency of the polymer backbone with both carbohydrates and sugars.

D-glucose + 4-imidazolecarboxaldehyde co-functionalization

The co-functionalization of **PAH** was performed in two steps (**Scheme 2.17**), first **PAH** was reacted with D-glucose in a 1:1 ratio for 24 h following the protocol previously used to a final concentration of 250 mM, then followed with the mixing of one equivalent of **PAH-Glc** with one equivalent of 4-imidazolecarboxaldehyde to a final concentration of 125 mM, then was let to react for 2 h at RT.



Scheme 2.17: PAH co-functionalization reaction with D-glucose and 4-imidazolecarboxaldehyde.

The first step of the functionalization with the carbohydrate obtained similar results as previously reported, with a ~40% D-glucose loading efficiency, then followed with the functionalization with the aldehyde that obtained a loading efficiency of ~40%. When monitoring the co-functionalization reaction sample by ^1H NMR (**Figure 2.16**) the generation of new broad signals that corresponded with the functionalization of D-glucose and 4-imidazolecarboxaldehyde into **PAH** could be observed, these changes in the proton environment of the co-functionalized spectrum are in agreement with the changes in proton environments reported when mono-functionalizing **PAH** with aldehydes or carbohydrates, confirming that the co-functionalization of **PAH** with both aldehydes and carbohydrates is possible.

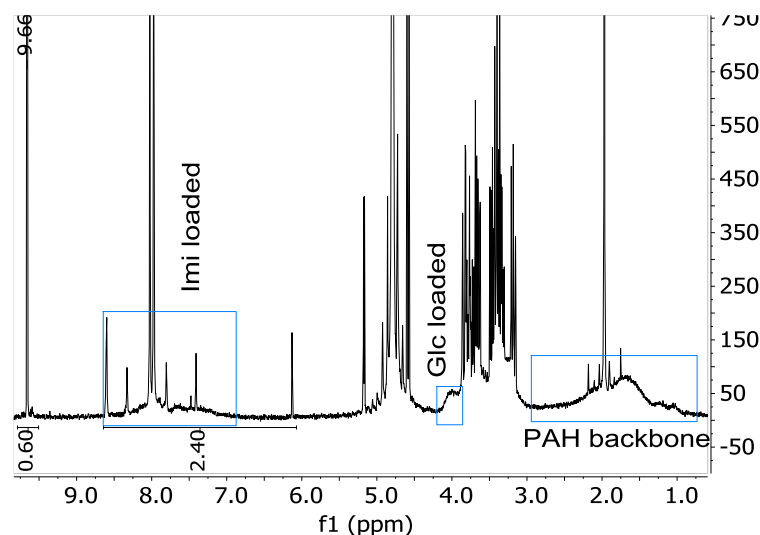
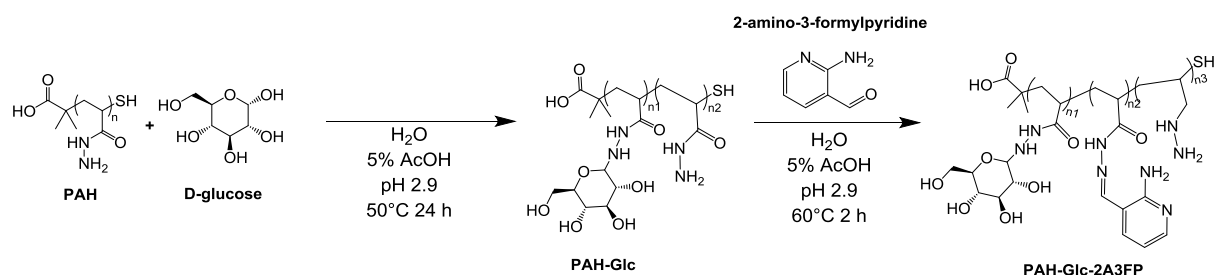


Figure 2.16: ^1H NMR in D_2O of PAH co-functionalization with D-glucose and 4-imidazolecarboxaldehyde.

D-glucose + 2-amino-3-formylpyridine co-functionalization

A functionalization reaction of **PAH** in two steps (**Scheme 2.18**) was performed to obtain a co-functionalized product at a final concentration of 125 mM.



Scheme 2.18: PAH co-functionalization reaction with D-glucose and 2-amino-3-formylpyridine.

The first step of the functionalization with the carbohydrate gave a ~40% of D-glucose loading efficiency as previously reported, then the second step reported a loading efficiency of ~33%. The characterization by ^1H NMR (**Figure 2.17**) showed the typical broad signals consistent with the loading of D-glucose and 2-amino-3-formylpyridine into **PAH**, that we could observe in the previous mono-functionalizations and that are in agreement with a successful co-functionalization reaction of **PAH**.

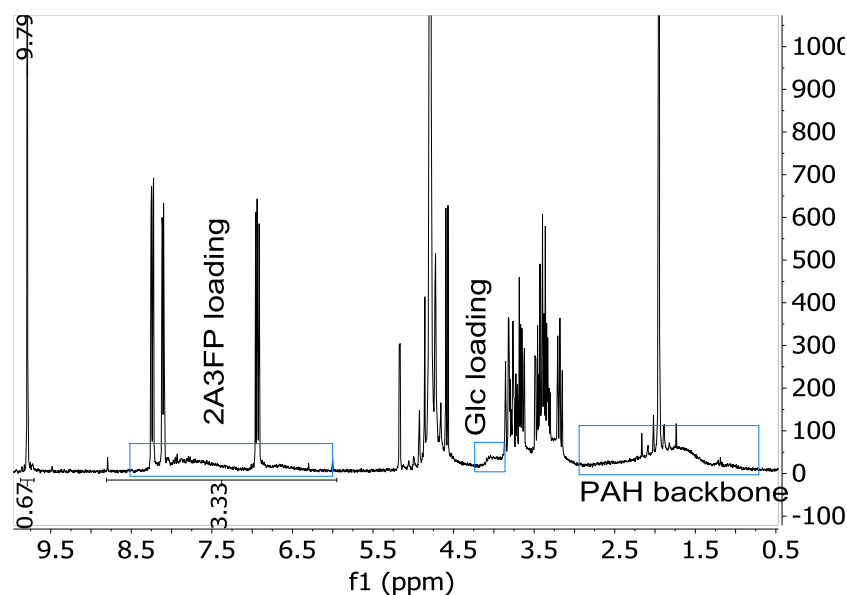
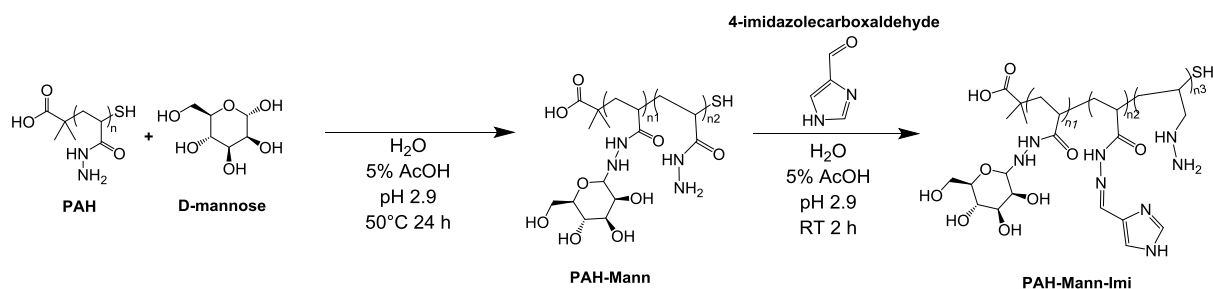


Figure 2.17: ^1H NMR in D_2O of PAH co-functionalization with D-glucose and 2-amino-3-formylpyridine.

D-mannose + 4-imidazolecarboxaldehyde co-functionalization

A co-functionalization reaction in two steps (**Scheme 2.19**) was performed. The first step reported a D-mannose loading of $\sim 40\%$, while the second step was of $\sim 40\%$ of 4-imidazolecarboxaldehyde functionalization.



Scheme 2.19: PAH co-functionalization reaction with D-mannose and 4-imidazolecarboxaldehyde.

The ^1H NMR spectra of the finished reaction (**Figure 2.18**) showed the signals corresponding to a successful co-functionalization of the sugar and the aldehyde, in agreement with the data previously reported.

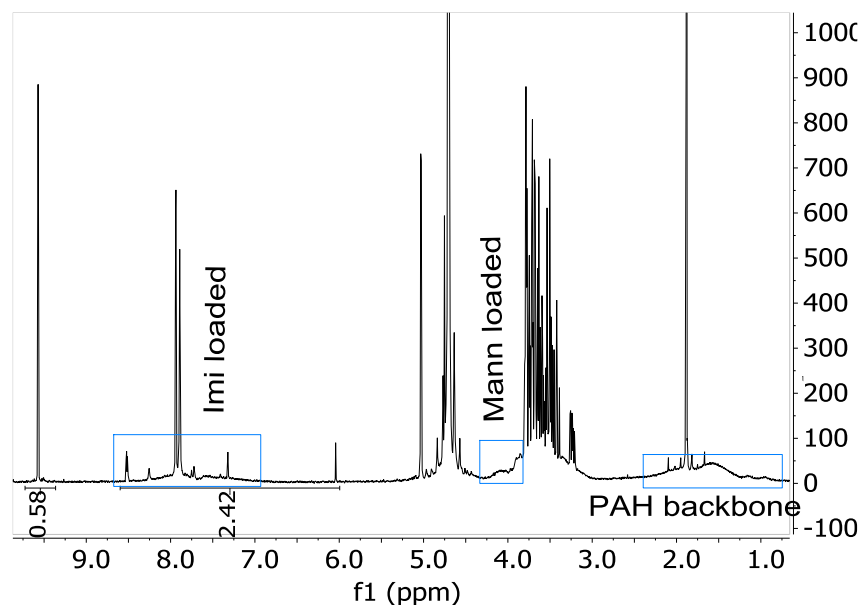
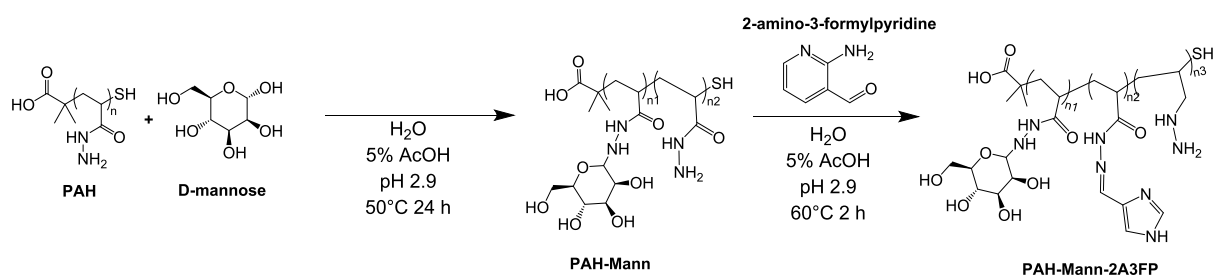


Figure 2.18: ^1H NMR in D_2O of PAH co-functionalization with D-mannose and 4-imidazolecarboxaldehyde.

Mannose + 2-amino-3-formylpyridine co-functionalization

The reaction in two steps (**Scheme 2.20**) reported a loading efficiency of ~40% of the initial equivalent of D-mannose, and ~40% of the initial equivalent of 2-amino-3-formylpyridine.



Scheme 2.20: PAH co-functionalization reaction with D-mannose and 2-amino-3-formylpyridine.

The ^1H NMR spectra of the finished reaction (**Figure 2.19**) showed the groups of broad signals corresponding to successful co-functionalization of the sugar and the aldehyde into the handles of **PAH**.

The results obtained from the co-functionalization experiments reported in this section demonstrated that **PAH** could be successfully co-functionalize with both carbohydrates and aldehydes in a two-step reaction under the aqueous acidic conditions of the 5% acetic acid buffer. The first functionalization reaction with carbohydrates gave ~40% of loading efficiency, and was in agreement with the experiments previously reported when testing mono-functionalizations with carbohydrates; the second step of the co-functionalization process with aldehydes provided a lower loading efficiency compared to what was previously reported when testing aldehydes mono-functionalizations (~80% for 4-imidazolecarboxaldehyde, and ~70% with 2-amino-3-formylpyridine).

The loading efficiency obtained was of ~40% when co-functionalizing with 4-imidazolecarboxaldehyde, and ~30% when loaded with 2-amino-3-formylpyridine, these results were not the expected, as it was anticipated that a full loading of the remaining 60% available hydrazide handles that were not functionalized by the first carbohydrate step was possible. The inability to achieve a full loading of the remaining polymer handles when co-functionalizing could be explained due to increasing steric hindrance as more handles are functionalized, or a the need for a higher equivalency of aldehydes used in the reaction setup to push the equilibrium of the system to achieve full conversion.

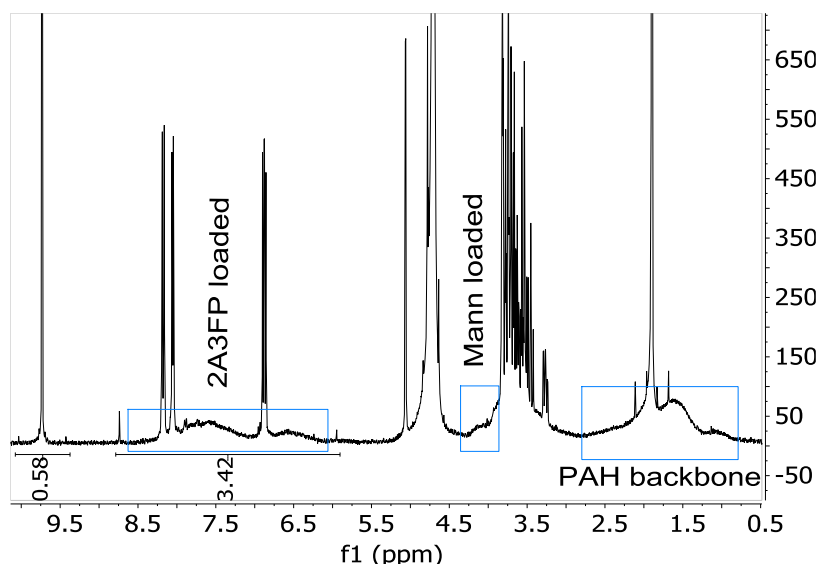


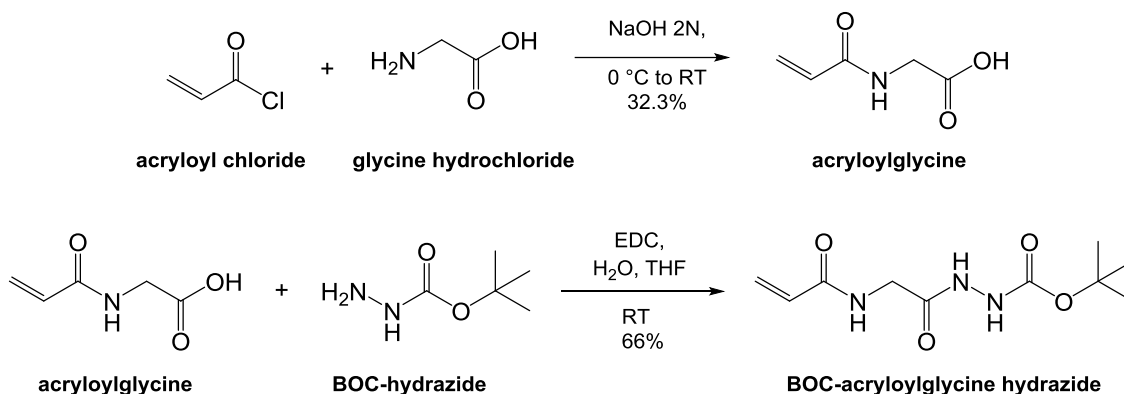
Figure 2.19: ¹H NMR in D₂O of PAH co-functionalization with D-mannose and 2-amino-3-formylpyridine.

Overall, the co-functionalization efficiency of the reactions achieved a ~80% (~40% carbohydrates, ~33-40% aldehydes) of **PAH** hydrazides handles loaded.

These results were considered a success as they proved that an efficient co-functionalization method in two-step reactions without the need of further purification with a high rate of loading efficiency was possible to co-functionalize **PAH**.

2.3.3 Synthesis, characterization, and functionalization of poly(acryloylglycine hydrazide)

To obtain the BOC-acryloylglycine hydrazide monomer it was decided to perform a two-step synthesis (**Scheme 2.21**). The first step comprised the synthesis and purification of acryloylglycine^{164, 165} through the acylation of glycine hydrochloride with acryloyl chloride; the second step was the coupling¹⁶¹ of the protected hydrazide *tert*-butyl carbazate (BOC-hydrazide) to the carboxylic acid of acryloylglycine to obtain BOC-acryloylglycine hydrazide.



Scheme 2.21: BOC-acryloylglycine hydrazide synthetic route.

2.3.3.1 Synthesis and characterization of acryloylglycine

For this step acryloyl chloride was added dropwise to a solution of glycine hydrochloride in NaOH 2N at 0 °C and saturated with NaCl. A white crystal was obtained after its purification by filtering and phase separation achieving 32.3% yield.

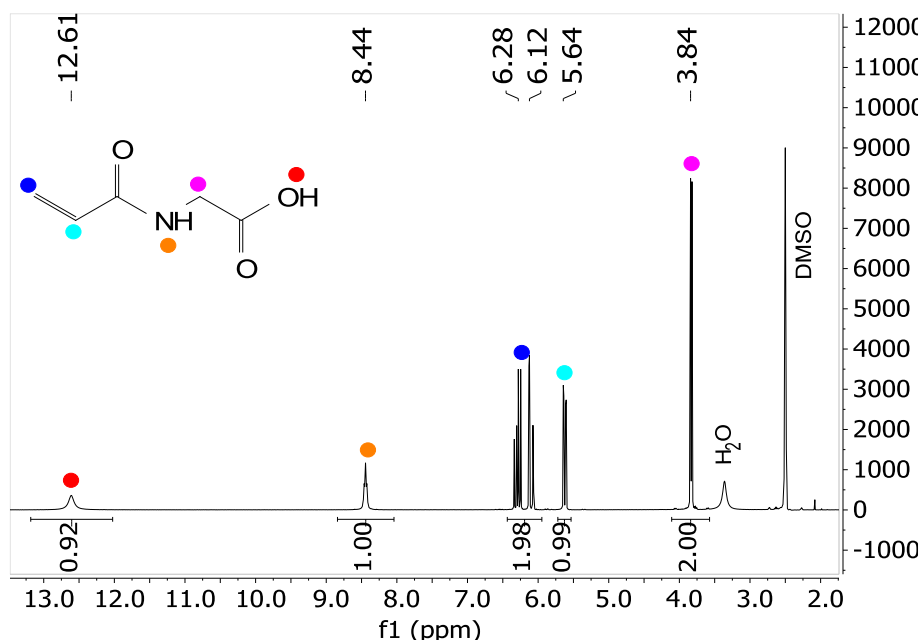


Figure 2.20: ¹H NMR of acryloylglycine in DMSO-*d*₆.

The product was characterized by ¹H NMR in DMSO-*d*₆, this technique allowed to analyse the proton environments of the product and its integration value so the signals that corresponded with the expected result could be checked and characterized to confirm that the desired product was obtained.

The proton environments (**Figure 2.20**) of the purified product consisted in a hydroxide, an amine, three alkenes, and one methylene. This was in agreement with the predicted shift and reported literature¹⁶⁵.

2.3.3.2 Synthesis and characterization of BOC-acryloylglycine

For the second step of the synthesis route BOC-hydrazide was reacted with acryloylglycine activated with 1-ethyl-3-(3-dimethylaminopropyl)carbodiimide (**EDC**) in a 1:2 mixture of water and THF due to the poor solubility of the BOC-hydrazide in water. This coupling reaction^{161, 166} generated an unknown yellow impurity that persisted until filtering and phase separation by solvent affinity. A recrystallization step was added after work-up to obtain an off-white powder achieving 66% yield.

This was the first report of BOC-acryloylglycine hydrazide, and hence a full characterization was needed to confirm that the desired product had been obtained.

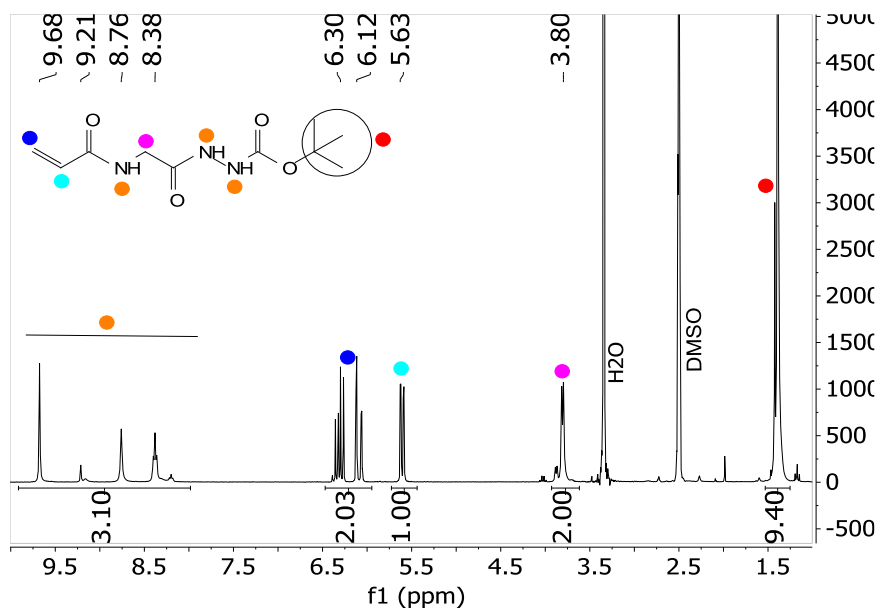


Figure 2.21: ¹H NMR of BOC-acryloylglycine hydrazide in DMSO-*d*₆.

The isolated product was analysed by ¹H NMR spectroscopy in DMSO-*d*₆ showing its proton environments (**Figure 2.21**) consisting of: an amide, a hydrazide, three alkenes, one methylene, and one alkyl. The integration values of these signals were in agreement with the results expected from the synthesis of BOC-acryloylglycine hydrazide

Further analysis of the NMR spectrum showed the presence of splitting on the signals corresponding to the amide, hydrazide, methylene and alkyl regions. An explanation for this signal splitting behaviour could be that all these signals were in fact rotamers due to these bonds being able to show cis/trans isomerism¹⁶⁷, as their integration values corresponded with the predicted integration values of the functional group of the monomer molecule and not with some reaction impurity. This was a behaviour that was previously observed when working with **PAH** and that happened to be caused by rotamers.

Rotamers are the product of conformational isomerism where isomers can just be interconverted by rotations of single bonds¹⁶⁸. Due to the energy barrier to free rotation being too high these isomers may exist for a relatively long time. When analysed by NMR spectroscopy, molecules with rotamers will show a split in the peaks of the atoms able to rotate freely instead of a sharp peak. This split will distribute the integration value of the atom between the isomers. For example if we have an amine

and a hydrazide with three protons the total value of the integration value of their rotamer peaks should be three, as seen in **Figure 2.21**.

To confirm the presence of rotamers the sample was analysed by variable temperature ^1H NMR spectroscopy (**Figure 2.22**). This characterization method consists in a steady increase of temperature per ^1H NMR analysis. This increase is aimed to also decrease the energy barrier of the system, making it easier for the free rotation of the bonds, diminishing the half-life of rotamers until the set of split peaks merge into a single signal. The experiment is then followed by a couple of ^1H NMR at lower temperatures until RT to check that the integrity of the molecule was not compromised during the experiment.

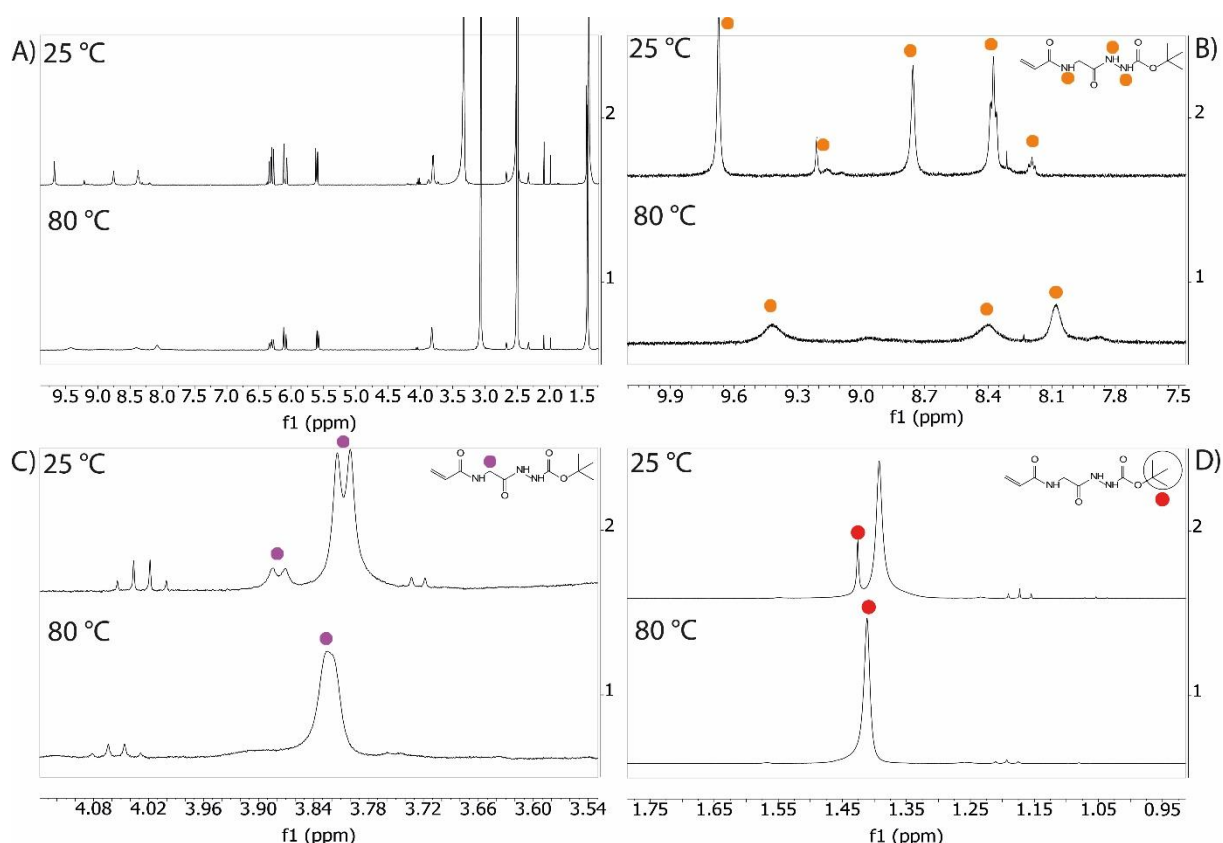


Figure 2.22: Comparison of BOC-acryloylglycine hydrazide high temperature ^1H NMR in $\text{DMSO}-d_6$ spectra at 25 °C versus 80 °C. A) Complete spectra. B) Amide and hydrazide region. C) Methylene region. D) Alkyl region.

An analysis in detail of the ^1H NMR at 25 °C versus 80 °C (**Figure 2.22**) showed how the suspected signals corresponding to the amide and hydrazide (B), methylene (C), and alkyl (D) regions merged when the experiment temperature reached 80 °C, confirming that the split in their signals corresponded with the presence of rotamers and was not due to impurities or the synthesis of the wrong product.

The monomer was also characterized by ^{13}C NMR spectroscopy in $\text{DMSO}-d_6$, this technique allowed to visualize the sample's carbon environment (**Figure 2.23**). When the spectrum was monitored it showed an environment composed of three carbonyls at 155.19, 164.81 and 168.55 ppm; two alkenes at

125.49 and 131.50 ppm; and three alkanes at 28.05, 40.25 and 79.15 ppm. This spectrum was in agreement with the predicted results of the synthesis of BOC-acryloylglycine hydrazide.

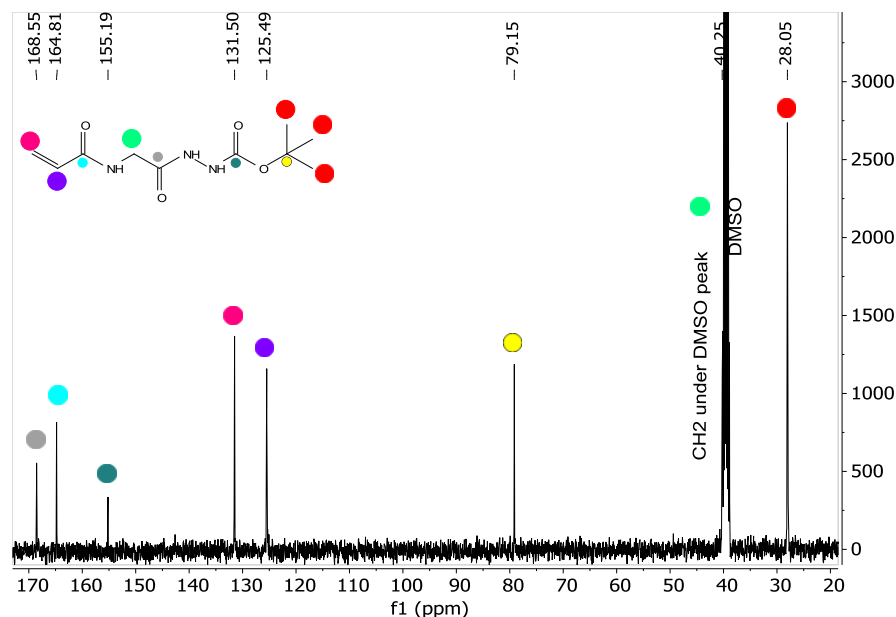


Figure 2.23: ^{13}C NMR in $\text{DMSO-}d_6$ spectra of BOC-acryloylglycine hydrazide

Electrospray ionization mass spectrometry (ESI-MS) was used to characterize the molecular weight of the monomer sample (**Figure 2.24**). The highest intensity peak of the spectrum observed at $m/z=266.12$ could be identified as corresponding to the molecular ion peak of BOC-acryloylglycine hydrazide plus sodium [$M=243+\text{Na}^+=23$]; Na^+ is a common contaminant on MS as it is prevalent even in clean glassware and MS grade solvents. The analysis also showed the presence of signals that corresponded with molecular weights lower and higher than the monomer, one of these peaks corresponded with the Mw of a dimer plus Na^+ at $m/z=509.23$.

It was suspected that the monomer sample could be reactive in the gas phase and be susceptible to form higher molecular weight ions via fragmentations and recombination, hence the presence of peaks of lower and higher molecular weight in the ESI-MS spectrum.

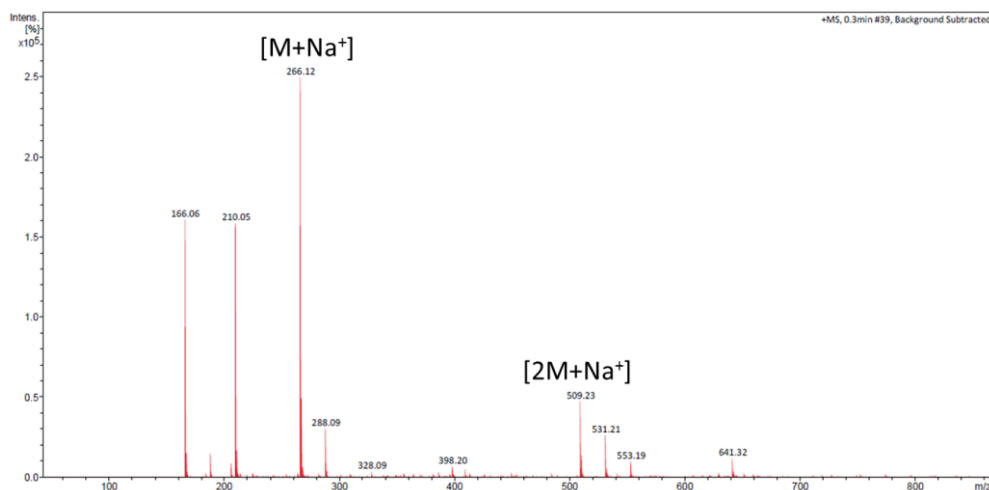


Figure 2.24: ESI MS spectrum showing the molecular peak of BOC-acryloylglycine hydrazide plus sodium at $m/z=266.12$.

IR spectroscopy (**Figure 2.25**) of the sample showed N-H stretch at $\sim 3246\text{ cm}^{-1}$, $\text{sp}^2\text{ C-H}_2$ stretch at $\sim 3000\text{ cm}^{-1}$ corresponding to the vinyl group, and three C=O stretches between $1647\text{--}1741\text{ cm}^{-1}$ corresponding to the three carbonyl presents in our molecule. This data was in agreement with the expected results.

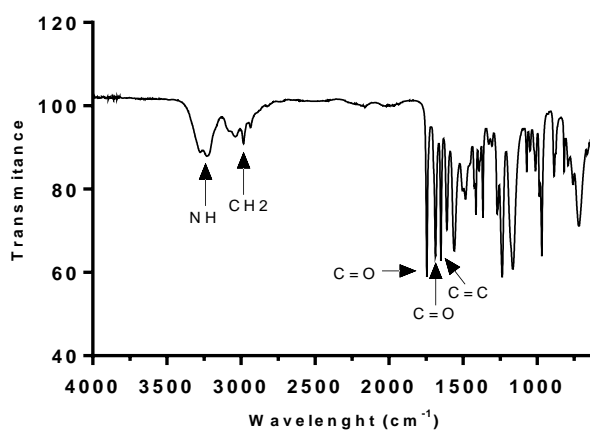
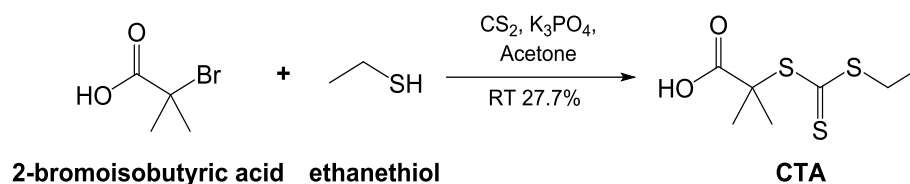


Figure 2.25: IR spectroscopy of BOC-acryloylglycine.

2.3.3.3 Polymerization study and characterization of poly(acryloylglycine hydrazide)

To continue with the polymerization of the monomer a suitable chain transfer agent able to polymerize acrylamides had to be chosen. 2-(ethylthiocarbonothioylthio)-2-methylpropanoic acid was chosen as RAFT agent, this molecule belongs to the family of trithiocarbamates, chain transfer agents that have proven their ability to run controlled polymerizations of acrylates^{161, 169}.

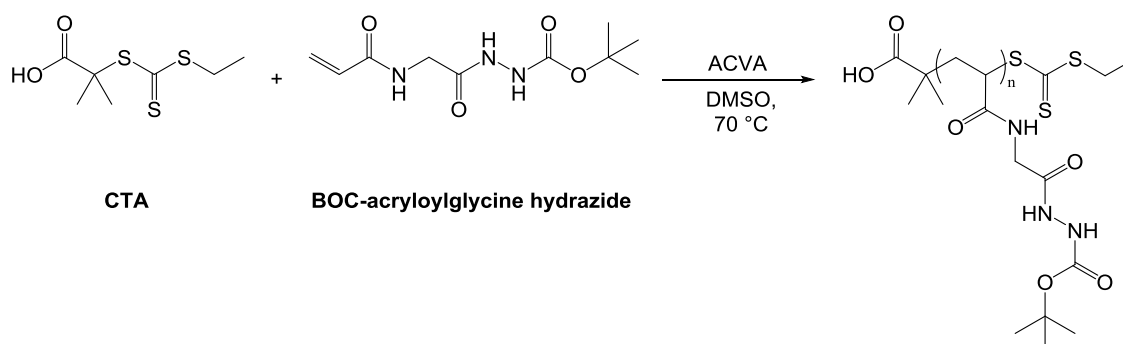
This **CTA** in particular had been previously used with success to polymerize **PAH**¹⁶¹ in our laboratory. This yellow compound was successfully synthesized following the reaction (**Scheme 2.22**) reported by Skey and O'Reilly¹⁷⁰.



Scheme 2.22: Synthesis route of 2-(ethylthiocarbonothioylthio)-2-methylpropanoic acid, the CTA chosen to perform RAFT polymerization of BOC-acryloylglycinehydrazide.

The next step once a functional synthetic route for the monomer was achieved was to decide the conditions suitable to perform the controlled polymerization. The reaction needed a solvent able to dissolve the monomer, a **CTA**, and an initiator ACVA. The BOC group makes the monomer insoluble in water, so it was decided that DMSO would be a suitable solvent as its boiling point of 189 °C is above the fragmentation temperatures of most initiators (ACVA decomposes at 70 °C) used for degenerative transfer radical polymerization processes such as RAFT and the monomer is soluble in it to a concentration of 1.25 M that allows for good kinetic consumption and conversions.

Having chosen the appropriate reaction conditions, the next step of the research was to carry on with the study of the polymerization (**Scheme 2.23**) of BOC-acryloylglycine hydrazide in DMSO.



Scheme 2.23: Proposed polymerization conditions of BOC-acryloylglycine hydrazide in DMSO.

The aim of this section was to elucidate the most favourable reaction conditions to obtain polymers of different molecular weights. To achieve this goal a series of kinetics experiments were carried changing the ratios between monomer, CTA, and initiator (M/CTA/ACVA). Samples of these polymerizations were taken at different times to monitor the monomer conversion by ^1H NMR spectroscopy and perform kinetics studies.

Syringic acid was used as integration standard to be able to compare conversion at different time points during the reaction (**Figure 2.26**); to do so the aromatic proton signals from the syringic acid found at 7.16 ppm were integrated and assigned a value of 1 proton then used to normalize the signals from the vinyl protons from the monomer found at 6.26, 6.07 and 5.58 and compared against a sample taken at t_0 . Part of these aliquots were also used to analyse the \bar{M}_n and \bar{M}_w of the polymerization over time.

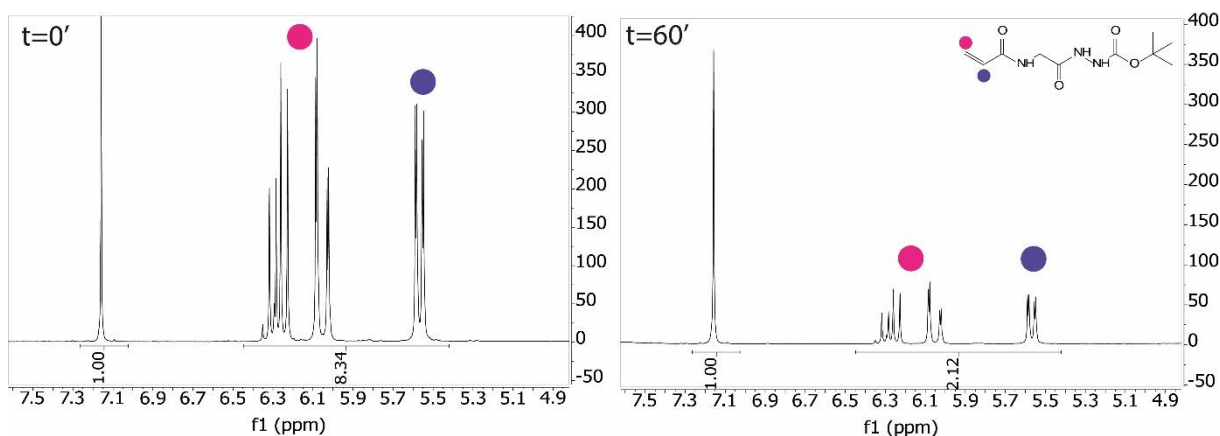


Figure 2.26: ^1H NMR of samples taken at t_0 (left) and t_{60} (right) from a polymerization of BOC-acryloylglycine hydrazide with CTA in $\text{DMSO}-d_6$ at 70°C using ACVA as radical initiator. Syringic acid was added to each sample prior analysis as integration standard, the integration of the monomer vinyl signals at 6.26, 6.07 and 5.58 were normalized against the integration value of the aromatic signal of syringic acid at 7.16, and were compared between samples to calculate its conversion percentage.

One of the most important properties when characterizing a polymer is determining properly its molecular weight.

The theoretical molecular weight ($\bar{M}_{n_{th}}$) can be compared with that obtained experimentally to measure if the polymerization was successful or not. All synthetic polymers are polydisperse due to the presence of chains of different lengths in any given sample, making it impossible to give a single value for the molecular weight, as the polymer usually exists as a Gauss distribution of polymer species of different chain lengths and molecular weights.

Characterization techniques like GPC (Gel Permeation Chromatography) are very important in polymer chemistry because they allow to analyse all the polymer species present in a sample and quantify their mass and number. Once the sample is analysed by GPC a statistical treatment of the data provided by the equipment can be performed to obtain \bar{M}_n and \bar{M}_w . \bar{M}_n (**Equation 2.4**) is defined as the statistical average molecular weight of all the polymer chains in a sample.

$$\bar{M}_n = \frac{\sum N_i M_i}{\sum N_i}$$

Equation 2.4: \bar{M}_n is the polymer average molecular weight of a polymer formula. M_i is the molecular weight of a chain and N_i is the number of chains of that molecular weight.

Mw (**Equation 2.5**) is the weight average molecular weight, and takes into account the molecular weight of a polymer species to determine its contribution to the molecular weight average. The higher the mass of a chain the bigger the contribution to Mw.

$$M_w = \frac{\sum N_i M_i^2}{\sum N_i M_i}$$

Equation 2.5: Mw is the weight average molecular weight of a polymer formula. M_i is the molecular weight of a chain and N_i is the number of chains of that molecular weight.

M_n and M_w allow to better understand the mass distribution of polymerizations, and can also be used to calculate (**Equation 2.6**) the dispersity (\mathcal{D}) of the species presents in a polymer sample. The larger \mathcal{D} is, the broader is the distribution of molecular weights of a polymer. A monodisperse polymer of $\mathcal{D}=1$ will have only one species of polymer, all with the same molecular weight and chain length. To put this in perspective, the best synthetic polymers used for GPC calibration have a $\mathcal{D}=1.02-1.10$.

$$\mathcal{D} = \frac{M_w}{M_n}$$

Equation 2.6: Dispersity (\mathcal{D}) index of a polymer sample

All the polymerization reactions were performed at 70°C with a $[M]=1.25$ M and then modified the ratios of M/CTA/ACVA to perform kinetic studies characterized by ^1H NMR, and molecular weight distributions characterized by GPC.

The study of BOC-acryloylglycine hydrazide polymerization began with the synthesis of polymers of projected DP_{50} , with a M/CTA/ACVA ratio of 100/2/0.4.

This configuration had worked successfully in the past to obtain **PAH**¹⁶¹ of good dispersities and projected molecular weight, and it will be useful to compare loading efficiencies between chains that were polymerized in the same conditions. An analysis of the kinetic performance of this polymerization (**A-B, Figure 2.27**) showed a decrease in the linear progression of the monomer conversion, reaching a plateau on the polymerization reaction at $t=45'$ with a monomer consumption of 93%.

The polymerization barely progressed during the next 3 h until reaching 95% of maximum monomer conversion at $t=180'$. This behaviour might be due to the increase of termination events in growing chains during the experiment until the progression of the polymerization is halted.

A new polymerization of projected DP_{50} following a ratio of 100/2/0.2 was performed.

This decrease in the initiator concentration was chosen to check if a slower polymerization reaction would decrease the occurrence of termination events and achieve a higher monomer conversion than the previous DP_{50} performed at 100/2/0.4. An analysis of the kinetic plot of the data (**A-B, Figure 2.27**) showed a linear progression of the polymerization until a plateau was reached at $t=150'$ with a monomer conversion of 90%; a decrease in the initiator ratio did not correct this behaviour, it just delayed it.

Samples from the polymerization experiments of projected DP₅₀ taken at different time points were analysed by GPC (**Figure 2.29**) and their Mn, Mn_{th} and Đ versus conversion were plotted (**Figure 2.28**) to monitor its behaviour. The analysis of the data showed a linear correlation between the monomer conversion and the increase of the polymer molecular weight Mn for both DP₅₀ polymers. The accuracy of the polymerizations could be tested comparing the characterized Mn of both polymers with their theoretical molecular weight over time. DP₅₀ 100/2/0.4 with a maximum conversion of 95% and 47.8 subunits had a theoretical molecular weight of 9748 g/mol while the experimental Mn calculated by GPC analysis was of 9174 g/mol. DP₅₀ 100/2/0.2 with a maximum conversion of 93.5% and 46.5 subunits had a theoretical molecular weight of 9539 g/mol and an experimental Mn calculated by GPC analysis of 8239 g/mol. Both polymers final Mn were close to their theoretical molecular weight, DP₅₀ 100/2/0.4 presented a Đ=1.22 while DP₅₀ 100/2/0.2 that had bigger disparity between Mn and its theoretical molecular weight and presented a Đ=1.30.

The next step was to test the capacity of the monomer to polymerize into DP₁₀₀ polymers, following a M/CTA/ACVA ratio of 100/1/0.4.

The kinetic study of this reaction (**C-D, Figure 2.27**) showed the same phenomena that was experienced with the DP₅₀ polymers. The polymerization began with a linear progression of monomer consumption until t=30' when the polymerization achieved a monomer conversion of 90% reaching a plateau, and slowly progressed to a maximum monomer conversion of 97% 3 h later (t=180').

It was decided to test how a decrease in the initiator concentration following a ratio of 100/1/0.2 would affect the polymerization of projected DP₁₀₀ reactions. The kinetic study (**C-D, Figure 2.27**) showed a linear consumption of monomer until the reaction reached a plateau at t=90' with a monomer conversion of 77%, the reaction continued until t=240' achieving a final monomer conversion of 89%.

The DP₁₀₀ polymerizations samples were analysed by GPC (**Figure 2.29**) and their Mn, Mn_{th} and Đ versus conversion was plotted (**Figure 2.28**). This data showed a linear correlation between the polymers molecular weight Mn and the increase in monomer conversion, and also a wide discrepancy between the experimental Mn and their theoretical molecular weight that was not observed during the polymerization of projected DP₅₀ **PAGH**. The theoretical molecular weight of DP₁₀₀ 100/1/0.4 with a maximum conversion of 97% and 97 subunits was of 19631 g/mol, while its calculated experimental Mn was of 15108 g/mol. This discrepancy seems to be due to a higher Đ=1.30 as the average molecular weight (Mn) of the polymerization gets a wider distribution; using Mw that accounts for the contribution of heavier chains to the polymer sample provided a polymer weight of 19583 g/mol, that was closer to the theoretical molecular weight of this polymer. The theoretical molecular weight for DP₁₀₀ 100/1/0.2 with a maximum monomer conversion of 89% and 89 subunits was of 17997 g/mol, while its Mn was of 22715 g/mol, with a Mw of 29922 and a Đ=1.32. It seems that the distribution of this polymerization was shifted towards a higher contribution of heavier chains.

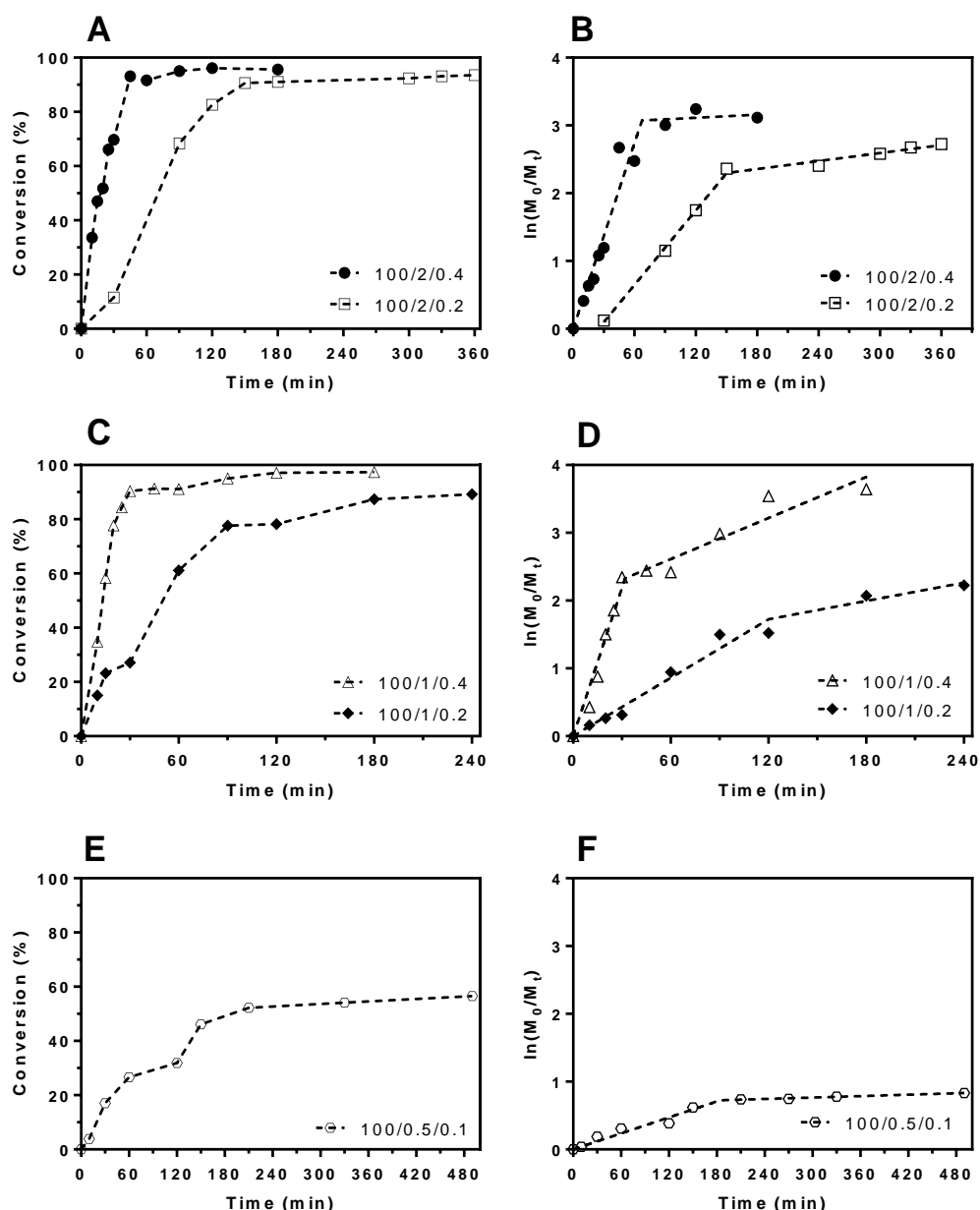


Figure 2.27: Graphical representation of BOC-acryloylglycine hydrazide kinetic studies (left column) and fractional concentration of monomer represented by $\ln(M_0/M_t)$ versus time (right column). A) DP_{50} kinetics. B) $DP_{50} \ln(M_0/M_t)$ versus time. C) DP_{100} kinetics. D) $DP_{100} \ln(M_0/M_t)$ versus time. E) DP_{200} kinetics. F) $DP_{200} \ln(M_0/M_t)$ versus time. Conditions for these experiments were: $[M]=1.25$ M, 70°C , $[\text{Monomer}]/[\text{CTA}]/[\text{ACVA}]$, and DMSO as solvent.

Finally, the capacity of the monomer to achieve polymerizations with a projected DP_{200} following a 100/0.5/0.1 ratio was tested.

The kinetic study of this reaction (E,F, **Figure 2.27**) showed a linear monomer consumption until a plateau was reached very early into the reaction at $t=210'$ with a monomer conversion of 52%, the reaction barely progressed until reaching 56% at $t=490'$.

When analysing the DP₂₀₀ sample by GPC (**Figure 2.28**, **Figure 2.29**) it could be observed that the reaction did not follow a linear progression between the monomer conversion and the increase in Mn like it did in previous DP₅₀ and DP₁₀₀ polymerizations. The theoretical molecular weight for DP₂₀₀ 100/0.5/0.1 with a maximum conversion of 56% and 112 subunits was of 22700 g/mol, while the experimental calculation done by GPC provided a Mn=15671 g/mol, a Mw=24826 g/mol, and a Đ=1.58. The average molecular weight of the sample (Mn) was far from the predicted weight due to the broad dispersity achieved during this polymerization.

Overall, RAFT polymerizations are expected to follow first order kinetics behaviour¹⁴⁹ with a linear trend of monomer consumption until full depletion. During the kinetics experiments (**Figure 2.27**) it could be observed how the polymerization rate initially followed first order kinetics behaviour, but shifted with a steep decline in monomer consumption that hindered the reaction speed and prevented full monomer conversion.

This behaviour happened as the reaction reaching a plateau after an initial linear growth. This phenomenon was previously reported in our laboratory by Crisan et al.¹⁶¹, and other members of the research group had dedicated efforts¹⁷¹ to elucidate successfully this behaviour. Crese et al.¹⁷¹ proved that the hydrazide of **BOC-PAH** (BOC-(poly acryloyl hydrazide)) can perform a nucleophilic attack on the **CTA** terminating its ability to be transferred between growing chains preventing further polymerization.

An increase in the occurrence of these termination events during the polymerization leads to the decline in monomer consumption to the point the reaction might be halted. Due to the similarities of structure in both polymers it is believed that this same behaviour happens (**Scheme 2.24**) during **BOC-PAGH** polymerizations, as the same **CTA** was used.

Creese et al.¹⁷¹ reported that the degradation of the **CTA** cannot be avoided, but the polymerizations conditions could be tweaked to outperform this undesirable behaviour when using low temperature initiators at 65 °C to obtain polymers of controlled Mn and Đ.

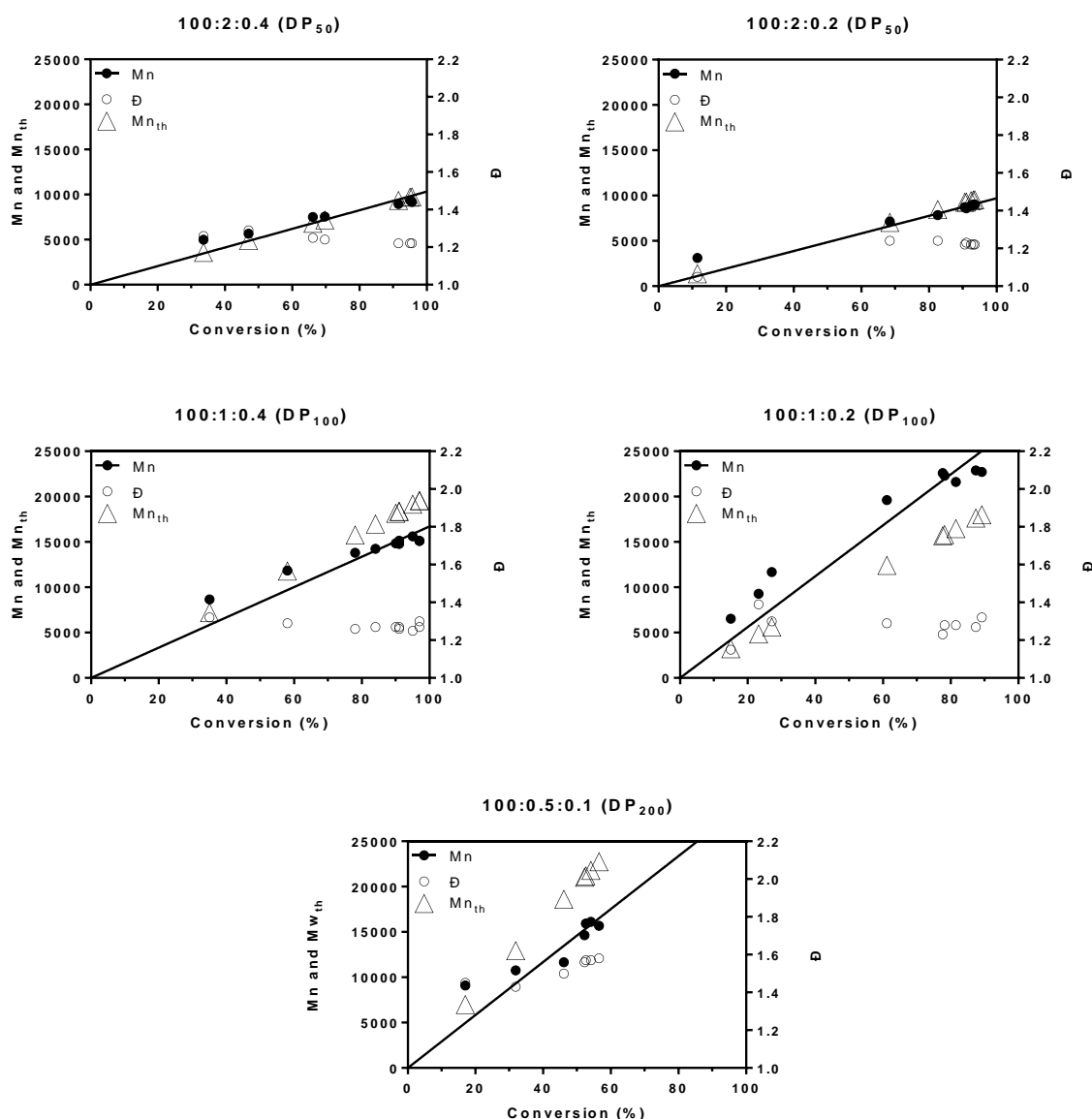


Figure 2.28: Graphic representation of M_n , $M_{n_{th}}$ and \bar{D} versus conversion of polymers of different projected DP. Conditions for these experiments were: $[M]=1.25$ M, 70°C , $[\text{Monomer}]/[\text{CTA}]/[\text{ACVA}]$, and DMSO as solvent. M_n and \bar{D} were calculated by GPC.

The GPC analysis (**Figure 2.29**) of the completed polymerization reactions confirmed that their samples molecular weight followed a Gaussian distribution. After a global analysis of the polymerizations characterizations by NMR and GPC (**Table 2.1**) it was concluded that it was possible to polymerize BOC-acrylylglycine hydrazide with good dispersities of polymers with projected DP_{50} and DP_{100} . A better control over the product of polymerizations of projected DP_{50} was achieved, with average molecular weights (M_n) closer to their predicted values ($M_{n_{th}}$), producing samples narrower distributions and therefore lower dispersities than for their DP_{100} counterparts. A decrease in the initiator ratio did not improve the dispersity and increased the reaction time in all polymerizations.

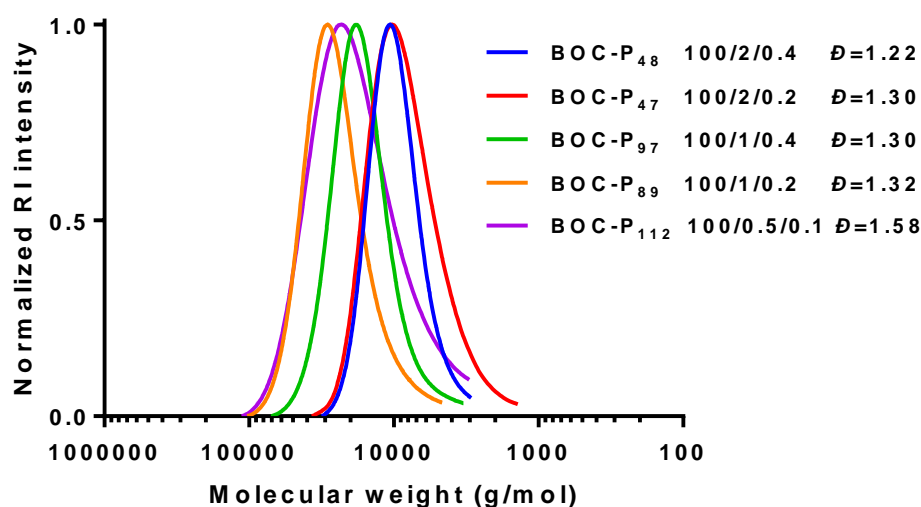
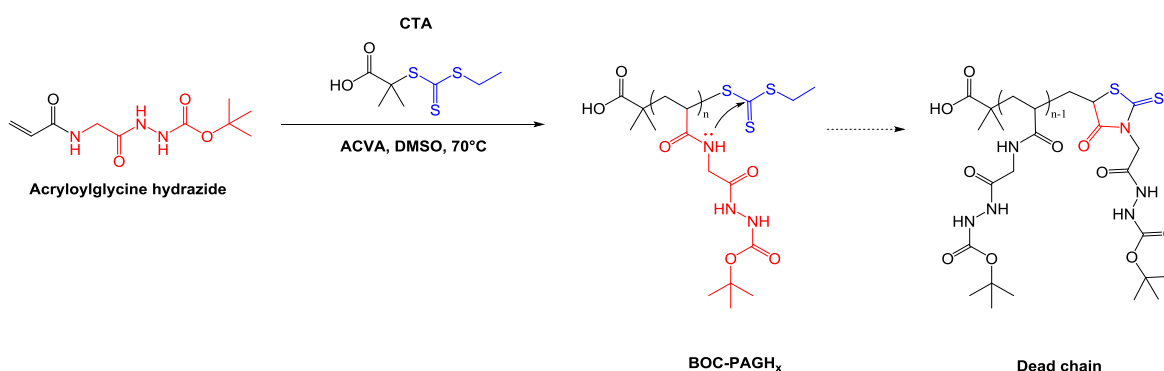


Figure 2.29: GPC chromatograms of BOC-P_x of different DPs.



Scheme 2.24: Adaptation to PAGH of the proposed CTA degradation by Creese et al.¹⁷¹ that leads to the termination events observed during the polymerization of the acryloylglycine hydrazide monomer.

In the case of DP₁₀₀ 100/1/0.2 it led to an increase in Mw and Mn, meaning that the distribution of the polymer was shifted towards species of bigger molecular weight than what was projected, hence the bigger Mw and Đ due to the higher contribution of these species to the overall polymer sample. The polymerization with intended DP₂₀₀ was considered a failure with the current conditions.

Longer projected DPs are expected to follow longer reaction times, increasing the accumulation of termination events by CTA degradation (**Scheme 2.24**) too early in the reaction.

Making a halt in the progression close to 50% of the monomer conversion generated a sample with a very broad distribution, leading to a too disperse sample that was far from the intended projected molecular weight and chain length.

Table 2.1: BOC-PAGH described in the kinetics studies.

	BOC-P ₄₈	BOC-P ₄₇	BOC-P ₉₇	BOC-P ₈₉	BOC-P ₁₁₂
[M]/[CTA]	50	50	100	100	100
[CTA]/[ACVA]	5	10	2.5	5	5
Max ρ (%) ¹	95.6	93.5	97.4	89.2	56.4
DP _{NMR} ²	47.8	46.75	97.4	89.2	112.8
Mn ³	9174	8239	15108	22715	15671
Mw ³	11210	10728	19583	29922	24826
Mn _{th} ⁴	9748	9539	19631	17997	22700
\bar{D} ³	1.22	1.30	1.30	1.32	1.58

Notes: (1) maximum conversion obtained through characterization by ¹H NMR. (2) Degree of polymerization considering the conversion % obtained by ¹H NMR. (3) Mn, Mw, and \bar{D} were calculated using GPC. (4) Predicted molecular weight.

The next step of this study was to characterize a purified sample of BOC-P_x. A new batch of BOC-P₃₈ (100/2/0.4, [M]=1.25 M, 70 °C, 1 h, 76% conversion) was polymerized, and purified by dialysis.

This step removes DMSO, unreacted monomer, and any other side product generated during the polymerization. The dialyzed solution was then lyophilized to remove the water allowing to obtain the polymer BOC-P₃₈ as an off-white powder that was characterized by ¹H NMR, UV-Vis, and GPC.

¹H NMR analysis of the purified BOC-P₃₈ (**Figure 2.30**) showed the presence of multiple broad peaks in the regions where functional groups of the monomer were identified previously, from 10-7.5 ppm corresponding to the amide and hydrazide regions, and the region from 4.75-3.5 ppm corresponding with the methylene region that was partially obscured by the water signal. The ¹H NMR spectrum also showed that there were a new set of broad signals from 2.25-1.0, the alkyl backbone of the polymer that was partially obscured by the DMSO signal, the BOC group, and the two methyl groups of the **CTA**. The presence of broadness in these signals are explained by tacticity, the relative stereochemistry of adjacent chiral centres within a macromolecule¹⁷². This phenomenon was expected, and another way to confirm that the sample was indeed a polymer. A similar proton environment was reported by Crisan et al.¹⁶¹ when researching **BOC-PAH**, a molecule with a similar structure as **BOC-PAGH**.

To obtain poly(acryloylglycine hydrazide) (**PAGH**) the BOC group needed to be cleaved. This was necessary to de-protect the hydrazide handle so it could be available to be functionalized with functional groups. To perform the de-protection, BOC-P₃₈ was dissolved into trifluoroacetic acid 99.5% (TFA, 1 mL for every 100 mg of sample) and was let to react overnight.

The TFA was evaporated by gently blowing with argon, then an equivalent volume of water was added. The result of the de-protection generated an acid solution of **PAGH** with TFA as a counter ion. To get rid of it the solution was neutralized with NaHCO₃ until no bubbling was observed, then dialyzed against water followed by lyophilization to obtain a white fluffy powder that was characterized by ¹H NMR, GPC and UV-Vis.

The solubility of **PAGH** was tested, so a suitable solvent for its characterization could be chosen. **PAGH** proved to be soluble in water but insoluble in organic solvents. Solubility in an organic solvent miscible with water was achieved by first dissolving **PAGH** in 5% AcOH in D₂O then adding 95% of DMSO.

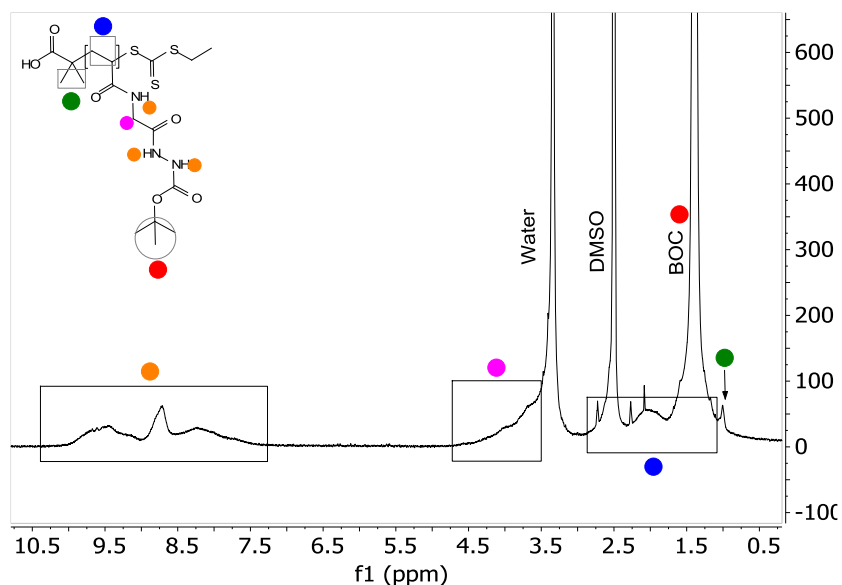


Figure 2.30: ^1H NMR spectrum of the purified BOC- P_{38} in $\text{DMSO}-d_6$.

A difference in colour was present between the protected **BOC-PAGH** and the de-protected **PAGH**.

It was believed that the off-white colour of the protected polymer was due to the presence of the **CTA** at the end of the polymer which has a trithiocarbonyl group with a distinctive yellow colour with a max absorbance peak at 305 nm. UV-VIS was used to analyse samples before and after de-protection with TFA to check for the presence of the trithiocarbonylthio group, as it was suspected that the neutralization process with NaHCO_3 might have cleaved it and that this was the cause in the difference in colours between BOC protected and de-protected polymers.

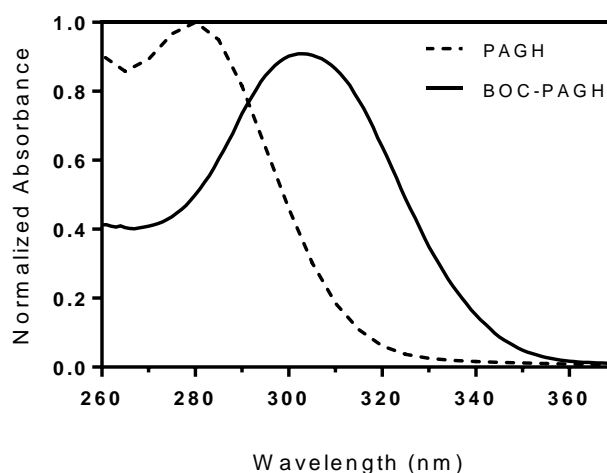
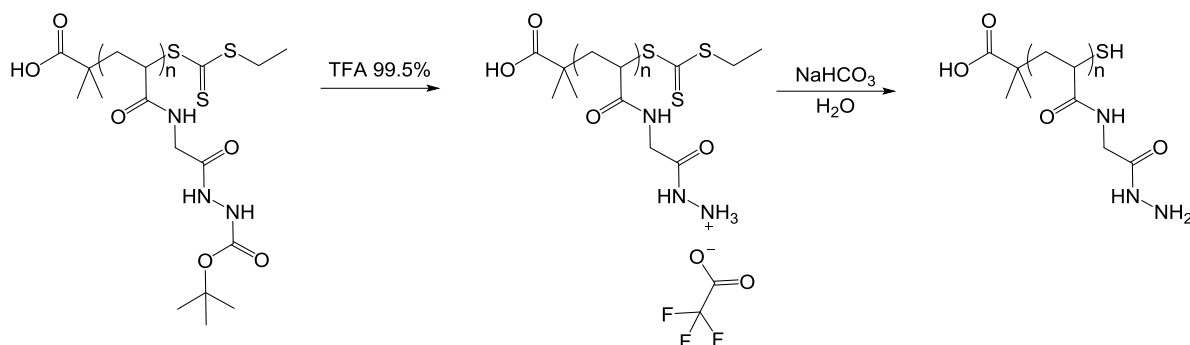


Figure 2.31: UV-Vis spectra of the protected versus de-protected poly(acryloylglycine hydrazide). The sample of PAGH DP_{38} was dissolved in ELGA water (deionised water), and the BOC-PAGH DP_{38} sample was dissolved in DMSO.

The UV-Vis analysis (**Figure 2.31**) confirmed that the de-protected sample had lost its maximum peak of absorbance at 305 nm shifting to a maximum peak of 280 nm. This shift in the molecule's absorbance had been reported previously in our lab with the use of this **CTA** in particular after the de-protection

and neutralization of **PAH**¹⁶¹ and is compatible with the transformation of the trithiocarbonylthio group (**Scheme 2.25**) into a thiol.



Scheme 2.25: De-protection and neutralization of BOC-poly(acryloylglycine hydrazide) to obtain poly(acryloylglycine hydrazide).

The next step on the study of **PAGH** was the characterization by ¹H NMR spectroscopy (**Figure 2.32**) of **P₃₈**. The ¹H NMR was performed in D₂O, and the proton environment showed broad signals corresponding with the methylene group between 4.3-3.5 ppm, the two signals corresponding to the alkyl backbone between 2.8-1.1 ppm, and the two methyl groups from the **CTA** between 1.0-0.9. NH and OH groups are not visible (**Figure 2.33**) by ¹H NMR spectroscopy when using D₂O as solvent due to the exchange of deuterium between the solvent and these functional groups.

A comparison between **P₃₈** ¹H NMR spectra before and after de-protection (**Figure 2.33**) showed the changes in the proton environment of the polymer.

The disappearance of the signal at 1.38 ppm corresponding to the BOC protecting group confirmed that the de-protection was successful, as the BOC signal was no longer obscuring the peaks that corresponded to the polymer backbone and the two methyl groups from the **CTA**.

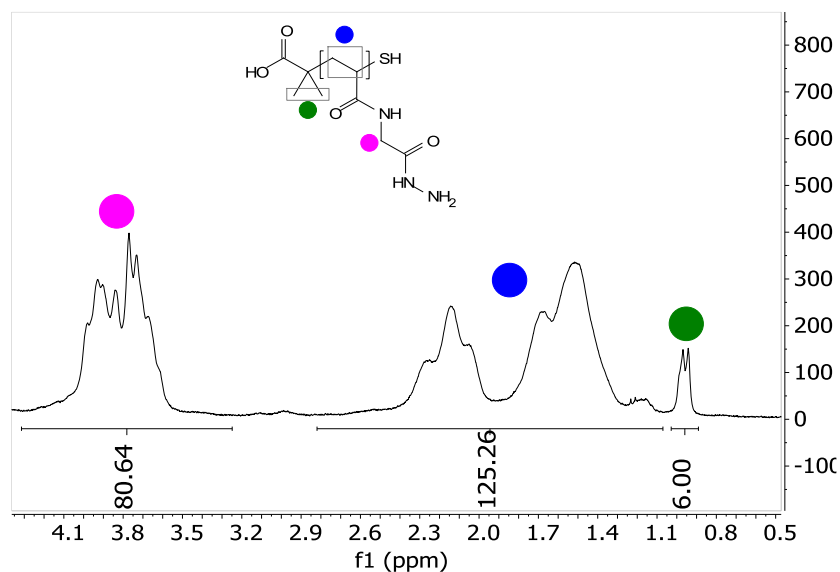


Figure 2.32: ¹H NMR spectroscopy of PAGH DP₃₈ in D₂O.

Now that the methyl groups from the **CTA** were completely visible they could be used to determine the degree of polymerization of the sample (**Figure 2.32**). Assigning six protons to the signals corresponding to the two methyl groups meant they could be used to correct the integration values corresponding to the backbone ($-\text{CH}_2-\text{CH}-$) and the methylene group (CH_2) signals.

This way the degree of polymerization of the sample could be estimated via ^1H NMR spectroscopy and compared with the value obtained during the polymerization of the protected monomer. When this approach was used to calculate the polymerization degree of **P₃₈** a DP value of 40-41 subunits was obtained, that was close to the one calculated from the polymer conversion (76% conversion of projected DP₅₀ gives a polymer of 38 subunits). These results validated the previous DP calculation and indicated that there was no loss of polymer subunits during the de-protection process.

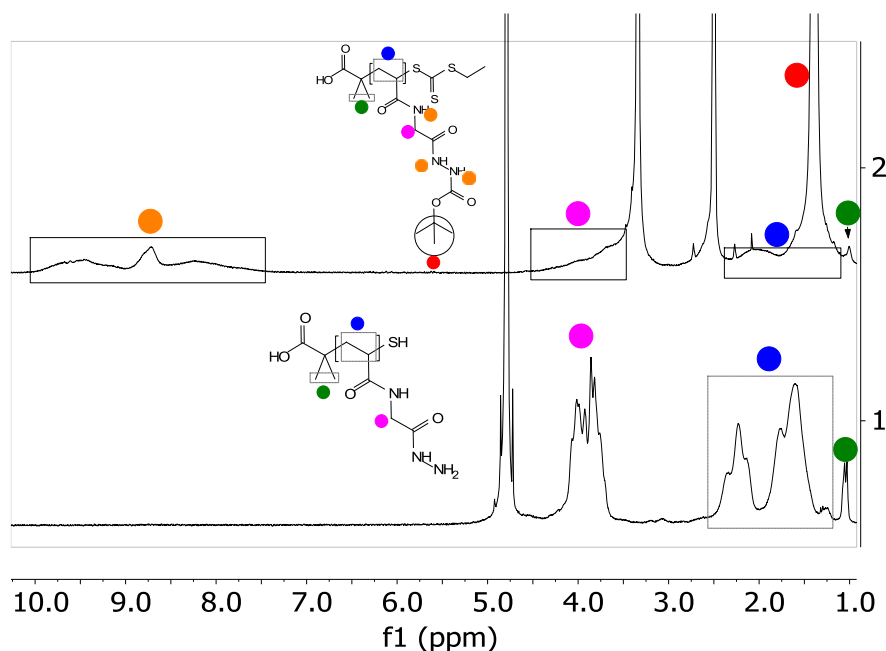


Figure 2.33: ^1H NMR spectra of **P₃₈** before (top, in $\text{DMSO}-d_6$) and after (down, in D_2O) de-protection with TFA.

To continue with the characterization and study of the de-protected polymer four new batches of **BOC-PAGH** were synthesized at $70\text{ }^\circ\text{C}$, $[\text{M}]=1.25\text{ M}$, with **M/CTA/ACVA** ratios of 100/2/0.4, 100/2/0.2, 100/1/0.4, and 100/1/0.2. Aliquots were taken after every polymerization, and they were characterized with GPC chromatography and ^1H NMR spectroscopy.

These polymer batches were de-protected with 99.5% TFA and dialyzed, then the **PAGH** samples were characterized using the same techniques and the results were compared (**Table 2.2** and **Figure 2.34**).

The data obtained by GPC (**Figure 2.34**) showed how the de-protection of the **PAGHs** have shifted their distribution towards species of lower molecular weight. This was an expected result due to the loss of the BOC group and part of the **CTA** during the de-protection reaction, and it is quantified when calculating their M_n and M_w , as seen in **Table 2.2**, therefore confirming the success of the de-protection process.

When checking polymer dispersity (**Table 2.2**), minor changes were observed ($\bar{D}=\pm 0.04$ -0.09) after the de-protection of the polymers compared to their protected counterparts. It was believed that this discrepancy was due to the use of different columns and calibration standards used on the GPC analysis of the polymers before and after de-protection, but overall their \bar{D} was maintained within a similar range even when accounting for these minor changes.

Table 2.2: PAGH batches used to measure the loading capacity with aldehydes and carbohydrates.

	BOC-P ₃₈	P ₃₈	BOC-P ₄₅	P ₄₅	BOC-P ₇₂	P ₇₂	BOC-P ₉₇	P ₉₇
p (%) ¹	76%	76%	90%	90%	72%	72%	97%	97%
M/CTA/ACVA	100/2/0.4	100/2/0.4	100/2/0.2	100/2/0.2	100/1/0.2	100/1/0.2	100/1/0.4	100/1/0.4
Mn ²	8239	6804	9869	7501	13537	8833	15295	9499
Mw ²	10728	8595	11436	9243	18753	13045	19992	12700
Mn_{th} ³	7796	5560	9191	6659	14570	10427	19552	14006
\bar{D} ²	1.30	1.26	1.16	1.23	1.39	1.48	1.31	1.34

Notes: (1) conversion was calculated by ¹H NMR integrating the vinyl regions at t_0 versus t_f . (2) Mn, Mw and \bar{D} was obtained by statistical analysis of the data obtained by GPC. (3) Predicted molecular weight.

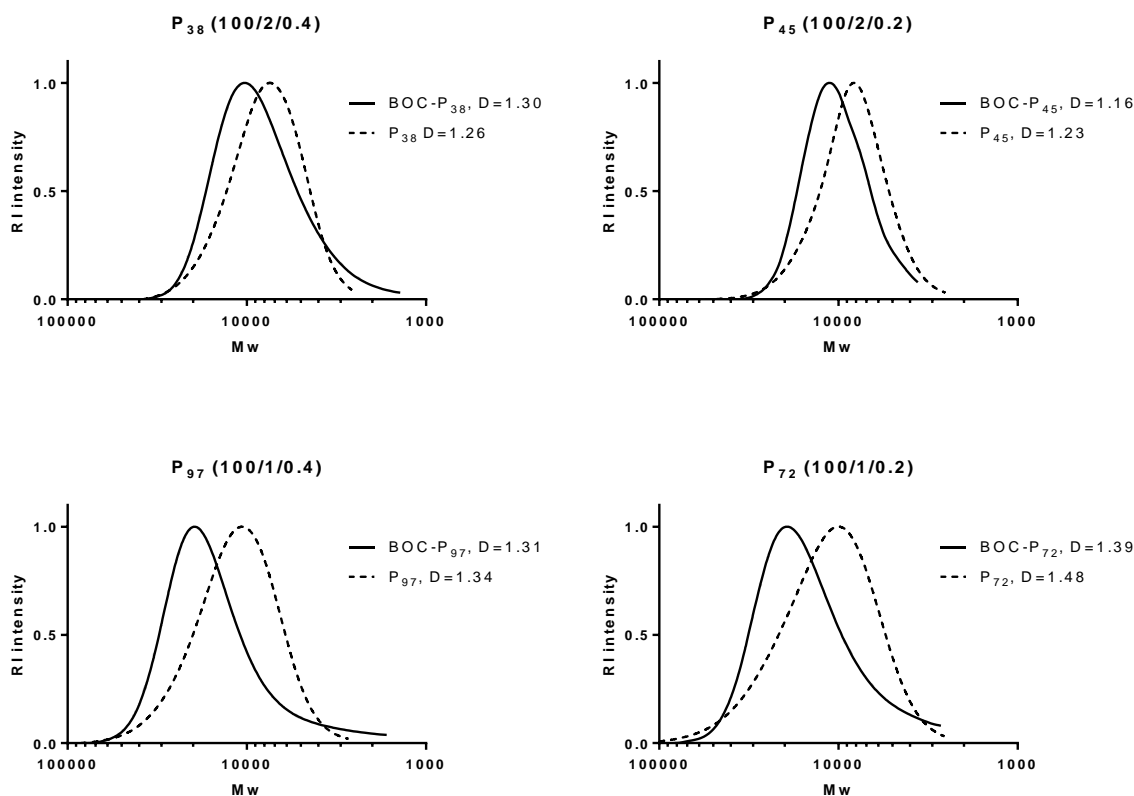


Figure 2.34: GPC analysis of PAGH polymers before and after de-protection with TFA.

This data confirmed that polymerizations with lower projected DP like **P₃₈** (Mn=6804, Mn_{th}=5560, \bar{D} =1.26) and **P₄₅** (Mn=7501, Mn_{th}=6659, \bar{D} =1.23) had better control over the final Mn than their heavier counterparts **P₇₂** (Mn=8833, Mn_{th}=10427, \bar{D} =1.39) and **P₉₇** (Mn=9499, Mn_{th}=14006, \bar{D} =1.31) with higher DPs. Polymers with higher DP have a wider range of polymer species; this affected their Mn

calculations and was the reason for a major discrepancy between the M_n obtained by GPC and the $M_{n_{th}}$ of **P₇₂** and **P₉₇**.

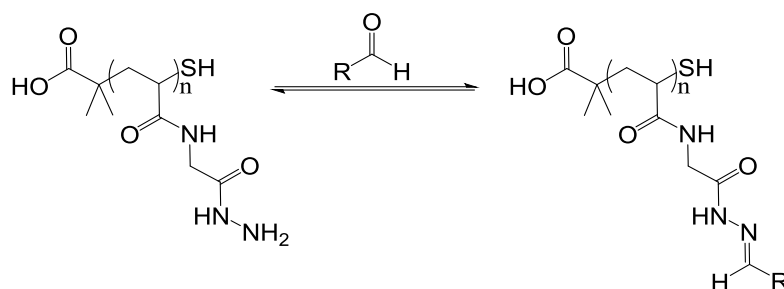
The experiments performed in this section of the **PAGH** study proved that the synthetic route for BOC-acryloylglycine hydrazide was achieved, that the conditions chosen to polymerize the monomer allowed to obtain **BOC-PAGH** with projected DPs from 50-100, and that the polymer could be easily de-protected to produce **PAGHs** of controlled M_n and \bar{D} .

Overall, this section was considered a success, and the following efforts were devoted to the study of the loading efficiency of **PAGH**.

2.3.3.4 Functionalization of poly(acryloylglycine hydrazide)

The next step of the **PAGH** research was to test its functionalization efficiency (**Scheme 2.26**) when coupled with a set of different aldehydes and carbohydrates.

Our research group had developed methods for the functionalization of poly hydrazides with aldehydes that were used by Crisan et al.¹⁶¹, and that were used in this part of the study. All functionalizations were made with a 1:1 ratio of aldehyde or sugar per polymer repeating subunit; solvent conditions depended of the functional group solubility. Therefore, basic water-soluble aldehydes were functionalized in 5% of AcOH in D₂O, acidic aldehydes were functionalized in D₂O with 100 mM Na₂HPO₄, and aldehydes insoluble in water were functionalized in 95% DMSO-d₆ with 5% AcOH in D₂O.



Scheme 2.26: PAGH functionalization.

The first step was to test if there was a noticeable difference in the loading efficiency of **PAGHs** of different DPs and if the hydrazones formed during the coupling reaction were stable over a time frame of 48 h. Polymers of **P₃₈**, **P₄₈**, **P₇₂**, and **P₉₇** were functionalized with 1 equivalent of 4-imidazolecarboxaldehyde (**Figure 2.35**) in 5% of AcOH in D₂O (pH 2.9), for 2 h of reaction time at RT, samples were taken and characterized by ¹H NMR at intervals of 2, 24, and 48 h after the end of the coupling reaction to check for the loading stability. The amount of the free aldehyde signal at 9.7 ppm was quantified by ¹H NMR to calculate the loading efficiency, with loading efficiencies (**Table 2.3**) of 65-80% of the aldehyde into **PAGH**.

This % of loading was constant over time within all polymers of different DPs. The NMRs taken at different time intervals also showed that there was not an increase of free aldehyde on the sample after 48 h, meaning that the formed hydrazones were stable in this time frame.

Table 2.3: Percentage of PAGH subunits functionalized by one equivalent of 4-imidazolecarboxaldehyde 2/24/48 h after the functionalization reaction in 5% AcOH in D₂O

	P₃₈-Imi	P₄₅-Imi	P₇₂-Imi	P₉₇-Imi
2 h	71%	79%	65%	78%
24 h	72%	78%	65%	79%
48 h	70%	76%	65%	80%

Note: functionalization efficiency was calculated by ¹H NMR of the spectra shown on Figure 2.35.

Once it was confirmed that the DP of **PAGH** polymer did not affect the loading efficiency and stability, it was decided to continue testing the **PAGH** functionalization with **P₃₈**. This polymer was created

following 100/2/0.4 ratios of M/CTA/ACVA, the same that was used by Crisan et al.¹⁶¹ **PAH**. This was useful to compare loading efficiencies between **PAH** and **PAGH** of similar DP.

The next step was to check if the loading efficiency of **PAGH** could be affected by a difference in the equilibrium of the equivalencies when performing functionalization experiments. For that purpose 1 equivalent of **P₃₈** was functionalized with 0.3/0.6/0.9/1.0 equivalents of 4-imidazolecarboxaldehyde (**Figure 2.36**), the reaction was performed in 5% of AcOH in D₂O (pH 2.9), for 2 h of reaction time at RT.

The samples taken at the end of the experiment were characterized by ¹H NMR, and the spectra showed that 0.3 and 0.6 equivalents were consumed completely leaving no free aldehyde signal at 9.7 ppm after the coupling reaction, while 0.9 and 1.0 equivalents were consumed to a maximum of a loading efficiency of 77% of the polymer subunits, pointing out that the maximum loading efficiency of 4-imidazolecarboxaldehyde might be determined by the loading conditions or the polymer steric hindrance.

A limit of 1:1 equivalent ratios to the **PAGH** functionalizations was established to control the amount of excess non-reacted functional groups that might have biological activity by themselves, that would prevent the use in-situ after functionalization adding undesirable purification steps that would slow the fast screen of libraries that the polymer was designed for, but this auto limitation might have hindered the potential of higher loading efficiencies as it could be theorised that pushing the equilibrium of the reaction using a higher functional group equivalency might have increased the functionalization efficiency.

There was another consideration, that as the functionalization progresses the steric hindrance between side chains does too, to the point where functionalized polymer subunits prevent the functionalization of free hydrazides.

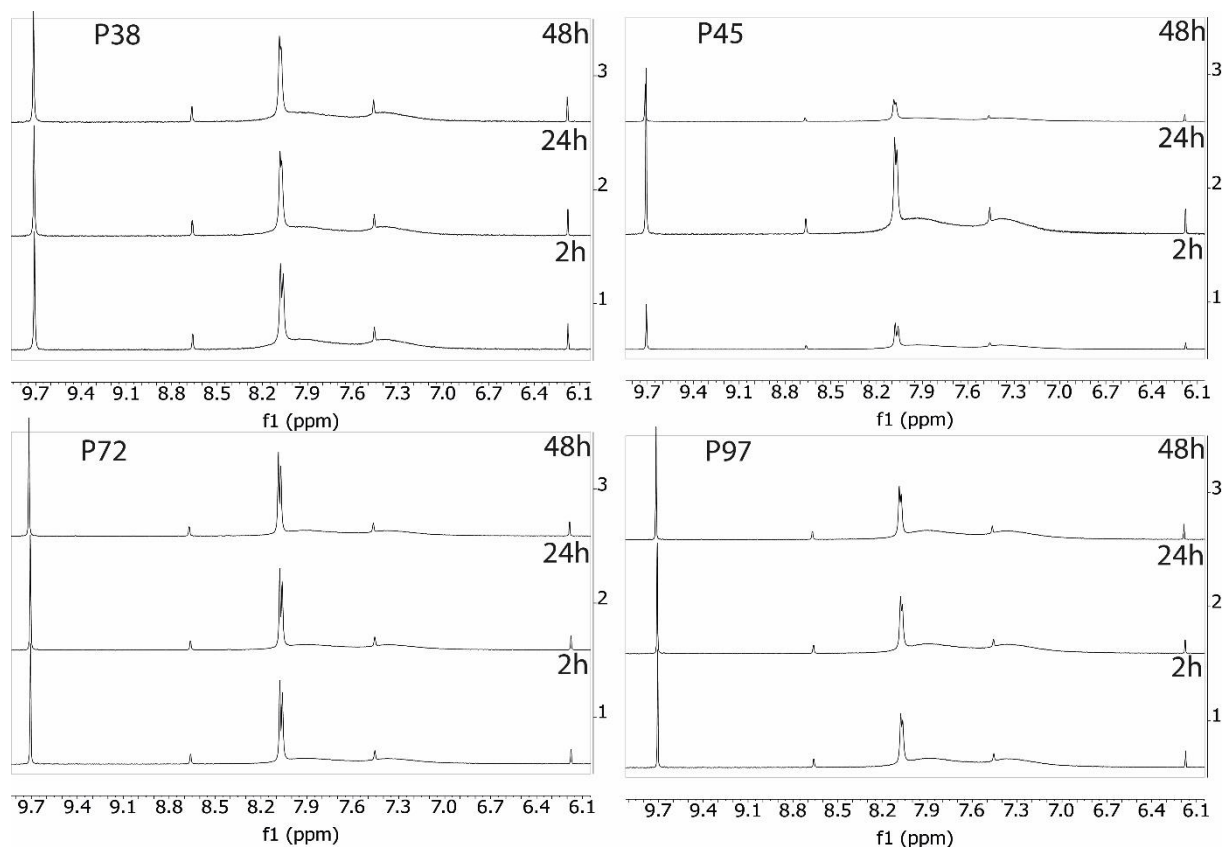


Figure 2.35: ^1H NMR spectroscopy in D_2O of the functionalization of PAGH of DP 38/45/72/97 with one equivalent of 4-imidazolecarboxaldehyde in aqueous 5% AcOH pH 2.9, 2/24/48 h after the end of the coupling reaction.

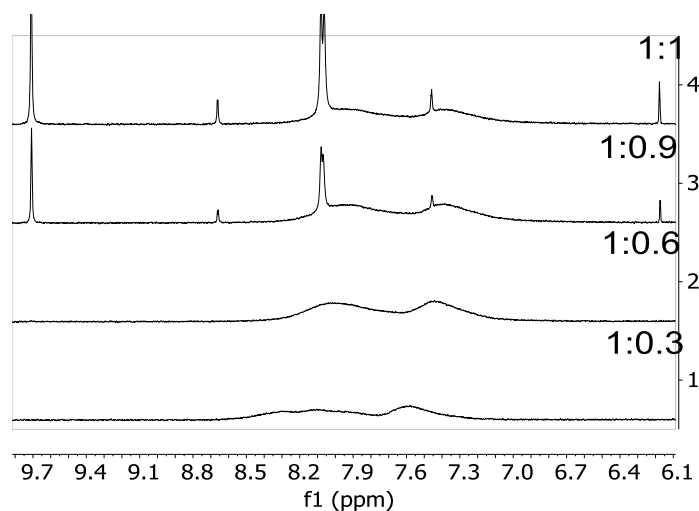


Figure 2.36: ^1H NMR spectroscopy in D_2O of the functionalization of P_{38} with 0.3/0.6/0.9/1.0 equivalents of 4-imidazolecarboxaldehyde in aqueous 5% AcOH pH 2.9.

Establishing that the hydrazone bond formed during the coupling reaction remained stable over time was a necessary step that allowed to continue the study of functionalization efficiency of **PAGH**. For that purpose, **P₃₈** was functionalized with an array of aldehydes in aqueous and organic loading conditions that could be expected when screening functional groups libraries.

The study of **PAGH** functionalization was performed with a selected group of functional groups representative of acidic and basic hydrophilic aldehydes like 4-imidazolecarboxaldehyde, glyoxylic acid, and DL-glyceraldehyde, and aldehydes that represent functional groups with biological motifs like pyridoxal phosphate and formyl uracil.

All **P₃₈** functionalization reactions were performed in a 1:1 ratio at 60 °C for a duration of 24 h, using different solvent conditions depending of the model aldehyde solubility used in the coupling experiment; the reactions were characterized by ¹H NMR spectroscopy. Aqueous acidic conditions were done in 5% AcOH in D₂O pH 2.9; aqueous basic conditions were done in 100 mM Na₂HPO₄ in D₂O pH 9.1; and organic conditions were done in a mixture of 95% DMSO-*d*₆ with a 5% of AcOH in D₂O. These loading conditions are based on the work previously performed by Crisan et al.¹⁶¹ and proved to be successful for functionalizing **PAH** with this group of model aldehydes.

It was decided to use 4-imidazolecarboxaldehyde (**Ald1**) as a model of the loading efficiency of basic hydrophilic aldehydes. A loading efficiency of 70% was reported when **P₃₈** was functionalized with one equivalent of 4-imidazolecarboxaldehyde (**Ald1**) under acidic aqueous conditions (**Table 2.3**). Further experiments of **Ald1** coupling under aqueous basic conditions proved unsuccessful as the aldehyde was insoluble in this coupling condition. The functionalization experiment performed under organic conditions proved to be successful, reporting a superior functionalization efficiency of 85% of **P₃₈** subunits (**Figure 2.37**) compared to the acidic aqueous conditions. The loading efficiency of **Ald1** was calculated by ¹H NMR, integrating the signals corresponding to the free aldehyde at 9.75 ppm against the signals corresponding to the broad peaks of **Ald1** integrated into the polymer that could be observed from 6.8-8.8 ppm. A total of three protons were assigned to all these signals. In normal circumstances the aldehyde group signal at 9.75 should be equal to one if 100% of **Ald1** was free in solution. The depletion on the intensity of this signal corresponded to that amount of aldehyde that had been functionalized into **P₃₈** subunits, giving a functionalization efficiency of 85% of the 1 equivalent used in the reaction.

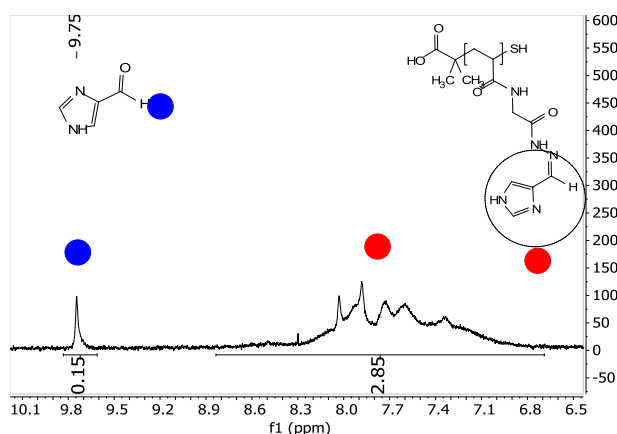


Figure 2.37: ¹H NMR spectrum of the 1:1 functionalization of **P₃₈** with 4-imidazolecarboxaldehyde (**P₃₈-Ald1**) in 5% AcOH in D₂O and 95% of DMSO-*d*₆.

Glyoxylic acid (**Ald2**) was chosen as one of the models of hydrophilic acid aldehydes for the study of **PAGH** functionalization. This molecule proved to be insoluble under the acidic aqueous conditions. Further coupling under basic conditions proved to be successful (**Figure 2.38**) with a functionalization

of 80% of the equivalent used in the coupling reaction. When the functionalization of **Ald2** was pursued under organic conditions a full conversion of the Ald2 equivalent used in the functionalization was observed, with the complete disappearance of the free aldehyde signal at 4.92ppm, meaning that 100% of the 1 equivalent of **Ald2** used in the reaction was coupled with **PAGH**. The loading efficiency of the **Ald2** reactions was monitored by calculating the depletion of the free aldehyde signal at 5.00 (basic aqueous) and 4.92 (organic) ppm.

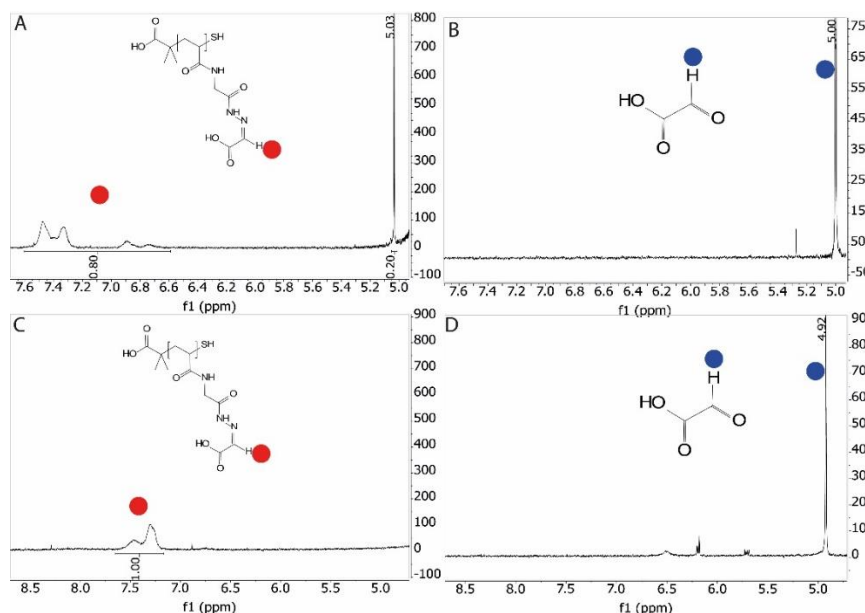


Figure 2.38: ^1H NMR spectrum of 1:1 functionalization of P_{38} with glyoxylic acid ($\text{P}_{38}\text{-Ald2}$). A) P_{38} functionalized with 1 equivalent of glyoxylic acid in 100 mM Na_2HPO_4 in D_2O pH 9.1. B) Glyoxylic acid control in 100 mM Na_2HPO_4 in D_2O pH 9.1. C) P_{38} functionalized with 1 equivalent of glyoxylic acid in 5% AcOH in D_2O and 95% of $\text{DMSO-}d_6$. D) Glyoxylic acid control in 5% AcOH in D_2O and 95% of $\text{DMSO-}d_6$.

Following the study of hydrophilic model aldehydes, the loading efficiency of DL-glyceraldehyde (**Ald3**) was tested and the reactions were characterized by ^1H NMR (**Figure 2.39**). **Ald3** proved to be soluble under all three loading conditions. When testing the coupling reactions under acidic, and basic aqueous conditions the free aldehyde signal expected between 9-10 ppm could not be used to calculate the loading efficiency of the reaction as it was not present on the ^1H NMR spectra. The approach taken was to infuse our the ^1H NMR samples with equimolar quantities of DMAP as integration standard, which was used to normalize the signals corresponding to the loaded **Ald3** into P_{38} subunits and calculate the loading efficiency of both reactions. The result of the functionalization reaction was of 88% under acidic aqueous conditions, and 53% under basic aqueous conditions. When testing the loading under organic conditions the same problem as the previous conditions was encountered; the aldehyde signal was not present in the NMR spectrum. In this case syringic acid was used as integration standard, because DMAP was not soluble in the solvent used for the ^1H NMR. For this characterization, the signal corresponding with the two methyl groups at 3.79 ppm were used to normalize the broad new signals corresponding to the functionalized aldehyde. Part of these signals were overlapping with a peak corresponding with two $-\text{CH}-$ from the syringic acid; subtracting these two protons from the integrated broad signals provided the functionalization efficiency of this reaction set at a 49% of the initial **Ald3** equivalent loaded into the polymer.

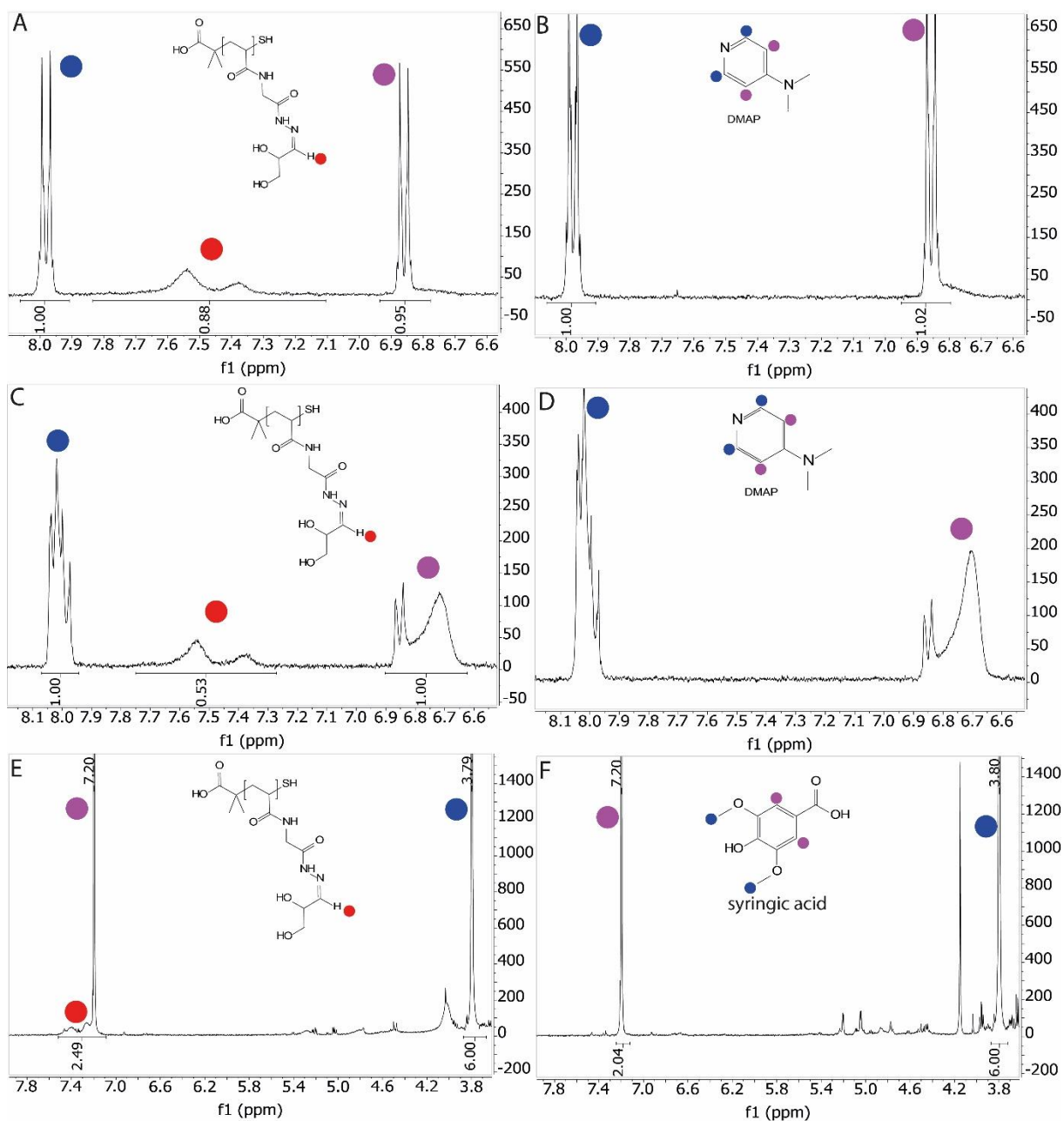


Figure 2.39: ^1H NMR spectra of the 1:1 functionalization of P_{38} with DL-glyceraldehyde (P₃₈-Ald3). A) 1:1 P_{38} functionalization with DL-glyceraldehyde in 5% AcOH in D_2O , with 1 equiv. quantity of DMAP as integration standard. B) DL-glyceraldehyde control in 5% AcOH in D_2O , with 1 equiv. quantity of DMAP as integration standard. C) 1:1 P_{38} functionalization with DL-glyceraldehyde in 100 mM Na_2HPO_4 in D_2O , with 1 equiv. quantity of DMAP as integration standard. D) DL-glyceraldehyde control in 100 mM Na_2HPO_4 in D_2O , with 1 equiv. quantity of DMAP as integration standard. E) 1:1 P_{38} functionalization with DL-glyceraldehyde in 5% AcOH in D_2O and 95% of $\text{DMSO}-d_6$, with 1 equiv. quantity of syringic acid as integration standard. F) DL-glyceraldehyde control in 5% AcOH in D_2O and 95% of $\text{DMSO}-d_6$, with 1 equiv. quantity of syringic acid as integration standard.

Pyridoxal phosphate (**Ald4**) was used as a model for a hydrophilic aldehyde with biological motifs, but was found to be only soluble under basic aqueous conditions. A functionalization of 93% of the **Ald4** equivalent used in the reaction was obtained after quantifying by ^1H NMR (**Figure 2.40**) the free aldehyde signal depletion at 10.33 ppm.

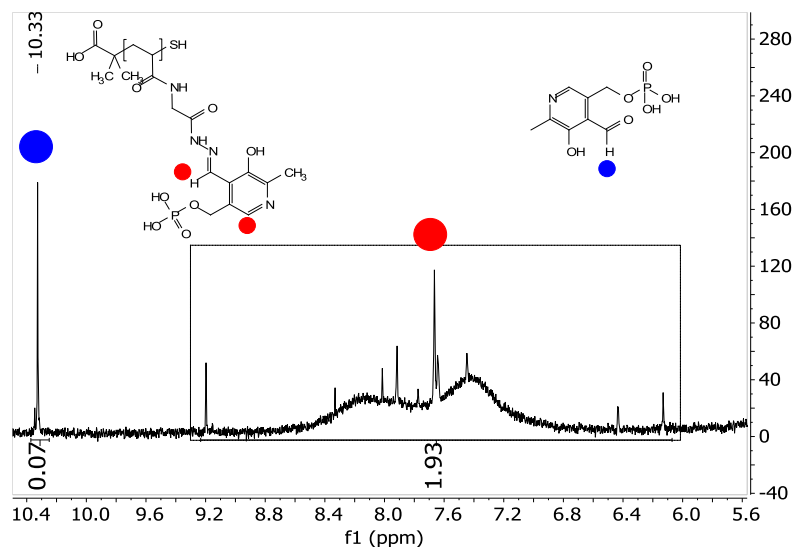


Figure 2.40: ^1H NMR spectrum of 1:1 functionalization of P_{38} with Pyridoxal Phosphate ($\text{P}_{38}\text{-Ald4}$) in 100 mM Na_2HPO_4 in D_2O pH 9.1.

Further testing of the loading efficiency of **PAGH** required the use of a hydrophobic model aldehyde with biological motifs, formyl uracil (**Ald5**) was chosen for that purpose as it was only soluble under organic conditions. Quantifying the depletion of the aldehyde signal at 9.73 ppm by ^1H NMR (**Figure 2.41**) allowed to calculate the loading efficiency of this aldehyde into the polymer that was quantified as 78% of the initial **Ald5** equivalent used in the coupling reaction. This result was particularly important as there are many biological applications like anti-microbial compounds¹⁷³ and gene delivery macromolecules¹⁷⁴ that require the use of functional groups with hydrophobic motifs.

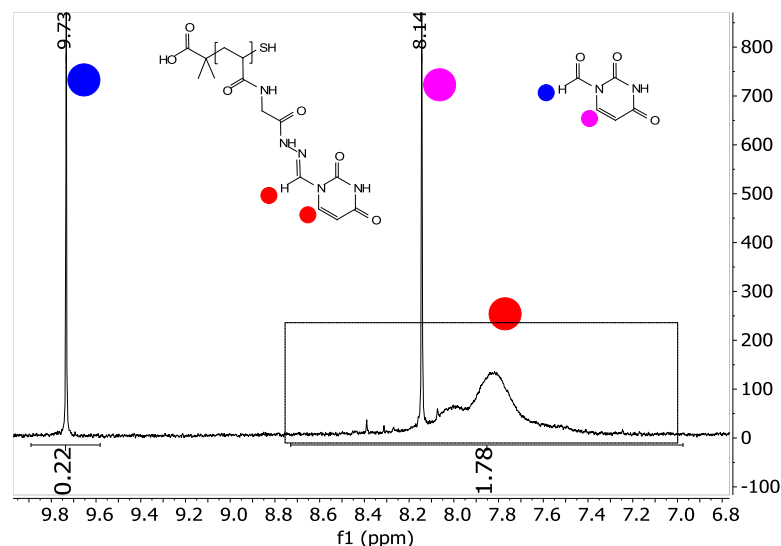


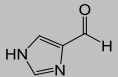
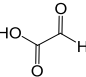
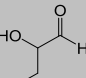
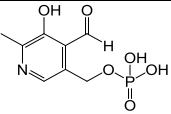
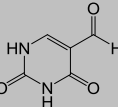
Figure 2.41: ^1H NMR spectrum of 1:1 functionalization of P_{38} with Formyl Uracil ($\text{P}_{38}\text{-Ald5}$) in 5% AcOH in D_2O and 95% of $\text{DMSO}-d_6$.

The results obtained during the loading testing of the polymer (**Table 2.4**) showed that the functionalization of **PAGH** was possible with an array of hydrophilic and hydrophobic aldehydes under the different conditions used. When the results obtained from the different model aldehydes (**Table 2.4**) were compared it could be observed how the loading efficiency of the reaction happened to be

dependent on their solubility into the solvent conditions used for these experiments. When aldehydes were soluble under different solvents, they achieved different loading efficiencies depending on the media used, pointing that higher efficiencies are linked with better solubility of the aldehyde.

One important result was that 100% of loading efficiency could be achieved when functionalizing **PAGH** with one equivalent of glyoxylic acid under organic conditions; this was against the previous assumption that steric hindrance might have been linked to not being able to achieve full conversion with some of the model aldehydes, pointing that the way to improve the functionalization efficiency is by tweaking the loading conditions either by improving solubility of the polymer and aldehydes or by pushing the equilibrium of the reaction by reacting with a higher aldehyde equivalency, something avoided due to adding extra undesirable purification steps.

Table 2.4: Loading efficiency of P_{38} when functionalized with 1 equivalent of different model aldehydes under acidic, basic, and organic loading conditions

Px-Aldx	Aldx	5% AcOH in D_2O pH 2.9	100 mM Na_2HPO_4 in D_2O pH 9.1	95% $DMSO-d_6$ 5% AcOH in D_2O
P₃₈-Ald1	 4-imidazolecarboxaldehyde	71%	—	85%
P₃₈-Ald2	 Glyoxylic acid	—	80%	100%
P₃₈-Ald3	 DL-Glyceraldehyde	85%	53%	49%
P₃₈-Ald4	 Pyridoxal phosphate	—	93%	—
P₃₈-Ald5	 Formyl uracil	—	—	78%

Notes: all experiments were characterized by 1H NMR after 24 h incubation at 60 °C. (—) aldehydes were insoluble in these conditions.

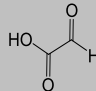
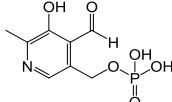
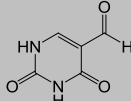
One of the aims of this project was to design **PAGH**, a hydrazide polymer that improved the loading efficiency of **PAH** by increasing the length of the side chains reducing steric hindrance. To compare functionalization efficiencies a new batch of a **PAH** of 37 subunits (**PAH₃₇**) was synthesized following Crisan et al.¹⁶¹ specifications. This **PAH₃₇** was the model used to compare functionalization results with **PAGH**, for that purpose an array of aldehydes were chosen to functionalize **PAH₃₇**, glyoxylic acid as a hydrophilic model aldehyde, pyridoxal phosphate as a hydrophilic model aldehyde with biological motifs, and formyl uracil as a hydrophobic model aldehyde with biological motifs. **PAH₃₇** was functionalized under the same conditions used to functionalize **PAGH**, and the results were characterized by 1H NMR spectroscopy.

When functionalizing **PAH** with glyoxylic acid (**Figure 2.42**) under aqueous basic conditions a loading efficiency of 75% of the **Ald2** equivalent used was calculated; this functionalization improved to a 98% when performed under organic conditions (**Figure 2.42**). The functionalization of **PAH** with pyridoxal phosphate under aqueous basic conditions reported (**Figure 2.43**) a loading efficiency of 97% of the

aldehyde 1 equivalent used in the reaction. The functionalization of the hydrophobic aldehyde formyl uracil under organic conditions performed with a loading efficiency of 78% (**Figure 2.44**).

The results obtained by the functionalization of **PAH₃₇** (**Table 2.5**) showed that the loading efficiencies of **PAH** were within the same range as the results obtained when **PAGH** was functionalized (**Table 2.4**) with the same aldehydes under the same loading conditions, and that the longer side chains of **PAGH** did not improve the loading efficiency. These results are in agreement with our hypothesis that steric hindrance is not involved in the lower functionalization efficiency of some reactions, and that it is a problem inherent to the loading conditions used during the functionalization experiments; the fact that aldehydes like glyoxylic acid and pyridoxal phosphate reach close to or full conversion of the equivalent used in the reaction with both **PAH** and **PAGH** is proof that full conversion is possible under certain conditions.

Table 2.5: Loading efficiency of PAH₃₇ when functionalized with 1 equivalent of different model aldehydes under acidic, basic, and organic loading conditions.

PAH _x -Aldx	Aldx		5% AcOH in D ₂ O pH 2.9	100 mM Na ₂ HPO ₄ in D ₂ O pH 9.1	95% DMSO- <i>d</i> ₆ 5% AcOH in D ₂ O
PAH ₃₇ -Ald2		Glyoxylic acid	—	75%	98%
PAH ₃₇ -Ald4		Pyridoxal phosphate	—	97%	—
PAH ₃₇ -Ald5		Formyl uracil	—	—	75%

Notes: all experiments were characterized by ¹H NMR after 24 h incubation at 60 °C. (—) aldehydes were insoluble in these conditions.

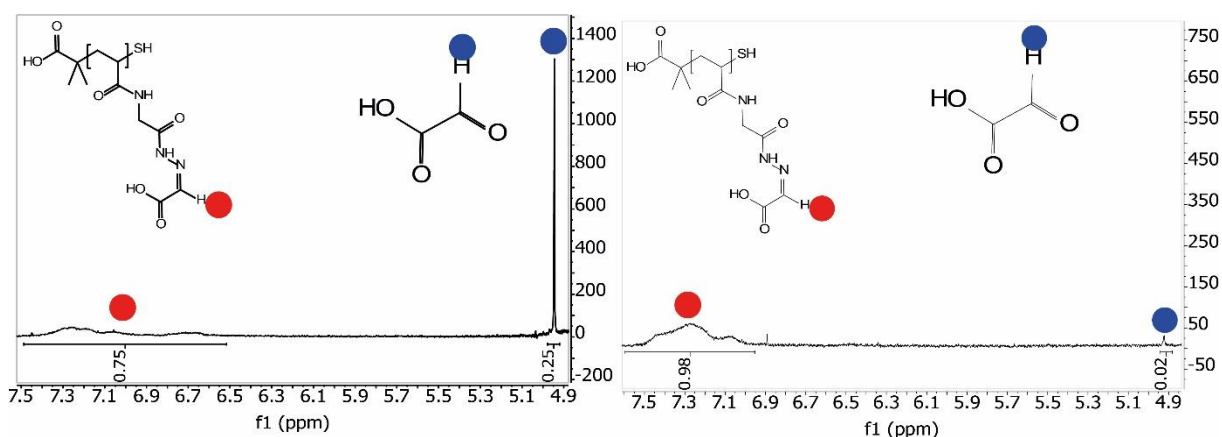


Figure 2.42: ¹H NMR spectrum of 1:1 functionalization of PAH₃₇ with Glyoxylic acid (PAH₃₇-Ald2). (Left) PAH₃₇ functionalized with 1 equivalent of glyoxylic acid in 100 mM Na₂HPO₄ in D₂O pH 9.1. (Right) P₃₈ functionalized with 1 equivalent of glyoxylic acid in 5% AcOH in D₂O and 95% of DMSO-*d*₆.

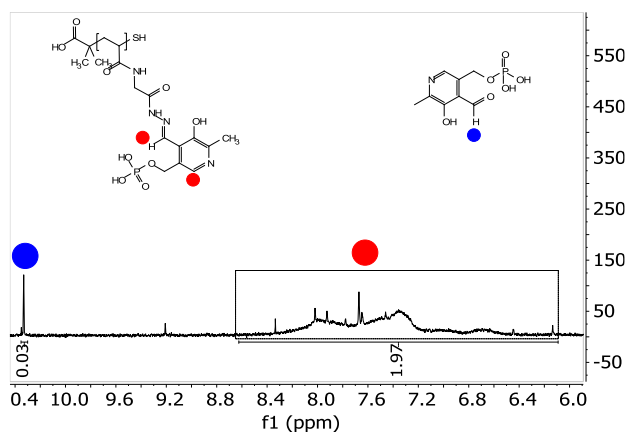


Figure 2.43: ^1H NMR spectrum of 1:1 functionalization of PAH_{37} with Pyridoxal Phosphate ($\text{PAH}_{37}\text{-Ald4}$) in 100 mM Na_2HPO_4 in D_2O pH 9.1.

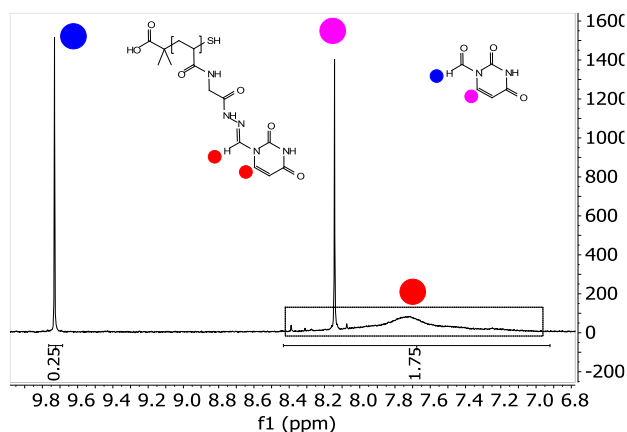


Figure 2.44: ^1H NMR spectrum of 1:1 functionalization of PAH_{37} with formyl uracil ($\text{PAH}_{37}\text{-Ald4}$) in 5% AcOH in D_2O and 95% of $\text{DMSO}-d_6$.

The study of the loading efficiency of **PAGH** with aldehydes was followed with the study of **PAGH** functionalization with carbohydrates under aqueous acidic conditions. The model **PAGH** used was the previously introduced **P₃₈** used for the aldehyde functionalization study. The loading efficiency of **P₃₈** was tested with the carbohydrates D-glucose and D-mannose as sugar models, following the same loading conditions used to functionalize **PAH₄₀** with carbohydrates in the previous section.

The ^1H NMR integral values of free α and β sugar isomers after the coupling with **P₃₈** were compared versus the integral values of 1 equivalent of the sugar alone in solution 24 h after the start of the coupling reaction (**Figure 2.45**) to quantify the percentage of sugar loaded into **P₃₈**. The loading efficiency under acidic conditions was of 40% for **P₃₈**+D-glucose, and 46% for **P₃₈**+D-mannose (**Table 2.6**).

Table 2.6: Percentage of maximum loading efficiency of P_{38} with 1 equivalent of carbohydrates under 5% AcOH in D_2O pH 2.9.

P_x -Carbohydrate	5% AcOH in D_2O pH 2.9
P_{38} +D-glucose	40%
P_{38} +D-mannose	46%

Note: all experiments were characterized by 1H NMR after 24 h incubation at 60 °C.

These **PAGH** carbohydrate functionalization experiments (**Table 2.6**) were within the same range as the ones obtained when **PAH** was functionalized with the same sugars under the same conditions, when a functionalization of 42% with PAH_{40} +D-glucose and 48% with PAH_{40} +D-mannose (**Figure 2.10** and **Figure 2.12**) was obtained; these results were in agreement with the ones observed when the loadings efficiencies with aldehydes of **PAGH** and **PAH** were compared, and therefore further confirm the hypothesis that the lower efficiencies of some functionalization experiments was not caused by steric hindrance but was an issue driven by the loading conditions used on the coupling reactions.

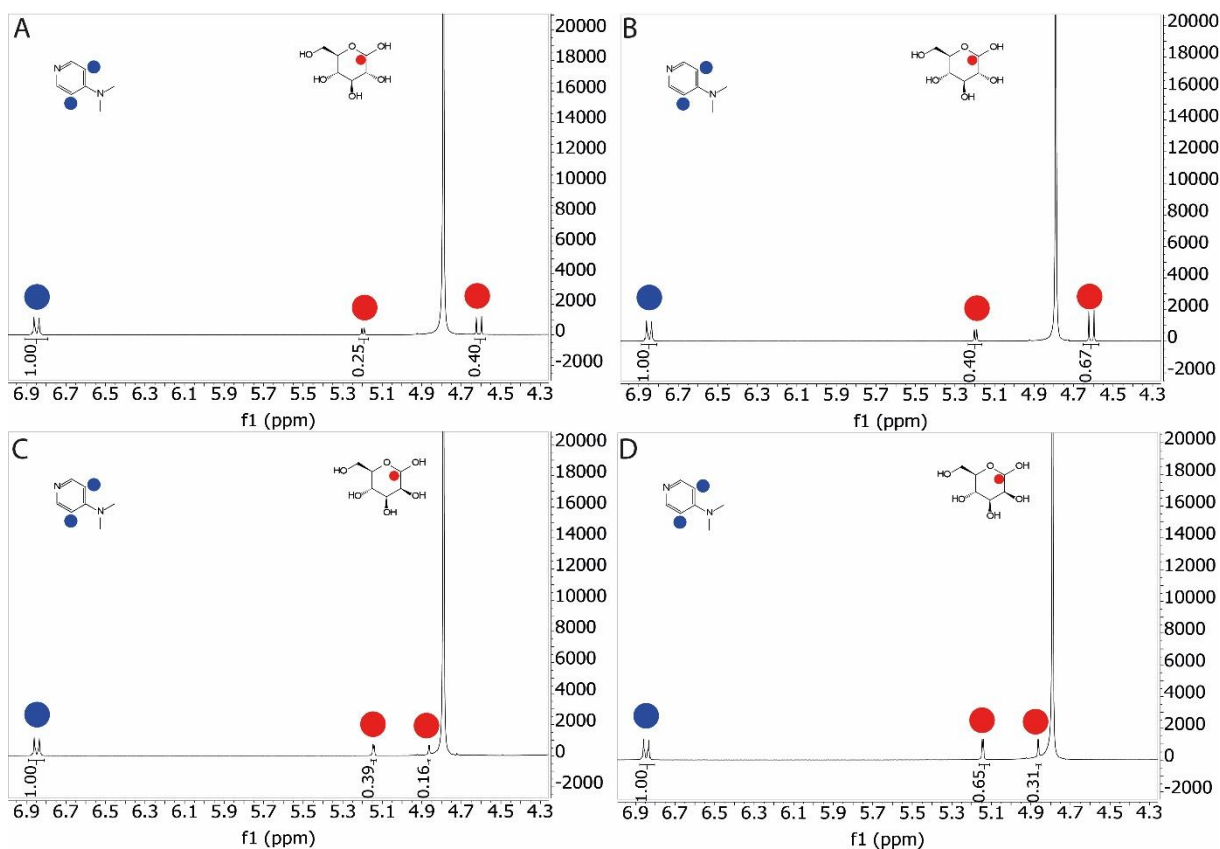


Figure 2.45: 1H NMR spectrum of 1:1 functionalization of P_{38} with sugars in 5% AcOH in D_2O , 24 h after the start of the reaction. A) P_{38} +D-glucose in 5% AcOH in D_2O . B) 1 equivalent of D-glucose in 5% AcOH in D_2O . C) P_{38} +D-mannose in 5% AcOH in D_2O . D) 1 equivalent of D-mannose in 5% AcOH in D_2O . DMAP was used as integration standard.

2.4 Summary

Part of this study was devoted to the study of **PAH**. Several experiments were performed towards the study of the **PAH** hydrazone bond formed after functionalization and its stability. The results of these experiments confirmed that the degree of functionalization remained constant over time, even when the samples were diluted twofold, showing that the system had reached thermodynamic equilibrium, in this state any aldehyde dissociation from the **PAH** would be compensated by the recoupling of a free aldehyde reforming the hydrazone. The data collected towards the study of **PAH** stability was published as part of Crisan et al.¹⁶¹.

The **PAH** study was followed with experiments that aimed to test its co-functionalization capabilities. A two-step reaction was designed to co-functionalize **PAH** with one type of aldehyde and one type of sugar. The results obtained from these functionalization experiments showed that the polymer scaffold could be co-functionalized efficiently in such manner, obtaining high loading efficiencies but never full conversion.

The development of a novel reliable synthesis route that allows for the generation of good amounts of the monomer BOC-acryloylglycine hydrazide was reported; its polymerization was achieved through RAFT chemistry, followed by a de-protection step that allowed to obtain **PAGH** scaffolds of diverse controlled molecular weights. This new scaffold was successfully used to study its potential to generate libraries of post-polymerization functionalized polymers via amino-carbonyl condensation with aldehydes and sugars in a variety of loading conditions. **PAGH** was designed to mimic **PAH** chemical structure but with longer hydrazide side chains that would avoid lower functionalizations that were hypothesised to be driven by steric hindrance.

Finally, the functionalization capabilities of **PAH** and **PAGH** were tested and compared. The loading efficiencies obtained were within the same range, confirming that steric hindrance was not involved in the lower efficiency of certain functional groups and that this was rather an issue driven by the loading conditions of the functionalization experiments.

2.5 Future work

From a synthetic point of view, the synthesis route of acryloylglycine and BOC-acryloylglycine could be further optimized to generate higher yields.

Regarding the polymerization of **PAGH**, a new **CTA** should be tested to avoid the terminations effects encountered during this study. The other option is to use the improved polymerization conditions devised by Creese et al.¹⁷¹ that managed to reduce the number of terminations effects that the **CTA** caused. Either way there is potential to improve the projected M_n and \bar{D} of **PAGH** polymers with newer conditions that avoid termination effects.

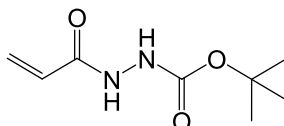
With regards of the biotechnological potential applicaitons of **PAH** and **PAGH**. Silicon glass surfaces could be modified by silanization¹⁷⁵ with 3-(trimethoxysilyl)propyl acrylate, this surface coating enables further modification of the glass surface. It could be possible to attach **PAH** or **PAGH** polymers by thiol–ene immobilisation¹⁷⁶ generating a polymer brush on the surface. That, for example, could interact with bacteria inducing biofilm formation that would be fixated on an abiotic surface.

2.6 Experimental

All chemicals were purchased from Sigma-Aldrich®, Fisher Scientific®, VWR® or Acros® and used without further purification. All solvents were Reagent grade or above, purchased from Sigma-Aldrich®, Fisher Scientific® or VWR® and used without further purification. Nuclear Magnetic Resonance (NMR) spectra were recorded on either a Bruker Avance III 300 MHz or a Bruker Avance III 400 MHz spectrometer. Chemical shifts are reported in ppm (units) referenced to the following solvent signals: dimethylsulfoxide (DMSO)-*d*₆ H 2.50 and D₂O H 4.79. Infrared (IR) spectra were recorded on a PerkinElmer Spectrum Two FT-IR spectrometer.

Gel Permeation Chromatography (GPC) was performed with a Shimadzu Prominence LC-20A fitted with a Thermo Fisher Refractomax 521 Detector and a SPD20A UV-vis Detector. Boc-Protected poly(acryloylglycine hydrazide) was analysed using 0.05 M LiBr in dimethylformamide (DMF) at 60 °C, or 0.005 M NH₄BF₄ in DMF at 50 °C, as the eluent and a flow rate of 1 mL min⁻¹. The instrument was fitted with a Polymer Labs PolarGel guard column (50 × 7.5 mm, 5 µm) followed by two PLGel PL1110–6540 columns (300 × 7.5 mm, 5 µm). Molecular weights were calculated based on a standard calibration method using polymethylmethacrylate. Poly(acryloylglycine hydrazide) Px was analysed using Dulbecco's Phosphate Buffered Saline 0.0095 M (PO₄) without Ca and Mg as the eluent and a flow rate of 1 mL min⁻¹. The instrument was fitted with an Agilent PL aquagel-OH column (300 × 7.5 mm, 8 mm) and run at 35 °C. Dialysis was performed in deionised water at room temperature for a minimum of 48 h using a Spectra/Por 6 1000 Molecular weight cut-off (MWCO) 38 mm width membrane.

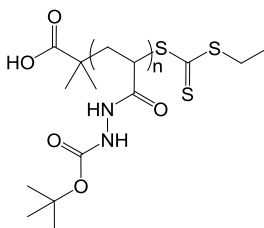
BOC-acryloyl hydrazide



Acrylic acid (3.733 mL, 54.95 mmol) and tert-butyl carbazate (6.002 g, 45.416 mmol) were dissolved in a 2:1 H₂O/THF mixture (120+60 mL) at RT. N-(3-dimethylaminopropyl)-N'-ethylcarbodiimide hydrochloride (EDC) (12.290 g, 64.11 mmol) was slowly added to the solution during 15 minutes and left stirring for 3 h. The crude reaction was extracted with EtOAc (3 x 75 mL) and the organic layer was washed with saturated NaHCO₃ (3 x 75 mL), H₂O (50 mL) and brine (2 x 50 mL). The organic phase was dried with anhydrous Na₂SO₄, the solvent was removed at reduced pressure to obtain a white solid crude product that was purified by recrystallization from EtOAc (70 °C to RT, followed by cooling in a freezer overnight) to afford (5.05 g, 50% yield) of a white crystalline powder identified as tert-Butyl 2-acryloylhydrazine-1-carboxylate (BOC-acryloyl hydrazide). *R*_f = 0.87 (100% EtOAc).

ν_{\max} (neat)/cm⁻¹ 3311m sh (N-H), 3221m sh (N-H), 2981w sh (C-H), 1715s sh (C=O), 1668s sh (C=O); δ_{H} (300 MHz, DMSO-*d*₆) [calibrated using (CHD₂) (CD₃)₂SO resonance at 2.50 ppm] 1.40 (s, 9H, C(CH₃)₃), 5.69 (dd, 1H, CH₂CH), 6.17-6.20 (m, 2H, CHCH₂), 8.84 (s, 1H, OC(O)NH), 9.79 (s, 1H, CHC(O)NH); δ_{C} (100 MHz, DMSO-*d*₆) [calibrated using (CD₃)₂SO resonance at 39.52 ppm] 28.1 (C(CH₃)₃), 79.2 (C(CH₃)₃), 126.2 (CH₂CH), 129.4 (CH₂CH), 155.3 (OC(O)NH), 164.3 (CHC(O)NH).

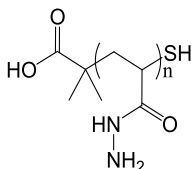
Poly(BOC-acryloyl hydrazide)



In a typical experiment 4,4'-azobis(4-cyanovaleric acid) (ACVA) (15.0 mg, 0.054 mmol) and CTA (72.3 mg, 0.268 mmol) were added sequentially to a solution of BOC-acryloyl hydrazide (2.50 g, 13.426 mmol) in DMSO (15 mL). A 50 μ L aliquot of this solution was taken (T_0) to aid in the calculation of conversion. The reaction mixture was sealed and degassed with argon for 30 min. The degassed solution was left to react at 70 °C for 6 h. The reaction was stopped by exposing it to air and cooling it at RT. A 50 μ L aliquot of this solution was taken (T_f) to calculate the rate of monomer conversion at the end of the polymerization. The polymer was purified by dialysis against water. The water was removed by lyophilisation and by drying in a desiccator with P₂O₅ to afford BOC-PAH as an offwhite powder (2.2 g, 73% yield).

UV (DMSO) λ_{max} 300 nm; ν_{max} (neat)/cm⁻¹ 3244m br (N-H), 2916w sh (C-H), 1642s br (C=O), 1523m sh (C=O); δ_{H} (300 MHz, DMSO-d₆) [calibrated using (CHD₂)(CD₃)SO resonance at 2.50 ppm] 1.41 (br, 11H, 9H in C(CH₃)₃, 2H in CHCH₂), 2.03 (br, 1H, CHCH₂), 8.60 (br, 1H, OC(O)NH), 9.22 (br, 1H, CHC(O)NH); Conversion 82%; DP (UV-Vis) 45; Mn (DMF GPC) 12778; \bar{D} (DMF GPC) 1.38.

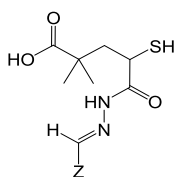
Poly(acryloyl hydrazide)



In a typical experiment, trifluoroacetic acid (TFA) (15 mL) was added dropwise to Poly(BOC-Acryloyl hydrazide) (1.5 g) and the yellow solution was stirred at RT and was let to react overnight. Excess of TFA was removed by blowing a steady stream of argon and the resulting oil was diluted in water (15 mL). The PAH·TFA salt formed was neutralised by adding NaHCO₃ until no foaming was observed. The crude polymer was purified by dialysis against water. The water was removed by lyophilisation and by drying in a desiccator with P₂O₅ to afford **PAH** as a white powder (650 mg, 92% yield).

ν_{max} (neat)/cm⁻¹ 3254w br (N-H), 1609m br (C=O), 1428s sh (C-C); δ_{H} (300 MHz, D₂O) [calibrated using HDO resonance at 4.79 ppm] 0.95 (s, 3H, C(CH₃)₃), 1.01 (s, 3H, C(CH₃)₃), 1.59-2.08 (br m, 3H x DP, CHCH₂); δ_{C} (100 MHz, D₂O) 34.3 (CHCH₂), 40.5 (CHCH₂), 174.9 (CHC(O)NH); DP (¹H NMR) 43; Mn (DPBS GPC) 8431; \bar{D} (DPBS GPC) 1.27.

Functionalization of poly(acryloyl hydrazide) with aldehydes

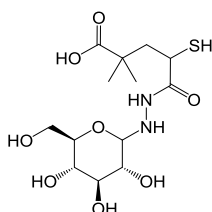


Depending on the solubility of the aldehydes different solvent conditions were used: 5% AcOH in D₂O pH 2.9 for hydrophilic aldehydes soluble in acidic conditions, 100 mM Na₂HPO₄ in D₂O pH 9.1 for hydrophilic aldehydes soluble in basic conditions, and 95% DMSO d₆ 5% AcOH in D₂O for aldehydes insoluble in water (water was still needed to dissolve PAGH as it is insoluble in DMSO).

To obtain a final concentration of 62.5 mM functionalized polymer, 10.70 mg (125 μ mol) of PAH was dissolved in 1 mL of the previously mentioned solvents, in a different vial the aldehyde (125 μ mol) was dissolved in 1 mL of the same solvent. Both stocks were mixed 1:1 volumes and incubated at 60 °C for 24 h, then were analysed by ¹H NMR spectroscopy.

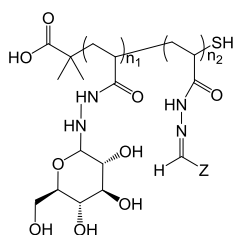
To obtain a final concentration of 125 mM functionalized polymer we dissolved 21.50 mg (250 μ mol) of PAH in 1 mL of the previously mentioned solvents, in a different vial the aldehyde (250 μ mol) was dissolved in 1 mL of the same solvent. Both stocks were mixed 1:1 volumes and incubated at 60 °C for 24 h, then were analysed by ¹H NMR spectroscopy.

Functionalization of poly(acryloyl hydrazide) with sugars



To obtain a final concentration of 125 mM functionalized polymer, 10.70 mg (250 μ mol) of PAH was dissolved in 1 mL of 5% AcOH in D₂O pH 2.9, in a different vial 250 μ mol of sugar was dissolved in 1 mL of the same solvent. Both stocks were mixed 1:1 volumes and incubated at 60 °C for 24 h, samples were taken and were spiked with DMAP as integration standard, then analysed by ¹H NMR spectroscopy and compared with sugar controls to quantify the amount of free sugar in solution.

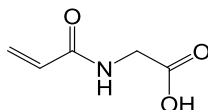
Co-functionalization of poly(acryloyl hydrazide) with sugars and aldehydes.



To obtain a final concentration of 125 mM co-functionalized polymer, 43 mg (500 μ mol) of PAH was dissolved in 1 mL of 5% AcOH in D₂O pH 2.9, in a different vial 500 μ mol of sugar was dissolved in 1

mL of the same solvent. Both stocks were mixed 1:1 volumes and incubated at 60 °C for 24 h, samples were taken and were spiked with DMAP as integration standard then were analysed by ^1H NMR spectroscopy and compared with sugar controls to quantify the amount of free sugar in solution. After the initial functionalization of PAH with the sugar took place, in a different vial the aldehyde (250 mmol) was dissolved in 1 mL of the same solvent. Both stocks were mixed 1:1 volumes and incubated at 60 °C for 24 h, then were analysed by ^1H NMR spectroscopy.

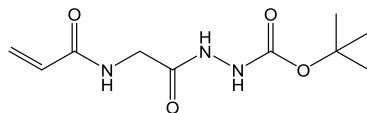
Acryloylglycine synthesis



Glycine hydrochloride (15.057g, 135 mmol) was dissolved in NaOH 2M (250 mL) and cooled in an ice bath. Acryloyl chloride (27.3 mL, 260 mmol) was added dropwise for 30 minutes. The mixture was let reacting overnight. The crude mixture was neutralized with HCL 36% until pH 1, then saturated with NaCl and extracted with EtOAc (75 x5). The organic phase was dried with anhydrous MgSO_4 , filtered, and the solvent was removed under reduced pressure to afford a crude white product. The crude product was purified by recrystallization from EtOAc (70 °C to RT, followed by cooling in freezer) to afford a white crystalline (5.62 g, 32.3% yield) powder identified as Acryloylglycine.

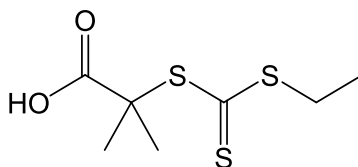
^1H NMR (300 MHz, $\text{DMSO}-d_6$) δ 12.61 (s, ^1H , OH), 8.44 (t, J = 5.9 Hz, 1H, NH), 6.68 – 5.24 (m, 3H, CH_2CH), 3.83 (d, J = 6.0 Hz, 2H, CH_2).

BOC-Acryloylglycine



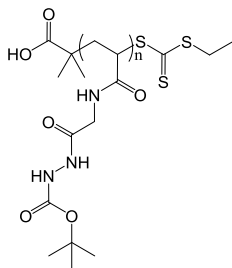
Acryloylglycine (3.83 g, 29.70 mmol) and tert-butyl carbazate (3.27 g, 25.26 mmol) were dissolved in a H_2O /THF mixture (2:1, 96 mL) at RT. N-(3-dimethylaminopropyl)-N'-ethylcarbodiimide hydrochloride (EDC) (6.64 g, 35.00 mmol) was added in portions to the solution over 15 minutes and left stirring overnight. The crude reaction was filtered then extracted with EtOAc (5 x 75 mL) and the organic layer was washed with saturated NaHCO_3 (75 mL), and H_2O (50 mL). The organic phase was dried with anhydrous MgSO_4 , filtered, and the solvent was removed under reduced pressure to afford a crude off white product. The crude product was purified by recrystallization from EtOAc (70 °C to RT, followed by cooling in freezer, and filtered) to afford a white powder (2.50 g, 40.7% yield) identified as Boc-protected Acryloylglycine. ^1H NMR (300 MHz, $\text{DMSO}-d_6$) δ 9.68 (s, 1H,), 8.76 (s, 1H), 8.29 (dt, J = 54.0, 5.7 Hz, 1H), 6.47 – 5.51 (m, 3H, $\text{CH}_2\text{-CH}$), 3.84 (dd, J = 21.4, 5.7 Hz, 2H, CH_2), 1.41 (d, J = 10.4 Hz, 9H $\text{C}(\text{CH}_3)_3$). ^{13}C NMR (101 MHz, $\text{DMSO}-d_6$) δ 168.55, 164.81, 155.19, 131.50, 125.49, 79.15, 28.05.

2-(((Ethylthio)carbonothioyl)thio)-2-methylpropanoic acid (CTA)



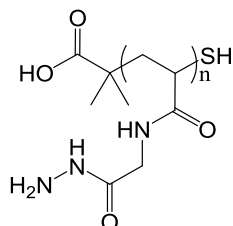
The synthesis route reported by Skey and O'Reilly¹⁷⁰ was followed. Ethanthiol (2.502 mL, 47.07 mmol), potassium phosphate (16.641 g, 78.40 mmol) and carbon disulphide (9.306 mL, 96.03 mmol) were dissolved in acetone (150 mL), after 90 minutes at RT bromoisobutyric acid (7.855 g, 47.04 mmol) was added, the reaction was let to react overnight at RT. The solution was filtered, and the solvent was removed under reduced pressure producing a crude orange oil that was dissolved in DCM (100 mL), washed with HCl 0.2M (50 mL x5), ELGA water (50 mL x2). The organic phase was dried with MgSO₄, filtered, and the solvent was removed under reduced pressure generating an orange oil. The oil was dissolved in 75% diethyl ether and 25% hexane and separated by column chromatography in silica gel. Fractions were collected and the solvent evaporated at reduced pressure, producing a yellow oil that was kept at reduced pressure until it solidified in the form of an orange solid. The product was purified by recrystallization from Hexane (55 °C to RT, followed by cooling in freezer at 18 °C, and filtered) to afford a yellow powder (2.880 g, 27.7% yield) identified as 2-(((Ethylthio)carbonothioyl)thio)-2-methylpropanoic acid. ¹H NMR (300 MHz, DMSO-d₆) δ (ppm) 12.59-13.22 (br, ¹H, COOH), 3.30 (q, 2H, SCH₂CH₃), 1.62 (s, 6H, ((CH₃)₂), 1.25 (t, 3H, CH₃).

Poly(BOC-acryloylglycine hydrazide)



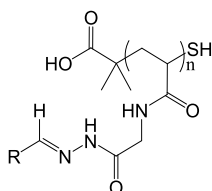
For a typical experiment Boc-acryloylglycine (1.0 g, 5.02 mmol), CTA (22.52 mg, 0.100 mmol) and ACVA (5.63 mg, 0.020 mmol) were added in sequence to 4.02 mL of DMSO and stirred until dissolved, A 50 µL aliquot of this solution was taken at this stage to aid in the calculation of conversion. The reaction mixture was then sealed and degassed with Argon for 30 min. The degassed solution was left to react at 70 °C for 4 h, and was stopped by exposing it to air and allowing it to cool down to room temperature. A 50 µL aliquot of this solution was taken to aid in the calculation of conversion, ranging from 80-90% for a DP₄₀₋₄₅. The polymer was purified by dialysis in ELGA water. The water was removed by lyophilisation and by drying in a desiccator with P₂O₅ to afford 800 mg of Boc-P₄₀ as an off-white powder (66% yield).

Poly(acryloylglycine hydrazide)



Trifluoroacetic acid 99.5% (TFA, 8 mL) was added dropwise to Boc-protected poly(acryloylglycine) (800 mg) and the yellow solution was stirred at RT and was let to react overnight. Excess of TFA was removed blowing Argon resulting into a yellow oil, that was diluted in ELGA water (8 mL), and the PAGH·TFA salt was neutralized with NaHCO₃ until no bubbling was observed. The solution was then dialyzed against water. The water was removed by lyophilization and by drying in a desiccator with P₂O₅ to afford 424 mg of **PAGH** as an off-white powder (89% yield).

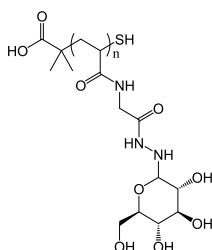
Functionalization of poly(acryloylglycine hydrazide) with aldehydes



Depending on the solubility of the aldehydes different solvent conditions were used: 5% AcOH in D₂O pH 2.9 for aldehydes soluble in acidic conditions, 100 mM Na₂HPO₄ in D₂O pH 9.1 for aldehydes soluble in basic conditions, and 95% DMSO-d₆ 5% AcOH in D₂O for aldehydes insoluble in water (water was still needed to dissolve PAGH as it is insoluble in DMSO).

To obtain a final concentration of 62.5 mM functionalized polymer, 17.855 mg (125 μmol) of PAGH was dissolved in 1 mL of the previously mentioned solvents, in a different vial the aldehyde (125 μmol) was dissolved in 1 mL of the same solvent. Both stocks were mixed 1:1 volumes and incubated at 60 °C for 24 h, then were analysed by ¹H NMR spectroscopy.

Functionalization of poly(acryloylglycine hydrazide) with sugars



To obtain a final concentration of 62.5 mM functionalized polymer, 17.855 mg (125 μmol) of PAGH was dissolved in 1 mL of 5% AcOH in D₂O pH 2.9, in a different vial 125 μmol of sugar was dissolved in 1 mL of the same solvent. Both stocks were mixed 1:1 volumes and incubated at 60 °C for 24 h, samples

were taken and were spiked with DMAP as integration standard then were analysed by ^1H NMR spectroscopy and compared with sugar controls to quantify the amount of free sugar in solution.

3. *Escherichia coli* aggregation and biofilm formation induced by RAFT polymers

3.1 Background

Escherichia coli as a model organism for biofilm study.

Escherichia coli is a facultative anaerobe gram-negative rod-shaped nonsporulating bacterium that can be inexpensively grown in laboratory conditions¹⁷⁷. Many *E. coli* strains in nature can be found in the form of biofilm communities attached to the biotic surface of the intestinal tract of animals in a commensal relationship with its host.

Occupying a niche in the gut microbiota it can prevent the colonization of pathogenic bacteria¹⁷⁸. As a facultative anaerobe, it can deplete oxygen generating anaerobic pockets in the gastrointestinal mucosal surface creating a thriving environment that strict anaerobes can colonize. However, there are also many pathogenic *E. coli* strains responsible of gastrointestinal and urinary tract infections, and also responsible for abiotic colonization and further infection of medical devices like urethral and intravascular catheters, prosthetic joints, shunts, and prosthetic grafts¹⁷⁹.

E. coli is of special interest in the biotechnological industry where is one of the favourite hosts for recombinant protein production. Most bioreactors use planktonic bacteria for the bio product harvest, but some recent studies have shown the potential use of biofilm bioreactors for this purpose¹³⁹.

E. coli is able to colonize biotic and abiotic surfaces, it has medical impact and industrial use, is easy to maintain and manipulate in laboratory conditions and there are many tools available for its modification, making it a prime candidate as a model organism for the study of biofilm formation.

One of the most widely used strains for the study of *E. coli* is K12, which was initially isolated in 1922¹⁸⁰ from a stool sample of a human patient convalescent of diphtheria. At the time, bacterial freezing stocks was not a widespread practice and many sub-lineages of K12 appeared¹⁸⁰ due to the fast accumulation of mutations in strains maintained under laboratory conditions¹⁸¹. This domestication led to the generation of a lineage of K12 strains that had genotypes different to the ones present in wild type *E. coli* isolates, these strains lacked any of the known *E. coli* virulence factors¹⁸² and were unable to colonize the human gut¹⁸³, making K12 strains safe non-pathogenic bacteria suitable for microbiological studies.

In this study two sub-lineages from K12 were used: *E. coli* K12 PHL628 (MG1655 *malA-kan ompR234*), and *E. coli* K12 PHL644 (MC4100 *malA-kan ompR234*), both strains derive from MG1655¹⁸⁴ and MC4100¹⁸⁵ respectively, which present phenotypes close to wild type *E. coli*.

Both of these strains present the allele *ompR234*⁶¹, that has a point mutation on the gene *ompR* that encodes for a mutant OmpR protein. This protein regulates the promoter of *csgD* a gene whose product controls the expression of the *csgA* gene responsible for curli production. This mutant variant from *ompR234* is more efficient at activating this promoter leading to an increase in curli expression and biofilm formation. This mutation is important as many domesticated laboratory strains of *E. coli*

K12 are unable to generate biofilms and this mutant allele confers them of the capability of expressing this phenotype.

3.2 Objectives

PAH and PAGH as a platform for microbiological applications

The main objective of this study was to test DP₄₀ functionalized polymers that were generated on chapter 1 (**Figure 3.1, Table 3.1**) and investigate if **PAH** and **PAGH** are a suitable platform for the study of functional groups in vivo with microbiological applications.

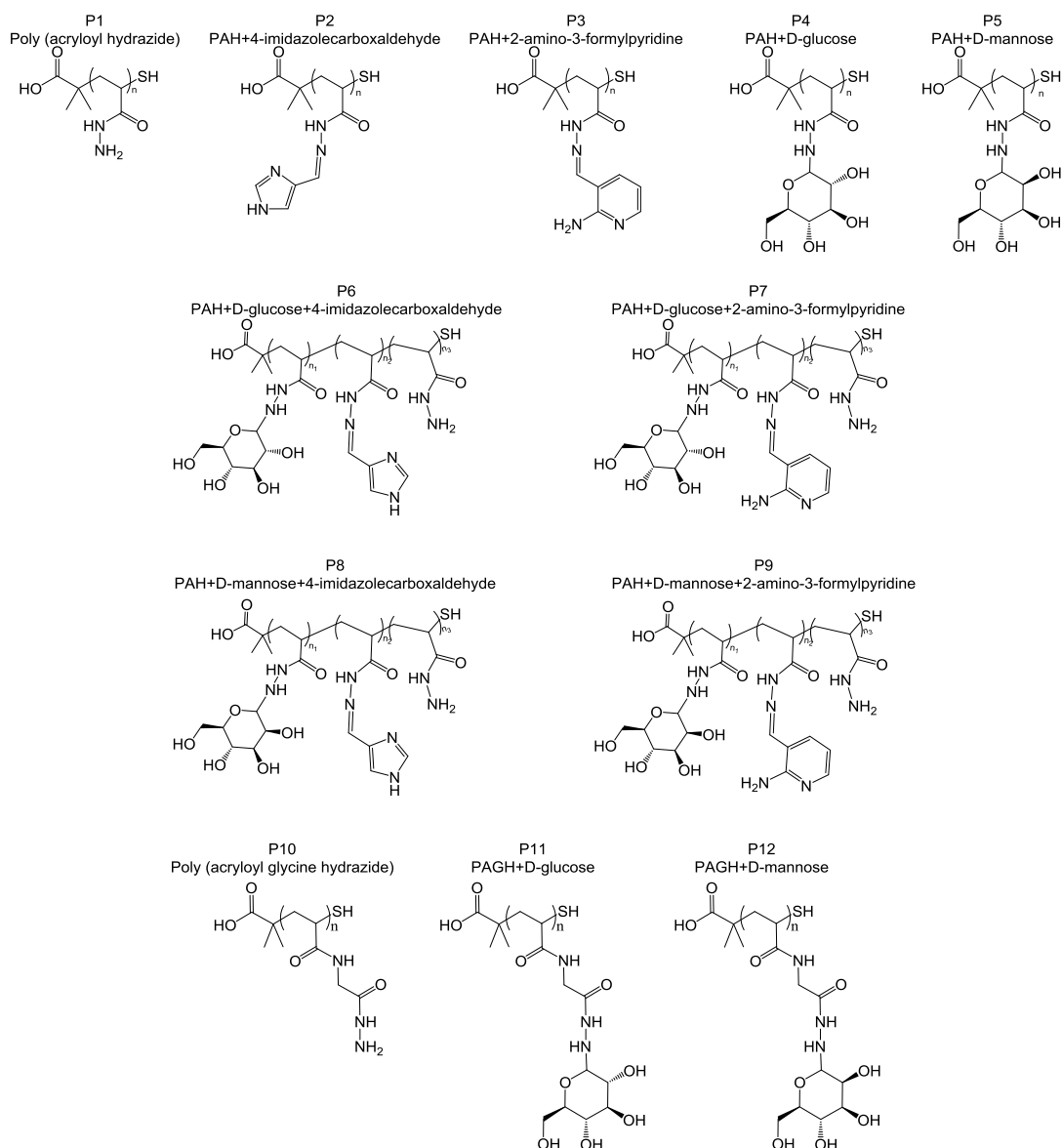


Figure 3.1: Library of functionalized PAH and PAGH polymers to be tested against *E. coli*.

It was believed that some of the generated polymers may have the potential to interact with *E. coli* in liquid solution and induce the formation of synthetic biofilm communities, either by interacting with membrane receptors and eliciting physiological changes that trigger aggregation, or by electrochemical interactions like charge compatibility to allow for the sequestering and clustering of bacteria. If successful, it could prove the potential of our functionalized polymers as a tool for microbiological applications.

Table 3.1: Library of functionalized PAH and PAGH polymers to be tested on *E. coli*.

Polymer	Functionalizations
P1	PAH scaffold
P2	PAH+4-imidazolecarboxaldehyde
P3	PAH+2-amino-3-formylpyridine
P4	PAH+D-glucose
P5	PAH+D-mannose
P6	PAH+ D-glucose + 4-midazolecarboxaldehyde
P7	PAH+ D-glucose + 2-amino-3-formylpyridine
P8	PAH+ D-mannose + 4-imidazolecarboxaldehyde
P9	PAH+ D-mannose + 2-amino-3-formylpyridine
P10	PAGH scaffold
P11	PAGH+ D-glucose
P12	PAGH+ D-mannose

3.3 Results and discussion

3.3.1 PAH as a platform for microbiological applications

3.3.1.1 Incubation assays

Prior to the start of the polymer testing on *E. coli* it was necessary to design a method that would allow to check if the bacteria aggregate after incubation with one of the polymers. It was theorised that if any of the polymers was successful in aggregating bacteria, part of the planktonic population would sink to the bottom of the water column (**Figure 3.2**).

The incubation experiments were performed on spectrophotometry cuvettes, that way the optic density (OD) of the bacterial sample could be measured over time. If any of the polymers achieved bacterial aggregation, inducing sedimentation to the bottom of the cuvette could be measured as a drop in the optic density of the sample.

Separate overnight cultures of strains PHL644 and PHL628 were grown from single cell colonies overnight (LB medium, 30 °C, 150 rpm). Bacteria cultures were washed with sterilized ELGA water (deionised water) discarding the LB medium to avoid any interference of the growth media with the incubation experiments. After the washing step, the optic density of the bacterial culture was measured at 600 nm (OD₆₀₀) via spectrophotometry then diluted with ELGA water until OD₆₀₀=1.

For every incubation experiment 953 µL of bacteria OD₆₀₀=1 was transferred to a spectrophotometry cuvette, then incubation with: 47 µL of 125 mM polymer to a final concentration of 6.17 mM, dissolved in either 5% AcOH in D₂O pH 2.9, 100 mM phosphate buffer pH 5.5, or ELGA water; or 47 µL of control (125 mM of free aldehydes in 5% AcOH in D₂O; 125 mM of free sugars in 5% AcOH in D₂O; 5% AcOH in D₂O; 100 mM phosphate buffer; or ELGA water). The optic density of the incubated bacterial samples was measured at 600 nm for 24 h and all the experiments were performed simultaneously.

Most of the polymer samples tested with *E. coli* were dissolved in a solution of 5% AcOH in D₂O pH 2.9, that was part of the chemical conditions necessary to functionalize the hydrazones of the polymer with the functional groups.

The polymers used to test the biological applications of **PAH** on *E. coli* were dissolved in buffers: 5% AcOH in D₂O pH 2.9, or 100 mM phosphate buffer pH 5.5. These samples were diluted 20.27fold when transferred into the cuvettes. Accounting for this dilution factor the final pH of cuvettes with samples dissolved on 5% AcOH in D₂O with a final concentration of 0.25% AcOH in D₂O would have an estimated pH of 4.2, while the samples incubated with a final concentration of 4.93 mM phosphate buffer would have an estimated pH of 6.8.

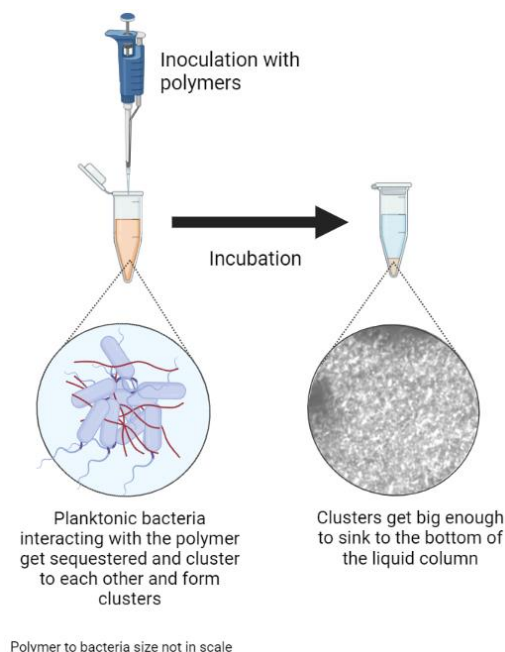


Figure 3.2: Proposed method for screening polymer induced bacterial aggregation.

Incubation with control buffers and ELGA water

The initial approach to the incubation studies was to establish a baseline behaviour of how the OD of the bacterial samples changed over time when they were incubated with the acidic buffer (5% AcOH in D₂O pH), basic buffer (100 mM phosphate buffer), and ELGA water (deionized water). This information was important as any divergent trends in the OD over time would point to a change induced by some of the polymer samples used in the study.

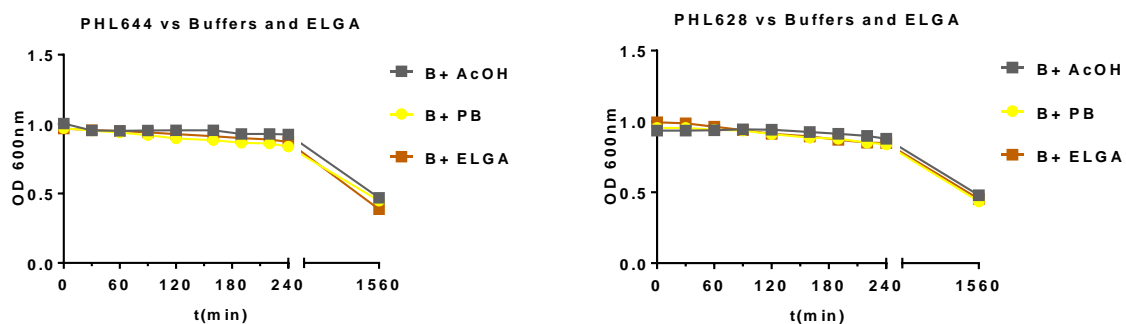


Figure 3.3: Spectrophotometry measurements of optic density ($\lambda = 600$ nm) taken over 24 h after the incubation of 953 μ L of *E. coli* PHL644 and *E. coli* PHL628 with: (B+ AcOH) 47 μ L of 5% AcOH in D₂O buffer. (B+ PB) 47 μ L of 100 mM phosphate buffer. (B+ ELGA) 47 μ L of ELGA water.

When the results were analysed a common trend could be observed (**Figure 3.3**), there was a small decline of the OD over time, reaching half of the initial OD 24 h after the beginning of the incubation assay due to the normal sedimentation of the bacteria. These controls also indicated that all the LB had been removed during the washing procedure. In the case that there were still significant remains

of a food source we would have witnessed an increase in the OD over time corresponding with bacterial growth.

Incubation with PAH scaffold P1

For the following experiment 953 μL of the bacterial strains were incubated with 47 μL of 125 mM **PAH** in different solvent conditions: AcOH 5% in D_2O buffer, 100 mM phosphate buffer, or ELGA water. The controls for this experiment were the results obtained when the bacterial strains were incubated with the control buffers and ELGA water (**Figure 3.3**).

The results from the incubation of both strains with the **PAH** scaffold **P1** (**Figure 3.4**) showed how the bacteria incubated with polymer samples dissolved on 5% AcOH in D_2O buffer had a fast decline on its OD after 60 minutes. This decline was due to a visible clustering of bacteria in the middle of the water column that was slowly sinking to the bottom; 4 h after the beginning of the incubation assay, most of the sample had sedimented to the bottom of the cuvette; and 24 h after the beginning of the experiment the OD of the sample had reached a value of 0, meaning that all the planktonic bacteria were now clustered at the bottom of the cuvette and that the spectrophotometer was only measuring the water column.

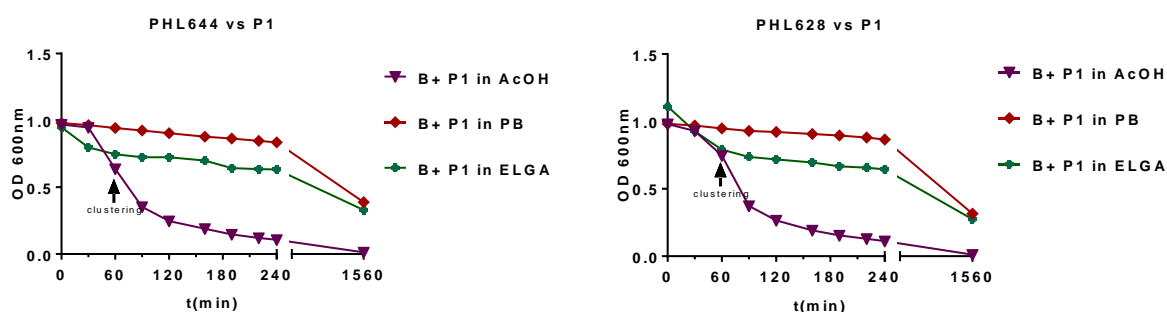


Figure 3.4: Spectrophotometry measurements of optic density ($\lambda = 600 \text{ nm}$) taken over 24 h after the incubation of 953 μL of *E. coli* PHL644 and *E. coli* PHL628 with: (B+ P1 in AcOH) 47 μL of P1 125 mM dissolved in 5% AcOH in D_2O buffer. (B+ P1 in PB) 47 μL of P1 125 mM dissolved in 100 mM phosphate buffer. (B+ P1 in ELGA) 47 μL of P1 125 mM dissolved in ELGA water. The final concentration of polymers in solution was of 6.17 mM.

The samples of strains PHL644 and PHL628 incubated with **P1** in 100 mM phosphate buffer at pH 5.5 and ELGA water showed a small decrease of OD over time until a value half of the initial OD=1 was reached 24 h after initial incubation, there was no clustering visible during these experiments. These results were similar to the ones obtained when strains PHL644 and PHL628 were incubated with 5% AcOH in D_2O buffer, 100 mM phosphate buffer, and ELGA water (**Figure 3.3**), when a similar trend was observed.

Incubation with aldehyde functionalized PAH P2 and P3

For the following test, 953 μL of the bacterial strains PHL644 and PHL628 were incubated separately with 47 μL of 125 mM **PAH** functionalized with 4-imidazolecarboxaldehyde (**P2**), and 47 μL of 125 mM **PAH** functionalized with 2-amino-3-formylpyridine (**P3**). The controls for this experiment were 953 μL of the bacterial strains incubated separately with 47 μL of 125 mM 4-imidazolecarboxaldehyde, and

47 μL of 125 mM 2-amino-3-formylpyridine. All polymers and aldehydes were dissolved in 5% AcOH in D_2O buffer.

When the aldehyde functionalized polymers **P2** and **P3** were tested on strains PHL644 and PHL628 (**Figure 3.5**) clustering was not observed, neither a fast decrease of the OD of the sample during the run of the experiment. In fact, the incubation with these two polymers had the result of increasing the OD of both samples over OD=1, that might be explained if these functionalized polymers have higher absorbance at this wavelength, something that the strains incubated with the free aldehydes controls did not show. Overall, bacterial samples incubated with polymers **P2** and **P3** and their aldehyde controls follow a similar pattern to the one described with the baseline bacterial controls (**Figure 3.3**), where OD decreases over time without forming clusters reaching and OD around 0.5 24 h after the beginning of the experiment.

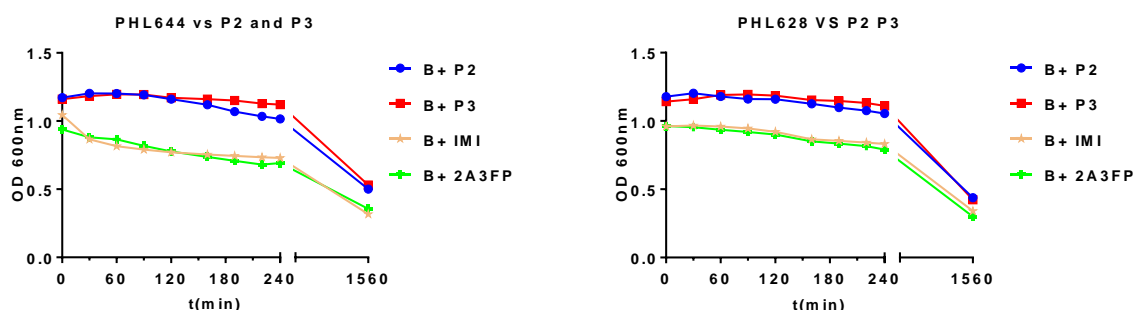


Figure 3.5: Spectrophotometry measurements of optic density ($\lambda = 600 \text{ nm}$) taken over 24 h after the incubation of 953 μL of *E. coli* PHL644 and *E. coli* PHL628 with: (B+ P2) 47 μL of P2 125 mM. (B+ P3) 47 μL of P3 125 mM. (B+ IMI) 47 μL of 4-imidazolecarboxaldehyde 125 mM. (B+ 2A3FP) 47 μL of 2-amino-3-formylpyridine 125 mM. Note: all polymer and control samples were dissolved in 5% AcOH in D_2O buffer. The final concentration of polymers in solution was of 6.17 mM.

Incubation with carbohydrate functionalized PAH P4 and P5

For the following test, 953 μL of the bacterial strains PHL644 and PHL628 were incubated separately with 47 μL of 125 mM **PAH** functionalized with D-glucose (**P4**), and 47 μL of 125 mM **PAH** functionalized with D-mannose (**P5**). The controls for this experiment were 953 μL of the bacterial strains incubated separately with 47 μL of 125 mM D-glucose, and 47 μL of 125 mM D-mannose. All polymers and carbohydrates were dissolved in 5% AcOH in D_2O buffer.

The experiments with carbohydrate functionalized **PAH** polymers **P4** and **P5** (**Figure 3.6**) provided results similar to what was observed when strains PHL644 and PHL628 were incubated with **P1** dissolved in 5% AcOH in D_2O (**Figure 3.4**). Both strains incubated with the sugar functionalized **PAH** showed signs of clustering 90 minutes after the beginning of the experiment compared to their controls (the strains incubated with the carbohydrates in 5% AcOH in D_2O) that presented the steady decrease of absorbance reported on the baseline controls when bacteria were incubated just with acidic buffer, basic buffer, and ELGA water (**Figure 3.3**). One thing to note is that not all the clusters induced by these polymers sank to the bottom of the water column, as some clusters remained attached to the walls of the cuvette during the first 4 h of the experiment, and explains why the decrease in OD was not as pronounced as what was observed when the bacteria were incubated with

P1 in 5% AcOH in D₂O (**Figure 3.4**). When the experiment reached its end after 24 h most of the bacteria in the samples incubated by **P4** and **P5** had sedimented to the bottom of the cuvette, while its respective controls had a value close to OD=0.5 similar what was observed with the baseline controls (**Figure 3.3**).

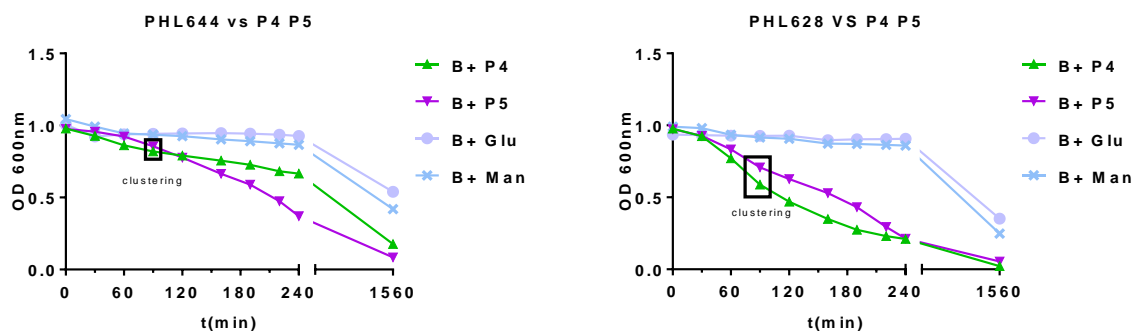


Figure 3.6: Spectrophotometry measurements of optic density ($\lambda = 600$ nm) taken over 24 h after the incubation of 953 μ L of *E. coli* PHL644 and *E. coli* PHL628 with: (B+ P4) 47 μ L of P4 125 mM. (B+ P5) 47 μ L of P5 125 mM. (B+ Glu) 47 μ L of D-glucose 125 mM. (B+ Man) 47 μ L of D-mannose 125 mM. Note: all polymer and control samples were dissolved in 5% AcOH in D₂O buffer. The final concentration of polymers in solution was of 6.17 mM.

Incubation with co-functionalized PAH P6 and P7

For the following test, 953 μ L of the bacterial strains PHL644 and PHL628 were incubated separately with 47 μ L of 125 mM **PAH** co-functionalized with D-glucose and 4-imidazolecarboxaldehyde (**P6**), and 47 μ L of 125 mM **PAH** functionalized with D-glucose and 2-amino-3-formylpyridine (**P7**). The controls for this experiment were 953 μ L of the bacterial strains incubated separately with 47 μ L of 125 mM D-glucose, 47 μ L of 125 mM 4-imidazolecarboxaldehyde, and 47 μ L of 125 mM 2-amino-3-formylpyridine. All polymers, carbohydrates, and aldehydes were dissolved in 5% AcOH in D₂O buffer.

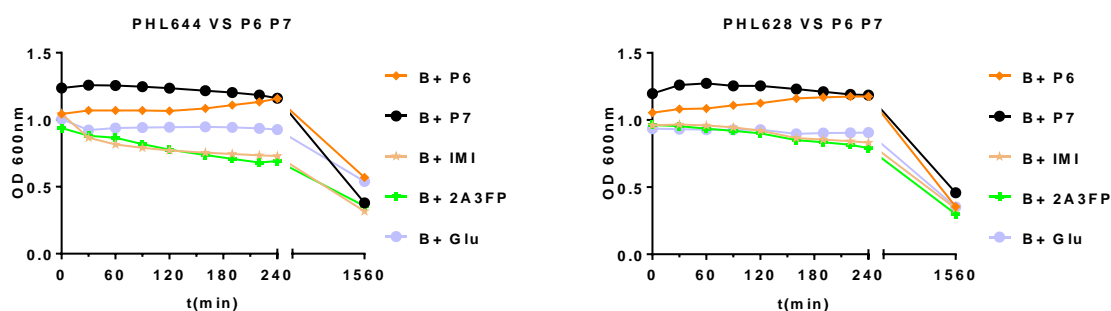


Figure 3.7: Spectrophotometry measurements of optic density ($\lambda = 600$ nm) taken over 24 h after the incubation of 953 μ L of *E. coli* PHL644 and *E. coli* PHL628 with: (B+ P6) 47 μ L of P6 125 mM. (B+ P7) 47 μ L of P7 125 mM. (B+ IMI) 47 μ L of 4-imidazolecarboxaldehyde 125 mM. (B+ 2A3FP) 47 μ L of 2-amino-3-formylpyridine 125 mM. (B+ Glu) 47 μ L of D-glucose 125 mM. Note: all polymer and control samples were dissolved in 5% AcOH in D₂O buffer. The final concentration of polymers in solution was of 6.17 mM.

The data obtained (**Figure 3.7**) showed how none of the co-functionalized polymers **P6** or **P7** were able to induce any aggregation on *E. coli*. The controls for this experiment showed the expected baseline

behaviour with a steady decline on OD until achieving a value close to 0.5 24 h after the beginning of the experiment. The bacterial samples incubated with **P6** and **P7** experienced an increase in the OD of the sample similar to what was observed with the samples that were incubated with polymers **P2** and **P3** (Figure 3.5) functionalized only with aldehydes, then had a steady decline over the duration of the experiment reaching values close to OD=0.5 by the end of the experiment.

Incubation with co-functionalized PAH P8 and P9

For the following test, 953 μL of the bacterial strains PHL644 and PHL628 were incubated separately with 47 μL of 125 mM **PAH** co-functionalized with D-mannose and 4-imidazolecarboxaldehyde (**P8**), and 47 μL of 125 mM **PAH** functionalized with D-mannose and 2-amino-3-formylpyridine (**P9**). The controls for this experiment were 953 μL of the bacterial strains incubated separately with 47 μL of 125 mM D-mannose, 47 μL of 125 mM 4-imidazolecarboxaldehyde, and 47 μL of 125 mM 2-amino-3-formylpyridine. All polymers, carbohydrates, and aldehydes were dissolved in 5% AcOH in D_2O buffer.

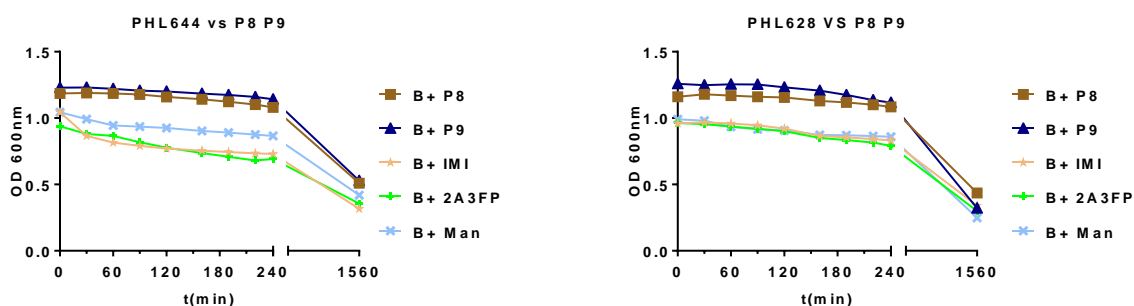


Figure 3.8: Spectrophotometry measurements of optic density ($\lambda = 600 \text{ nm}$) taken over 24 h after the incubation of 953 μL of *E. coli* PHL644 and *E. coli* PHL628 with: (B+ P8) 47 μL of P8 125 mM. (B+ P9) 47 μL of P9 125 mM. (B+ IMI) 47 μL of 4-imidazolecarboxaldehyde 125 mM. (B+ 2A3FP) 47 μL of 2-amino-3-formylpyridine 125 mM. (B+ Man) 47 μL of D-mannose 125 mM. Note: all polymer and control samples were dissolved in 5% AcOH in D_2O buffer. The final concentration of polymers in solution was of 6.17 mM.

Similarly to what was observed with the other co-functionalized polymers, **P8** and **P9** were not able to induce aggregation in strains PHL644 or PHL628 (Figure 3.8), but they generated a slight increase in the OD of the samples incubated with the polymer. Both samples and controls followed the baseline trend with small decreases of OD over time, reaching close to half the initial OD after 24 h.

3.3.1.2 Light microscopy of incubated bacteria

The spectrophotometry assay allowed to analyse the effect of the polymers on *E. coli* from a quantitative standpoint, but it was considered necessary to supplement these experiments with a visual insight of what was happening to the bacteria that were being clustered by **P1**, **P4**, and **P5** dissolved in 5% AcOH in D₂O. Right after the end of the spectrophotometry assay samples from the cuvettes were taken and transferred to slides to visualize under optic microscopy at a magnification of 1000x (**Figure 3.9**, **Figure 3.10**, **Figure 3.11**, **Figure 3.12**).

Light microscopy pictures (**Figure 3.9**, **Figure 3.11**) of *E. coli* PHL644 and PHL628 showed how most of the bacterial population incubated with **P1** in 5% AcOH in D₂O buffer was part of big clusters of bacteria surrounded by what appeared to be an external matrix. When looking at the pictures of the controls of this experiment, it could be observed how bacteria incubated with **P1** in phosphate buffer and ELGA water had no clustering effect on strains PHL644 and PHL628 as most of the population observed was free floating bacteria. These results were in agreement with what was measured during the spectrophotometry assay, and the drop in OD caused by **P1** in 5% AcOH in D₂O buffer was due to its ability to aggregate and cluster *E. coli*.

There was no observable clustering or aggregation when analysing the pictures corresponding with the bacteria incubated with aldehyde functionalized PAH **P2** and **P3** (**Figure 3.9**, **Figure 3.11**). These results were in agreement with what was measured during the spectrophotometry assay.

The images corresponding to the assays performed when the bacteria were incubated with the carbohydrate functionalized PAH **P4** and **P5** (**Figure 3.10**, **Figure 3.12**) showed how they were able to induce aggregation in both strains of *E. coli*, as most of the sample was part of big clusters embedded into what seemed to be extracellular matrix. These pictures validated the result that were obtained through spectrophotometry where drops of OD were reported after 90 minutes of incubation, and confirmed that they were the result of **P4** and **P5** inducing bacterial aggregation, clustering, and sedimentation.

Light microscopy pictures of bacteria incubated with co-functionalized polymers **P6**, **P7**, **P8**, and **P9** (**Figure 3.10**, **Figure 3.12**) showed how some bacteria in these samples were part of minor clusters, but most of the samples screened by optic microscopy remained as individual planktonic bacteria, this might be the cause of why there was no sudden drop in the optic density of the incubated samples during the spectrophotometry assay, maybe because these polymers have poor aggregation capabilities, not strong enough to cluster and sediment most of the bacteria in the water column.

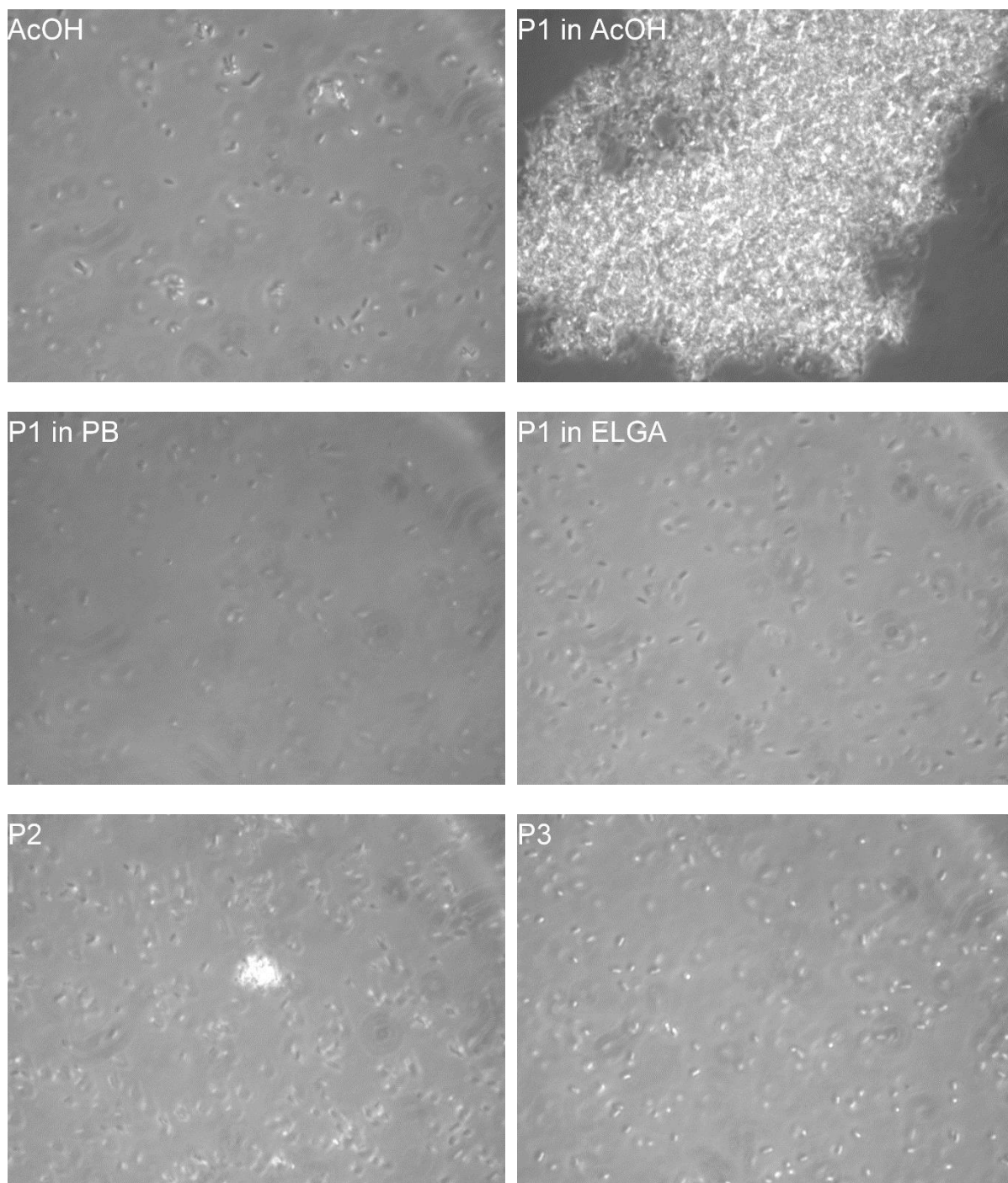


Figure 3.9: Light microscopy pictures taken at 1000X magnification of *E. coli* PHL644 26H after initial incubation. (AcOH) bacteria incubated with 47 μ L of 5% AcOH in D₂O buffer. (P1 in AcOH) bacteria incubated with 47 μ L of 125 mM P1 in 5% AcOH in D₂O buffer. (P1 in PB) bacteria incubated with 47 μ L of 125 mM P1 in 100 mM phosphate buffer. (P1 in ELGA) bacteria incubated with 47 μ L of 125 mM P1 in ELGA water. (P2) bacteria incubated with 47 μ L of 125 mM P2 in 5% AcOH in D₂O buffer. (P3) bacteria incubated with 47 μ L of 125 mM P3 in 5% AcOH in D₂O buffer. The final concentration of polymers in solution was of 6.17 mM.

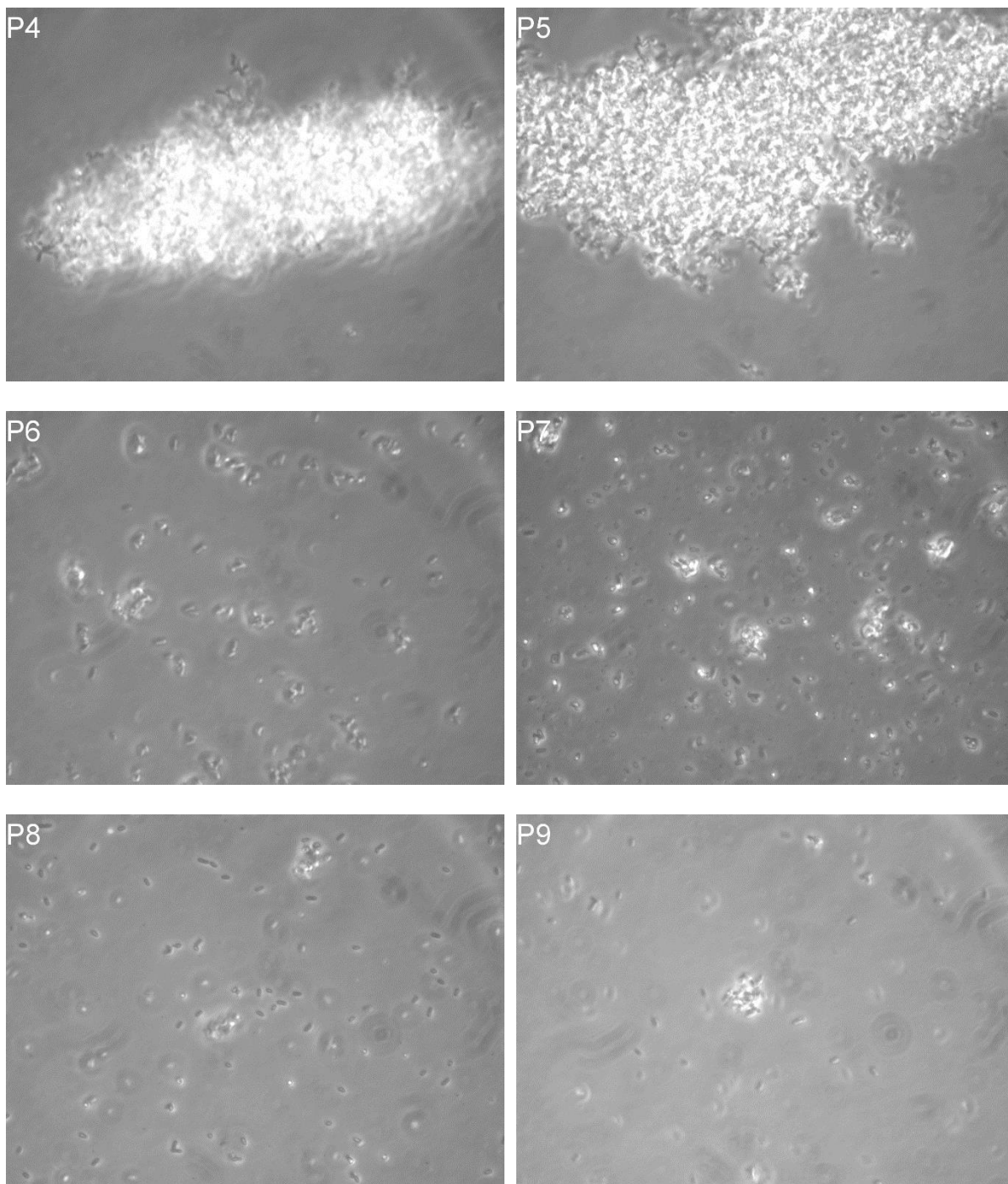


Figure 3.10: Light microscopy pictures taken at 1000X magnification of *E. coli* PHL644 26H after initial incubation. (P4) bacteria incubated with 47 μL of 125 mM P4. (P5) bacteria incubated with 47 μL of 125 mM P5. (P6) bacteria incubated with 47 μL of 125 mM P6. (P7) bacteria incubated with 47 μL of 125 mM P7. (P8) bacteria incubated with 47 μL of 125 mM P8. (P9) bacteria incubated with 47 μL of 125 mM P9. Note: all polymer samples in this figure were dissolved in 5% AcOH in D_2O buffer. The final concentration of polymers in solution was of 6.17 mM.

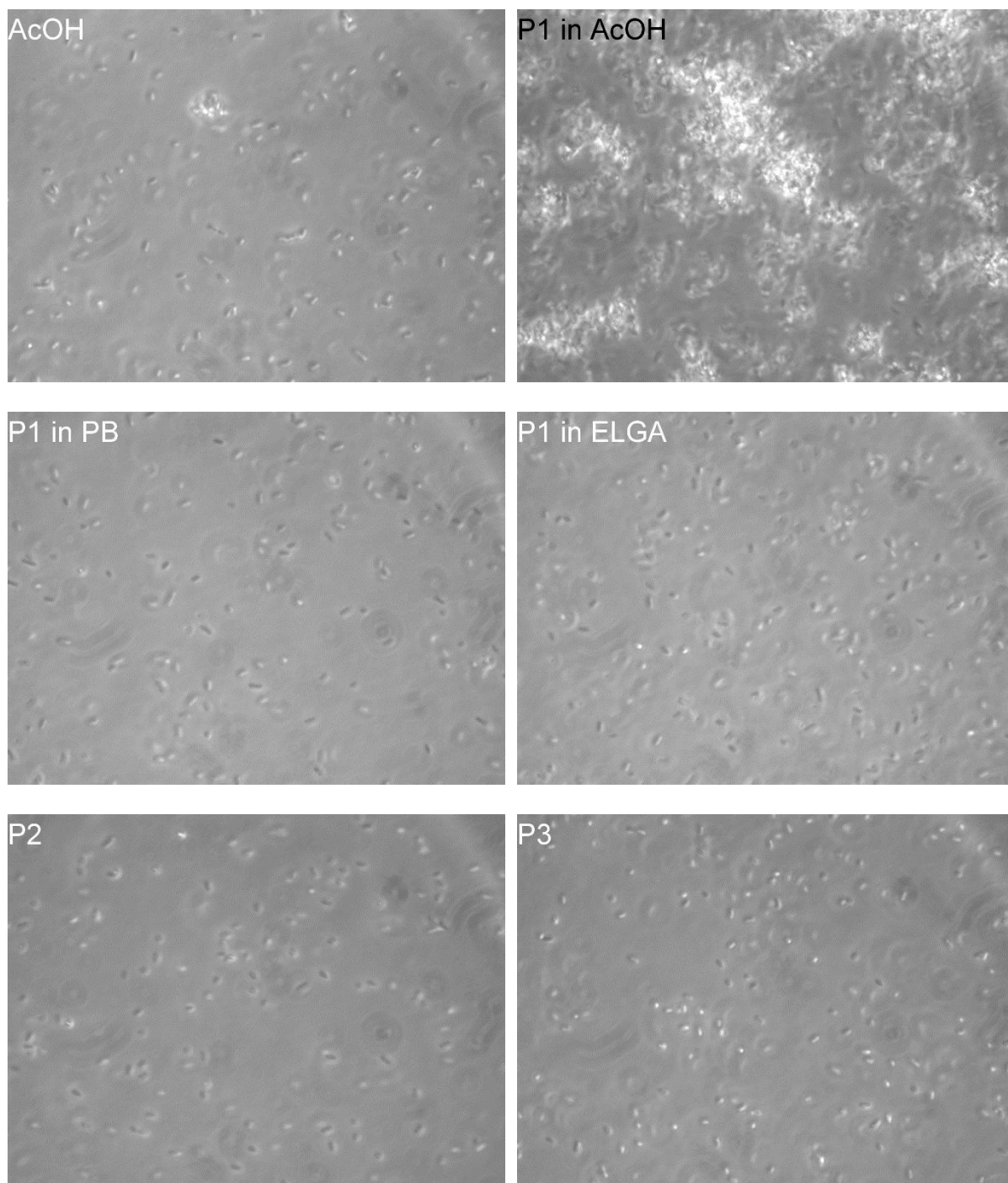


Figure 3.11: Light microscopy pictures taken at 1000X magnification of *E. coli* PHL628 26H after initial incubation. (AcOH) bacteria incubated with 47 μ L of 5% AcOH in D₂O buffer. (P1 in AcOH) bacteria incubated with 47 μ L of 125 mM P1 in 5% AcOH in D₂O buffer. (P1 in PB) bacteria incubated with 47 μ L of 125 mM P1 in 100 mM phosphate buffer. (P1 in ELGA) bacteria incubated with 47 μ L of 125 mM P1 in ELGA water. (P2) bacteria incubated with 47 μ L of 125 mM P2 in 5% AcOH in D₂O buffer. (P3) bacteria incubated with 47 μ L of 125 mM P3 in 5% AcOH in D₂O buffer. The final concentration of polymers in solution was of 6.17 mM.

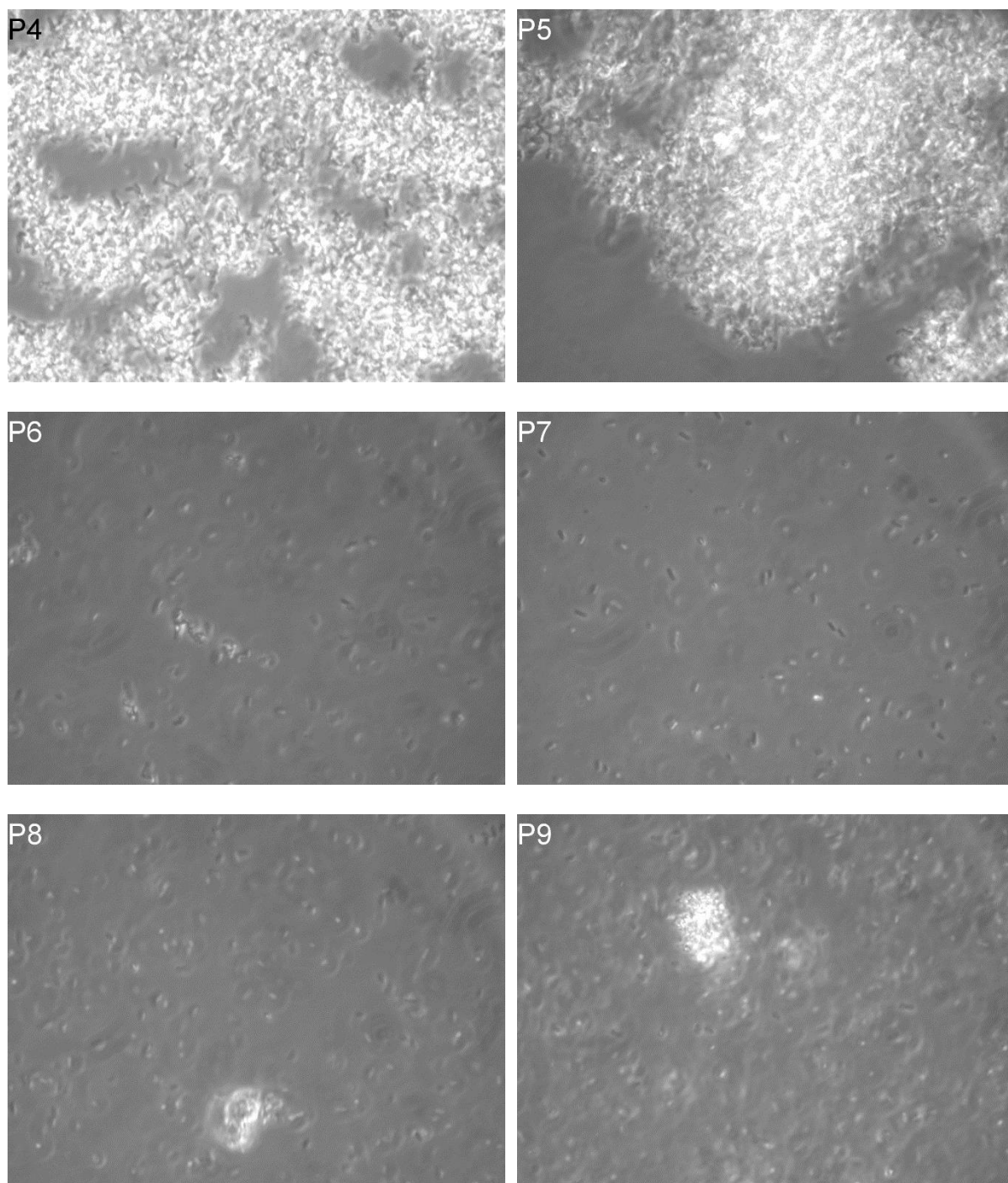


Figure 3.12: Light microscopy pictures taken at 1000X magnification of *E. coli* PHL628 26H after initial incubation. (P4) bacteria incubated with 47 μ L of 125 mM P4. (P5) bacteria incubated with 47 μ L of 125 mM P5. (P6) bacteria incubated with 47 μ L of 125 mM P6. (P7) bacteria incubated with 47 μ L of 125 mM P7. (P8) bacteria incubated with 47 μ L of 125 mM P8. (P9) bacteria incubated with 47 μ L of 125 mM P9. Note: all polymer samples in this figure were dissolved in 5% AcOH in D₂O buffer. The final concentration of polymers in solution was of 6.17 mM.

After these initial results a new incubation assay was performed with **P1**, **P4**, and **P5** 125 mM dissolved in 5% AcOH in D₂O buffer with a final concentration of 6.17 mM on *E. coli* PHL644 in Eppendorf centrifuge tubes. This experiment was performed so clustering induced by these polymers (**Figure 3.13**) could be documented 2 h after the beginning of the incubation assay. A fast aggregation and sedimentation of bacteria could be observed induced by **P1** after 60 minutes, followed by **P4** and **P5**

after 90 minutes. What was interesting is that while **P1** induced clusters sank directly to the bottom of the container, many of the **P4** and **P5** induced bacterial aggregates remained attached to the container walls, while some fell to the bottom of the container.

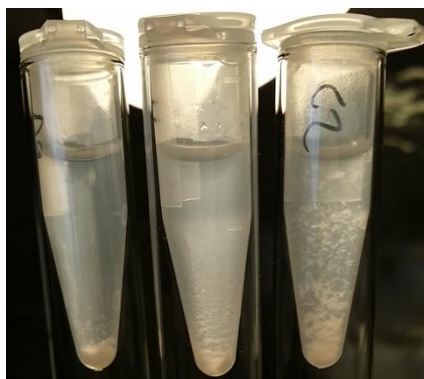


Figure 3.13: Pictures of *E. coli* PHL644 incubated 2 h (from left to right) with P1, P4 and P5, showing visible bacterial clusters and sedimentation. Polymers were dissolved in 5% AcOH in D₂O buffer to a final concentration of 6.17 mM.

3.3.1.3 Dead/alive fluorescence microscopy

There were concerns regarding the source of the clustering effect, if it was the product of the effect of the polymers in acidic solution, or if it was the product of a combination of dead bacteria due the acidic conditions and the effect of the polymers in acidic solution both contributing to the clustering effect observed when *E. coli* was incubated with **P1**, **P4**, and **P5** dissolved in the 5% AcOH in D₂O buffer.

E. coli can grow at moderate acidic conditions¹⁸⁶ (pH 4.0-5.0) to be able to colonize hosts intestinal tract, this acid tolerance is dependent on the presence of minimal medium (pH 4.0) or rich growing mediums (pH > or = 4.5)^{187, 188}. It even can survive several hours at pH as low as 2^{189, 190}, a trait necessary to survive going through the stomach of potential hosts.

The acidity at what *E. coli* is estimated to be at during the incubation experiments was around pH 4.2. Although this pH was within the range of acidity that *E. coli* can grow, the incubated bacteria were stripped of the LB growing medium to avoid interference with the tests of **PAH** effects on the bacteria. *E. coli* tolerance to an acidic environment might be hindered by the lack of growth media, as it could lead to its inability to dedicate metabolic efforts to activate its acidic stress response systems to modulate the lipid composition of its membrane and improve its intracellular pH homeostasis¹⁸⁶ to increase its acidic tolerance.

To get better information about the viability of the bacteria after the incubation experiments it was decided to replicate the incubation experiments then perform a dead/alive assay with bacterial samples taken from the spectrophotometry cuvettes right at the end of the assay.

The incubation experiments of strains PHL644 and PHL628 (**Figure 3.14** and **Figure 3.15**) provided expected results where only **P1**, **P4**, and **P5** in 5% AcOH in D₂O were able to induce bacterial aggregation in both strains, while neither of the other polymers or controls achieved any aggregation.

When the incubation experiment was completed, bacterial samples of the *E. coli* PHL644 and PHL628 incubated with **P1**, **P4**, and **P5** dissolved in 5% AcOH in D₂O buffer were taken, and a cell viability assay was performed on them.

This test is based in the combination of two fluorescent dyes: SYTO 9 (green) and propidium iodide (red) that bind to nucleic acids. The way this test works is that it checks for the integrity of the cell membrane: SYTO 9 is a green fluorescent dye that can diffuse through healthy or compromised membranes, while propidium iodide (PI) cannot get into a cell unless the cell membrane is compromised. So there would be two populations of cells in a sample with this combination of dyes: green stained cells that are healthy, and dead cells that are stained by the red and the green dye and whose cell membrane has been compromised.

After staining the bacterial samples with SYTO 9 and PI a series of pictures were taken at 1000X using fluorescence microscopy to check for the viability of the clusters made by polymers **P1**, **P4**, and **P5** dissolved in 5% AcOH in D₂O.

The results (**Figure 3.16** to **Figure 3.21**) showed that most of the bacteria clustered by **P1**, **P4**, and **P5** dissolved in 5% AcOH in D₂O, were aggregated in green stained clusters, and only a few cells per sample were stained red, this meant that most cells had been stained by SYTO 9 but not PI.

Only red stained cells had their cell membrane compromised and were dead. This result is indicative that most of the bacterial population that had been aggregated by action of the polymers was viable and their cell membrane had not been compromised after an incubation period of 2 h.

These results were promising as they allowed for a visual screen of the bacterial populations confirming that most of the aggregated bacteria were viable. However, the experiment had limitations as it was not quantitative and did not provide with a tangible value that allowed to compare the cell viability of polymer incubated bacteria versus their controls.

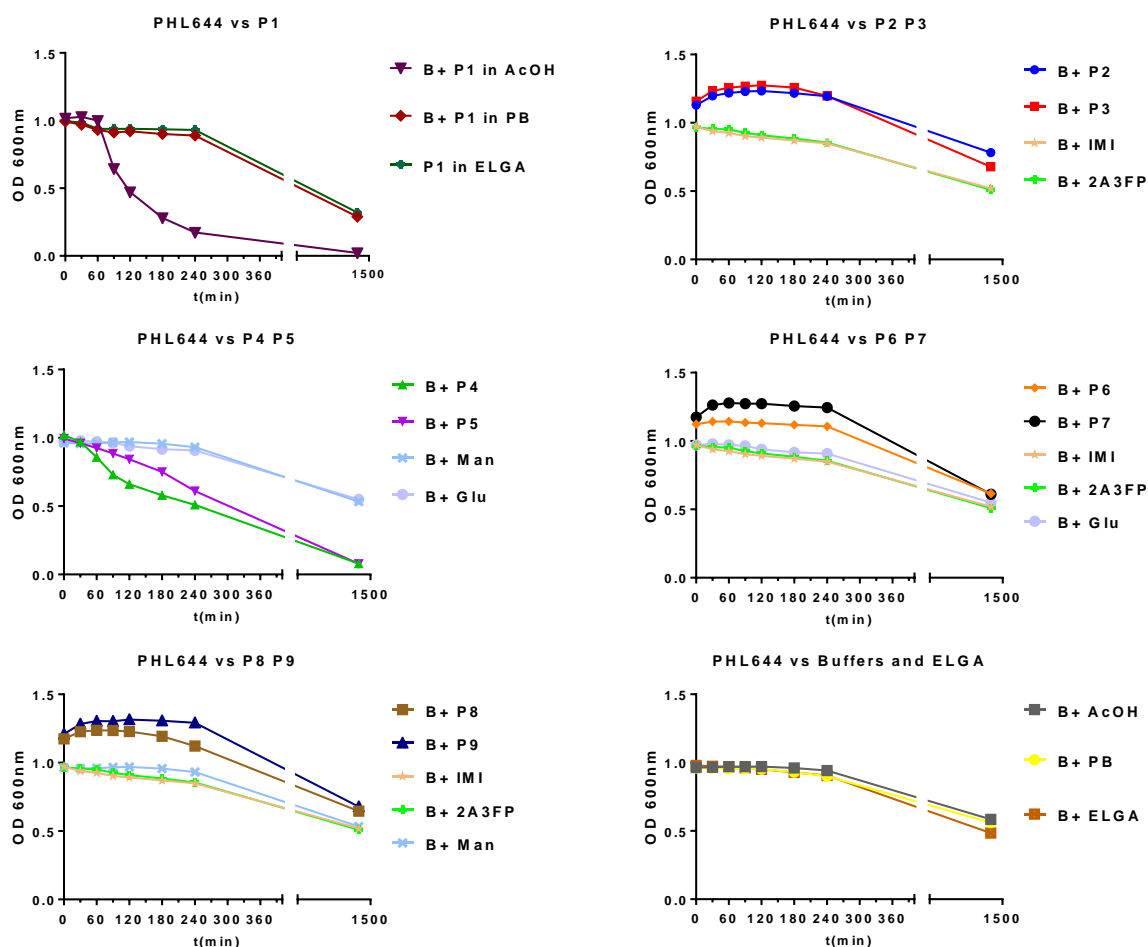


Figure 3.14: Spectrophotometry measurements of optic density ($\lambda=600$ nm) taken over 24 h of *E. coli* PHL644 incubated with: (B+ P1 in AcOH) 47 μ L of 125 mM P1 in 5% AcOH in D₂O buffer. (B+ P1 in PB) 47 μ L of 125 mM P1 in 100 mM phosphate buffer. (B+ P1 in ELGA) 47 μ L of 125 mM P1 in ELGA water. (B+ P2) 47 μ L of 125 mM P2 in 5% AcOH in D₂O buffer. (B+ P3) 47 μ L of 125 mM P3 in 5% AcOH in D₂O buffer. (B+ P4) 47 μ L of 125 mM P4 in 5% AcOH in D₂O buffer. (B+ P5) 47 μ L of 125 mM P5 in 5% AcOH in D₂O buffer. (B+ P6) 47 μ L of 125 mM P6 in 5% AcOH in D₂O buffer. (B+ P7) 47 μ L of 125 mM P7 in 5% AcOH in D₂O buffer. (B+ P8) 47 μ L of 125 mM P8 in 5% AcOH in D₂O buffer. (B+ P9) 47 μ L of 125 mM P9 in 5% AcOH in D₂O buffer. (B+ IMI) 47 μ L of 125 mM 4-imidazolecarboxaldehyde in 5% AcOH in D₂O buffer. (B+ 2A3FP) 47 μ L of 125 mM 2-amino-3-formylpyridine in 5% AcOH in D₂O buffer. (B+ Glu) 47 μ L of 125 mM D-glucose in 5% AcOH in D₂O buffer. (B+ Man) 47 μ L of 125 mM D-mannose in 5% AcOH in D₂O buffer. (B+ AcOH) 47 μ L of 5% AcOH in D₂O buffer. (B+ PB) 47 μ L of 100 mM phosphate buffer. (B+ ELGA) 47 μ L of ELGA water. The final concentration of polymers in solution was of 6.17 mM.

So far no noticeable difference between both strains incubated by the polymers was witnessed, so it was decided to follow the rest of this chapter experiments using *E. coli* PHL644 due to time constraints.

The next step studying cell viability was to follow this experiment with one that allowed to quantify cell mortality when bacteria were clustered with the polymers. Therefore, a colony forming unit (CFU) test was performed comparing between strain PHL644 incubated with **P1**, **P4**, and **P5** dissolved in 5% AcOH in D₂O and their respective controls following the same conditions as mentioned before.

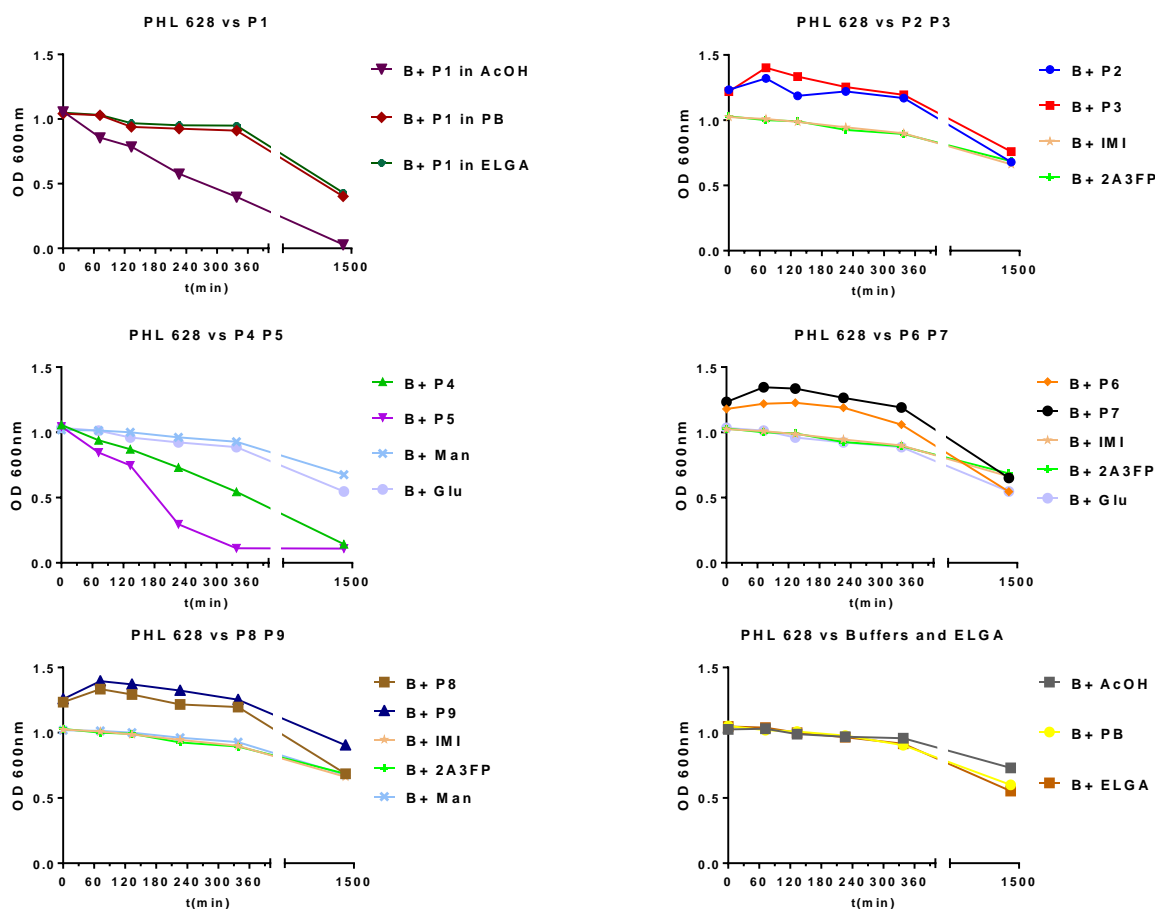


Figure 3.15: Spectrophotometry measurements of optic density ($\lambda = 600$ nm) taken over 24 h of *E. coli* PHL628 incubated with: (B+ P1 in AcOH) 47 μ L of 125 mM P1 in 5% AcOH in D₂O buffer. (B+ P1 in PB) 47 μ L of 125 mM P1 in 100 mM phosphate buffer. (B+ P1 in ELGA) 47 μ L of 125 mM P1 in ELGA water. (B+ P2) 47 μ L of 125 mM P2 in 5% AcOH in D₂O buffer. (B+ P3) 47 μ L of 125 mM P3 in 5% AcOH in D₂O buffer. (B+ P4) 47 μ L of 125 mM P4 in 5% AcOH in D₂O buffer. (B+ P5) 47 μ L of 125 mM P5 in 5% AcOH in D₂O buffer. (B+ P6) 47 μ L of 125 mM P6 in 5% AcOH in D₂O buffer. (B+ P7) 47 μ L of 125 mM P7 in 5% AcOH in D₂O buffer. (B+ P8) 47 μ L of 125 mM P8 in 5% AcOH in D₂O buffer. (B+ P9) 47 μ L of 125 mM P9 in 5% AcOH in D₂O buffer. (B+ IMI) 47 μ L of 125 mM 4-imidazolecarboxaldehyde in 5% AcOH in D₂O buffer. (B+ 2A3FP) 47 μ L of 125 mM 2-amino-3-formylpyridine in 5% AcOH in D₂O buffer. (B+ Glu) 47 μ L of 125 mM D-glucose in 5% AcOH in D₂O buffer. (B+ Man) 47 μ L of 125 mM D-mannose in 5% AcOH in D₂O buffer. (B+ AcOH) 47 μ L of 5% AcOH in D₂O buffer. (B+ PB) 47 μ L of 100 mM phosphate buffer. (B+ ELGA) 47 μ L of ELGA water. The final concentration of polymers in solution was of 6.17 mM.

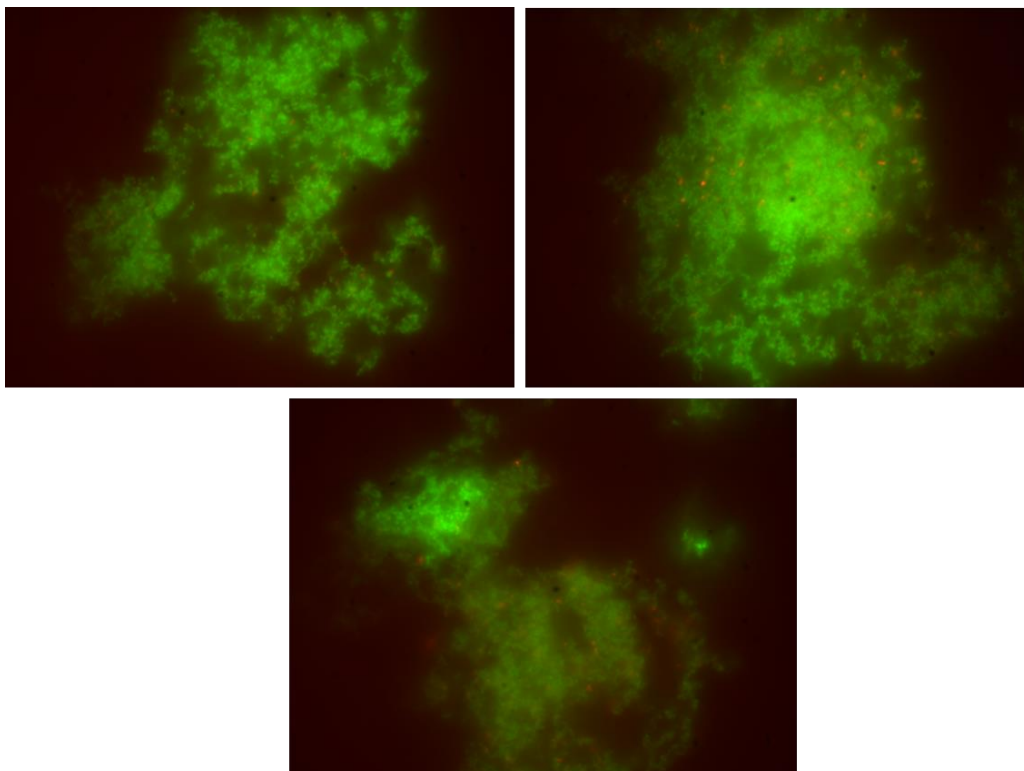


Figure 3.16: Fluorescence microscopy (1000X) pictures of SYTO9/PI stained *E. coli* PHL644 24 h after being incubated with P1 in 5% AcOH in D₂O buffer. The panels are three examples of aggregation taken from the same sample. The final concentration of polymers in solution during the incubation period was of 6.17 mM.

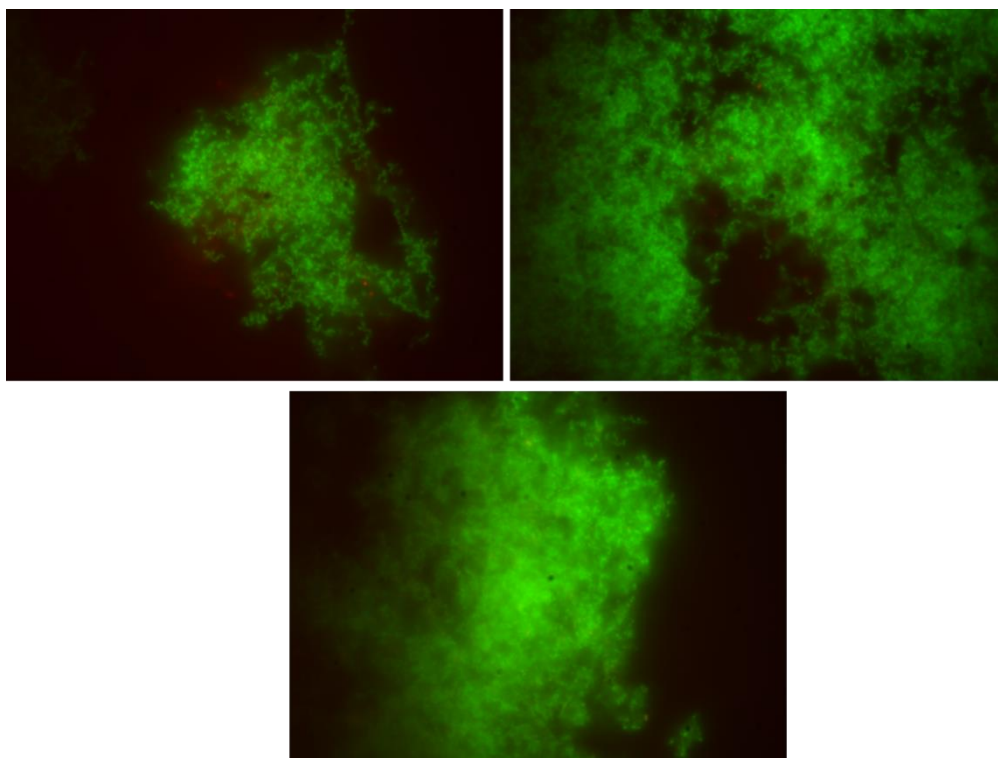


Figure 3.17: Fluorescence microscopy (1000X) pictures of SYTO9/PI stained *E. coli* PHL644 24 h after being incubated with P4 in 5% AcOH in D₂O buffer. The panels are three examples of aggregation taken from the same sample. The final concentration of polymers in solution during the incubation period was of 6.17 mM.

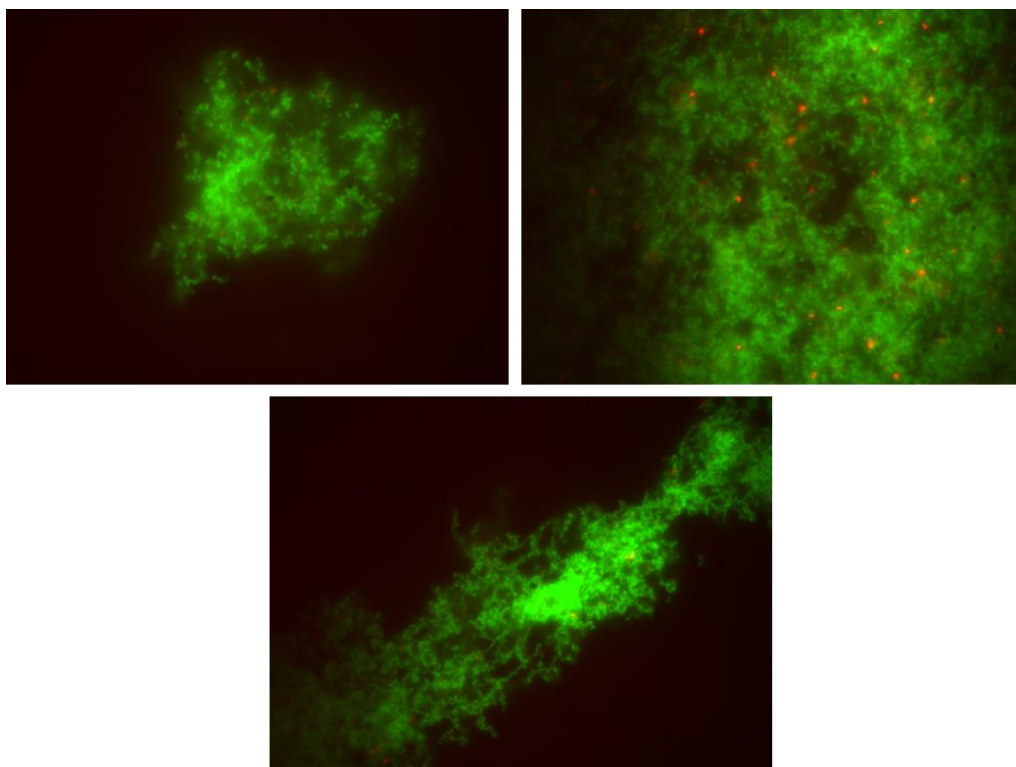


Figure 3.18: Fluorescence microscopy (1000X) pictures of SYTO9/PI stained *E. coli* PHL644 24 h after being incubated with P5 in 5% AcOH in D₂O buffer. The panels are three examples of aggregation taken from the same sample. The final concentration of polymers in solution during the incubation period was of 6.17 mM.

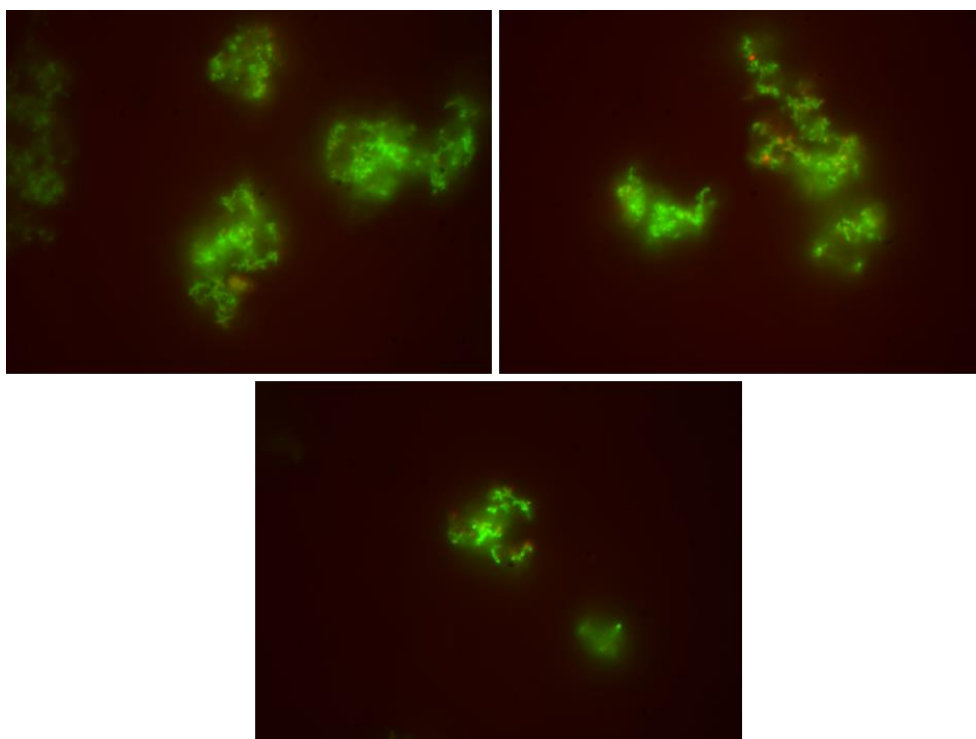


Figure 3.19: Fluorescence microscopy (1000X) pictures of SYTO9/PI stained *E. coli* PHL628 24 h after being incubated with P1 in 5% AcOH in D₂O buffer. The panels are three examples of aggregation taken from the same sample. The final concentration of polymers in solution during the incubation period was of 6.17 mM.

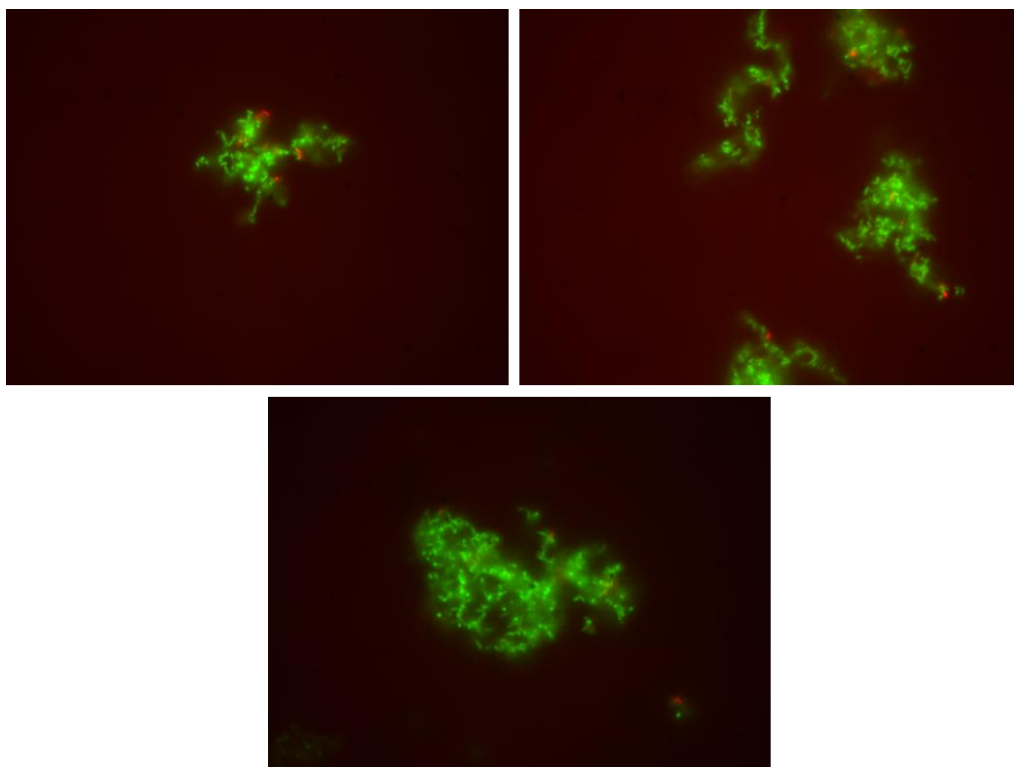


Figure 3.20: : Fluorescence microscopy (1000X) pictures of SYTO9/PI stained *E. coli* PHL628 24 h after being incubated with P4 in 5% AcOH in D₂O buffer. The panels are three examples of aggregation taken from the same sample. The final concentration of polymers in solution during the incubation period was of 6.17 mM.

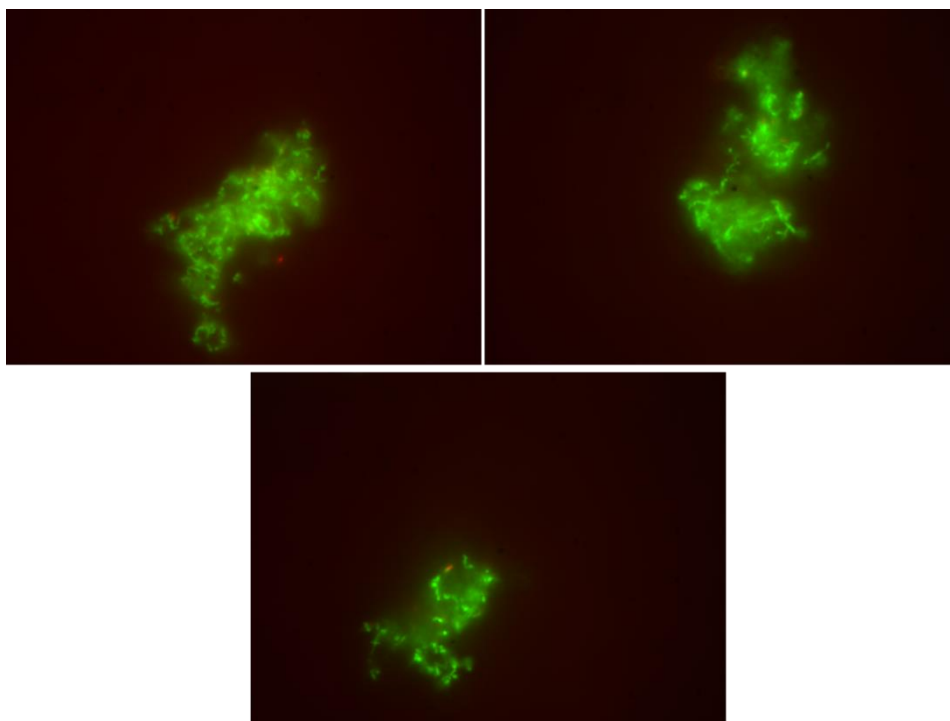


Figure 3.21: : Fluorescence microscopy (1000X) pictures of SYTO9/PI stained *E. coli* PHL628 24 h after being incubated with P5 in 5% AcOH in D₂O buffer. The panels are three examples of aggregation taken from the same sample. The final concentration of polymers in solution during the incubation period was of 6.17 mM.

3.3.1.4 Colony forming unit assay

This experiment was performed to quantify bacteria viability after being incubated with polymers that induced aggregation on strain PHL644.

A new incubation experiment was performed with the same conditions, this time in 1 ml Eppendorf microtubes with the same final concentrations. PHL644 was incubated with polymers **P1**, **P4**, and **P5**, then their respective controls D-glucose, D-mannose, all dissolved in 5% AcOH in D₂O buffer. Other controls for this experiment were bacteria incubated only with 5% AcOH in D₂O, bacteria incubated with ELGA water, and dead bacteria killed by heat shock.

After an incubation period of 24 h, the Eppendorf tubes were vortexed for 30 minutes. However, the clusters were extremely resilient and there were always aggregated bacteria remaining on the water column of the samples aggregated by polymers **P1**, **P4**, and **P5**. It was decided to sonicate each sample (including the ones that did not aggregate) at 5 kHz for 10 minutes then follow with another 30 minutes of vortex until clusters were not noticeable on the liquid column.

Samples were taken to perform serial dilutions in 100 mM phosphate buffer that were plated in twelve replicates at a final dilution of 10^6 on LB agar, then were incubated at 30°C for 24 h.

When analysing the results (**Figure 3.22**) it was necessary to first identify the baseline CFU/ml of bacteria that had been incubated for 24 h without anything but ELGA added to it (B+). The baseline of healthy bacteria for this sample was of $\sim 600 \times 10^6$ CFU/ml, and any decrease from this range would mean that there is an increase mortality due to the substances added to strain PHL644 during the incubation experiments.

The CFU count of bacteria incubated with **P1**, **P4**, and **P5** and the carbohydrate controls (**Figure 3.22**) remained between ~ 100 - 200×10^6 . There seemed to be a decrease in the number of CFU/ml in all samples incubated with polymers or controls compared with the baseline control (B+), although they remained at the same order of magnitude of 10^8 CFU.

This decrease in CFU might have been due to an increased mortality induced by the 5% AcOH in D₂O buffer used to dissolve the polymers and the carbohydrate controls, as AcOH has been shown to have bactericidal properties^{191, 192}. This was confirmed by the CFU counts from strain PHL644 solely incubated with 5% AcOH in D₂O buffer. Those samples showed a decreased CFU count of $\sim 36 \times 10^6$ an order of magnitude lower (10^7) than the rest of the samples.

Overall, the diminished CFU formation of the bacteria incubated and clustered by polymers **P1**, **P4**, and **P5** was considered noteworthy, but the fact that it remained within the same order of magnitude than the baseline control (B+) was indicative that this was not a hindrance for their use as biomaterials able to induce bacterial aggregation.

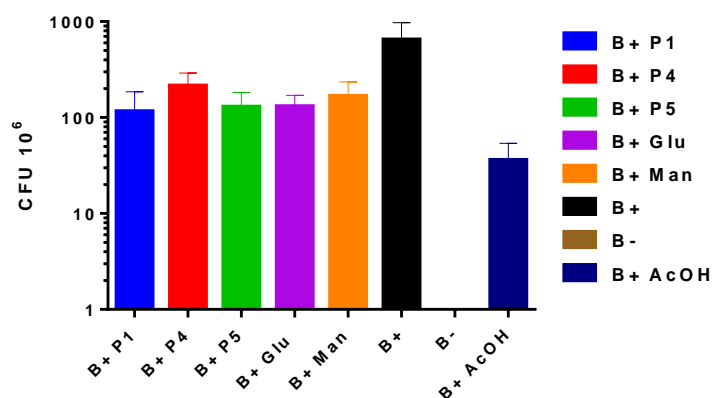


Figure 3.22: CFU count of CFU at a dilution factor of 10^6 on plate after 24 h of incubation with polymers and controls. (B+) is the baseline control of bacteria incubated without anything but ELGA water. 9530 μL of $\text{OD}_{600}=1$ PHL644 was incubated with: (B+ P1) 470 μL of 125 mM P1 dissolved in 5% AcOH in D_2O . (B+ P4) 470 μL of 125 mM P4 dissolved in 5% AcOH in D_2O . (B+ P5) 470 μL of 125 mM P5 dissolved in 5% AcOH in D_2O . (B+ Glu) 470 μL of 125 mM D-glucose dissolved in 5% AcOH in D_2O . (B+ Man) 470 μL of 125 mM D-glucose dissolved in 5% AcOH in D_2O . (B+ AcOH) 470 μL of 5% AcOH in D_2O . (B-) heat shock dead bacteria. The final concentration of polymers in solution during the incubation period was of 6.17 mM.

3.3.1.5 Crystal violet assay

One of the main properties of biofilm communities is their ability to generate a three-dimensional matrix of EPS as structural support and protect the community. One of the ways to measure the production of EPS is to quantify the attachment to abiotic surfaces, the logic being that if more EPS is produced it allows for a better colonization of surfaces. A method to measure the presence of bacteria on abiotic surface is to stain them with crystal violet, a purple dye that binds to negatively charged molecules found in the EPS and bacteria alike¹⁹³, then wash it out and measure its absorbance comparing results between samples,

PHL644 was grown on LB medium then washed and diluted on ELGA water until $OD_{600}=1$, then 190.6 μ L of PHL644 was transferred to 96 microtiter well plates then incubated them with 9.4 μ L of 125 mM **P1**, **P4**, and **P5** dissolved in 5% AcOH in D_2O to a final backbone concentration of 6.17 mM, or an equivalent volume of their controls [125 mM D-glucose or 125 mM D-mannose dissolved in 5% AcOH in D_2O ; or an equivalent volume of 5% AcOH in D_2O]. Another two controls were introduced in this experiment: a control of PHL644 $OD_{600}=1$ with an equivalent volume of ELGA water added, and a control PHL644 of $OD_{600}=1$ killed by heat shock with the same volume of ELGA water added. The microtiter plates were then incubated for 24 h at 30°C and 150 rpm.

Following the incubation period, the supernatant and planktonic bacteria were removed from the microtiter wells. 200 μ L of 0.5% w/v crystal violet solution (CV) in ELGA water was added to each well then incubated for 30 minutes. After the incubation period the CV was removed and washed, then 200 μ L of 95% ethanol was added to each well to solubilize any CV that might have been attached to the cells colonizing the abiotic surface of the plate and their EPS, the wells were incubated for another 10 minutes then its absorbance was measured at 550 nm.

Six wells were used for each sample of the experiment, and the crystal violet assay was performed three times.

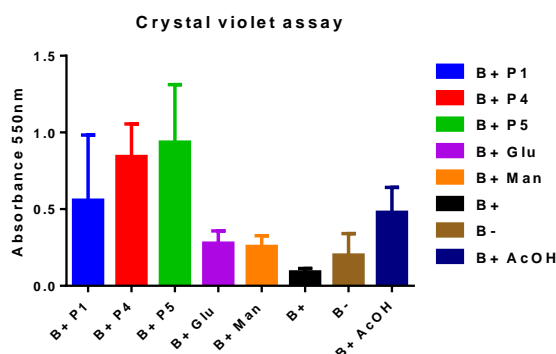


Figure 3.23: Absorbance ($\lambda=550$) results from crystal violet staining of PHL644 attached to abiotic surfaces. (B+) is PHL644 positive control, 190.6 μ L of bacteria incubated with 9.4 μ L of ELGA water. (B-) is the PHL644 negative control, 190.6 μ L of bacteria killed by heat shock treatment and incubated with 9.4 μ L of ELGA water. (B+ AcOH) 190.6 μ L of bacteria were incubated with 9.4 μ L of 5% AcOH in D_2O . (B+ P1) 190.6 μ L of bacteria were incubated with 9.4 μ L of 125 mM P1 dissolved in 5% AcOH in D_2O . (B+ P4) 190.6 μ L of bacteria were incubated with 9.4 μ L of 125 mM P4 dissolved in 5% AcOH in D_2O . (B+ P5) 190.6 μ L of bacteria were incubated with 9.4 μ L of 125 mM P5 dissolved in 5% AcOH in D_2O . (B+ Glu) 190.6 μ L of bacteria were incubated with 9.4 μ L of 125 mM D-glucose dissolved in 5% AcOH in D_2O . (B+ Man) 190.6 μ L of bacteria were incubated with 9.4 μ L of 125 mM D-mannose dissolved in 5% AcOH in D_2O . The final concentration of polymers in during the incubation period solution was of 6.17 mM.

The aim of this experiment was to dye the bacteria and EPS attached to the well plate surface, to obtain quantifiable data that allowed to compare OD intensity between polymers and polymer free controls to elucidate if the polymers not only induced bacterial aggregation but the production of EPS promoting abiotic surface colonization.

When analysing the results of the CV assay (**Figure 3.23**) it was observed that the lower absorbance value obtained was the one corresponding to bacteria that had been incubated free of any ligands or polymers (B+, **Figure 3.23**). This result was expected, as that sample should have been mostly healthy planktonic bacteria with barely any attachment to abiotic surfaces. This result was considered the baseline, and any increase in absorbance should be due to attachment of biologic material to the abiotic surfaces of the wells.

The next step was to observe the results provided by the bacteria killed by heat shock treatment (B-, **Figure 3.23**), a noticeable increase in absorbance was measured. Dead bacteria have lost their ability to maintain the integrity of their membranes¹⁹⁴ leaking their organic contents to the medium they are immersed, this could be the reason why there was an increased level of absorbance compared to the B+ sample, because part of the organic matter from dead bacteria could have attached to the walls of the microtiter wells.

A similar pattern was observed from the results obtained of staining the wells that kept bacteria incubated with an equivalent volume of 5% AcOH (B+ AcOH, **Figure 3.23**). The B+ AcOH samples presented a higher absorbance than the B+. When the CFU assay was performed it was apparent that samples of PHL644 incubated only with an equivalent volume of 5% AcOH in D₂O presented an increased mortality of one order of magnitude compared to their B+ counterparts, but there were still enough viable cells after the incubation experiment. It could be hypothesised that the content of these dead cells could be attached to the walls of the microtiter plate facilitating the adhesion of live cells onto it contributing to an increased level of colonization, and hence an increased level of absorbance from stained organic matter.

The results of the crystal violet assay (B+ P1, B+ P4, B+ P5, **Figure 3.23**) showed that the samples incubated with the polymers **P1**, **P4**, and **P5** presented higher values of absorbance than their controls that translated as a higher level of surface colonization. It could also be observed that there was a difference in the results obtained for the different polymers during the experiment, as the polymer backbone (**P1**) alone gave a lower absorbance values in this assay, compared with the polymers functionalized with D-glucose (**P4**) and D-mannose (**P5**).

This could be explained if PHL644 were able to recognize the carbohydrate repetitive units of the polymer triggering physiological changes that promote surface colonization. There could be a correlation between the higher level of absorbance in the samples incubated with the polymers and an enhanced level of surface colonization (compared to their controls) that is triggered by the synthetic aggregation generated by the polymeric materials.

3.3.1.6 Confocal laser microscopy

One of the main properties of biofilms is their ability to develop three dimensional structures to support their communities. Simple light microscopy was able to provide two-dimensional images that were used previously to screen the changes induced by **PAH** polymers in *E. coli* but it cannot provide a visual three-dimensional representation of the aggregated communities induced by the effect of the polymers.

One of the methods used by researchers to study biofilm structures is the use of confocal laser microscopy. This technique uses a confocal microscope able to take stacks of pictures on the vertical axis over the same focal point. These pictures can later be merged with computer software to create a three-dimensional model that allow for the three-dimensional study of a sample.

The aim of this experiment was to provide a visual three-dimensional representation of bacteria aggregated by polymers **P1**, **P4**, and **P5** dissolved in 5% AcOH in D₂O.

PHL644 OD₆₀₀=1 in ELGA water was transferred to 2x4 microtiter plates then incubated with polymers **P1**, **P4**, or **P5** dissolved in 5% AcOH in D₂O to a final concentration of 6.17 mM. The samples were then incubated at 30 °C and 150 rpm for 24 h.

The samples were stained with SYTO 9 and PI, and an inverted confocal laser microscopy was used to take pictures of 2x2 microscope fields at 1000x using the red and green fluorescent filters. Three-dimensional stacks of pictures were assembled using the software NIS elements (**Figure 3.24** to **Figure 3.26**).

It was not possible to take pictures of the controls, as they all were in planktonic state and it is not possible to take pictures of fast-moving objects.

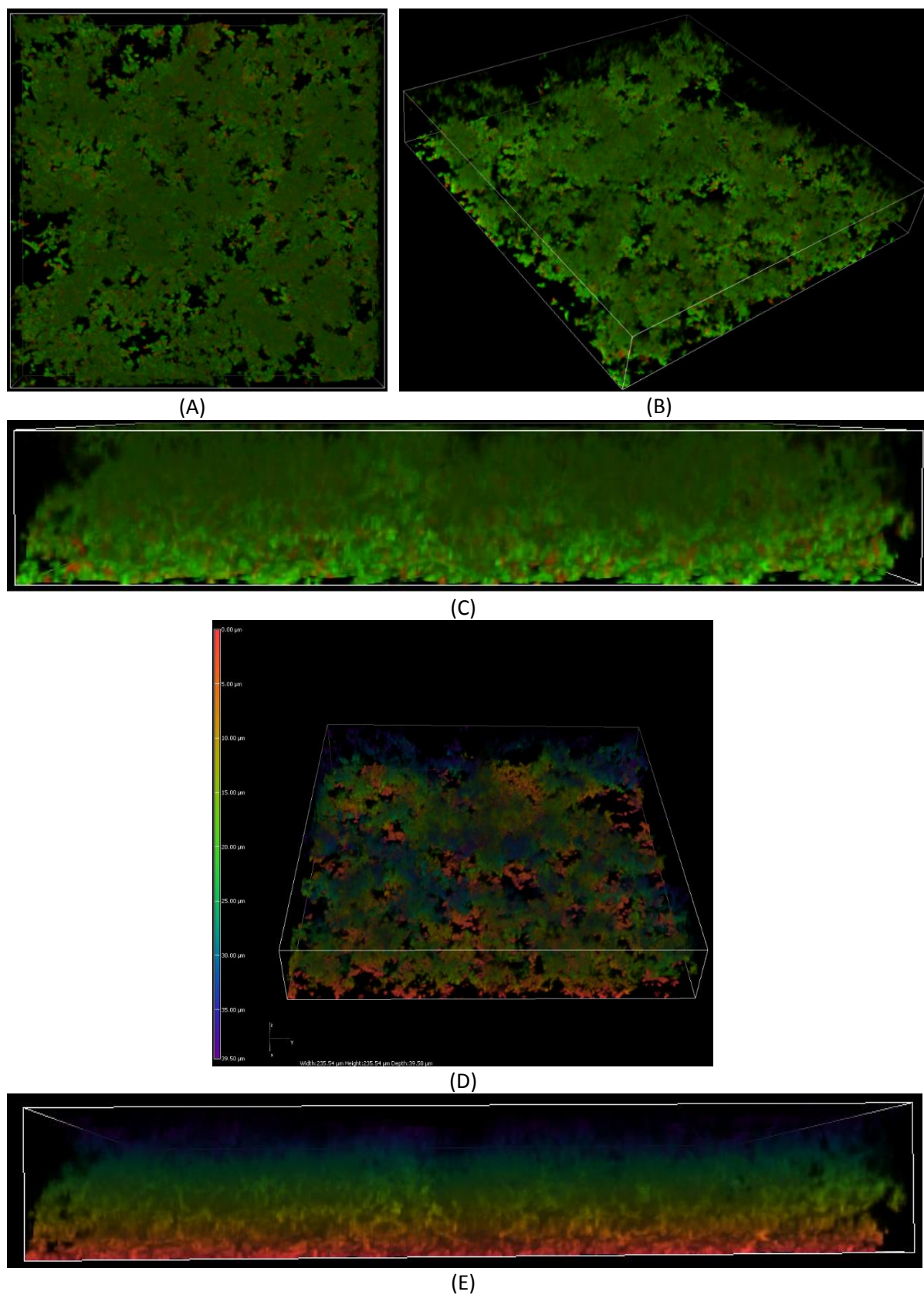


Figure 3.24: 3D model obtained by confocal laser microscopy of PHL644 24h after being incubated with P1 dissolved in 5% AcOH in D₂O (pH 2.9). (A) top view, (B) isometric view, and (C) side view of cells stained with fluorescent dyes SYTO 9/PI. (D) tilted and side (E) view colour grading to provide a visual queue of the height distribution of the 3D community (fluorescence dyes are not visible using this height grading method). The size of the stack was 235.54x235.54x39.50 μm.

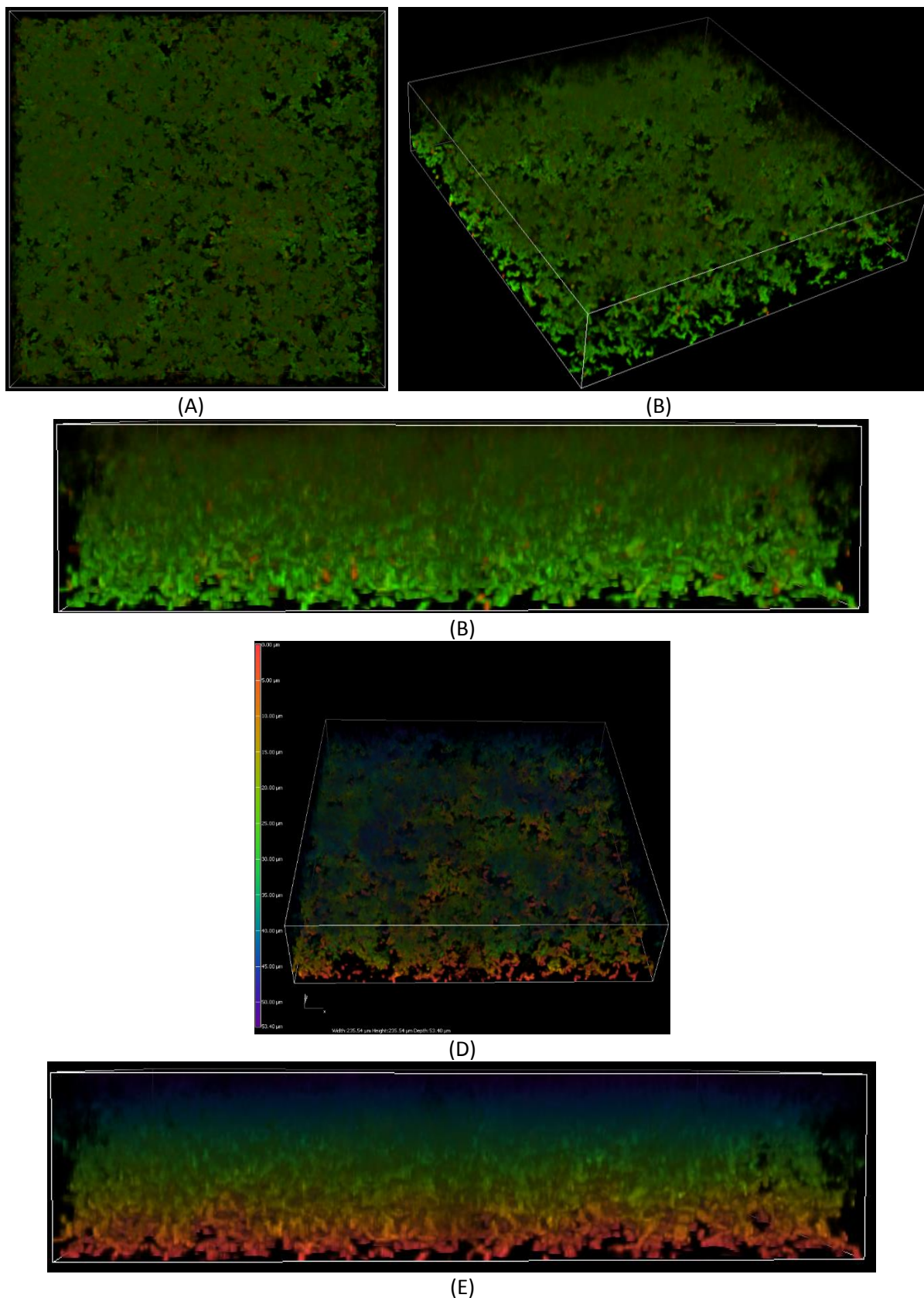


Figure 3.25: 3D model obtained by confocal laser microscopy of PHL644 24h after being incubated with P4 dissolved in 5% AcOH in D₂O (pH 2.9). (A) top view, (B) isometric view, and (C) side view of cells stained with fluorescent dyes SYTO 9/PI. (D) tilted and side (E) view colour grading to provide a visual queue of the height distribution of the 3D community (fluorescence dyes are not visible using this height grading method). The size of the image was 235.54x235.54x53.40 μm.

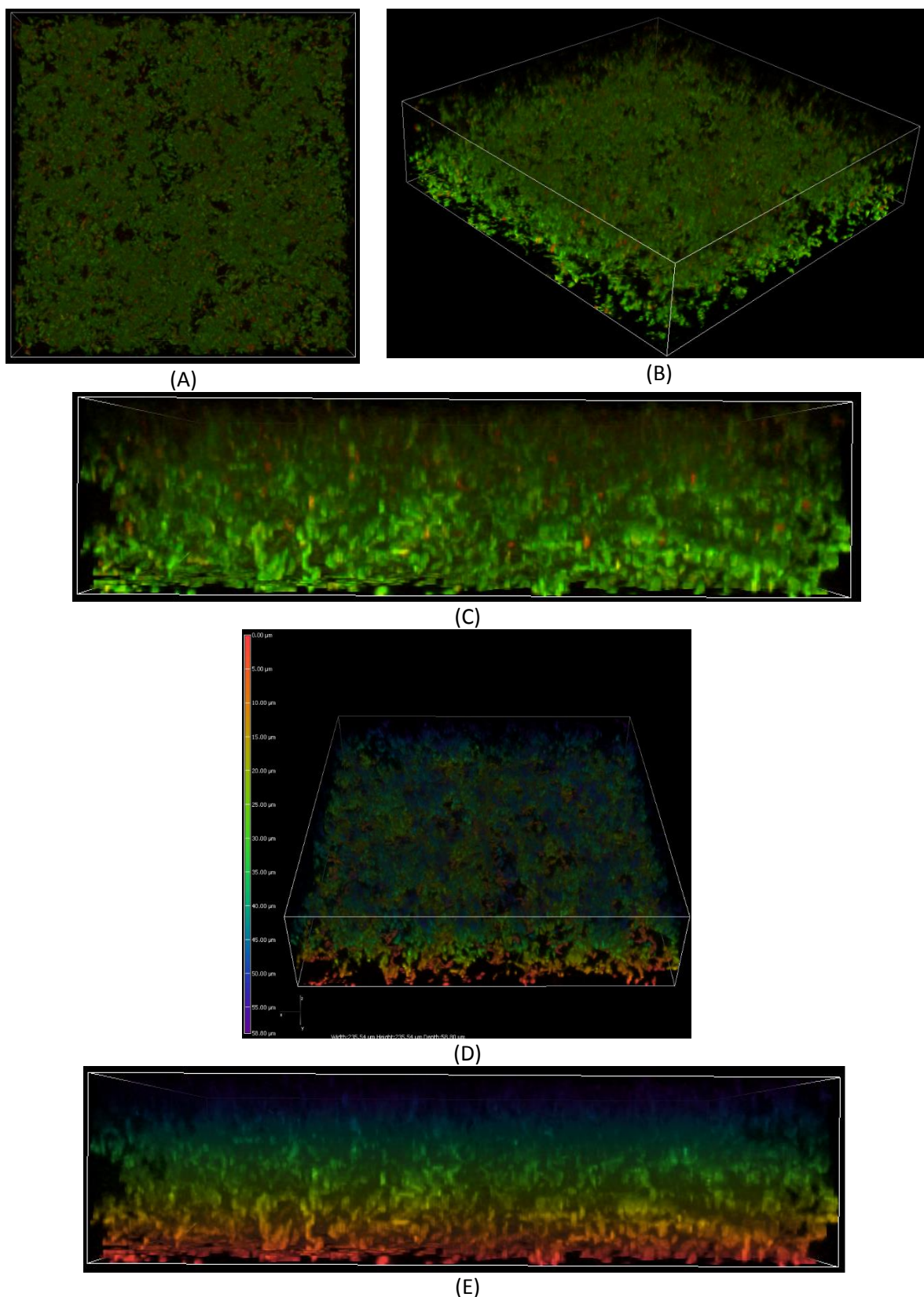


Figure 3.26: : 3D model obtained by confocal laser microscopy of PHL644 24h after being incubated with P5 dissolved in 5% AcOH in D₂O (pH 2.9). (A) top view, (B) isometric view, and (C) side view of cells stained with fluorescent dyes SYTO 9/PI. (D) tilted and side (E) view colour grading to provide a visual queue of the height distribution of the 3D community (fluorescence dyes are not visible using this height grading method). The size of the image was 235.54x235.54x58.80 μm .

The 3D models by merging the vertical stack of pictures taken by laser confocal microscopy (**Figure 3.24** to **Figure 3.26**) showed that the samples PHL644 incubated by **P1**, **P4**, and **P5** dissolved in 5% AcOH in D₂O (pH 2.9) were forming three-dimensional communities 24 h after being exposed to the polymers. It could also be observed that most of the cells of the community were stained by green fluorescence dye SYTO 9 and a few were stained by PI, meaning that most of the bacteria embedded in the 3D matrix were alive.

The software used to merge the stack of confocal microscopy pictures allowed to assign a colour grading depending of the height of the sample (**Figure 3.24** to **Figure 3.26**). Through this method it could be observed a disparity in the thickness of the communities formed depending on the polymer used to induce aggregation.

When PHL644 was incubated with **P1**, it developed into a three-dimensional community that presented a maximum height of 39.50 µm (**Figure 3.24**), the sample incubated with **P4** showed a maximum height of 53.40 µm (**Figure 3.25**), while the one that was incubated with **P5** (**Figure 3.26**) had a maximum height of 58.80 µm. This was the maximum height at what bacteria presence was observed through microscopy and this experiment did not provide means to calculate the average height of each sample.

This experiment pointed that there was a correlation between the results obtained in the crystal violet assay and the maximum height of the three-dimensional population when PHL644 was incubated with different polymers. The results from the crystal violet assay (**Figure 3.23**) showed that there was a trend where there was an increased degree of surface colonization that depended on the polymer used to induce aggregation and biofilm formation on *E. coli* with **P5>P4>P1**.

A similar trend was observed when it came to the maximum thickness of the three-dimensional community when analysing the three-dimensional confocal microscopy stacks. It was hypothesised that polymers **P4** and **P5** were able to induce a higher level of EPS production than **P1**, which contributed to a higher thickness of the biofilm colony and an increase in surface colonization.

3.3.1.7 Discussion

The experiments and tests performed during the research of the biological applications of polymers **P1**, **P4**, and **P5** showed their capability to aggregate and induce the formation of synthetic biofilm communities with a three-dimensional structure. But it was necessary to explain the main driving factor responsible for the initial aggregation of bacteria.

At first, when the aggregation experiments were designed, the **PAH** backbone **P1** was used as a control without expecting positive results, but instead it proved to be successful in aggregating *E. coli*, but only when the bacteria were incubated with the backbone dissolved under the acidic conditions of the 0.25% AcOH in D₂O buffer (final concentration of the samples dissolved in 5% AcOH buffer during the incubation experiments) at a final pH around 4.2. **P1** did not induce any aggregation when it was dissolved in the slightly acid 4.93 mM phosphate buffer (final concentration of the samples dissolved in 100 mM phosphate buffer during the incubation experiments) at final pH around 6.8, or under neutral conditions of ELGA water.

The chemical structure of **P1** remained the same, but the solvent environment was what changed. Under these conditions it was believed that the 0.25% AcOH buffer solution was able to donate their H⁺ charges to the hydrazide groups that were then protonated into a positively charged species R-NH-NH₃⁺.

E. coli surfaces are negatively charged due to the dissociation of phosphate and carbonyl groups on the LPS and peptidoglycan of the cell walls^{195, 196}. This partial negative charge all around the bacteria surface might have made it possible for the protonated **PAH** to interact with it by charge compatibility, inducing bridging (**Figure 3.27**) between neighbouring bacteria that induced bacterial aggregation that led to clustering and synthetic biofilm formation.

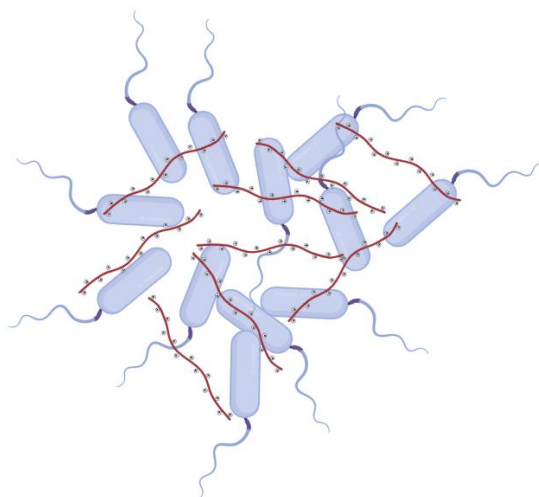


Figure 3.27: Proposed P1 aggregation mechanism by electrostatic charge compatibility between the positively charged backbone and the negatively charged surface bacteria. Polymers versus bacteria not to scale.

It is proposed that there is a limiting factor regarding the amount of available protonated hydrazide subunits that induce bacterial aggregation. The **PAH** backbone **P1** alone was able to induce a fast aggregation with 100% of their subunits free of functionalization. Meanwhile, during the testing of

functionalized polymers **P2**, **P3**, **P6**, **P7**, **P8**, and **P9** with a degree of functionalization around 70-80% of the subunits, no aggregation could be observed or measured, neither through spectrophotometry nor through light microscopy. While the polymers **P4** and **P5** with a functionalization of 40-48% had enough available protonated hydrazides to induce bacterial aggregation.

Therefore, the amount of free protonated hydrazides was believed to be the main driving factor for the initial bacterial aggregation and sedimentation, it seems that a lower count on the available protonated hydrazides is what made the process slower when using **P4** and **P5** compared to the backbone **P1**.

It is important to also consider the possibility that 0.25 % AcOH buffer increased mortality contributes to the aggregation effect of the polymers **P1**, **P4**, and **P5**. The CFU assay confirmed that samples incubated with a final concentration of 0.25% AcOH buffer experienced an increased mortality of cells compared to the positive controls that were not incubated with any ligand or buffers, although remaining in the same order of magnitude of viable cells per ml.

The results obtained from the crystal violet assay showed that bacteria incubated just with a final concentration of 0.25% AcOH buffer and without polymers experienced increased levels of surface colonization compared to positive controls that were incubated without any ligands or buffers.

It is possible that this increased mortality could have contributed to the aggregation phenomenon establishing a foundation of dead cells that alive bacteria and polymers could interact with contributing to the aggregation phenomenon.

When it comes to the physiological changes, quantifiable differences were observed between bacteria that were aggregated by **P1**, and the communities that were aggregated by carbohydrate functionalized polymers **P4** and **P5**. The data obtained from the crystal violet assays showed a higher surface colonization compatible with an increase in EPS production from three dimensional communities of *E. coli* elicited by **P4** and **P5**, compared to the backbone **P1** effect that induced a notable but lower surface colonization.

This data is compatible with the confocal microscopy experiments performed. It was observed that the biofilm communities induced by **P4** and **P5** were thicker, with a maximum height of 53.40 μm and 58.80 μm respectively, compared with the thickness of the communities induced by **P1** where the maximum height was of 39.50 μm .

This data suggests that there is a higher generation of EPS that supports a thicker community in the communities induced by **P4** and **P5**, but how?

The main reason that carbohydrates were chosen as functional groups to test on *E. coli* was due to their similarity to repetitive moieties that are recognized by *E. coli* surface receptors when colonizing the epithelia of its hosts⁵³. Fimbrial adhesins have been shown to be antagonists of carbohydrates present in the glycocalyx epithelia⁵³⁻⁵⁵, not only mediating bacteria-substrate interaction but also eliciting internal signalling on the bacteria that prepare the microorganism for colonization. One of these structures is the fimbriae type 1 FimH present in *E. coli*, this fimbriae possess an adhesin on its end that is a known antagonist for D-mannose and D-mannosides^{163, 197}.

It is proposed that the action mechanism for the synthetic biofilm formation elicited by the polymers could be driven by the aggregation induced by to charge compatibility between the positively charged hydrazides of the polymers and the negatively charged surface of *E. coli*.

Once this initial aggregation happens the bacteria could be able to initiate cell to cell signalling recognizing they are part of a community eliciting physiological changes to pass from a planktonic lifestyle to a sessile part of a biofilm. It is hypothesised that the increased EPS production and thickness of the biofilm produced by the carbohydrate functionalized polymers **P4** and **P5** were induced by *E. coli* recognizing the carbohydrate repetitive moieties present in the functionalized polymers after the initial aggregation inducing an elevated production of EPS that generates a thicker biofilm community.

Although the data collected during this study was extensive, it remains inconclusive regarding the leading effect that causes the aggregation capabilities of **P1**, **P4**, and **P5**. It could only be hypothesised the cause that made the polymers effective with the data available at the moment of writing this thesis.

The main aim of this study was to test materials that could induce biofilm formation on demand, and that was achieved. But for these materials to be effective as tools for biotechnological applications a further study should be performed focusing on the metabolic viability of *E. coli* within the synthetic biofilms induced by polymers **P1**, **P4**, and **P5**. As the experiments designed to test their aggregation capabilities did not have any media to support growth or metabolic activity.

3.3.2 PAGH as a platform for microbiological applications

PAGH polymers were tested on PHL644 samples to check for bacterial aggregation.

The aggregation assay that was performed previously with PAH polymers was replicated using PAGH polymers. PHL644 $OD_{600}=1$ in ELGA, was incubated with 125 mM stocks (to a final concentration of 6.17 mM) of polymers **P10**, **P11** and **P12** dissolved in 5% AcOH in D_2O (to a final concentration of 0.25%). The OD_{600} of the sample was measured by spectrophotometry for 24 h.

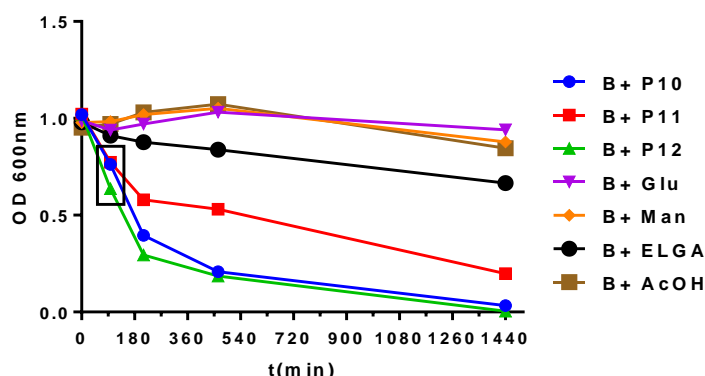


Figure 3.28: Spectrophotometry measurements of optic density ($\lambda = 600$ nm) taken over 24 h when *E. coli* PHL644 was incubated with 6.17 mM of P10, P11, P12 and their respective controls. (B+ P10) 953 μ L of PHL644 incubated with 47 μ L of 125 mM P10 dissolved in 5% AcOH in D_2O . (B+ P11) 953 μ L of PHL644 incubated with 47 μ L of 125 mM P11 dissolved in 5% AcOH in D_2O . (B+ P12) 953 μ L of PHL644 incubated with 47 μ L of 125 mM P12 dissolved in 5% AcOH in D_2O . (B+ Glu) 953 μ L of PHL644 incubated with 47 μ L of 125 mM D-glucose dissolved in 5% AcOH in D_2O . (B+ Man) 953 μ L of PHL644 incubated with 47 μ L of 125 mM D-mannose dissolved in 5% AcOH in D_2O . (B+ ELGA) 953 μ L of PHL644 incubated with 47 μ L ELGA water. (B+ AcOH) 953 μ L of PHL644 incubated with 47 μ L of 5% AcOH in D_2O .

Analysing the plotted data of the aggregation assay (**Figure 3.28**) it could be observed that samples incubated with both the **PAGH** backbone **P10** and the carbohydrate functionalized polymers **P11** and **P12** induced aggregation on PHL644.

The aggregation of PHL644 only happened with the bacterial samples incubated by these polymers and not in any of the controls. The aggregation was fast as it happened under the 90 minutes after the beginning of the experiment, and the bacterial clusters were big enough to be seen with the naked eye.

Pictures taken 24 h after the initial incubation (**Figure 3.29**) showed how most of the bacteria that initially was in a planktonic state had aggregated and sank to the bottom of the water column, while the control with PHL644 without being incubated by any polymer had remained without any visible aggregation.

This preliminary data was in agreement with the results obtained when *E. coli* was incubated with **PAHs** **P1**, **P4**, and **P5** polymers with a similar structure to **PAGHs** **P10**, **P11**, and **P12**, suggesting that they might have a similar action over *E. coli* inducing aggregation and synthetic biofilm formation under the acidic conditions of 0.25% AcOH buffer.

No further experiments were performed with any of the **PAGH** polymers due to time constraints.



Figure 3.29: Cuvettes used for the PAGH aggregation experiment 24 hours after the beginning of the assay. Aggregation can be observed at the bottoms of the cuvettes incubated with polymers P10, P11 and P12, while the bacteria of the control without any ligands (Bact+H₂O) remained in planktonic state. For this experiment 953 μ L of PHL644 were incubated with: (P10) 47 μ L of 125 mM P10 dissolved in 5% of AcOH in D₂O. (P11) 47 μ L of 125 mM P11 dissolved in 5% of AcOH in D₂O. (P12) 47 μ L of 125 mM P12 dissolved in 5% of AcOH in D₂O. (Bact+H₂O) 47 μ L of ELGA water.

3.4 Summary

A method for fast throughput testing of microbiological applications of **PAH** functionalized polymers was designed and tested.

It was reported that **PAH**, **PAH-Glucose**, and **PAH-Mannose**, were able to induce fast aggregation of *E. coli* eliciting synthetic biofilm formation 24 h after initial incubation with 6.17 mM of polymers in 0.25% AcOH buffer.

Quantitative analyses were performed, concluding that the cell viability was partially compromised but with most of the aggregated population surviving and able to generate new colonies. **PAH**, **PAH-Glucose**, and **PAH-Mannose** induced an increase in surface colonization and production of EPS compared to planktonic *E. coli* and other controls. It could be observed how **PAH-Glucose**, and **PAH-Mannose** were able to generate a higher increase in EPS production than **PAH**.

Laser confocal microscopy was used to generate three-dimensional models of the bacterial communities generated by these polymers 24 h after the initial incubation. These models allowed to witness the three-dimensional structure of the synthetic biofilm generated due to the action of the polymers **PAH**, **PAH-Glucose**, and **PAH-Mannose**. It was observed that the biofilm communities generated by **PAH-Glucose**, and **PAH-Mannose** presented an increased thickness compared to the ones induced by **PAH**.

It was theorized that the bacterial aggregation was driven by charge compatibility between the protonated hydrazides and the negatively charged bacterial surface, and that **PAH-Glucose** and **PAH-Mannose** were inducing a further physiological change in *E. coli* interacting with surface receptors like Fimbriae type 1 FimH.

The preliminary test of the microbiological applications of 6.17 mM of **PAGH**, **PAGH-Glucose**, and **PAGH-Mannose** in a final concentration of 0.25% AcOH was tested on *E. coli*, obtaining similar results than the polymers **PAH**, **PAH-Glucose**, and **PAH-Mannose**. **PAGH**, **PAGH-Glucose**, and **PAGH-Mannose** were able to induce aggregation showing potential applications for the testing of functional groups with biological applications.

3.5 Future work

Further study of the synthetic biofilm communities induced by **PAH** polymers is necessary to understand if there is future in their potential applications as biotechnological platforms.

A proposed experiment would be to use a *E. coli* strain carrying a GFP plasmid then induce bacterial aggregation by the means explained in this study. Subsequently transfer the synthetic biofilm community to a minimal media environment and check for the integrity of the tree-dimensional community as well as the GFP activity.

3.6 Experimental

Bacterial strains

This research used two strains derived from *E. coli* K-12: *E. coli* K12 PHL628 (MG1655 *malA-kan ompR234*), and *E. coli* K12 PHL644 (MC4100 *malA-kan ompR234*). Both of these strains derive from MG1655¹⁸⁴ and MC4100¹⁸⁵ respectively, and present the allele *ompR234*⁶¹.

E. coli K12 PHL644 (MC4100 *malA-kan ompR234*) was part of the laboratory stocks. *E. coli* K12 PHL628 (MG1655 *malA-kan ompR234*) was provided by Dr Paolo Landini.

Strains were maintained in multiple frozen stocks in 50% glycerol/dH₂O at -80°C.

Bacterial cultures

All liquid bacterial cultures were started from single bacterial colonies (grown on LB agar) using LB as food source. 200 ml of LB on 500 ml conical flask was incubated at 30°C and shaking of 150 rpm overnight.

Bacterial cultures were then centrifuged at 4000 rpm, the supernatant discarded and an equivalent volume of sterilized ELGA water was added, the pellet was then resuspended, this process was performed twice to get rid of any remains of LB. The OD of the culture was measured at a $\lambda=600$ nm then diluted with sterilized ELGA water until OD₆₀₀=1.

Aggregation assays

Separate overnight cultures of strains PHL644 and PHL628 were grown from single colonies following the standard growing conditions: 200 ml of LB on a 500 mL conical flask, at 30 °C, shaking of 150 rpm. This was followed by washing the bacteria centrifuging at 4000 rpm discarding the supernatant and adding an equivalent volume of sterile ELGA water. Bacterial pellets were resuspended via vortex agitation, and the process was repeated twice to ensure that most of the LB was eliminated. This step was performed to avoid any interference of the growth media with the incubation experiments.

After the washing step the optic density (OD) of the bacterial culture was measured at 600 nm (OD₆₀₀) via spectrophotometry then diluted with ELGA water until OD₆₀₀=1. 953 μ L of strains PHL644 and PHL628 OD₆₀₀=1 was transferred to spectrophotometry cuvettes; every cuvette was devised as an individual experiment where one of the bacteria strains would be incubated with one polymer or one control. 47 μ L from 125 mM of polymers stocks (either dissolved in 5% AcOH in D₂O pH 2.9, 100 mM phosphate buffer pH 5.5, or sterile ELGA water) was added per cuvette, while controls were incubated with 47 μ L of either: 125 mM of free aldehydes in 5% AcOH in D₂O pH 2.9; 125 mM of free sugars in 5% AcOH in D₂O pH 2.9; 5% AcOH in D₂O pH 2.9; 100 mM phosphate buffer pH 5.5; or ELGA water.

The optic density of the incubated bacterial samples was measured at 600 nm for 24h. The samples were kept inside an incubator at 30 °C and 150 rpm between readings.

Fluorescent dyes stocks

Stocks of the green fluorescent dye SYTO 9 were prepared by mixing 4 μL of SYTO 9 with 96 μL of ELGA water. Stocks of the red fluorescent dye Propidium Iodide were prepared by mixing 200 μL of PI with 800 μL of ELGA water. Fluorescent stocks were maintained in a fridge protected from direct light. Both fluorescent dyes were purchased from Thermo Fisher Scientific.

Light and fluorescence microscopy

A microscope LEICA DM300 was used.

5 μL of SYTO 9 stocks and 150 μL of PI stocks were added to 1 ml cuvettes with 953 μL of bacteria that had been incubated with 47 μL polymers or controls 24 h prior, then they were incubated a further 15 minutes before taking samples. 10 μL of bacterial samples were taken from the bottom of the cuvettes and placed on a glass slide with a cover on top, a drop of immersion oil was placed on top of the cover and pictures were taken at 1000X. Each picture was taken by triplicates: one without any filter, one with a GFP filter, and an additional one with a RFP filter. GFP and RFP pictures were later merged using FIJI software (release 2017 May 30) to assemble the fluorescent viability pictures.

Heat shock treated bacteria

Overnight cultures of strains PHL644 were grown from single colonies following the standard growing conditions: 200 mL of LB on a 500 mL conical flask, at 30 °C, shaking of 150 rpm. This was followed by washing the bacteria centrifuging at 4000 rpm discarding the supernatant and adding an equivalent volume of sterile ELGA water. Bacterial pellets were resuspended via vortex agitation, and the process was repeated twice to ensure that most of the LB was eliminated. This step was performed to avoid any interference of the growth media with the incubation experiments. $\text{OD}_{600}=1$ in ELGA water bacteria was incubated at 70 °C for 2 h.

CFU experiments

953 μL of bacterial culture $\text{OD}_{600}=1$ was transferred to 1.5 mL centrifuge Eppendorf's then 47 μL of 125 mM polymers or controls were added to the bacteria for a total volume of 1 mL, then incubated at 30 °C and 150 rpm for 24 h. Each Eppendorf was sonicated on a water bath at 5 kHz for 10 minutes then vortexed until clusters were no longer noticeable on the liquid column, samples were taken and serial dilutions were performed in phosphate buffer that were plated in triplicates at a final dilution of 10^6 on LB agar that were incubated 30°C for 24 h.

Crystal violet assay

190.6 μL of strain PHL644 at $\text{OD}_{600}=1$ in ELGA water was transferred to 96 microtiter well plates, then incubated with 9.4 μL of 125 mM stocks of polymers or an equivalent volume of controls (9.4 μL of 125 mM D-glucose or 125 mM D-mannose dissolved in 5% AcOH in D_2O ; 9.4 μL of 5% AcOH in D_2O ; 9.4 μL of ELGA water). This experiment also had a negative control of 190.6 μL heat shock treated bacteria (dead) incubated with 9.4 μL of ELGA water.

The plates were then incubated for 24 h at 30°C 150 rpm. Following the incubation period, the plate was turned down removing the supernatant and planktonic bacteria, then gently submerging the plate into a tub of ELGA water, followed by a removal of the liquid to wash any remaining planktonic bacteria. The process was repeated once, then 200 µL of 0.5% w/v crystal violet solution in ELGA water was added in each well, then incubated for 30 minutes.

After the incubation procedure the crystal violet dye was removed, then submerged again in a tub of ELGA water to remove the remaining crystal violet not attached to the microtiter well plate walls. The dye removal was performed on a stack of laboratory roll paper, the process was repeated until no more crystal violet was rinsed with the water.

The next step was to add 200 µL of 95% ethanol to solubilize the crystal violet attached to the cells colonizing the abiotic surface of the plate and their EPS. The 95% ethanol was incubated for 10 minutes, then pipetted out into spectrophotometry cuvettes to measure the absorbance of the samples at 550 nm using 95% ethanol as a blank.

Confocal scanning laser microscopy

190.6 µL of PHL644 OD₆₀₀=1 was transferred to 2x5 microtiter glass flat bottom well plates then incubated them with 9.4 µL of 125 mM polymers to a final concentration of 6.17 mM of **P1**, **P4**, and **P5**, or an equivalent volume of controls (9.4 µL of 125 mM D-glucose or 125 mM D-mannose dissolved in 5% AcOH in D₂O; 9.4 µL of 5% AcOH in D₂O; 9.4 µL of ELGA water).

The plates were then incubated for 24 h at 30°C 150 rpm. 10 µL of phosphate buffer was added to the wells, then 1 µL of SYTO 9 stock and 30 µL of PI stock were added per well followed by an incubation period of 15 minutes. Stacked pictures of the wells were taken using a Nikon A1R inverted confocal/TIRF, every stacked picture was taken by triplicated using a laser with an excitation/emission of 488.0/490-560 for the green channel, a laser with 561.4/680-750 for the red channel, and an additional picture without any laser. Nikon proprietary software NIS elements 5.21 was used to merge the green and red channels and to provide a three-dimensional composition of the stacked pictures.

4. References

1. Dalton, H.M. and P.E. March, *Molecular genetics of bacterial attachment and biofouling*. Current Opinion in Biotechnology, 1998. **9**(3): p. 252-255.
2. Vert, M., et al., *TERMINOLOGY FOR BIORELATED POLYMERS AND APPLICATIONS (IUPAC RECOMMENDATIONS 2012)*. Handbook of Biochemistry and Molecular Biology, 5th Edition, ed. R.L. Lundblad and F.M. Macdonald. 2018. 885-902.
3. Romling, U. and C. Balsalobre, *Biofilm infections, their resilience to therapy and innovative treatment strategies*. Journal of Internal Medicine, 2012. **272**(6): p. 541-561.
4. Flemming, H.C. and J. Wingender, *The biofilm matrix*. Nature Reviews Microbiology, 2010. **8**(9): p. 623-633.
5. Patel, R., *Biofilms and antimicrobial resistance*. Clinical Orthopaedics and Related Research, 2005(437): p. 41-47.
6. Costa, O.Y.A., J.M. Raaijmakers, and E.E. Kuramae, *Microbial Extracellular Polymeric Substances: Ecological Function and Impact on Soil Aggregation*. Frontiers in Microbiology, 2018. **9**.
7. Flemming, H.C., et al., *Biofilms: an emergent form of bacterial life*. Nature Reviews Microbiology, 2016. **14**(9): p. 563-575.
8. Peng, J.S., W.C. Tsai, and C.C. Chou, *Inactivation and removal of Bacillus cereus by sanitizer and detergent*. International Journal of Food Microbiology, 2002. **77**(1-2): p. 11-18.
9. Goldberg, J., *Biofilms and antibiotic resistance: a genetic linkage*. Trends in Microbiology, 2002. **10**(6): p. 264-264.
10. Chen, M.J., Z. Zhang, and T.R. Bott, *Direct measurement of the adhesive strength of biofilms in pipes by micromanipulation*. Biotechnology Techniques, 1998. **12**(12): p. 875-880.
11. Lewis, K., *Persister cells and the riddle of biofilm survival*. Biochemistry-Moscow, 2005. **70**(2): p. 267-+.
12. Lewis, K., *Multidrug tolerance of biofilms and persister cells*, in *Bacterial Biofilms*, T. Romeo, Editor. 2008. p. 107-131.
13. Costerton, W., et al., *The application of biofilm science to the study and control of chronic bacterial infections*. Journal of Clinical Investigation, 2003. **112**(10): p. 1466-1477.
14. Marotta, M., et al., *Degradation of dental plaque glucans and prevention of glucan formation using commercial enzymes*. Process Biochemistry, 2002. **38**(1): p. 101-108.
15. Liesegang, T.J., *Contact lens - Related microbial keratitis .2. Pathophysiology*. Cornea, 1997. **16**(3): p. 265-273.
16. Bott, T.R., *Techniques for reducing the amount of biocide necessary to counteract the effects of biofilm growth in cooling water systems*. Applied Thermal Engineering, 1998. **18**(11): p. 1059-1066.
17. Klahre, J. and H.C. Flemming, *Monitoring of biofouling in papermill process waters*. Water Research, 2000. **34**(14): p. 3657-3665.
18. Halabi, M., et al., *Non-touch fittings in hospitals: a possible source of Pseudomonas aeruginosa and Legionella spp*. Journal of Hospital Infection, 2001. **49**(2): p. 117-121.
19. Kumar, C.G. and S.K. Anand, *Significance of microbial biofilms in food industry: a review*. International Journal of Food Microbiology, 1998. **42**(1-2): p. 9-27.
20. Yoo, J.A. and X.D. Chen, *An emission pattern of a thermophilic bacteria attached to or imbedded in porous supports*. International Journal of Food Microbiology, 2002. **73**(1): p. 11-21.
21. Nemati, M., G.E. Jenneman, and G. Voordouw, *Mechanistic study of microbial control of hydrogen sulfide production in oil reservoirs*. Biotechnology and Bioengineering, 2001. **74**(5): p. 424-434.

22. Scott, E., S.F. Bloomfield, and C.G. Barlow, *AN INVESTIGATION OF MICROBIAL-CONTAMINATION IN THE HOME*. Journal of Hygiene, 1982. **89**(2): p. 279-293.
23. Rayner, J., R. Veeh, and J. Flood, *Prevalence of microbial biofilms on selected fresh produce and household surfaces*. International Journal of Food Microbiology, 2004. **95**(1): p. 29-39.
24. Nicolella, C., M.C.M. van Loosdrecht, and J.J. Heijnen, *Wastewater treatment with particulate biofilm reactors*. Journal of Biotechnology, 2000. **80**(1): p. 1-33.
25. Wang, Z.-W. and S. Chen, *Potential of biofilm-based biofuel production*. Applied Microbiology and Biotechnology, 2009. **83**(1): p. 1-18.
26. Edwards, S.J. and B.V. Kjellerup, *Applications of biofilms in bioremediation and biotransformation of persistent organic pollutants, pharmaceuticals/personal care products, and heavy metals*. Applied Microbiology and Biotechnology, 2013. **97**(23): p. 9909-9921.
27. Tsoligkas, A.N., et al., *Engineering Biofilms for Biocatalysis*. Chembiochem, 2011. **12**(9): p. 1391-1395.
28. Qureshi, N., et al., *Biofilm reactors for industrial bioconversion processes: employing potential of enhanced reaction rates*. Microbial Cell Factories, 2005. **4**.
29. Jacqueline, C. and J. Caillon, *Impact of bacterial biofilm on the treatment of prosthetic joint infections*. Journal of Antimicrobial Chemotherapy, 2014. **69**: p. 37-40.
30. Sauer, F.G., et al., *Bacterial pili: molecular mechanisms of pathogenesis*. Current Opinion in Microbiology, 2000. **3**(1): p. 65-72.
31. Donlan, R.M., *Biofilms: Microbial life on surfaces*. Emerging Infectious Diseases, 2002. **8**(9): p. 881-890.
32. Kostakioti, M., M. Hadjifrangiskou, and S.J. Hultgren, *Bacterial Biofilms: Development, Dispersal, and Therapeutic Strategies in the Dawn of the Postantibiotic Era*. Cold Spring Harbor Perspectives in Medicine, 2013. **3**(4).
33. Pratt, L.A. and R. Kolter, *Genetic analysis of Escherichia coli biofilm formation: roles of flagella, motility, chemotaxis and type I pili*. Molecular Microbiology, 1998. **30**(2): p. 285-293.
34. Genevaux, P., S. Muller, and P. Bauda, *A rapid screening procedure to identify mini-Tn10 insertion mutants of Escherichia coli K-12 with altered adhesion properties*. Fems Microbiology Letters, 1996. **142**(1): p. 27-30.
35. Wood, T.K., et al., *Motility influences biofilm architecture in Escherichia coli*. Applied Microbiology and Biotechnology, 2006. **72**(2): p. 361-367.
36. O'Toole, G.A. and R. Kolter, *Flagellar and twitching motility are necessary for Pseudomonas aeruginosa biofilm development*. Molecular Microbiology, 1998. **30**(2): p. 295-304.
37. Klausen, M., et al., *Involvement of bacterial migration in the development of complex multicellular structures in Pseudomonas aeruginosa biofilms*. Molecular Microbiology, 2003. **50**(1): p. 61-68.
38. Klausen, M., et al., *Biofilm formation by Pseudomonas aeruginosa wild type, flagella and type IV pili mutants*. Molecular Microbiology, 2003. **48**(6): p. 1511-1524.
39. Watnick, P.I. and R. Kolter, *Steps in the development of a Vibrio cholerae El Tor biofilm*. Molecular Microbiology, 1999. **34**(3): p. 586-595.
40. Lemon, K.P., D.E. Higgins, and R. Kolter, *Flagellar motility is critical for Listeria monocytogenes biofilm formation*. Journal of Bacteriology, 2007. **189**(12): p. 4418-4424.
41. Prigent-Combaret, C., et al., *Developmental pathway for biofilm formation in curli-producing Escherichia coli strains: role of flagella, curli and colanic acid*. Environmental Microbiology, 2000. **2**(4): p. 450-464.
42. Pratt, L.A. and R. Kolter, *Genetic analyses of bacterial biofilm formation*. Current Opinion in Microbiology, 1999. **2**(6): p. 598-603.
43. Geesey, G.G., *Bacterial behavior at surfaces*. Current Opinion in Microbiology, 2001. **4**(3): p. 296-300.

44. Schmidt, J., et al., *The Pseudomonas aeruginosa Chemotaxis Methyltransferase CheR1 Impacts on Bacterial Surface Sampling*. Plos One, 2011. **6**(3).
45. Wu, Y. and F.W. Outten, *IscR Controls Iron-Dependent Biofilm Formation in Escherichia coli by Regulating Type I Fimbria Expression*. Journal of Bacteriology, 2009. **191**(4): p. 1248-1257.
46. Banin, E., M.L. Vasil, and E.P. Greenberg, *Iron and Pseudomonas aeruginosa biofilm formation*. Proceedings of the National Academy of Sciences of the United States of America, 2005. **102**(31): p. 11076-11081.
47. Dunne, W.M., *Bacterial adhesion: Seen any good biofilms lately?* Clinical Microbiology Reviews, 2002. **15**(2): p. 155-+.
48. Beloin, C., A. Roux, and J.M. Ghigo, *Escherichia coli biofilms*, in *Bacterial Biofilms*, T. Romeo, Editor. 2008. p. 249-289.
49. Hung, C.S., et al., *Structural basis of tropism of Escherichia coli to the bladder during urinary tract infection*. Molecular Microbiology, 2002. **44**(4): p. 903-915.
50. Waksman, G. and S.J. Hultgren, *Structural biology of the chaperone-ushe pathway of pilus biogenesis*. Nature Reviews Microbiology, 2009. **7**(11): p. 765-774.
51. Welch, R.A., et al., *Extensive mosaic structure revealed by the complete genome sequence of uropathogenic Escherichia coli*. Proceedings of the National Academy of Sciences of the United States of America, 2002. **99**(26): p. 17020-17024.
52. Hadjifrangiskou, M., et al., *Transposon Mutagenesis Identifies Uropathogenic Escherichia coli Biofilm Factors*. Journal of Bacteriology, 2012. **194**(22): p. 6195-6205.
53. Orndorff, P.E., et al., *Immunoglobulin-mediated agglutination of and biofilm formation by Escherichia coli K-12 require the type 1 pilus fiber*. Infection and Immunity, 2004. **72**(4): p. 1929-1938.
54. Duncan, M.J., et al., *The distinct binding specificities exhibited by enterobacterial type 1 fimbriae are determined by their fimbrial shafts*. Journal of Biological Chemistry, 2005. **280**(45): p. 37707-37716.
55. Martinez, J.J., et al., *Type 1 pilus-mediated bacterial invasion of bladder epithelial cells*. Embo Journal, 2000. **19**(12): p. 2803-2812.
56. Harris, S.L., et al., *ISOLATION AND CHARACTERIZATION OF MUTANTS WITH LESIONS AFFECTING PELLICLE FORMATION AND ERYTHROCYTE AGGLUTINATION BY TYPE-1 PILIATED ESCHERICHIA-COLI*. Journal of Bacteriology, 1990. **172**(11): p. 6411-6418.
57. Moreira, C.G., et al., *Role of type I fimbriae in the aggregative adhesion pattern of enteroaggregative Escherichia coli*. Fems Microbiology Letters, 2003. **226**(1): p. 79-85.
58. Beloin, C., et al., *Global impact of mature biofilm lifestyle on Escherichia coli K-12 gene expression*. Molecular Microbiology, 2004. **51**(3): p. 659-674.
59. Renner, L.D. and D.B. Weibel, *Physicochemical regulation of biofilm formation*. Mrs Bulletin, 2011. **36**(5): p. 347-355.
60. Smyth, C.J., et al., *Fimbrial adhesins: Similarities and variations in structure and biogenesis*. Fems Immunology and Medical Microbiology, 1996. **16**(2): p. 127-139.
61. Vidal, O., et al., *Isolation of an Escherichia coli K-12 mutant strain able to form biofilms on inert surfaces: Involvement of a new ompR allele that increases curli expression*. Journal of Bacteriology, 1998. **180**(9): p. 2442-2449.
62. Cookson, A.L., W.A. Cooley, and M.J. Woodward, *The role of type 1 and curli fimbriae of Shiga toxin-producing Escherichia coli in adherence to abiotic surfaces*. International Journal of Medical Microbiology, 2002. **292**(3-4): p. 195-205.
63. Uhlich, G.A., P.H. Cooke, and E.B. Solomon, *Analyses of the red-dry-rough phenotype of an Escherichia coli O157 : H7 strain and its role in biofilm formation and resistance to antibacterial agents*. Applied and Environmental Microbiology, 2006. **72**(4): p. 2564-2572.
64. Ghigo, J.M., *Natural conjugative plasmids induce bacterial biofilm development*. Nature, 2001. **412**(6845): p. 442-445.

65. Reisner, A., et al., *Development and maturation of Escherichia coli K-12 biofilms*. Molecular Microbiology, 2003. **48**(4): p. 933-946.
66. Romling, U., *Molecular biology of cellulose production in bacteria*. Research in Microbiology, 2002. **153**(4): p. 205-212.
67. Zogaj, X., et al., *Production of cellulose and curli fimbriae by members of the family Enterobacteriaceae isolated from the human gastrointestinal tract*. Infection and Immunity, 2003. **71**(7): p. 4151-4158.
68. Prigent-Combaret, C. and P. Lejeune, *Monitoring gene expression in biofilms*. Biofilms, 1999. **310**: p. 56-79.
69. Agladze, K., X. Wang, and T. Romeo, *Spatial periodicity of Escherichia coli K-12 biofilm microstructure initiates during a reversible, polar attachment phase of development and requires the polysaccharide adhesin PGA*. Journal of Bacteriology, 2005. **187**(24): p. 8237-8246.
70. Wang, X., J.F. Preston, and T. Romeo, *The pgaABCD locus of Escherichia coli promotes the synthesis of a polysaccharide adhesin required for biofilm formation*. Journal of Bacteriology, 2004. **186**(9): p. 2724-2734.
71. Danese, P.N., L.A. Pratt, and R. Kolter, *Exopolysaccharide production is required for development of Escherichia coli K-12 biofilm architecture*. Journal of Bacteriology, 2000. **182**(12): p. 3593-3596.
72. Harmsen, M., et al., *An update on Pseudomonas aeruginosa biofilm formation, tolerance, and dispersal*. Fems Immunology and Medical Microbiology, 2010. **59**(3): p. 253-268.
73. Friedman, L. and R. Kolter, *Two genetic loci produce distinct carbohydrate-rich structural components of the Pseudomonas aeruginosa biofilm matrix*. Journal of Bacteriology, 2004. **186**(14): p. 4457-4465.
74. Jackson, K.D., et al., *Identification of psl, a locus encoding a potential exopolysaccharide that is essential for Pseudomonas aeruginosa PAO1 biofilm formation*. Journal of Bacteriology, 2004. **186**(14): p. 4466-4475.
75. Ma, L., et al., *Analysis of Pseudomonas aeruginosa conditional Psl variants reveals roles for the Psl polysaccharide in adhesion and maintaining biofilm structure postattachment*. Journal of Bacteriology, 2006. **188**(23): p. 8213-8221.
76. Starkey, M., et al., *Pseudomonas aeruginosa Rugose Small-Colony Variants Have Adaptations That Likely Promote Persistence in the Cystic Fibrosis Lung*. Journal of Bacteriology, 2009. **191**(11): p. 3492-3503.
77. Leid, J.G., et al., *The exopolysaccharide alginate protects Pseudomonas aeruginosa biofilm bacteria from IFN-gamma-mediated macrophage killing*. Journal of Immunology, 2005. **175**(11): p. 7512-7518.
78. Fuqua, W.C., S.C. Winans, and E.P. Greenberg, *QUORUM SENSING IN BACTERIA - THE LUXR-LUXI FAMILY OF CELL DENSITY-RESPONSIVE TRANSCRIPTIONAL REGULATORS*. Journal of Bacteriology, 1994. **176**(2): p. 269-275.
79. Surette, M.G., M.B. Miller, and B.L. Bassler, *Quorum sensing in Escherichia coli, Salmonella typhimurium, and Vibrio harveyi: A new family of genes responsible for autoinducer production*. Proceedings of the National Academy of Sciences of the United States of America, 1999. **96**(4): p. 1639-1644.
80. Valentini, M. and A. Filloux, *Biofilms and Cyclic di-GMP (c-di-GMP) Signaling: Lessons from Pseudomonas aeruginosa and Other Bacteria*. Journal of Biological Chemistry, 2016. **291**(24): p. 12547-12555.
81. Simm, R., et al., *GGDEF and EAL domains inversely regulate cyclic di-GMP levels and transition from sessility to motility*. Molecular Microbiology, 2004. **53**(4): p. 1123-1134.
82. Hong, S.H., J. Lee, and T.K. Wood, *Engineering global regulator Hha of Escherichia coli to control biofilm dispersal*. Microbial Biotechnology, 2010. **3**(6): p. 717-728.

83. Rigolin, M.S.M., et al., *Effect of the aging of titanium and zirconia abutment surfaces on the viability, adhesion, and proliferation of cells and the adhesion of microorganisms*. Journal of Prosthetic Dentistry, 2019. **122**(6).
84. Bilgili, D., et al., *Surface properties and bacterial adhesion of bulk -fill composite resins*. Journal of Dentistry, 2020. **95**.
85. Hori, K. and S. Matsumoto, *Bacterial adhesion: From mechanism to control*. Biochemical Engineering Journal, 2010. **48**(3): p. 424-434.
86. Rijnaarts, H.H.M., et al., *DLVO and steric contributions to bacterial deposition in media of different ionic strengths*. Colloids and Surfaces B-Biointerfaces, 1999. **14**(1-4): p. 179-195.
87. Gottenbos, B., et al., *Initial adhesion and surface growth of Pseudomonas aeruginosa on negatively and positively charged poly(methacrylates)*. Journal of Materials Science-Materials in Medicine, 1999. **10**(12): p. 853-855.
88. Zhu, X.Y., et al., *Polyion Multi layers with Precise Surface Charge Control for Antifouling*. Acs Applied Materials & Interfaces, 2015. **7**(1): p. 852-861.
89. Kovacevic, D., et al., *Influence of Polyelectrolyte Multilayer Properties on Bacterial Adhesion Capacity*. Polymers, 2016. **8**(10).
90. Guo, S.S., et al., *Tailoring Polyelectrolyte Architecture To Promote Cell Growth and Inhibit Bacterial Adhesion*. Acs Applied Materials & Interfaces, 2018. **10**(9): p. 7882-7891.
91. Ueshima, M., et al., *Manipulation of bacterial adhesion and proliferation by surface charges of electrically polarized hydroxyapatite*. Journal of Biomedical Materials Research, 2002. **60**(4): p. 578-584.
92. Terada, A., et al., *The effect of surface charge property on Escherichia coli initial adhesion and subsequent biofilm formation*. Biotechnology and Bioengineering, 2012. **109**(7): p. 1745-1754.
93. Song, F., H. Koo, and D. Ren, *Effects of Material Properties on Bacterial Adhesion and Biofilm Formation*. Journal of Dental Research, 2015. **94**(8): p. 1027-1034.
94. Feng, G.P., et al., *Bacterial attachment and biofilm formation on surfaces are reduced by small-diameter nanoscale pores: how small is small enough?* Npj Biofilms and Microbiomes, 2015. **1**.
95. Lorenzetti, M., et al., *The Influence of Surface Modification on Bacterial Adhesion to Titanium-Based Substrates*. Acs Applied Materials & Interfaces, 2015. **7**(3): p. 1644-1651.
96. Yuan, Y., et al., *Surface characteristics influencing bacterial adhesion to polymeric substrates*. Rsc Advances, 2017. **7**(23): p. 14254-14261.
97. Verhorstert, K.W.J., et al., *In Vitro Bacterial Adhesion and Biofilm Formation on Fully Absorbable Poly-4-hydroxybutyrate and Nonabsorbable Polypropylene Pelvic Floor Implants*. Acs Applied Materials & Interfaces, 2020. **12**(48): p. 53646-53653.
98. Ozkan, E., et al., *Fabrication of Bacteria- and Blood-Repellent Superhydrophobic Polyurethane Sponge Materials*. Acs Applied Materials & Interfaces, 2020. **12**(46): p. 51160-51173.
99. Yoon, S.H., et al., *Superhydrophobic and superhydrophilic nanocomposite coatings for preventing Escherichia coli K-12 adhesion on food contact surface*. Journal of Food Engineering, 2014. **131**: p. 135-141.
100. Bollen, C.M.L., P. Lambrechts, and M. Quirynen, *Comparison of surface roughness of oral hard materials to the threshold surface roughness for bacterial plaque retention: A review of the literature*. Dental Materials, 1997. **13**(4): p. 258-269.
101. Medilanski, E., et al., *Influence of the surface topography of stainless steel on bacterial adhesion*. Biofouling, 2002. **18**(3): p. 193-203.
102. Arnold, J.W. and G.W. Bailey, *Surface finishes on stainless steel reduce bacterial attachment and early biofilm formation: Scanning electron and atomic force microscopy study*. Poultry Science, 2000. **79**(12): p. 1839-1845.

103. BoulangePetermann, L., J. Rault, and M.N. BellonFontaine, *Adhesion of Streptococcus thermophilus to stainless steel with different surface topography and roughness*. Biofouling, 1997. **11**(3): p. 201-&.
104. Flint, S.H., J.D. Brooks, and P.J. Bremer, *Properties of the stainless steel substrate, influencing the adhesion of thermo-resistant streptococci*. Journal of Food Engineering, 2000. **43**(4): p. 235-242.
105. Tide, C., et al., *The influence of welding procedures on bacterial colonization of stainless steel weldments*. Journal of Food Engineering, 1999. **42**(2): p. 85-96.
106. Scheuerman, T.R., A.K. Camper, and M.A. Hamilton, *Effects of substratum topography on bacterial adhesion*. Journal of Colloid and Interface Science, 1998. **208**(1): p. 23-33.
107. Cheng, Y.F., G.P. Feng, and C.I. Moraru, *Micro- and Nanotopography Sensitive Bacterial Attachment Mechanisms: A Review*. Frontiers in Microbiology, 2019. **10**.
108. Feng, G.P., et al., *Alumina surfaces with nanoscale topography reduce attachment and biofilm formation by Escherichia coli and Listeria spp.* Biofouling, 2014. **30**(10): p. 1253-1268.
109. Dickson, M.N., et al., *Nanopatterned polymer surfaces with bactericidal properties*. Biointerphases, 2015. **10**(2).
110. Garrido, K.D., et al., *Impact of conditioning film on the initial adhesion of E. coli on polysulfone ultrafiltration membrane*. Journal of Industrial and Engineering Chemistry, 2014. **20**(4): p. 1438-1443.
111. Barnes, L.M., et al., *Effect of milk proteins on adhesion of bacteria to stainless steel surfaces*. Applied and Environmental Microbiology, 1999. **65**(10): p. 4543-4548.
112. Parkar, S.G., et al., *Factors influencing attachment of thermophilic bacilli to stainless steel*. Journal of Applied Microbiology, 2001. **90**(6): p. 901-908.
113. Jullien, C., et al., *Physico-chemical and hygienic property modifications of stainless steel surfaces induced by conditioning with food and detergent*. Biofouling, 2008. **24**(3): p. 163-172.
114. Koo, H., et al., *Exopolysaccharides Produced by Streptococcus mutans Glucosyltransferases Modulate the Establishment of Microcolonies within Multispecies Biofilms*. Journal of Bacteriology, 2010. **192**(12): p. 3024-3032.
115. Hwang, G., et al., *The role of conditioning film formation in Pseudomonas aeruginosa PAO1 adhesion to inert surfaces in aquatic environments*. Biochemical Engineering Journal, 2013. **76**: p. 90-98.
116. Lazzara, T.D., et al., *Benefits and Limitations of Porous Substrates as Biosensors for Protein Adsorption*. Analytical Chemistry, 2011. **83**(14): p. 5624-5630.
117. Tuson, H.H. and D.B. Weibel, *Bacteria-surface interactions*. Soft Matter, 2013. **9**(17): p. 4368-4380.
118. Halder, P., et al., *A novel approach to determine the efficacy of patterned surfaces for biofouling control in relation to its microfluidic environment*. Biofouling, 2013. **29**(6): p. 697-713.
119. Lee, Y.K., et al., *Flow analysis and fouling on the patterned membrane surface*. Journal of Membrane Science, 2013. **427**: p. 320-325.
120. Marmur, A., *Underwater superhydrophobicity: Theoretical feasibility*. Langmuir, 2006. **22**(4): p. 1400-1402.
121. Epstein, A.K., et al., *Liquid-infused structured surfaces with exceptional anti-biofouling performance*. Proceedings of the National Academy of Sciences of the United States of America, 2012. **109**(33): p. 13182-13187.
122. Lai, C.Q., *Bacterial Attachment, Aggregation, and Alignment on Subcellular Nanogratings*. Langmuir, 2018. **34**(13): p. 4059-4070.
123. Dorken, G., et al., *Aggregation by depletion attraction in cultures of bacteria producing exopolysaccharide*. Journal of the Royal Society Interface, 2012. **9**(77): p. 3490-3502.

124. Perez-Soto, N., et al., *Engineering microbial physiology with synthetic polymers: cationic polymers induce biofilm formation in Vibrio cholerae and downregulate the expression of virulence genes* (vol 8, pg 5291, 2017). Chemical Science, 2018. **9**(39): p. 7715-7715.
125. Lindhorst, T.K., *Small Molecule Ligands for Bacterial Lectins: Letters of an Antiadhesive Glycopolymer Code*, in *Glycopolymer Code: Synthesis of Glycopolymers and their Applications*. 2015, RSC Polymer Chemistry Series. p. 1-16.
126. Yan, X.B., et al., *Glycopolymers as Antiadhesives of E. coli Strains Inducing Inflammatory Bowel Diseases*. Biomacromolecules, 2015. **16**(6): p. 1827-1836.
127. Petrie, L., et al., *Enumeration and characterization of iron(III)-reducing microbial communities from acidic subsurface sediments contaminated with uranium(VI)*. Applied and Environmental Microbiology, 2003. **69**(12): p. 7467-7479.
128. de Liphay, J.R., et al., *In situ exposure to low herbicide concentrations affects microbial population composition and catabolic gene frequency in an aerobic shallow aquifer*. Applied and Environmental Microbiology, 2003. **69**(1): p. 461-467.
129. von Canstein, H., et al., *Species diversity improves the efficiency of mercury-reducing biofilms under changing environmental conditions*. Applied and Environmental Microbiology, 2002. **68**(6): p. 2829-2837.
130. Löffler, F.E., K.M. Ritalahti, and S.H. Zinder, *DEHALOCOCCOIDES AND REDUCTIVE DECHLORINATION OF CHLORINATED SOLVENTS*, in *Bioaugmentation for Groundwater Remediation*, H.F. Stroo, A. Leeson, and C.H. Ward, Editors. 2013. p. 39-88.
131. Kruger, M.C., et al., *Bacterial metabolism of environmental arsenic-mechanisms and biotechnological applications*. Applied Microbiology and Biotechnology, 2013. **97**(9): p. 3827-3841.
132. Zhao, Y.X., et al., *Insights into biofilm carriers for biological wastewater treatment processes: Current state-of-the-art, challenges, and opportunities*. Bioresource Technology, 2019. **288**.
133. Wu, L., et al., *Denitrifying biofilm processes for wastewater treatment: developments and perspectives*. Environmental Science-Water Research & Technology, 2021. **7**(1): p. 40-67.
134. Ottengraf, S.P.P., *BIOLOGICAL-SYSTEMS FOR WASTE-GAS ELIMINATION*. Trends in Biotechnology, 1987. **5**(5): p. 132-136.
135. Sun, J., et al., *Sulfide removal and sulfur production in a membrane aerated biofilm reactor: Model evaluation*. Chemical Engineering Journal, 2017. **309**: p. 454-462.
136. Todhanakasem, T., et al., *Zymomonas mobilis Biofilm Reactor for Ethanol Production Using Rice Straw Hydrolysate Under Continuous and Repeated Batch Processes*. Frontiers in Microbiology, 2019. **10**.
137. Liu, D., et al., *Biobutanol production in a Clostridium acetobutylicum biofilm reactor integrated with simultaneous product recovery by adsorption*. Biotechnology for Biofuels, 2014. **7**.
138. Cotton, J.C., A.L. Pometto, and J. Gvozdenovic-Jeremic, *Continuous lactic acid fermentation using a plastic composite support biofilm reactor*. Applied Microbiology and Biotechnology, 2001. **57**(5-6): p. 626-630.
139. Soares, A., et al., *Recombinant protein expression in biofilms*. Aims Microbiology, 2019. **5**(3): p. 232-250.
140. Li, Z., et al., *Rapid recruitment of hydrogen-producing biofilms for hydrogen production in a moving bed biofilm reactor by a sequential immobilization and deoxygenization approach*. Bioresource Technology, 2020. **317**.
141. Chiefari, J., et al., *Living free-radical polymerization by reversible addition-fragmentation chain transfer: The RAFT process*. Macromolecules, 1998. **31**(16): p. 5559-5562.
142. Keddie, D.J., *A guide to the synthesis of block copolymers using reversible-addition fragmentation chain transfer (RAFT) polymerization*. Chemical Society Reviews, 2014. **43**(2): p. 496-505.

143. Ren, J.M., et al., *Star Polymers*. Chemical Reviews, 2016. **116**(12): p. 6743-6836.
144. Moad, G., *RAFT (Reversible addition-fragmentation chain transfer) crosslinking (co)polymerization of multi-olefinic monomers to form polymer networks*. Polymer International, 2015. **64**(1): p. 15-24.
145. Moad, G., *RAFT polymerization to form stimuli-responsive polymers*. Polymer Chemistry, 2017. **8**(1): p. 177-219.
146. Pereira, S.O., A. Barros-Timmons, and T. Trindade, *Polymer@gold Nanoparticles Prepared via RAFT Polymerization for Opto-Biodetection*. Polymers, 2018. **10**(2).
147. Boyer, C., et al., *Bioapplications of RAFT Polymerization*. Chemical Reviews, 2009. **109**(11): p. 5402-5436.
148. Jenkins, A.D., R.G. Jones, and G. Moad, *Terminology for reversible-deactivation radical polymerization previously called "controlled" radical or "living" radical polymerization (IUPAC Recommendations 2010)*. Pure and Applied Chemistry, 2010. **82**(2): p. 483-491.
149. Goto, A. and T. Fukuda, *Kinetics of living radical polymerization*. Progress in Polymer Science, 2004. **29**(4): p. 329-385.
150. Zhong, M.J. and K. Matyjaszewski, *How Fast Can a CRP Be Conducted with Preserved Chain End Functionality?* Macromolecules, 2011. **44**(8): p. 2668-2677.
151. Perrier, S., *50th Anniversary Perspective: RAFT Polymerization-A User Guide*. Macromolecules, 2017. **50**(19): p. 7433-7447.
152. Keddie, D.J., et al., *RAFT Agent Design and Synthesis*. Macromolecules, 2012. **45**(13): p. 5321-5342.
153. compiled by Alan, D.M. and W. Andrew, *Compendium of chemical terminology : IUPAC recommendations*. 1997: Second edition. Oxford [Oxfordshire] ; Malden, MA : Blackwell Science, 1997.
154. Gauthier, M.A., M.I. Gibson, and H.A. Klok, *Synthesis of Functional Polymers by Post-Polymerization Modification*. Angewandte Chemie-International Edition, 2009. **48**(1): p. 48-58.
155. Blasco, E., et al., *50th Anniversary Perspective: Polymer Functionalization*. Macromolecules, 2017. **50**(14): p. 5215-5252.
156. van Dongen, M.A., C.A. Dougherty, and M.M.B. Holl, *Multivalent Polymers for Drug Delivery and Imaging: The Challenges of Conjugation*. Biomacromolecules, 2014. **15**(9): p. 3215-3234.
157. Creese, O., *Linear polymers to target Vibrio cholerae adhesion and physiology*. 2019, University of Birmingham. p. 22.
158. Ji, K., et al., *Triazine-Substituted and Acyl Hydrazones: Experiment and Computation Reveal a Stability Inversion at Low pH*. Molecular Pharmaceutics, 2015. **12**(8): p. 2924-2927.
159. Lim, R.K.V. and Q. Lin, *Bioorthogonal chemistry: recent progress and future directions*. Chemical Communications, 2010. **46**(10): p. 1589-1600.
160. Godula, K. and C.R. Bertozzi, *Synthesis of Glycopolymers for Microarray Applications via Ligation of Reducing Sugars to a Poly(acryloyl hydrazide) Scaffold*. Journal of the American Chemical Society, 2010. **132**(29): p. 9963-9965.
161. Crisan, D.N., et al., *Poly(acryloyl hydrazide), a versatile scaffold for the preparation of functional polymers: synthesis and post-polymerisation modification*. Polymer Chemistry, 2017. **8**(31): p. 4576-4584.
162. Crisan, D.N., *Polymeric scaffolds as building blocks for nanomaterials with biomedical applications*. 2018, University of Birmingham.
163. Klein, T., et al., *FimH Antagonists for the Oral Treatment of Urinary Tract Infections: From Design and Synthesis to in Vitro and in Vivo Evaluation*. Journal of Medicinal Chemistry, 2010. **53**(24): p. 8627-8641.
164. Auernheimer, J., et al., *Photoswitched cell adhesion on surfaces with RGD peptides*. Journal of the American Chemical Society, 2005. **127**(46): p. 16107-16110.

165. Barbucci, R., et al., *VINYL-POLYMERS CONTAINING AMIDO AND CARBOXYLIC GROUPS AS SIDE SUBSTITUENTS .1. SYNTHESIS OF N-ACRYLOYL-GLYCINE AND N-ACRYLOYL-6-CAPROIC ACID AND THEIR GRAFTING ON CELLULOSE MEMBRANES*. Polymer, 1989. **30**(9): p. 1751-1757.
166. Montalbetti, C. and V. Falque, *Amide bond formation and peptide coupling*. Tetrahedron, 2005. **61**(46): p. 10827-10852.
167. Laursen, J.S., et al., *Cis-Trans Amide Bond Rotamers in beta-Peptoids and Peptoids: Evaluation of Stereoelectronic Effects in Backbone and Side Chains*. Journal of the American Chemical Society, 2013. **135**(7): p. 2835-2844.
168. Moss, G.P., *Basic terminology of stereochemistry*. Pure and Applied Chemistry, 1996. **68**(12): p. 2193-2222.
169. Yasayan, G., et al., *Well-defined polymeric vesicles with high stability and modulation of cell uptake by a simple coating protocol*. Polymer Chemistry, 2012. **3**(9): p. 2596-2604.
170. Skey, J. and R.K. O'Reilly, *Facile one pot synthesis of a range of reversible addition-fragmentation chain transfer (RAFT) agents*. Chemical Communications, 2008(35): p. 4183-4185.
171. Creese, O., et al., *Poly(Boc-acryloyl hydrazide): the importance of temperature and RAFT agent degradation on its preparation*. Polymer Chemistry, 2019. **10**(41): p. 5645-5651.
172. Ebdon, J.R., *Introduction to polymers (second edition) R. J. Young and P. A. Lovell Chapman and Hall, London, 1991. pp. 443, price £16.95. ISBN 0-412-30640-9 (PB); ISBN 0-412-30630-1 (HB)*. Polymer International, 1992. **27**(2): p. 207-208.
173. Gabriel, G.J., et al., *Infectious disease: Connecting innate immunity to biocidal polymers*. Materials Science & Engineering R-Reports, 2007. **57**(1-6): p. 28-64.
174. Priegue, J.M., J. Montenegro, and J.R. Granja, *Single-Nucleotide-Resolution DNA Differentiation by Pattern Generation in Lipid Bilayer Membranes*. Small, 2014. **10**(18): p. 3613-3618.
175. Szkop, M., B. Kliszcz, and A.A. Kasprzak, *A simple and reproducible protocol of glass surface silanization for TIRF microscopy imaging*. Analytical Biochemistry, 2018. **549**: p. 119-123.
176. Biggs, C.I., S. Edmondson, and M.I. Gibson, *Thiol-ene immobilisation of carbohydrates onto glass slides as a simple alternative to gold-thiol monolayers, amines or lipid binding*. Biomaterials Science, 2015. **3**(1): p. 175-181.
177. Sharma, G., et al., *Escherichia coli biofilm: development and therapeutic strategies*. Journal of Applied Microbiology, 2016. **121**(2): p. 309-319.
178. Tenaillon, O., et al., *The population genetics of commensal Escherichia coli*. Nature Reviews Microbiology, 2010. **8**(3): p. 207-217.
179. Reisner, A., et al., *Type 1 Fimbriae Contribute to Catheter-Associated Urinary Tract Infections Caused by Escherichia coli*. Journal of Bacteriology, 2014. **196**(5): p. 931-939.
180. Bachmann, B.J., *PEDIGREES OF SOME MUTANT STRAINS OF ESCHERICHIA-COLI K-12*. Bacteriological Reviews, 1972. **36**(4): p. 525-557.
181. Liu, B., et al., *Natural Escherichia coli isolates rapidly acquire genetic changes upon laboratory domestication*. Microbiology-Sgm, 2017. **163**(1): p. 22-30.
182. Muhldorfer, I. and J. Hacker, *GENETIC-ASPECTS OF ESCHERICHIA-COLI VIRULENCE*. Microbial Pathogenesis, 1994. **16**(3): p. 171-181.
183. Smith, H.W., *SURVIVAL OF ORALLY-ADMINISTERED ESCHERICHIA-COLI-K12 IN ALIMENTARY-TRACT OF MAN*. Nature, 1975. **255**(5508): p. 500-502.
184. Blattner, F.R., et al., *The complete genome sequence of Escherichia coli K-12*. Science, 1997. **277**(5331): p. 1453-+.
185. Peters, J.E., T.E. Thate, and N.L. Craig, *Definition of the Escherichia coli MC4100 genome by use of a DNA array*. Journal of Bacteriology, 2003. **185**(6): p. 2017-2021.
186. Xu, Y., et al., *An acid-tolerance response system protecting exponentially growing Escherichia coli*. Nature Communications, 2020. **11**(1).

187. Pienaar, J.A., A. Singh, and T.G. Barnard, *Acid-happy: Survival and recovery of enteropathogenic Escherichia coli (EPEC) in simulated gastric fluid*. Microbial Pathogenesis, 2019. **128**: p. 396-404.
188. Lin, J.S., et al., *COMPARATIVE-ANALYSIS OF EXTREME ACID SURVIVAL IN SALMONELLA-TYPHIMURIUM, SHIGELLA-FLEXNERI, AND ESCHERICHIA-COLI*. Journal of Bacteriology, 1995. **177**(14): p. 4097-4104.
189. Harden, M.M., et al., *Acid-Adapted Strains of Escherichia coli K-12 Obtained by Experimental Evolution*. Applied and Environmental Microbiology, 2015. **81**(6): p. 1932-1941.
190. Foster, J.W., *Escherichia coli acid resistance: Tales of an amateur acidophile*. Nature Reviews Microbiology, 2004. **2**(11): p. 898-907.
191. Entani, E., et al., *Antibacterial action of vinegar against food-borne pathogenic bacteria including Escherichia coli O157 : H7*. Journal of Food Protection, 1998. **61**(8): p. 953-959.
192. Ryssel, H., et al., *The antimicrobial effect of acetic acid-An alternative to common local antiseptics?* Burns, 2009. **35**(5): p. 695-700.
193. Stiefel, P., et al., *Is biofilm removal properly assessed? Comparison of different quantification methods in a 96-well plate system*. Applied Microbiology and Biotechnology, 2016. **100**(9): p. 4135-4145.
194. Guyot, S., et al., *Physiological responses of Escherichia coli exposed to different heat-stress kinetics*. Archives of Microbiology, 2010. **192**(8): p. 651-661.
195. Goulter, R.M., I.R. Gentle, and G.A. Dykes, *Issues in determining factors influencing bacterial attachment: a review using the attachment of Escherichia coli to abiotic surfaces as an example*. Letters in Applied Microbiology, 2009. **49**(1): p. 1-7.
196. Warnes, S.L., V. Caves, and C.W. Keevil, *Mechanism of copper surface toxicity in Escherichia coli O157:H7 and Salmonella involves immediate membrane depolarization followed by slower rate of DNA destruction which differs from that observed for Gram-positive bacteria*. Environmental Microbiology, 2012. **14**(7): p. 1730-1743.
197. Scharenberg, M., et al., *Kinetic Properties of Carbohydrate-Lectin Interactions: FimH Antagonists*. Chemmedchem, 2014. **9**(1): p. 78-83.